ABSTRACT

Title of dissertation: WAVE SCATTERING PROPERTIES IN COMPLEX SCATTERING SYSTEMS: ZEROS AND POLES OF THE SCATTERING MATRIX

Lei Chen
Doctor of Philosophy, 2022

Dissertation directed by: Professor Steven M. Anlage
Department of Physics

Wave scattering properties in complex scattering systems have been of great interest to both the physics and engineering communities because of their useful characterizations of such systems and significant value for applications. The most common tool for studying such properties – the scattering (S)-matrix, can be fully represented by its zeros and poles in the complex energy/frequency plane. There has been substantial effort to understand the scattering properties and wave phenomena inside complex systems in the past, both theoretical and experimental, which in turn has led to significant advancement in many applications: wavefront shaping (WFS), coherent perfect absorption (CPA), wireless power transfer, electromagnetic interference (EMI), etc.

In this dissertation, I will summarize the recent progress and interest regarding an intriguing wave phenomenon – coherent perfect absorption (CPA) in complex scattering systems. We have successfully implemented CPA protocols in generic complex scattering systems without any geometric or hidden symmetries, which greatly extends CPA beyond its initial concept as the time-reversal of a laser cavity. Under such efforts, we have also established a convenient approach

for control of the local losses inside the network system, which helped us to uncover the mystery of matching the imaginary part of the S-matrix zero to the uniform loss of the system. We thus developed the theoretical representation of the S-matrix by its zeros and poles, and generalized the traditional Wigner time delay to a complex quantity in sub-unitary scattering systems. We have revealed the inherent connection between the complex Wigner time delay and coherent perfect absorption, and can utilize the new complex Wigner time delay idea for extracting S-matrix zeros and poles in a practical system. We have also studied the statistical properties of the complex generalization of Wigner time delay for subunitary wave-chaotic scattering systems, and demonstrated excellent agreement between theory and experiments. Finally, we have extended this scheme to a comprehensive time delay analysis framework, including Wigner, transmission, and reflection time delays. This approach offers us the capability to systematically analyze the poles and zeros of the scattering matrix of any complex scattering system. We then apply the new transmission time delay method on a two-channel microwave graph realization of the Aharonov–Bohm ring from mesoscopic physics, and demonstrate the dependence of non-reciprocal transport behavior on the de-phasing rate.

The ultimate goal is to completely control the scattering properties of complex systems by manipulating the zeros and poles of the S-matrix, for example by adding losses in the system or changing the coupling of the scattering channels, etc. Such a capability will be extremely useful for understanding the wave properties of complex scattering systems, and for controlling the wave behavior in optics, electromagnetics, acoustics, quantum transport in condensed matter systems, etc.

WAVE SCATTERING PROPERTIES IN COMPLEX SCATTERING SYSTEMS: ZEROS AND POLES OF THE SCATTERING MATRIX

by

Lei Chen

Dissertation submitted to the Faculty of the Graduate School of the
University of Maryland, College Park in partial fulfillment
of the requirements for the degree of
Doctor of Philosophy
2022

Advisory Committee:
Professor Steven M. Anlage, Chair/Advisor
Professor Thomas M. Antonsen Jr.
Professor Cheng Gong
Professor Thomas E. Murphy
Professor Lourdes G. Salamanca-Riba, Dean's Representative

Dedication

To my beloved parents:

Hongyan Wu and Yuanxi Chen

Acknowledgments

It has been a long time since I started my Ph.D. journey. Now looking back, I am very proud of all the achievements I have done during my Ph.D., and I am excited about all the contributions I have made to the scientific world. Most importantly, all these accomplishments wouldn't have been possible without the enormous support I have received from my mentors, friends, and my family. I would like to show my sincere appreciation to those who have helped me along the way here.

Firstly, I would like to express my greatest gratitude to my advisor and mentor Prof. Steven M. Anlage. He is always enthusiastic and passionate about the advancement of science. It is such a pleasure talking with him on my research progress and discussing about recent experiments. There are not many advisors who not only have broad interests on various research topics but also know a lot of technical details. Prof. Anlage is one of them. I feel extremely luckily to have him as my advisor in my early career of doing fundamental research as a Ph.D. student. He has guided me into this field and helped me grow as an independent researcher.

I would also like to thank Prof. Thomas M. Antonsen Jr. and Prof. Edward Ott for their advice and guidance on various wave chaos projects. I sincerely admire their wisdom and insights as distinguished scientists. It is such an inspiration to see these smart people with great mindsets working in the field making scientific advancements. I would also like to express my gratitude to Prof. Tsampikos Kottos at Wesleyan University and Prof. Yan V. Fyodorov at King's College

London. My collaborations with them have formed a solid foundation for this dissertation, and have helped me develop my own appetite for research. I want to thank Prof. Cheng Gong, Prof. Thomas E. Murphy, and Prof. Lourdes G. Salamanca-Riba for serving on my disseration committee and offering valuable comments on my thesis.

Ph.D. life can be struggling, but it was a great experience working with my colleagues in the group. I would like to thank all group members Bakhrom Oripov, Seokjin Bae, Min Zhou, Shukai Ma, Jingnan Cai, Tamin Tai, Chung-Yang Wang, Jared Erb, Isabella Giovannelli, and Arthur Carlton-Jones, for all the happy times we have spent together and all the beautiful memories we shared. I am also thankful for all the fruitful discussions with Tornike Ghutishvili, Benjamin Frazier, and Farasatul Adnan. I would like to sincerely thank all my friends here at Maryland, inclduing Chen Bai, Jun Wang, Yuqian Hu, Yi Liu, Si Dong, and Shiyue Yu, for their companion and support. Their friendship has made this Ph.D. journey a precious experience in my life. It is impossible to remember all, and I apologize to those I've inadvertently left out.

Finally, I cannot thank enough to my family for their undying love and endless support. I am always confident and brave for all the challenges ahead of me, because my parents Hongyan Wu and Yuanxi Chen have unaltered faith in me. I am forever indebted to them, for all the things and efforts they have done to support me no matter who I am or who I want to become. I am grateful to my sister Xi Chen who loves and cares about me very much, and I thank Justin Wiechers for supporting me during my Ph.D. journey.

I would like to acknowledge the support from the AFOSR under COE Grant FA9550-15-10171, the ONR under Grants N000141912481, the DARPA WARDEN Grant No. HR00112120021, and the Maryland Quantum Materials Center.

Table of Contents

List of Figures

List of Abbreviations

AB	Aharonov–Bohm
AWG	Arbitrary Waveform Generator
BTRI	Broken Time-Reversal Invariance
CPA	Coherent Perfect Absorption
CST	Computer Simulation Technology
CWTD	Complex Wigner Time Delay
EMI	Electromagnetic Interference
FD	Frequency Domain
GOE	Gaussian Orthogonal Ensemble
GSE	Gaussian Symplectic Ensemble
GUE	Gaussian Unitary Ensemble
GWS	Generalized Wigner-Smith
PDF	Probability Density Function
$\mathcal{PT}$	Parity-Time
PTFE	polytetrafluoroethylene
RCM	Random Coupling Model
RF	Radio Frequency
RMT	Random Matrix Theory
S-matrix	Scattering Matrix
SMA	SubMiniature version A
SPCW	Silver Copper Clad Steel
TD	Time Domain
TR	Time-Reversal
TRI	Time-Reversal Invariance
TRIB	Time-Reversal Invariance Breaking

VNA Vector Network Analyzer

WFS Wavefont Shaping
WSO Wigner-Smith Operator
WTD Wigner Time Delay

Chapter 1: Introduction

1.1 Chaos and Complex Scattering Systems

Chaos is a very interesting and complex phenomenon in both theory and in the real world. A slight difference in the initial conditions would lead to surprisingly different long-term behaviors in such dynamical systems. Such unpredictable patterns and randomness have inspired people to develop the chaos theory in many areas: weather and climate, complex scattering, and even the stock market. In this dissertation I am focusing on the wave chaos aspect of this broad subject, and studying the wave scattering properties in a complex reverberant cavity. Such a system must be large enough compared to the wavelength, have multiple paths across or through it that result in wave interference, and be reverberant in character. The system should be complex (having many interfering paths for the waves) and not too simple. Fig. 1.1 demonstrates in a chaotic cavity how a slightly different initial condition for a ray would result in a vastly different ray trajectory after a few bounces. In the case of finite-wavelength waves, it is no longer possible to study their trajectory, but their propagation can be quite complex, filling the enclosed space very quickly [7]. There are many different kinds of chaotic cavities: a three-dimensional metallic GigaBox [8, 9], a two-dimensional quarter bow-tie billiard [10, 11], and one-dimensional graphs, etc. These cavities/billiards demonstrate wave chaotic behaviors, and produce universal statistical properties which can be well described by the Random Matrix Theory (RMT) [12–14]. However,

most practical systems also show deviations from universal chaotic behavior due to non-ideal coupling between the waves and the enclosure, short orbits [15], mixed chaotic and regular phase space [16] (perhaps arising from parallel walls or soft boundaries), inhomogeneous loss, etc. Thus it is far more important to develop and implement new semi-classical theory, for better characterization of such complex scattering systems in the real world.

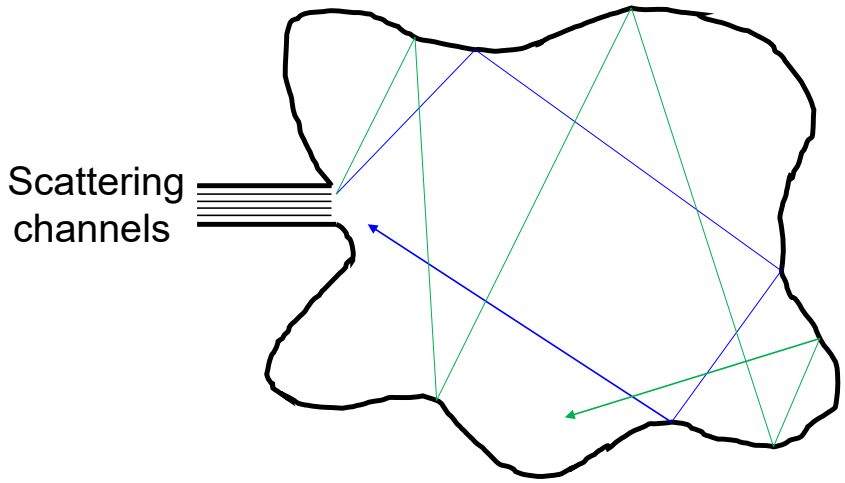

Figure 1.1: Schematic of a ray-chaotic enclosure connected to the outside world by a number of scattering channels. Shown are two chaotic ray trajectories in an irregular cavity due to different incident angles, but starting from the same location.

In order to study chaos and many complex scattering systems, the Wave Chaos Group at the University of Maryland has developed a powerful theory called the Random Coupling Model (RCM). The theory has worked out quite beautifully with experimental data and applies to many generic chaotic cavities [7, 17–26].

In the RCM, the fluctuating impedance matrix $\hat{Z}_{\text{cav}}$ of a chaotic cavity can be formulated as:

$$\hat{Z}_{\text{cav}} = i\text{Im}[\hat{Z}_{\text{rad}}] + \text{Re}[\hat{Z}_{\text{rad}}]^{1/2}\ \hat{z}\ \text{Re}[\hat{Z}_{\text{rad}}]^{1/2}, \tag{1.1}$$

where $\hat{Z}_{\text{rad}}$ is the radiation impedance matrix which describes the system-specific features related to the coupling ports (scattering channels), and $\hat{z}$ the normalized impedance matrix is an universal fluctuation quantity predicted by the random matrix theory (RMT). The normalized impedance matrix $\hat{z}$ can be modelled as:

$$\hat{z}(k_0) = -\frac{i}{\pi} \sum_n \frac{w_n w_n^T}{\frac{k_0^2 - k_n^2}{\Delta k^2} + i\alpha}, \tag{1.2}$$

where w_n describes the coupling coefficient of each mode n to the ports, k_0 is the wavenumber of interest, k_n is the wave number of mode n, Δk^2 is the mean mode spacing of the closed system, and α is the loss parameter defined to describe the uniform loss strength of the system ($\alpha = \frac{k_0^2}{\Delta k^2 Q}$, Q is the qualify factor of the closed system). In the RCM, the statistical fluctuating properties of the normalized impedance matrix $\hat{z}$ is only dependent on the single loss parameter α.

1.2 Microwave Networks and Quantum Graphs

Complex over-moded networks have been used to model mesoscopic quantum transport [27], electromagnetic energy propagation through multiply-connected arrays of compartments, and chains of coupled electromagnetic cavities [26]. In wave chaos studies [28–31], they have been proposed as a simple, yet powerful platform (Quantum Graph) which under specific conditions [32–34] demonstrates all generic wave phenomena of systems with underlying classical chaotic dynamics. Their main advantage is that they allow for an exact semiclassical expansion while their wave scattering description is particularly transparent, inspiring the development and implementation of semiclassical [28–30, 35] and super-symmetric [31–34, 36] tools. Specifically, fully connected networks with incommensurate bond-lengths, under specific conditions [32–34],

display universal statistical properties of various observables which are hypothesized to be described by random matrix theory (RMT) [12, 13]. In the case of fully connected networks with a small number of bonds [37], these deviations from RMT universality have already been identified in Ref. [28] (see also [35, 38]) using semiclassics and their origin has been traced back to the presence of short periodic orbits that are trapped along individual bonds of the graph. Subsequent theoretical studies [30–34, 36] have further established conditions under which RMT universality can be restored, while experimental implementations of graphs in the microwave realm [39–43] have provided additional evidence of the origin of these deviations [37, 44, 45]. Thus this microwave networks platform, being a typical complex scattering system without any geometric symmetries and with controlled time-reversal symmetries, and demonstrating both the extreme sensitivity to perturbations and typical deviations from universal statistical behavior [45] – due to system-specific features – is an ideal surrogate for studying wave scattering properties in real-world scattering systems.

1.3 Coherent Perfect Absorption

Coherent perfect absorption (**CPA**) has been appealing to physicists and engineers for both its fundamental and technological relevance. On the technological level its implementation promises the realization of a family of wave-based devices performing highly-selective and tunable absorption in a manner that goes beyond the traditional concept of impedance matching. On the fundamental level, CPA has initially been associated with the concept of time-reversal symmetry, one of the most fundamental symmetries in nature. In its original conception CPA was proposed as the time-reversal of a laser cavity [46, 47]: Specifically, it is a lossy cavity that

acts as a perfect interferometric trap for incident radiation, provided that its spatial distribution matches the one that would be emitted from the same cavity if the loss mechanism is substituted by a corresponding gain mechanism i.e. if the cavity turns into a laser. Practically speaking, the CPA process works by injecting waves of particular amplitude and phase (coherent illumination) [47] from a number of input channels and causing them to interfere and to be completely absorbed by losses in the system. Remarkably, even an arbitrarily small amount of loss can be used to completely absorb the incident radiation if the system is sufficiently reverberant [48].

1.4 Time Delays: Wigner, Transmission, and Reflection

Wigner time delay [49] is an extremely important physical quantity when considering the general problem of scattering from a complex system by means of excitations coupled through one or more scattering channels. The scattering matrix S describes the transformation of a set of input excitations on M channels into the set of outputs $|\psi_{\text{out}}\rangle$ as $|\psi_{\text{out}}\rangle = S\,|\psi_{\text{in}}\rangle$.

A measure of how long the excitation resides in the interaction region is provided by the time delay, related to the energy derivative of the scattering phase(s) of the system. This quantity and its variation with energy and other parameters can provide useful insights into the properties of the scattering region and has attracted research attention since the seminal works by Wigner [49] and Smith [50]. A review on theoretical aspects of time delays with emphasis to solid state applications can be found in [51]. Various aspects of time delay have recently been shown to be of direct experimental relevance for manipulating wave fronts in complex media [52–54]. Time delays are also long known to be directly related to the density of states of the open scattering system, see discussions in [51] and more recently in [55, 56].

In analogy to the Wigner time delay, people are also very interested in the transmission/reflection time delays [57–60]. Unlike Wigner time delay, the transmission and reflection time delays are always complex due to the fact that they are computed from sub-matrices of the full S-matrix, which are non-unitary even in the flux-conserving limit. The transmission/reflection time delays also have their own zeros and poles, which have direct impacts on the transmission/reflection property with many promising engineering applications [61–63].

1.5 Zeros and Poles of the S-matrix

The scattering (S)-matrix has been an extremely useful tool for characterizing the scattering properties of nearly any kind of scattering system. It can be modelled by the distribution of poles and associated zeros in the complex energy plane, which are most clearly seen when one addresses its determinant. In the unitary (zero loss) limit, the poles and zeros of the determinant form complex conjugate pairs across the real axis in the energy plane. In the presence of any loss, the poles and zeros are no longer complex conjugates, but if the loss is spatially-uniform their positions are still simply related by a uniform shift. This is no longer the case for spatially-localized losses, with poles and zeros migrating in a complicated way to new locations, subject to certain constraints. For a passive lossy system the poles always remain in the lower half of the complex energy plane, while the zeros can freely move between the two sides of the real axis. Among other things, rising recent interest in characterizing S-matrix complex zeros, as well as their manifestation in physical observables, is strongly motivated by the phenomenon of coherent perfect absorption [48], see [2, 57, 58, 64, 65] and references therein. In history, the poles of the S-matrix has been viewed as the excitation modes/resonances of the system, and now the zeros

of the S-matrix can be seen as the absorption modes/resonances of the system.

Lately, there has been renewed interest in the properties of the scattering matrix in the complex frequency plane [66]. This landscape is decorated with the poles and zeros of the scattering matrix, most of which lie off of the real frequency axis. Identifying the locations of these features gives tremendous insight into the scattering properties of the system, and the movement of these features in the complex plane as the system is perturbed is also of great interest. Knowledge of pole/zero information has practical application in the design of microwave circuits [67], microwave bandpass filters [61], (where uniformity of transmission time delay is critical [68]), transmission through mesoscopic structures [69], and the creation of embedded eigenstates [66, 70, 71], among many other examples. Knowledge of the S-matrix singularities in the complex plane allows one to create coherent virtual absorption through excitation of an off-the-real-axis zero [72], or virtual gain through the excitation of an off-the-real-axis pole [73], or resonant enhancement of the spontaneous-decay rate of quantum emitters in the vicinity of single plasmonic nanoparticles [74]. There is also interest in finding the non-trivial zeros of the Riemann zeta function by mapping them onto the zeros of the scattering amplitude of a quantum scattering system [75]. Perturbing a given system and bringing a scattering zero to the real axis enables coherent perfect absorption of all excitations incident on the scattering system [1,46,48]. Engineering the collision of zeros and poles to create new types of scattering singularities is also of interest for applications such as sensing [59, 60, 63, 66, 76].

1.6 Generalized Wigner-Smith Operator

The traditional Wigner-Smith time-delay operator Q is constructed from the S-matrix by way of a frequency derivative: $Q = -iS^{-1}dS/d\omega$. This matrix operator has been widely used to study the time delays, or "proper delay times", which describe the time dependence of a scattering process in the scattering channels [77–80]. People have used it to create particle-like scattering state [52,81,82], spatiotemporal control of light transmission [83], wavefront shaping in complex media [84, 85], and other applications. A more general class of Wigner–Smith operators was recently introduced [86] by generalizing Q to feature a derivative of S with respect to an arbitrary parameter x, rather than to just frequency ω. These generalized Wigner–Smith (GWS) operators can be written as $Q_x = -iS^{-1}dS/dx$, where the parameter x can be any meaningful parameter in the system which affects the scattering process. A couple of examples of x could be the rotation angle of the target which yields the angular momentum transferred to it; the target position which provides the momentum transfer; the radius of a circular target which gives control over the radiation pressure exerted on it; or the dielectric constant value which determines the wave intensity inside the target [54]. Other choices of x can be quite interesting as well, e.g. the magnetic flux, the control voltage of a meta-surface, the coupling strength of a port or channel, and etc. These parameters provide another degree of freedom for manipulating the zeros and poles of the S-matrix, thus offering more capability in engineering the scattering matrix/process [87].

1.7 Outline of the Dissertation

In Chapter 2, I will talk in more detail about Coherent Perfect Absorption (CPA), and some deficiencies associated with the previous efforts to measure CPA. Then we experimentally demonstrate the concept of coherent perfect absorption in a microwave graph constructed from coaxial cables connected by Tee-junctions. By adding a simple variable lossy attenuator into the system, we can effectively identify the CPA frequencies as the complex zeros of the scattering matrix which crosses the real axis and achieve perfect absorption in this chaotic setup. Most importantly, our experimental set-up allows us to demonstrate that the concept of CPA can be extended beyond the case where time-reversal (TR) symmetry holds, by introducing a circulator into the microwave graph. The contents discussed in this chapter is based on my published paper: Lei Chen, Tsampikos Kottos, and Steven M. Anlage, "Perfect Absorption in Complex Scattering Systems with or without Hidden Symmetries," *Nature Communications* **11**, 5826 (2020). [1]

In Chapter 3, more background material and previous research about the Wigner time delay will be introduced. The statistics of Wigner time delay in the lossless limit has been well studied by theorists, but relatively little research has been done for the case when loss or decoherence is present. In this chapter we will introduce a complex generalization of Wigner time delay by carefully considering the effects of introducing loss into the system. Through a series of experiments on microwave analogs of quantum graphs in which we have precision control of the loss strength inside the system, we demonstrate the evolution of the complex Wigner time delay spectrum along with the migration of the scattering matrix zeros and poles. This work further establishes a bridge between time delay and Coherent Perfect Absorption (CPA), offering new opportunities for achieving CPA at arbitrary energy/frequency in complex scattering systems. The analysis and

results in this study would be of great interest to researchers in wave/quantum chaotic scattering, mesoscopic physics, wavefront-shaping, perfect absorption, tunable metasurfaces, etc. The contents discussed in this chapter is based on my published paper: Lei Chen, Steven M. Anlage, and Yan V. Fyodorov, "Generalization of Wigner Time Delay to Sub-Unitary Scattering Systems," *Phys. Rev. E* **103**, L050203 (2021). [2]

In Chapter 4, after successful generalization of Wigner time delay to the sub-unitary scattering systems, more efforts about new statistics of the complex Wigner time delay will be shown. We study the statistical properties of the complex generalization of Wigner time delay τ_W for sub-unitary wave chaotic scattering systems. We first demonstrate theoretically that the mean value of the $\mathrm{Re}[\tau_W]$ distribution function for a system with uniform absorption strength η is equal to the fraction of scattering matrix poles with imaginary parts exceeding η. The theory is tested experimentally with an ensemble of microwave graphs with either one or two scattering channels, and showing broken time-reversal invariance and variable uniform attenuation. The experimental results are in excellent agreement with the developed theory. The tails of the distributions of both real and imaginary time delay are measured and are also found to agree with theory. The results are applicable to any practical realization of a wave chaotic scattering system in the short-wavelength limit, including quantum wires and dots, acoustic and electromagnetic resonators, and quantum graphs. The contents discussed in this chapter is based on my published paper: Lei Chen, Steven M. Anlage, Yan V. Fyodorov, "Statistics of Complex Wigner Time Delays as a counter of S-matrix poles: Theory and Experiment," *Phys. Rev. Lett.* **127**, 204101 (2021). [3]

In Chapter 5, we will develop a more comprehensive time delay analysis framework as an extension to the complex Wigner time delay analysis method. We identify the poles and zeros of the scattering matrix of a simple quantum graph by means of systematic measurement and

analysis of Wigner, transmission, and reflection complex time delays. We examine the ring graph because it displays both shape and Feshbach resonances, the latter of which arises from an embedded eigenstate on the real frequency axis. Our analysis provides a unified understanding of the so-called shape, Feshbach, electromagnetically-induced transparency, and Fano resonances, on the basis of the distribution of poles and zeros of the scattering matrix in the complex frequency plane. It also provides a first-principles understanding of sharp resonant scattering features, and associated large time delay, in a variety of practical devices, including photonic microring resonators, microwave ring resonators, and mesoscopic ring-shaped conductor devices. Our analysis is the first use of reflection time difference, as well as the first comprehensive use of complex time delay, to analyze experimental scattering data. The contents discussed in this chapter is based on my published paper: Lei Chen and Steven M. Anlage, "Use of Transmission and Reflection Complex Time Delays to Reveal Scattering Matrix Poles and Zeros: Example of the Ring Graph," *Phys. Rev. E* **105**, 054210 (2022). [4]

In Chapter 6, I will demonstrate a two-channel microwave graph realization of the Aharonov–Bohm ring, and study its scattering properties in both the frequency domain and the time domain. We mimic the non-reciprocal mesoscopic transport behavior with a microwave gyrator, made up of circulators and open/short circuits. The objective is to demonstrate anisotropic transport in the presence of finite de-phasing, in the intermediate regime between purely quantum and purely classical transport. We study the time delay properties of the Aharonov–Bohm ring graph through simulation and experiment, both in the frequency domain and the time domain. We demonstrate the non-reciprocal transport properties with the Aharonov–Bohm ring graph as a function of attenuation, and show the 3:1 ratio of the transmission time delays in both directions. This establishes the analogy between mesoscopic and microwave Aharonov–Bohm rings, and offers the

capability of simulating a non-trivial mesoscopic conductor with a microwave graph.

In the end, Chapter 7 will conclude all previous work and results in this dissertation. I will talk about the future work and other potential interests related to this work. The importance of this dissertation research and how it can lead to various interesting applications will also be discussed.

Chapter 2: Perfect Absorption in Complex Scattering Systems

2.1 Overview

CPA phenomena have been theoretically proposed in a number of contributions [46, 64, 65, 88–92], but only a few experimental works have reported a realization of CPA. At first it was demonstrated with free-space counter-propagating waves impinging on lossy slabs in the form of semiconductors [47], metasurfaces [93], graphene-based structures [94], Parity-Time ($\mathcal{PT}$) symmetric electronic circuits [95] and $\mathcal{PT}$-symmetric quantum well waveguides that act as both a laser and CPA absorber [96], and acoustic systems [97, 98]. Multi-port CPA was also achieved using a diffraction grating and lossy plasmonic modes (this work employed a pair of non-reciprocal scattering channels, but did not break time-reversal invariance) [99]. Most of these experimental demonstrations of CPA have generally been performed in open systems with freely counter-propagating waves arriving on a loss center at normal incidence. Such a configuration puts a strong constraint on the loss required to achieve CPA (e.g. 50% single-beam absorption [100]), and this is a significant limitation of such free space optical approaches. In summary, these early demonstrations used highly symmetric structures and excitation conditions to achieve CPA. Now the challenge is to considerably generalize the phenomenon and realize CPA in complex wave settings without special geometrical or hidden symmetries. It is clear that reverberations, hypersensitive complex interference, and system specific characteristics (e.g.

bouncing orbits in stadium billiards, coexistence of islands of regular dynamics in a chaotic sea of phase space of the underlying ray settings, mixed symmetries etc) blended with losses present in complex wave systems constitute a challenge for achieving CPA. Recently a demonstration of CPA was achieved in a multiple scattering environment with many input and output channels, implementing effectively a time-reversal of a random laser [101]. This demonstration, however, utilized the conventional anti-laser concept, and is limited to a mechanically-tunable loss element. It is desirable to expand the range of CPA to include complex and chaotic scattering environments of all kinds. Importantly, one has to investigate the applicability of CPA under controllable time-reversal symmetry violation conditions.

In more precise terms, there are a number of deficiencies associated with the previous efforts to measure CPA. Some of these schemes failed to directly measure the outgoing waves from the system, but deduced the CPA condition by calculating the output signals based upon combinations of data (usually the scattering matrix) taken under other (non-CPA) conditions. Obviously, a CPA platform that will allow for a direct measurement of the output signal will open-up many technological opportunities, as proposed in the photonic context [48]. Secondly, the degree to which the CPA condition is achieved has only been quantitatively demonstrated to a limited extent, typically 1 part in 10^2, not at all close to the expected ideal outcome. Third, the previous experimental efforts have implemented loss in a way that is difficult to control and systematically vary, such as the thickness of a slab, or the temperature variation of conductivity. Finally, all previous works have been limited to systems that display time-reversal invariance (**TRI**) for the wave propagation (beyond the trivial TRI-breaking effects of dissipation).

Here we experimentally demonstrate the concept of coherent perfect absorption in a generalized setting where the weakly lossy cavity is a complex scattering system without any spe-

cial geometric symmetries. We implement this scenario using a fully connected microwave network constructed from coaxial cables connected by Tee-junctions. By adding a convenient electronically-tuned lossy attenuator, we can continuously and precisely control the nearly ideal CPA conditions, thus clearly identifying the CPA frequencies as the complex zeros of the scattering matrix which cross the real frequency axis and achieving perfect absorption in this complex scattering setting. Most importantly, our experimental set-up allows us to demonstrate that the concept of CPA can be extended beyond the case where time-reversal (**TR**) symmetry holds, greatly expanding the impact and utility of the CPA phenomenon. The latter can be achieved by introducing a circulator into the microwave graph [40]. Such analysis proves that the concept of CPA goes far beyond its initial conception as a "time-reversed laser". Our experimental platform, due to its elegant simplicity, provides a convenient tool for the study of CPA in generic complex scattering systems having neither geometric nor dynamical symmetries. Importantly, it can be employed for the development of semiclassical schemes that utilize system-specific characteristics [55, 102, 103] aiming to the optimization of CPA traps. Finally, we have also confirmed the viability of CPAs in a two-dimensional quarter bow-tie chaotic billiard demonstrating beyond doubt that their formation occurs irrespective of the degree of complexity of the scattering process. Our results are general and apply to a variety of complex (i.e. without geometric or hidden symmetries) wave settings, ranging from optics and microwaves to acoustics and matter waves.

2.2 Experimental Setup for S-matrix Measurement

Our experiment utilizes a tetrahedral microwave graph formed by coaxial cables and Tee-junctions [37, 104]. A variable attenuator is attached to one internal node of the graph (see Fig.

2.1). The system is coupled to external transmission lines attached to N specific nodes of the graph. In our specific set-up we utilize $N = 2$. Each coupling transmission line (red solid lines in Fig. 2.1) is a coaxial cable supporting a single propagating mode connecting to one port of the Vector Network Analyzer (VNA). The plane of calibration of the VNA is at the point where the transmission line attaches to the port of the graph (see red dashed line in Fig. 2.1). The S-matrix of the experimental setup is measured under many settings of the variable attenuator.

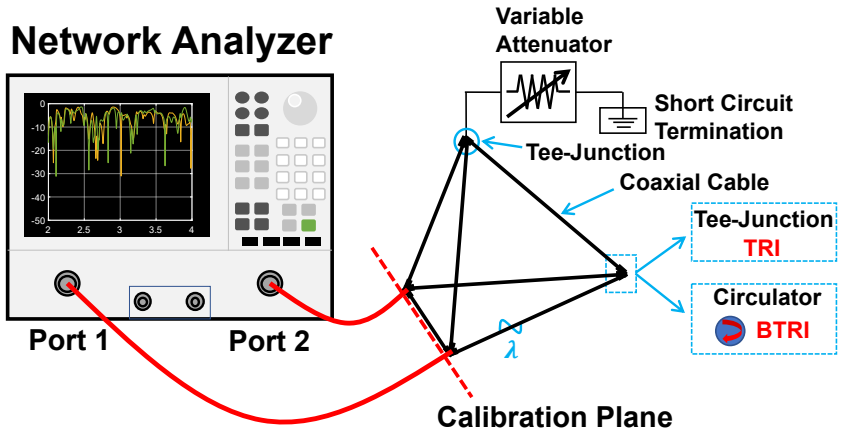

Figure 2.1: Schematic experimental setup of the S-matrix measurement. The tetrahedral graph is formed by coaxial cables connected with Tee-junctions. One node of the graph is loaded with a voltage variable attenuator to provide parametric variation of the scattering system. One other node (blue dashed box) is made from either a Tee-junction (TRI) or a 3-port circulator (BTRI) to create a TRI system or a broken-TRI system, respectively.

The tetrahedral microwave graph used in this work is constructed from six coaxial cables connected by coaxial Tee-junctions. The cables are semi-flexible SF-141 coaxial cables, each of different length, with SMA male connectors on both ends (Model SCA49141) obtained from Fairview Microwave, Inc. The dielectric material of the cable is solid polytetrafluoroethylene (PTFE), which has a relative dielectric constant of 2.1. The inner conductor of the cable is silver plated copper clad steel (SPCW), and has a diameter of 0.036 inch (0.92 mm); while the outer shield is a copper-tin composite which has an inner diameter of 0.117 inch (2.98 mm). The di-

electric loss tangent of the medium is $\tan\delta = 0.00028$ at 3 GHz, and the resistivity of the metals in the cable is $\rho = 4.4 \times 10^{-8}\ \Omega \cdot \text{m}$ at 20 °C. Both of these contribute to the uniform loss of the coaxial cables. The lengths of the six cables are 13, 14, 15, 16, 18 and 20 inch. The total length of the graph is then approximately 2.44 m, giving rise to a mean spacing between modes of 42.4 MHz, which is constant as a function of frequency. On one node of the graph (see Fig. 2.1), two Tee-junctions form a four-way adapter where a voltage variable attenuator (HMC346ALC3B from Analog Devices, Inc.) is connected to one connector. A short circuit termination is connected to the other end of the attenuator. Using a Keithley power supply (2231A-30-3), the attenuation of the variable attenuator is continuously swept by varying the supplied voltage from 4.00 V to 7.00 V. To find the appropriate CPA condition of the setup, we perform the S-matrix measurement of the graph (using the PNA-X N5242A from Agilent Technologies, Inc.) in the frequency range from 10 MHz to 18.01 GHz (at 96,001 equidistant frequency points) which includes about 420 modes of the closed graph, with varying attenuation from about 2 dB to 12 dB (which includes the insertion loss of the variable attenuator). The attenuation is swept with a step size of roughly 0.1 dB. In the case of a BTRI microwave graph, a ferrite circulator (Model CT-3042-O from UTE Microwave Inc.) is added to one node of the graph (see Fig. 2.1). The circulator has an operational frequency range from 2 GHz to 4 GHz, which constrains the frequency range of measurement accordingly. By connecting the microwave graph to a two-port VNA, with a coupling strength of about 0.68, we can obtain the S-matrix of the system under different attenuation configurations.

2.3 Results

2.3.1 Analysis of the CPA State

The wave transport properties of the microwave network are succinctly summarized by the $N \times N$ complex scattering matrix S. The latter connects the incoming and outgoing waves through these N channels as $\phi_{\rm out} = S\phi_{\rm in}$, where $\phi_{\rm out}$ ($\phi_{\rm in}$) is an N-component vector of outgoing (incoming) wave amplitudes and phases that defines the scattered outgoing (incoming) field in the channel-mode space. In the case of coherent perfect absorption all input energy is absorbed by the system, thus requiring $\phi_{\rm out}$ to be zero. This physical condition is mathematically formulated by the requirement that $S\phi_{\rm in} = 0$ for non-zero $\phi_{\rm in}$. The latter condition is equivalent to the requirement that the S-matrix is not invertible i.e. it has a zero eigenvalue $\lambda_S = 0$. The associated eigenvector provides the incident waveform configuration that leads to a CPA. Note that this requirement does not violate any constraints of the S-matrix, which in the case of CPAs is sub-unitary due to the presence of an absorbing center inside the scattering domain. Let us finally point out that both the scattering matrix $S = S(\omega)$ and consequently its eigenvalues $\lambda_S = \lambda_S(\omega)$ are functions of the frequency ω of the incident waveform. From the mathematical perspective, one cannot exclude the possibility to have complex ω's as roots of the CPA condition $\lambda_S(\omega) = 0$. These complex zeros, however, are unphysical since they do not correspond to incident propagating plane waves and therefore have to be excluded from the set of acceptable CPA solutions. Of course, the reality of ω is not an issue in the experimental analysis since the measured S-matrix is always evaluated at real frequencies. From the above discussion, we deduce that a specific cavity (corresponding to a fixed connectivity, lengths of the cables of the graph, and loss strength) might

support multiple CPAs i.e. different frequencies $\omega \neq \omega'$ for which the corresponding sub-unitary scattering matrices $S(\omega) \neq S(\omega')$ have a zero eigenvalue in their spectrum. We speculate that such multiple CPA scenarios will have higher probability to occur when the scattering matrices $S(\omega)$ and $S(\omega')$ are uncorrelated – a property that can be quantified by the rate with which the autocorrelation function $C(\chi) \equiv \mathcal{R}e\left\{\langle S_{\alpha,\beta}(\omega) S^*_{\alpha',\beta'}(\omega+\chi)\rangle\right\}$ goes to zero ($\langle\cdots\rangle$ indicates a spectral averaging). An interesting future research effort would be to identify rigorous conditions under which such multiple CPAs can occur. We point out that a related analysis for the density of complex zeros of the S-matrix of a chaotic system has been recently carried out in [65] (see also Ref. [58]).

A straightforward way to determine experimentally the CPA conditions is via a direct evaluation of the eigenvalues $\{\lambda\}$ of the measured S matrix and subsequent identification of the frequency ω for which the spectrum contains a zero. Such a direct process, however, is tedious and in many occasions it turns out to be ineffective in our search for a true zero eigenvalue of the scattering matrix. Instead, we have utilized the parametric dependence of the S-matrix on the local attenuation strength in order to establish the zero eigenvalue condition. Specifically, we exploit simultaneously the frequency (wavelength) and local losses (attenuation) as two free parameters which allow us to exploit a larger parameter space for the identification of true S-matrix zeros. Once the CPA condition is satisfied, the required local loss and stimulus frequency are identified, and the corresponding S-matrix eigenvector which defines the CPA incoming stimulus wave amplitudes and phases (i.e. coherent excitation) is evaluated. The corresponding injected coherent monochromatic waveform results in a zero outgoing signal from all N scattering channels of the system. It should be noted that this procedure is entirely general and doesn't depend on the nature of the wave physics setting or on the degree of chaoticity that characterize the wave scattering

process in the system.

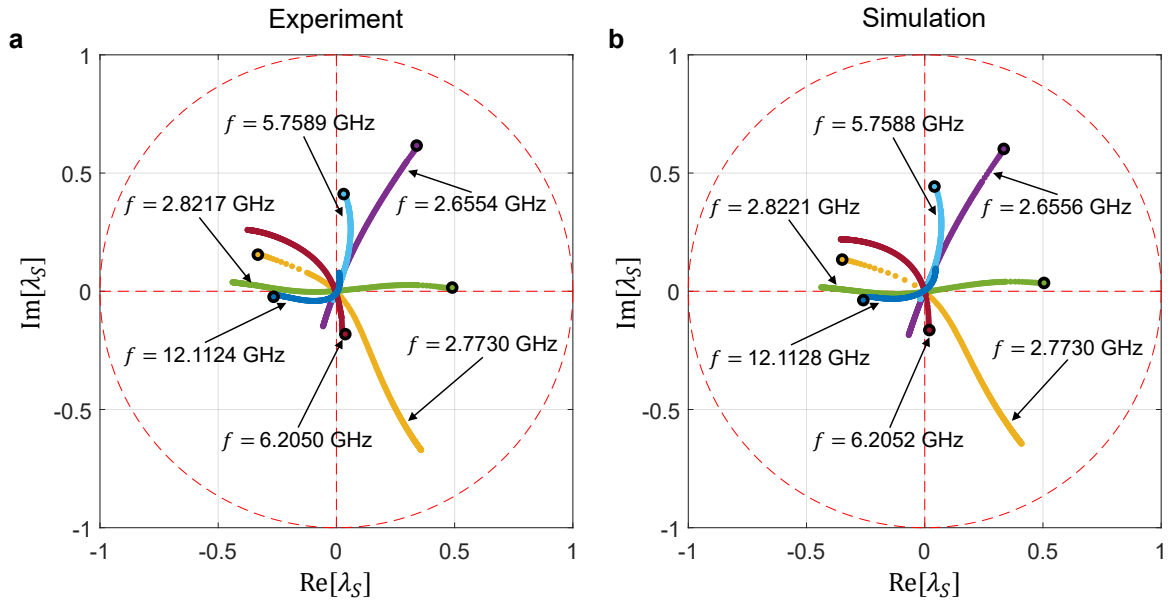

Figure 2.2: Plot of selected S-matrix eigenvalues as a function of attenuator setting in the tetrahedral graph showing examples of near-zero-crossing trajectories. Selected eigenvalues of the S-matrix are plotted in the complex λ_S plane, where the red dashed circle represents the unit circle. The panel **a** shows experimental data, while panel **b** shows data from the simulation. Each trajectory represents one frequency (color coded), and the corresponding frequency for each trace is labelled in the figure. The black circle at the start of every trajectory indicates the initial eigenvalue at minimum attenuation, and as attenuation increases, the eigenvalue goes nearly through the origin in the complex plane. This figure is taken from Ref. [1].

Following this approach, the 2×2 scattering matrix of the graph is acquired using the setup of Fig. 2.1. The measurement is taken from 10 MHz to 18 GHz which includes about 420 modes of the closed graph. The calibrated S-matrix of the 2-port graph is then measured under different attenuation settings ranging from 2 dB to 12 dB (which includes the insertion loss of the variable attenuator). Implementing a matrix diagonalization technique, the complex eigenvalues λ_S of the S-matrix are found for each frequency and attenuator setting. A limited number of these eigenvalues are found to approach the origin in the complex λ_S plane (see Fig. 2.2). These near-zero crossings are then examined in detail. Through this method, the specific frequencies

and attenuation values at the zero-crossing CPA state, as well as the required excitation relative magnitude and phase at the two ports (S-matrix eigenvector) are then determined.

To compare with the experimental results, we set up a comparable simulation model in CST (Computer Simulation Technology) Studio. CST is commercial software specifically designed for electromagnetic field simulation, and we use the Circuits & Systems module to simulate the microwave graph. All individual components in the graph experiment, e.g. coaxial cables and Tee-junctions, are modeled by their measured S-matrix data at the exact same frequency points used in the experiment. The S-matrix data for the variable attenuator are measured at the designated supply voltages from 4.00 V to 7.00 V. The S-matrix data are imported as TOUCHSTONE file blocks in the simulation model, and correctly capture the electrical characteristics of all components. The imported S-matrices are then combined in the same topology as the graph of interest. Therefore, following the same procedure as in the experiment, we can verify the CPA phenomena in the simulation as well.

2.3.2 Verification of the CPA State

Using the information obtained from the S-matrix measurement, the CPA conditions are identified, and we can directly test them experimentally. In order to create the coherent stimulus signals, we use a two-source VNA (PNA-X N5242A from Agilent Technologies, Inc.) to serve as the RF signal source and measure the incoming and outgoing wave energies as well. The PNA-X has two built-in RF sources which provides great convenience for us to individually adjust the amplitudes of the two input excitation signals. The relative phase difference of the two input signals is controlled by adding a manual coaxial phase shifter (Model 3753B from L3Harris

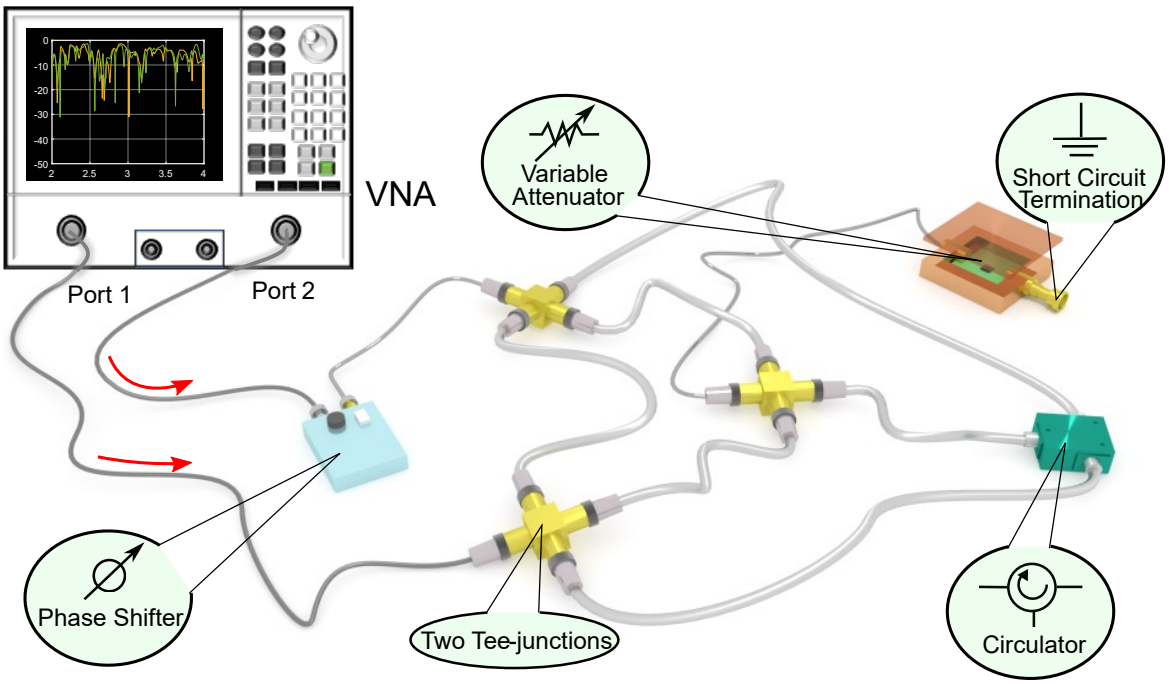

Figure 2.3: Experimental setup of the CPA state measurement. A PNA-X (network analyzer with two internal sources) is used to generate microwaves with well-defined frequency and relative amplitudes at the two ports as the CPA state excitation signals. Coherent phase control between the two excitation signals is realized by placing a phase shifter between port 2 of the network analyzer and the graph. The outgoing and returning waves are directly measured by the PNA-X. On the right side of the figure is the tetrahedral microwave graph formed by coaxial cables and Tee-junctions. The four-way adapter shown in the figure is realized by connecting two Tee-junctions together in the real experiment. One node of the graph is loaded with a variable attenuator to provide parametric variation of the scattering system. One other node is made from either a Tee-junction (TRI) or a 3-port circulator (BTRI) to create a TRI system or a broken-TRI system, respectively. This figure is taken from Ref. [1].

Narda-MITEQ) between the VNA and port 2 of the graph (see Fig. 2.3). When signals are sent from both ports of the network analyzer simultaneously, it should be possible to observe the coherent perfect absorption, namely no microwave signals should emerge from the graph through either of the ports. The VNA measures both the outgoing and incoming waves at the plane of calibration, hence the CPA condition can be directly confirmed with this setup.

2.3.3 Observation of the CPA State in the TRI System

Under the CPA condition, a nearly perfect absorption is achieved, and it has been verified using four independent parametric sweep measurements (see Fig. 2.4). Both experimental and numerical data are plotted in the same figure. Parameters swept include the microwave frequency (wavelength), attenuation of the variable attenuator embedded in the graph, amplitude of excitation signal at port 1, and phase of excitation signal at port 2, while keeping other settings unchanged at the CPA condition. The input wave power and outgoing wave power are directly measured while changing the system configuration or the input stimulus setting. The ratio of outgoing signal power over input signal power ($P_{\text{out}}/P_{\text{in}}$) acquires values as low as 10^{-5} at the CPA condition, and both experiment and simulation show similar behavior upon deviation from the CPA conditions. Fig. 2.4 demonstrates that the minimum outgoing power is measured at precisely the CPA condition, and rapidly increases in a cusp-like manner as any of the parameters deviate from that condition.

To emphasize the importance of having a reverberant cavity instead of a bare attenuator only, we measure the power ratio of the bare attenuator (see Fig. 2.4(b) inset) under the same settings as in the complex networks. From the inset, we can see that in the absence of the graph, the attenuator can only absorb a small fraction of the incident power ($P_{\text{out}}/P_{\text{in}} > 10^{-1}$). This illustrates the importance of having the complex network as the cavity to create the CPA condition.

Due to the extreme sensitivity to perturbations and internal system details, it is naturally difficult to create a numerical model of a complex scattering system that reproduces all of its properties in detail. The numerical simulations in Figs. 2.2, 2.4 and 2.7 are based on S-parameter mea-

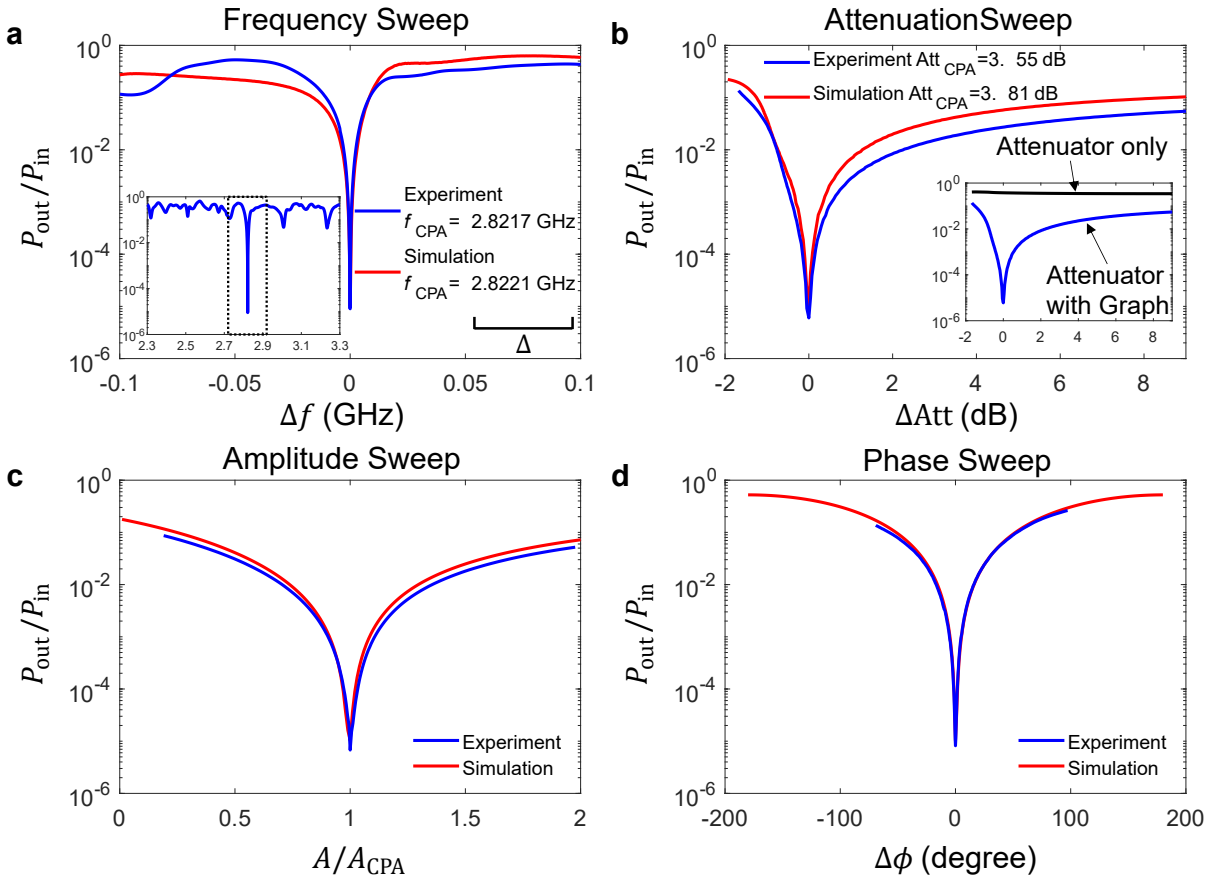

Figure 2.4: Evidence of CPA in the complex network under four independent parametric sweeps. Plots are normalized so that CPA conditions are in the center of the parameter variation range. The closest frequency CPA condition for the simulation is plotted along with the experimental data. **a** | Measured ratio of output power P_{out} to input power P_{in} as the microwave frequency sent into both ports of the graph is simultaneously swept near the CPA frequency ($\Delta f = f - f_{\text{CPA}}$). Inset shows the output-to-input power ratio response for a larger frequency range around the resonance, and the dashed box corresponds to the frequency range shown in **a**. The output-to-input power ratio shows a sharp dip close to 10^{-5} at the CPA frequency (f_{CPA}) in both experiment and simulation. The scale bar of the mean mode spacing Δ is shown in the plot for reference. **b** | Output to input power ratio obtained by varying the attenuation of the variable attenuator in the graph, while the other waveform characteristics (CPA frequency and waveform) are equal to the ones set in **a**. ΔAtt is the attenuation normalized by Att_{CPA} from the CPA condition. Inset shows the absorption difference between the attenuator only and the attenuator embedded in the graph. **c,d** | Output to input power ratio obtained by changing the amplitude A (**c**) and phase difference $\Delta\phi$ (**d**) separately of the two excitation signals required for the CPA state. The absorption of power reaches its maximum at the CPA configuration, and quickly deteriorates for even small offset from the CPA condition. All experimental results are obtained by direct measurement of the input and output RF powers. This figure is taken from Ref. [1].

surements of each individual component of the graph (Tee-junctions and coaxial cables) which are then combined with the same topology as the full graph to yield high-fidelity descriptions of the data. It should be noted that a numerical model of the graph employing idealized components (e.g. without taking into account the frequency dependence of their impedance) also shows the CPA conditions, although at different frequencies and attenuator settings. The models demonstrate that the CPA results are generic to complex scattering systems, establishing the breadth and generality of our results.

2.3.4 Simulation of the CPA & "Anti-CPA" State

Both the variable attenuator and the microwave graph cavity play important roles in the formation of CPAs. At the same time, in realistic settings there are other elements that might also contribute to the total absorption. To rule out their influence in the CPA protocol we have evaluated their contribution to the total power absorption using the idealized simulation model shown in Fig. 2.5(a). In order to better understand the power distribution inside the system under CPA conditions, we adapt an idealized simulation model in CST. In this model, nodes constructed from Tee-junctions are set to be ideal (no loss), and the attenuator is set to have no frequency-dependent characteristics, and the coaxial cables have uniform attenuation properties. Fig. 2.5(b) shows that the voltage amplitudes at the four nodes in the graph under CPA condition are roughly equal. As shown in Fig. 2.5(c), most of the power (i.e. more than 80%) is absorbed by the variable attenuator, and the rest is absorbed by the coaxial cables, which contribute to a spatially-uniform absorption inside the system. There is very little reactive power in the graph under the CPA condition, as opposed to the "Anti-CPA" state where a large amount of reactive

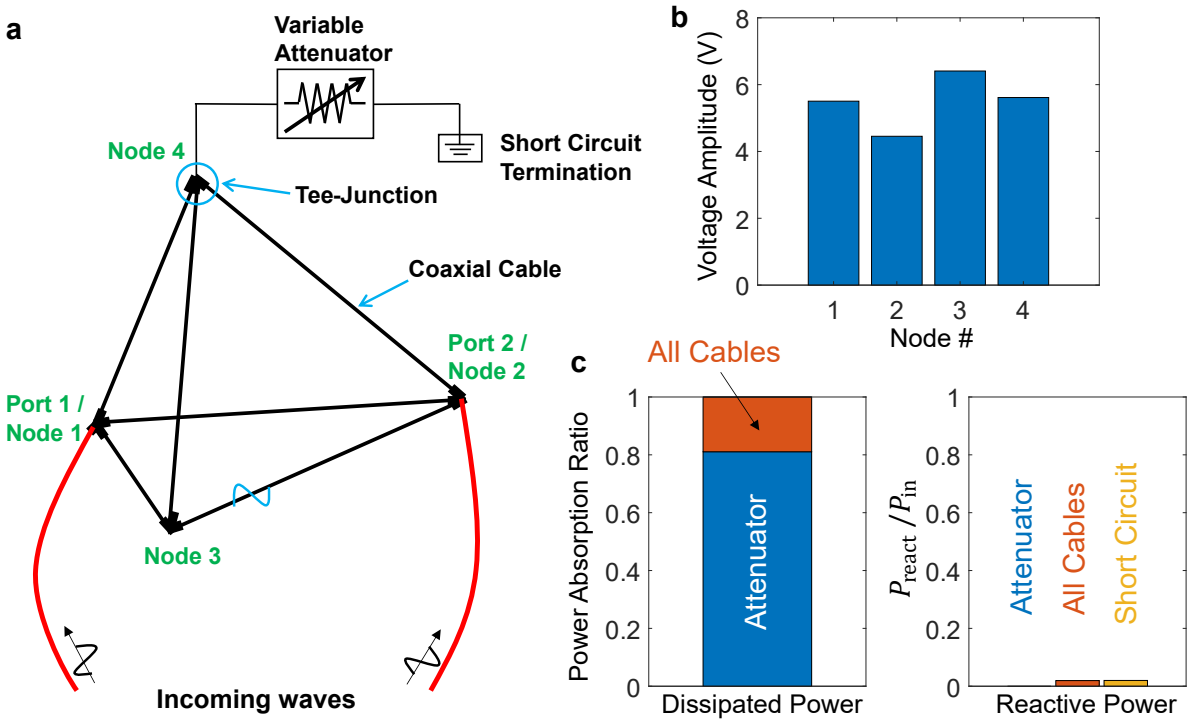

Figure 2.5: Voltage profile and power distribution of CPA state in idealized simulation. **a** | Schematic of the microwave graph with labelled ports under CPA condition at 2.2999 GHz in simulation. **b** | Voltage profiles of four nodes in the graph under CPA condition. **c** | Power distribution among the graph components under the CPA condition. Left plot shows that about 80% of the power are being dissipated on the attenuator, while the remainder is dissipated in the uniformly attenuated cables. Right plot shows reactive power on the cables and short circuit. Compare with the "Anti-CPA" condition in 2.6. This figure is taken from Ref. [1].

power circulates in the system (see Fig. 2.6(c)). Therefore, Fig. 2.5 exactly demonstrates what the theory predicts: the coherent perfect absorption is the combined effect of localized loss and intricate wave interferences, providing a perfect destructive interferometric trap for the incident radiation. The importance of these specific interferences that are induced via the above CPA protocol, and its dominance over other (non-universal) effects is even more appreciated in the case of our tetrahedral graph. Here, short periodic orbits associated with an enhanced backscattering at the vertices promote a trapping of the electromagnetic field in individual cables of the graph (i.e. a scarring effect [33–35, 45]) which might not include the lossy element (attenuator). Therefore,

one could argue that their presence poses fundamental difficulties for the realization of CPAs due to a localized lossy center which is placed somewhere else inside the cavity. Our experimental results demonstrate beyond doubt that the interference imposed via the CPA protocol prevail over all these non-universal features, leading to a (almost) perfect absorption of the coherent incident radiation. Since the existence of non-universal features of various origin are typical in any realistic complex system, we expect that the development of a semiclassical theory of CPA (which utilize non-universal features), will lead to a better design of optimal traps. Complex networks can offer a fertile platform for developing and testing such theories.

We then introduce a new operator – the Absorption Matrix $A \equiv \mathbb{1} - S^{\dagger}S$ to analyze the "Anti-CPA" state [64]. We point out that A is a Hermitian, positive semi-definite operator. The magnitude of its eigenvalues α span the interval [0,1] and the corresponding eigenvectors $|\alpha\rangle$ are orthogonal. It is easy to show that the eigenvector associated with the eigenvalue $\alpha_{\max} = 1$ is the CPA waveform that we have identified previously from the analysis of the zeroes of the S-matrix. It follows that the components of the eigenvector which is associated with the minimum eigenvalue $\alpha_{\min}$ provides the shape of the incident waveform which will lead to minimal absorption. We refer to such a scattering field as the "Anti-CPA" state. The extreme case of $\alpha = 0$ is associated with a scattering field that avoids completely the vertex where the attenuator is located. We verify this effect by observing the voltage profile and energy distribution in the system under "Anti-CPA" stimulus at the same frequency in the simulation (see Fig. 2.6(a)). In Fig. 2.6(b), the voltage on each node is much smaller than the voltage at CPA state (compare with Fig. 2.5(b)), and the voltage on node 4 where the attenuator is attached is particularly small. Under this condition, the total power absorption ratio is only 0.13, and nearly no power is absorbed by the attenuator (see Fig. 2.6(c)), which characterizes the "Anti-CPA" state. Nevertheless, there

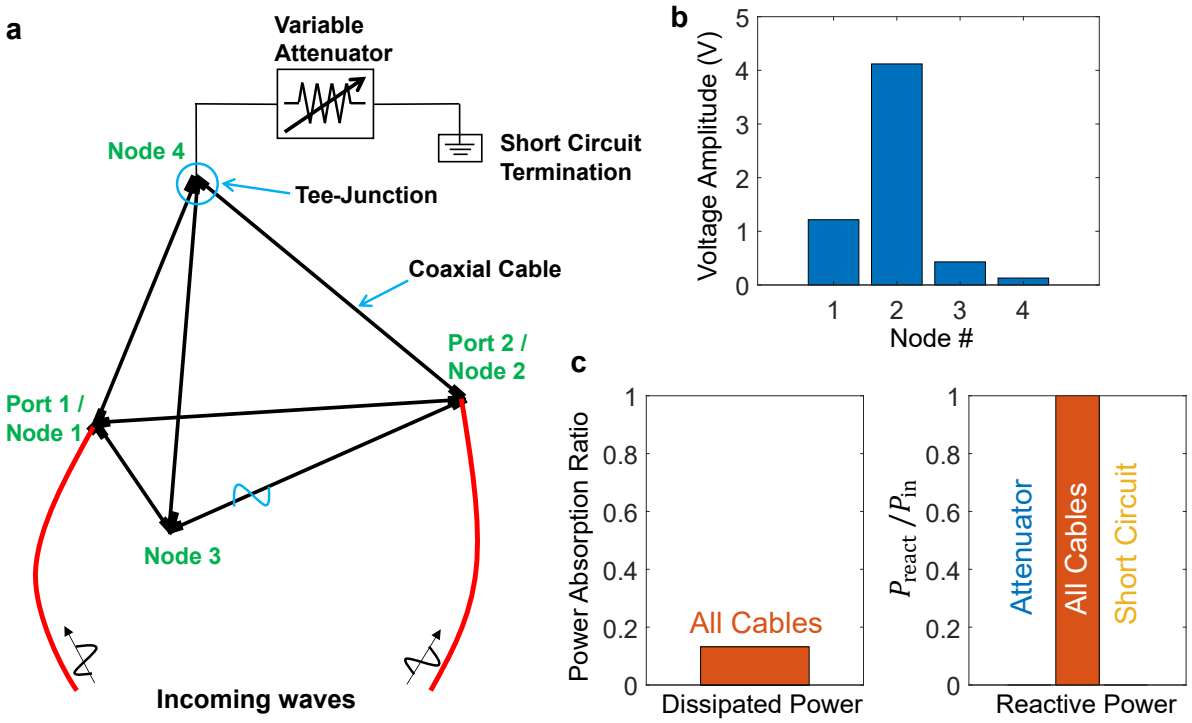

Figure 2.6: Voltage profile and power distribution of the "Anti-CPA" state in idealized simulation. **a** | Schematic of the microwave graph with labeled ports under CPA condition at 2.2999 GHz in simulation. **b** | Voltage profiles of four nodes in the graph under the "Anti-CPA" condition. The voltage amplitude on Node 4, where the absorbing attenuator is attached, is much less than the voltage amplitude on other nodes. **c** | Power distribution among the graph components under the "Anti-CPA" condition. Left plot shows that very little power (less than 15%) are absorbed by the graph, and almost no power is dissipated by the attenuator. Right plot shows reactive power on the cables. This figure is taken from Ref. [1].

is a great deal of reactive power present in the system (compare with Fig. 2.5(c)).

2.3.5 Extending CPA beyond Time-Reversal Invariance

After exploring the formation of a CPA in a TRI tetrahedral microwave graph, we turned our focus to a graph with BTRI (Broken-Time Reversal Invariance). CPA associated with violated time-reversal symmetry is unconventional, and challenges the idea that CPA is simply a time-reversed laser action [46, 47]. Driven by such motivation, we introduced a circulator [40]

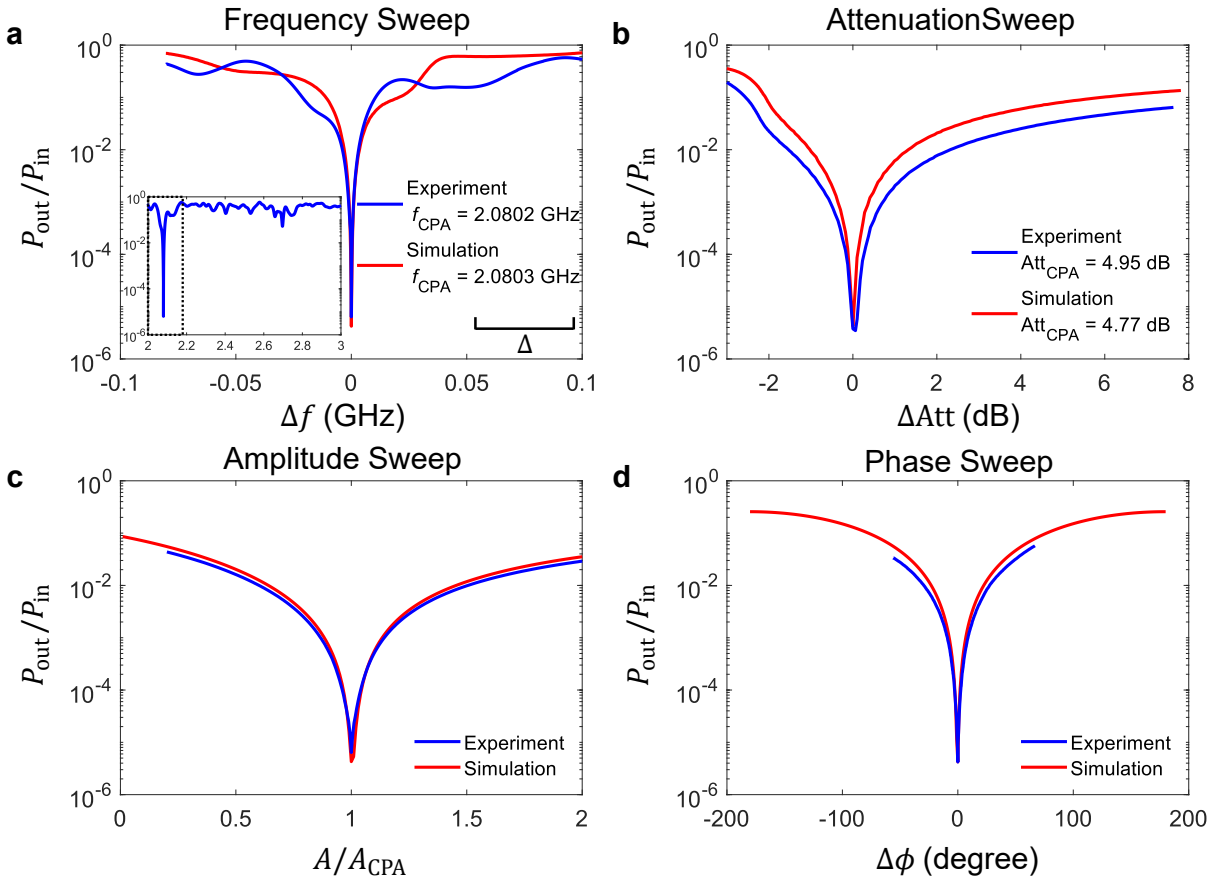

Figure 2.7: Evidence of CPA in the complex network with BTRI under four independent parametric sweeps. Plots are normalized so that CPA conditions are in the center of the parameter variation range. The closest CPA frequency condition for the simulation is plotted along with the experimental data. **a** | Measured ratio of output power P_{out} to input power P_{in} as the microwave frequency sent into both ports of the graph is simultaneously swept near the CPA frequency ($\Delta f = f - f_{\text{CPA}}$). Inset shows the output-to-input power ratio response for a larger frequency range around the resonance, and the dashed box corresponds to the frequency range shown in **a**. The output-to-input power ratio shows a sharp dip below 10^{-5} at the CPA frequency (f_{CPA}) in both experiment and simulation. The scale bar of the mean mode spacing Δ is shown in the plot for reference. **b** | Output to input power ratio obtained by varying the attenuation of the variable attenuator in the graph, while the other waveform characteristics (CPA frequency and waveform) are equal to the ones set in **a**. ΔAtt is the attenuation normalized by Att_{CPA} from the CPA condition. **c,d** | Output to input power ratio obtained by changing the amplitude A (**c**) and phase difference $\Delta\phi$ (**d**) separately of the two excitation signals required for the CPA state. All experimental results are obtained by direct measurement of the input and output RF powers. This figure is taken from Ref. [1].

($2-4$ GHz) at one internal node of the tetrahedral graph (see Fig. 2.1), which allows us to violate the TRI in a controllable manner. Previous work demonstrated that the statistics of the microwave graph impedance (or reaction matrix) changed from that characterized by the Gaussian orthogonal ensemble of random matrices (appropriate for TRI systems) to the Gaussian unitary ensemble (appropriate for BTRI systems) with the addition of this circulator [40, 105, 106].

Following the same procedure as for the TRI graph experiment, the CPA conditions are found by evaluating the eigenvalues of the S-matrix. After that, similar sweep measurements are done as in the TRI case to directly verify the formation of a CPA in the BTRI graph. Our experimental measurements are reported in Fig. 2.7 and confirm the formation of a CPA despite the naive expectation that the presence of a non-reciprocal element (circulator) in the system should weaken the coherence between incident waves, as seen in the eigenfunctions of BTRI wave chaotic systems [107]. The simulations from our modeling are reported in the same figure and show the same behavior as the experimental data. The formed CPAs show the same characteristic features (e.g. sharp resonance, sensitivity to various parameters, abrupt drop of outgoing signal) as the ones reported in the TRI case. We therefore conclude that the CPA protocol applies even to BTRI systems.

2.3.6 CPA in 2D Chaotic Quarter Bow-Tie Billiard

To further challenge the robustness of the CPA protocols we have also implement them using a two-dimensional quarter bow-tie cavity, shown in the inset of Fig. 2.8. Such cavities are known to demonstrate chaotic dynamics in the classical (ray) limit and have been used in the past as an archetype system for wave chaos studies [10, 17–19]. The quarter bow-tie billiard has

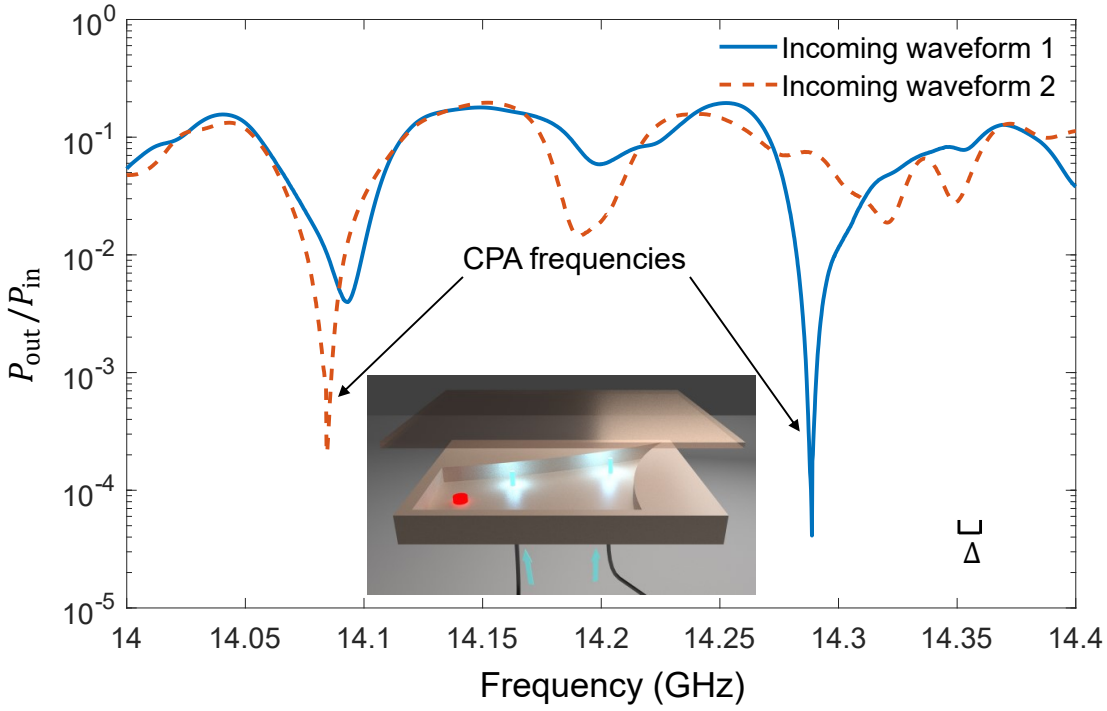

Figure 2.8: Demonstration of two CPA states in the quarter bow-tie billiard. A two-dimensional quarter bow-tie billiard (see inset) is used to test the CPA protocols. The red dot on the bow-tie represents the location of a point-like variable loss in the cavity. Through analysis of the S-matrix, two CPA states are found at the same system configuration. By injecting two different CPA waveforms, the measured ratios of output power P_{out} to input power P_{in} as a function of the microwave frequency are plotted together. The different incoming waveforms support two different CPA states with different CPA frequencies. The scale bar of the mean mode spacing Δ is shown in the plot as well. This figure is taken from Ref. [1].

an area of $A = 0.115m^2$. The brass cavity has a horizontal length of 17.0 inch (43.2 cm), and a vertical length of 8.5 inch (21.6 cm). The upper arc radius is 42.0 inch (106.68 cm), and the right arc has a radius of 25.5 inch (64.8 cm). The height of the cavity is $d = 0.3125$ inch (7.9 mm), which makes it a quasi-2D billiard below the cutoff frequency of $f_{max} = c/(2d) = 18.9$ GHz. The local losses have been incorporated via the same voltage variable attenuator which is attached to the top plate of the billiard by means of a coaxial port at the red dot position in the schematic (see inset of Fig. 2.8). A stub tuner (1819D from Maury Microwave Corporation) is

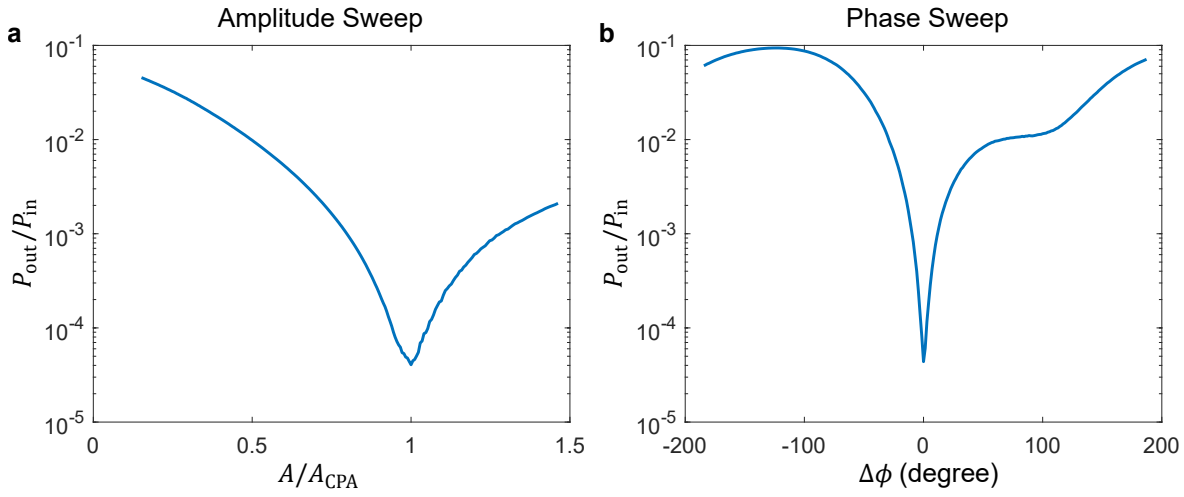

Figure 2.9: Evidence of CPA in the quarter bow-tie billiard under two independent parametric sweeps. Measurements are performed for the CPA state at $f = 14.2888$ GHz in the quarter bow-tie billiard. Output to input power ratio obtained by changing the amplitude A at port 1 (**a**) and phase difference $\Delta\phi$ at port 2 (**b**) separately of the two excitation signals required for the CPA state. All experimental results are obtained by direct measurement of the input and output RF powers. This figure is taken from Ref. [1].

used to tune the coupling between the variable attenuator and the cavity. There are two additional coupling ports on the top plate of the bow-tie billiard for measurements. Following the same experimental procedure as previously discussed, we have identified the CPA conditions and injected the corresponding CPA waveform into the cavity. Due to the higher mode density in two-dimensional billiards, an interesting feature is the appearance of two zeros $\lambda(\omega_1) = \lambda(\omega_2) = 0$ at the same attenuation strength but two different frequencies. At these frequencies (keeping the attenuation parameter fixed), the system supports two different CPA waveforms identified by two different eigenvectors of the S-matrix. We have confirmed this statement via a direct injection of these specific waveforms into the cavity and measuring the corresponding output power versus frequency for a fixed attenuation (see Fig. 2.8). At the CPA frequencies we find that the output power associated with these two distinct waveforms drops sharply as one expects from a CPA.

Therefore a CPA set-up can be utilized as a fast tunable switch where incident monochromatic radiation from one port of the cavity is interferometrically suppressed by a control signal that is injected from the other port.

For the CPA state at $f = 14.2888$ GHz (see the blue line in Fig. 2.8) in the quarter bow-tie billiard, we perform the other two independent parametric sweep measurements, following the same procedure as used in Figs. 2.4 and 2.7. The amplitude sweep and phase sweep measurements shown in Fig. 2.9 demonstrate similar characteristic features, which demonstrate a CPA state in the two-dimensional quarter bow-tie billiard.

2.4 Discussion and Conclusions

The implementation of CPA in generic complex scattering systems opens up a number of interesting applications beyond the ones that we have already discussed (e.g. reconfigurable switching). The first is long-range wireless electromagnetic power transfer technologies that seek to deliver significant electromagnetic power to a single designated object located inside a complex scattering enclosure many wavelengths away from the source. Current approaches utilize multiple scattering and interfering wave trajectories connecting power source and target through either time-reversal [108, 109] or phase conjugation of microwave signals [110] that involve either large bandwidth or a large numbers of channels. These methods suffer from low efficiency as well as radiation safety concerns. A CPA-based method would require only that the target employs a tunable loss, or other tunable scattering property [111–113], and that the source employs only a small number of channels to measure the S-matrix of the enclosure to find the CPA condition. Once CPA is established, the source would output a coherent energetic

signal that would be maximally absorbed at the desired target, with minimal loss elsewhere in the environment. As an added benefit other users can utilize the same bandwidth to perform other tasks (e.g. information transfer) utilizing the "Anti-CPA" condition, alleviating frequency crowding concerns.

A second application concerns sensing of minute changes in a scattering environment. There will be a sensitive change in absorbed energy, or output power from a complex scattering structure, due to any perturbation of the system from the CPA condition, as illustrated by the cusp-like features in Figs. 2.4, 2.7 and 2.8. This arises from the shift of the scattering matrix zero off of the real-frequency-axis, and the dramatic alteration of the scattering matrix is a very direct and easy to measure property. This sensing protocol is simpler than the frequency splitting of degenerate modes created by a perturbation to an optical resonator tuned to an exceptional point [114], for example. Our CPA approach, which relies on the natural complexity of the cavity, is generic and will work in any wavelength regime (or for any wave phenomenon) as long as it is performed in a complex scattering environment.

A third example application is a CPA protocol for secure communications. Consider that the absorber is a target receiver embedded at an unknown location in a complex environment. Due to the complexity of the environment (multipaths with sensitive interference), transfer of information from an outside source occurs only if the emitter prepares and injects a very specific waveform. The waveform has to be determined by the absorber property as well as the environment information, and is rapidly altered as soon as the absorber changes its property. The CPA conditions (absorption and frequency) could be utilized to create a unique key to encrypt the communication and secure the transmission process. Through this method one can establish a secure communication protocol between the emitter and the absorber. A related application is

to utilize CPA as a switch for an arbitrary incident signal at one frequency. For a given waveform incident through the ports of the system one can arrange the relative amplitude/phase of a control wave injected into the CPA cavity to create complete absorption of an incident signal at the same frequency. Switching back and forth between the CPA and anti-CPA control waves will toggle the incident signal to a maximum extent.

In summary we demonstrate the implementation of CPA protocols in generic complex scattering systems without any geometric or hidden symmetries. The primary platform that has been used in our investigations was a microwave realization of a quantum graph consisting of a complex network of coaxial cables where time-reversal symmetry can be preserved or violated in a controllable manner. Irrespective of the symmetry, the CPA condition has been realized through continuous tuning of a localized lossy component and its efficiency has been tested by means of direct measurement of RF power coming out of the graph. As much as 99.999% of the injected power are absorbed by the system. To get additional confirmation of the efficacy of our experimental CPA protocols in complex systems, we have also tested them successfully in a chaotic microwave bow-tie cavity. Our work demonstrates that CPA can indeed be achieved even in the case of complex (or chaotic) scattering set-ups where small variations in the form of the incoming waves or of the scattering system might lead to dramatic changes in the scattering fields. These findings establish the validity of CPA protocols, independent of the degree of complexity of the wave transport phenomena, originating either from the influence of system-specific features in the scattering process or from the presence or the absence of an underlying classical chaotic dynamics. Importantly, our work generalizes the operations and settings for CPA beyond its initial assumptions of time-reversal symmetry and is expected to motivate practical applications, including designing efficient absorbers, sensitive reconfigurable switches, enabling practical long-range

wireless power transfer, and associated high-efficiency energy conversion systems. The extreme sensitivity of absorption to parametric variation away from the CPA condition can be utilized for ultra-sensitive detectors and secure communication links. These ideas translate to all forms of complex wave scattering, including audio acoustics and solid-body vibro-acoustics. For future work, the CPA phenomenon can be extended to the nonlinear regime [115] by introducing nonlinear elements into the system.

Chapter 3: Generalization of Wigner Time Delay to Sub-Unitary Scattering Systems

3.1 Overview

Wigner time delay has been traditionally studied for the unitary scattering systems. For the case of flux-conserving scattering in systems with no losses, the S-matrix is unitary and its eigenvalues are phases $e^{i\theta_a}, a = 1, 2, ..., M$. These phases are functions of the excitation energy E and one can then define several different measures of time delay, see e.g. [51, 77], such as partial time delays associated with each channel $\tau_a = d\theta_a/dE$, the proper time delays which are the eigenvalues of the Wigner-Smith matrix $\hat{Q} = i\hbar \frac{dS^\dagger}{dE} S$, and the Wigner delay time which is the average of all the partial time delays ($\tau_{\rm W} = \frac{1}{M}\sum_{a=1}^{M} \tau_a = \frac{1}{M} Tr[\hat{Q}]$).

A rich class of systems in which properties of various time delays enjoyed thorough theoretical attention is scattering of short-wavelength waves from classically chaotic systems, e.g. billiards with ray-chaotic dynamics or particles on graphs, e.g. such as considered in [116]. Various examples of chaotic wave scattering (quantum or classical) have been observed in nuclei, atoms, molecules, ballistic two-dimensional electron gas billiards, and most extensively in microwave experiments [14, 22, 41, 117–119]. In such systems time delays have been measured starting from the pioneering work [120], followed over the last three decades by measurement

of the statistical properties of time delay through random media [121, 122] and microwave billiards [123]. Wigner time delay for an isolated resonance described by an S-matrix pole at complex energy $E_0 - i\Gamma$ has a value of $Q = 2\hbar/\Gamma$ on resonance, hence studies of the imaginary part of the S-matrix poles probe one aspect of time delay [124–129]. In the meantime, the Wigner-Smith operator (WSO) was utilized to identify minimally-dispersive principal modes in coupled multi-mode systems [83, 130]. A similar idea was used to create particle-like scattering states as eigenstates of the WSO [52, 81, 82]. A generalization of the WSO allowed maximal focus on, or maximal avoidance of, a specific target inside a multiple scattering medium [54, 86].

Time delays in wave-chaotic scattering are expected to be extremely sensitive to variations of excitation energy and scattering system parameters, and will display universal fluctuations when considering an ensemble of scattering systems with the same general symmetry. Universality of fluctuations allows them to be efficiently described using the theory of random matrices [77, 131–139]. Alternative theoretical treatments of time delay in chaotic scattering systems successfully adopted a semi-classical approach, see [55] and references therein.

Despite the fact that standard theory of wave-chaotic scattering deals with perfectly flux-preserving systems, in any actual realisation such systems are inevitably imperfect, hence absorbing, and theory needs to take this aspect into account [140]. Interestingly, studying scattering characteristics in a system with weak uniform (i.e. spatially homogeneous) losses may even provide a possibility to extract time delays characterizing idealized system without losses. This idea has been experimentally realized already in [120] which treated the effect of sub-unitary scattering by means of the unitary deficit of the S-matrix. In this case consider the Q-matrix defined through the relation $S^\dagger S = 1 - (\gamma\Delta/2\pi)Q_{UD}$, where γ is the dimensionless 'absorption rate' and Δ is the mean spacing between modes of the closed system. In the limit of vanishing absorption

rate $\gamma \to 0$ such Q_{UD} can be shown to coincide with the Wigner-Smith time delay matrix for a lossless system, but formally one can extend this as a definition of Q for any $\gamma > 0$. Note that this version of time delay is always real and positive. Various statistical aspects of time delays in such and related settings were addressed theoretically in [79, 141–143].

Experimental data is often taken on sub-unitary scattering systems and a straightforward use of the Wigner time delay definition yields a complex quantity. In addition, both the real and imaginary parts acquire both negative and positive values, and they show a systematic evolution with energy/frequency and other parameters of the scattering system. This clearly calls for a detailed theoretical understanding of this complex generalization of the Wigner time delay. It is necessary to stress that many possible definitions of time delays which are equivalent or directly related to each other in the case of a lossless flux-conserving systems can significantly differ in the presence of flux losses, either uniform or spatially localized. In the present chapter we focus on a definition that can be directly linked to the fundamental characteristics of the scattering matrix - its poles and zeros in the complex energy plane, making it useful for fully characterizing an arbitrary scattering system. Note that S-matrix poles have been objects of long-standing theoretical [144–152] and experimental [124–126, 128] interest in chaotic wave scattering, whereas S-matrix zeroes started to attract research attention only recently [1, 57, 58, 64, 65, 72, 101, 129, 153, 154].

3.2 Complex Wigner Time Delay

3.2.1 Definition

In our exposition we use the framework of the so-called "Heidelberg Approach" to wave-chaotic scattering reviewed from different perspectives in [155, 156] and [157]. Let H be the $N \times N$ Hamiltonian which is used to model the closed system with ray-chaotic dynamics, W denoting the $N \times M$ matrix of coupling elements between the N modes of H and the M scattering channels, and by A the $N \times L$ matrix of coupling elements between the modes of H and the L localized absorbers, modelled as L absorbing channels. [1] The total unitary S-matrix, of size $(M+L) \times (M+L)$ describing both the scattering and absorption on equal footing, has the following block form, see e.g. [65]:

$$\mathcal{S}(E) = \begin{pmatrix} 1_M - 2\pi i W^\dagger D^{-1}(E) W & -2\pi i W^\dagger D^{-1}(E) A \\ -2\pi i A^\dagger D^{-1}(E) W & 1_L - 2\pi i A^\dagger D^{-1}(E) A \end{pmatrix}, \tag{3.1}$$

where we defined $D(E) = E - H + i(\Gamma_W + \Gamma_A)$ with $\Gamma_W = \pi W W^\dagger$ and $\Gamma_A = \pi A A^\dagger$.

The upper left diagonal $M \times M$ block of $\mathcal{S}(E)$ is the experimentally-accessible sub-unitary scattering matrix and is denoted as $S(E)$. The presence of uniform-in-space absorption with strength η can be taken into account by evaluating the S-matrix entries at complex energy: $S(E+$

[1] This way of modelling the localized absorbers as additional scattering channels is close in spirit to the so-called dephasing lead model of decoherence introduced in: M. Büttiker, Role of quantum coherence in series resistors, Phys. Rev. B **33**, 3020 (1986) and further developed in P. W. Brouwer and C. W. J. Beenakker, Voltage-probe and imaginary-potential models for dephasing in a chaotic quantum dot, Phys. Rev. B **55**, 4695 (1997).

$i\eta) \coloneqq S_\eta(E)$. The determinant of such a sub-unitary scattering matrix $S_\eta(E)$ is then given by:

$$\det S_\eta(E) \coloneqq \det S(E+i\eta) \tag{3.2}$$

$$= \frac{\det[E-H+i(\eta+\Gamma_A-\Gamma_W)]}{\det[E-H+i(\eta+\Gamma_A+\Gamma_W)]} \tag{3.3}$$

$$= \prod_{n=1}^{N} \frac{E+i\eta-z_n}{E+i\eta-\mathcal{E}_n}, \tag{3.4}$$

In the above expression we have used that the S-matrix zeros z_n are complex eigenvalues of the non-self-adjoint/non-Hermitian matrix $H+i(\Gamma_W-\Gamma_A)$, whereas the poles $\mathcal{E}_n = E_n - i\Gamma_n$ with $\Gamma_n > 0$ are complex eigenvalues of yet another non-Hermitian matrix $H-i(\Gamma_W+\Gamma_A)$, frequently called in the literature "the effective non-Hermitian Hamiltonian" [77, 144, 152, 156–158]. Note that when localized absorption is absent, i.e. $\Gamma_A = 0$, the zeros z_n and poles $\mathcal{E}_n$ are complex conjugates of each other, as a consequence of S-matrix unitarity for real E and no uniform absorption $\eta = 0$. Extending to locally absorbing systems the standard definition of the Wigner delay time as the energy derivative of the total phase shift we now deal with a complex quantity:

$$\tau_W(E;A,\eta) \coloneqq \frac{-i}{M}\frac{\partial}{\partial E}\log\det S_\eta(E) \tag{3.5}$$

$$= \text{Re}\ \tau_W(E;A,\eta) + i\text{Im}\ \tau_W(E;A,\eta), \tag{3.6}$$

$$\text{Re}\ \tau_W(E;A,\eta) = \frac{1}{M}\sum_{n=1}^{N}\left[\frac{\text{Im}\ z_n-\eta}{(E-\text{Re}\ z_n)^2+(\text{Im}\ z_n-\eta)^2} + \frac{\Gamma_n+\eta}{(E-E_n)^2+(\Gamma_n+\eta)^2}\right], \tag{3.7}$$

$$\text{Im}\ \tau_W(E;A,\eta) = -\frac{1}{M}\sum_{n=1}^{N}\left[\frac{E-\text{Re}\ z_n}{(E-\text{Re}\ z_n)^2+(\text{Im}\ z_n-\eta)^2} - \frac{E-E_n}{(E-E_n)^2+(\Gamma_n+\eta)^2}\right] \tag{3.8}$$

Equation (3.7) for the real part is formed by two Lorentzians for each mode of the closed

system, potentially with different signs. This is a striking difference from the case of the flux-preserving system in which the conventional Wigner time delay is expressed as a single Lorentzian for each resonance mode [159]. Namely, the first Lorentzian is associated with the nth zero while the second is associated with the corresponding pole of the scattering matrix. The widths of the two Lorentzians are controlled by system scattering properties, and when Im $z_n \to \eta \pm 0$ the first Lorentzian in Eq. (3.7) acquires the divergent, delta-functional peak shape, of either positive or negative sign, centered at $E =$ Re z_n. Note that the first term in Eq. (3.8) changes its sign at the same energy value. These properties are indicative of the "perfect resonance" condition, with divergence in the real part of the Wigner time delay signalling the wave/particle being perpetually trapped in the scattering environment. In different words, the energy of the incident wave/particle is perfectly absorbed by the system due to the finite losses.

The pair of equations (3.7, 3.8) forms the main basis for our consideration. In particular, we demonstrate in Appendix A.1 that in the regime of well-resolved resonances Eqs. (3.7) and (3.8) can be used for extracting the positions of both poles and zeros in the complex plane from experimental measurements, provided the rate of uniform absorption η is independently known. We would like to stress that in general the two Lorentzians in (3.7) are centered at different energies because generically the pole position E_n does not coincide with the real part of the complex zero Re z_n.

From a different angle it is worth noting that there is a close relation between the objects of our study and the phenomenon of the so called Coherent Perfect Absorption (CPA) discussed in Chapter 2 which attracted considerable attention in recent years, both theoretically and experimentally [1,46,48,101,160]. Namely, the above-discussed match between the uniform absorption strength and the imaginary part of scattering matrix zero $\eta =$ Im z_n simultaneously ensures the

determinant of the scattering matrix to vanish, see Eq. (3.4). This is only possible when $|\psi_{\text{out}}\rangle = 0$ despite the fact that $|\psi_{\text{in}}\rangle \neq 0$, which is a manifestation of CPA, see e.g. [64, 65].

3.2.2 Experimental Setup

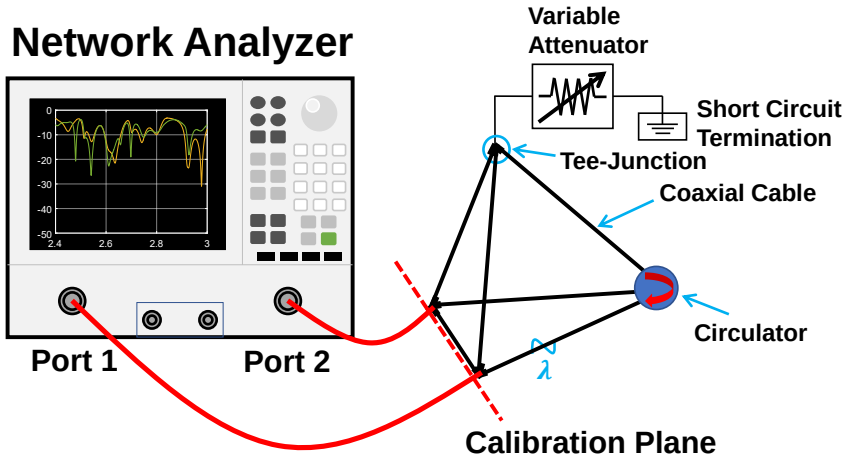

Figure 3.1: Schematic of the graph experimental setup. The lumped loss Γ_A is varied by changing the applied voltage to the variable attenuator. The nodes involving connections of the graph to the network analyzer, and the graph to the lumped loss, are made up of a pair of Tee-junctions. This figure is taken from Ref. [2].

We focus on experiments involving microwave graphs [1, 39, 41, 161] for a number of reasons. First, they provide for complex scattering scenarios with well-isolated modes amenable to detailed analysis. We thus avoid the complications of interacting poles and related interference effects [162]. Graphs also allow for convenient parametric control such as variable lumped lossy elements, variable global loss, and breaking of time-reversal invariance. We utilize an irregular tetrahedral microwave graph formed by coaxial cables and Tee-junctions, having $M = 2$ single-mode ports, and broken time-reversal invariance. A voltage-controlled variable attenuator is attached to one internal node of the graph (see Fig. 3.1), providing for a variable lumped loss ($L = 1$, the control variable Γ_A). The coaxial cables and tee-junctions have a roughly uniform

and constant attenuation produced by dielectric loss and conductor loss, which is parameterized by the uniform loss parameter η. The 2-port graph has a total electrical length of $L_e = 3.89$ m, a mean mode spacing of $\Delta = c/2L_e = 38.5$ MHz, and a Heisenberg time $\tau_{\rm H} = 2\pi/\Delta = 163$ ns. The graph has equal coupling on both ports, characterized by a nominal value of $T_a = 0.9450$ at a frequency of 2.6556 GHz. [2]

It should be noted that there are two widely-used conventions for the evolution of the phase of the complex S-matrix elements with increasing frequency. Microwave network analyzers utilize a convention in which the phase of the scattering matrix elements *decreases* with increasing frequency. Here we adopt the convention used in the theoretical literature that the phase of S-matrix elements *increases* with increasing frequency.

3.2.3 Comparison of Theory and Experiments

After obtaining the 2×2 S-matrix data of tetrahedral graph under different attenuation settings, we follow Eqs. (3.5) and (3.6) to calculate the complex Wigner time delay in this setup. Figure 3.2 shows the evolution of complex time delay for a single isolated mode of the $M = 2$ port tetrahedral microwave graph as Γ_A is varied. The complex time delay is evaluated as in Eq. (3.5) based on the experimental $S(f)$ data, where f is the microwave frequency, a surrogate for energy E. Note that the (calibrated) measured S-parameter data is directly used for calculation of the complex time delay without any data pre-processing. The resulting real and imaginary parts of the time delay vary systematically with frequency, adopting both positive and negative values, depending on frequency and lumped loss in the graph. These variations are well-described by the

[2] The coupling strength T_a is determined by the value of the radiation S-matrix ($T_a = 1 - |S_{\rm rad}|^2$). The radiation S is measured when the graph is replaced by 50 Ω loads connected to the three output connectors of each node attached to the network analyzer test cables.

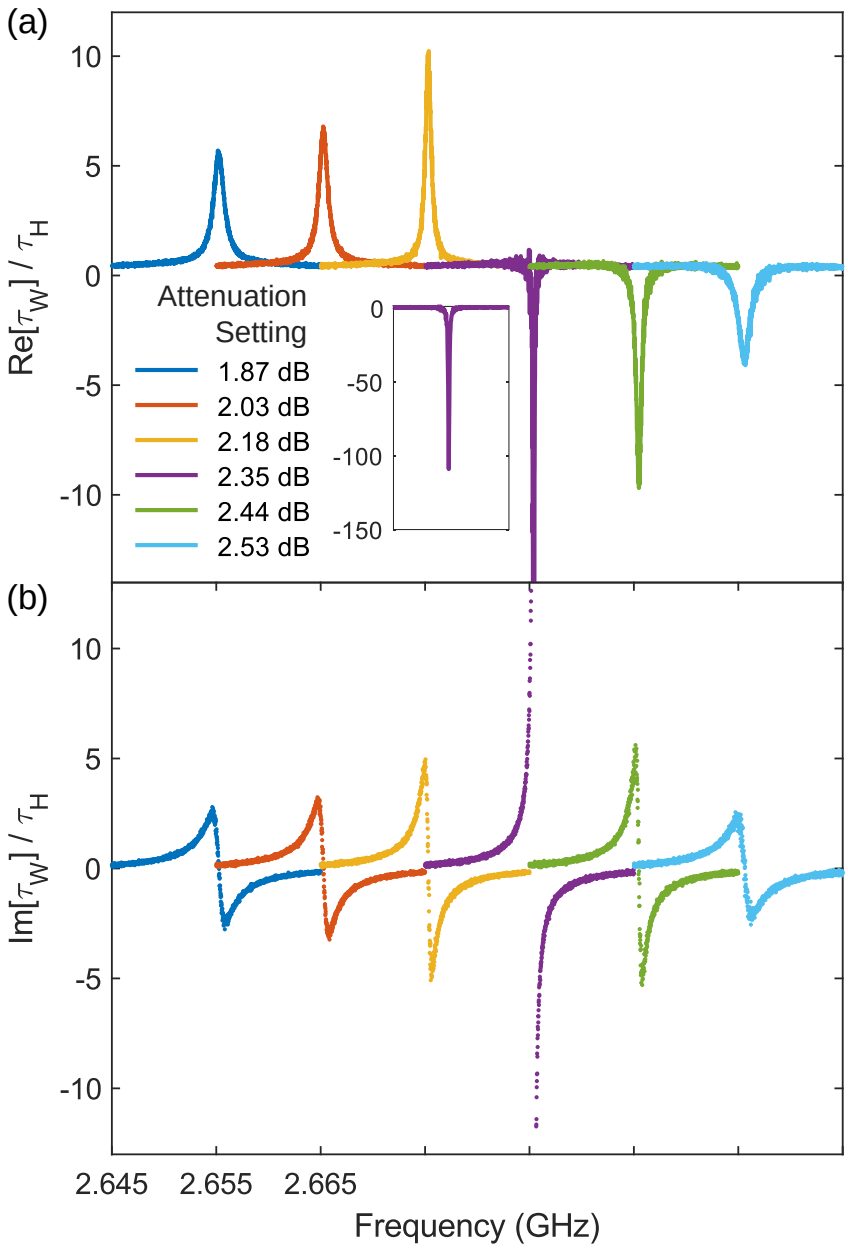

Figure 3.2: Experimental data of both real and imaginary parts of Wigner time delay $\mathrm{Re}[\tau_W]$ and $\mathrm{Im}[\tau_W]$ (normalized by the Heisenberg time τ_H) as a function of frequency under different attenuation settings for a single isolated mode. For each attenuation setting, the data is plotted from 2.645 GHz to 2.665 GHz. For clarity, plots with higher attenuation setting are shifted 0.01 GHz from the previous one. Inset shows the entire range of $\mathrm{Re}[\tau_W]$ for attenuation setting of 2.35 dB. This figure is taken from Ref. [2].

theory given above.

Figure 3.3 clearly demonstrates that two Lorentzians are required to correctly describe the

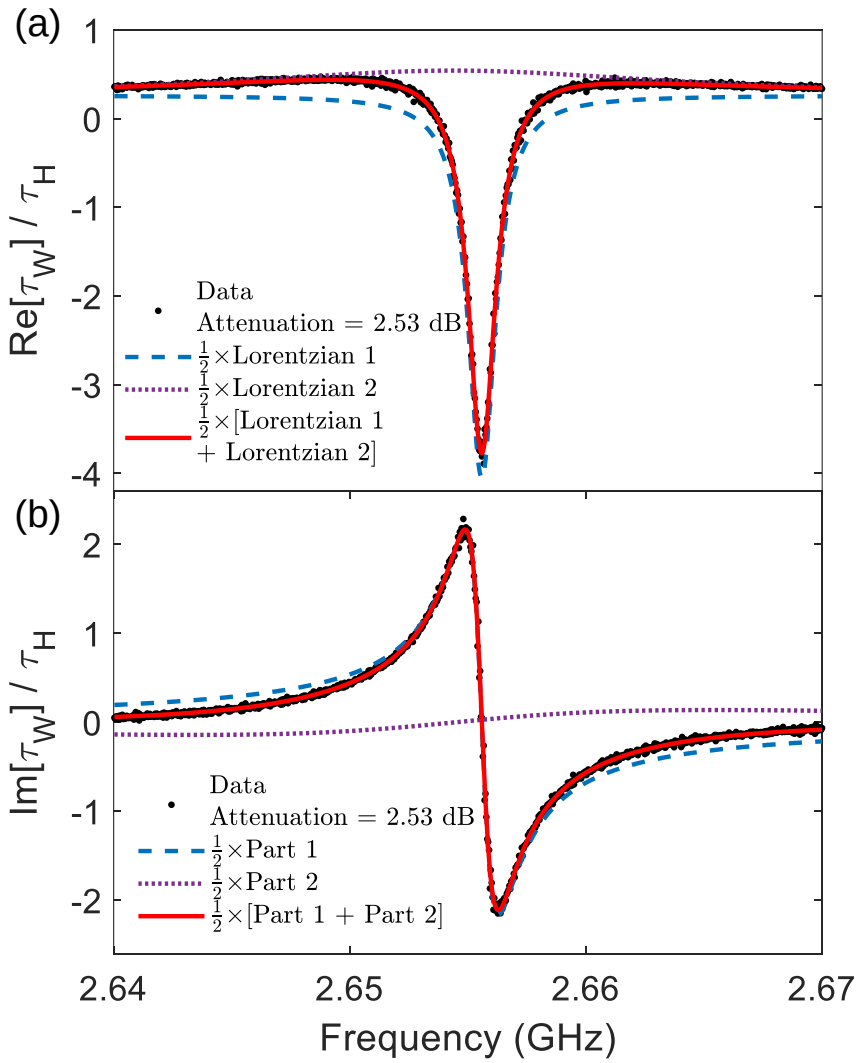

Figure 3.3: Demonstration of the two-Lorentzian nature of the real and imaginary parts of the Wigner time delay as a function of frequency. The fitting parameters in these two plots are: Re $z_n = 2.6556$ GHz, $E_n = 2.6544$ GHz, Im $z_n - \eta = -7.1065\times10^{-4}$ GHz, and $\Gamma_n + \eta = 0.0110$ GHz. The constants used in the Re$[\tau_W]$ and Im$[\tau_W]$ fits are $C_{\mathrm{R}} = 0.26$ and $C_{\mathrm{I}} = -0.0018$ in units of τ_{H}. This figure is taken from Ref. [2].

frequency dependence of the real part of the time delay. The two Lorentzians have different widths in general, given by the values of Im $z_n - \eta$ and $\Gamma_n + \eta$, and in this case the Lorentzians also have opposite sign. The frequency dependence of the imaginary part of the time delay also requires two terms, with the same parameters as for the real part, to be correctly described. The data in Fig. 3.2(a) also reveals that Re$[\tau]$ goes to very large positive values and suddenly changes

sign to large negative values at a critical amount of local loss. For another attenuation setting of the same mode it was found that the maximum delay time was 337 times the Heisenberg time, showing that the signal resides in the scattering system for a substantial time.

3.2.4 Extracting Zero and Pole of S-matrix from Data

The measured complex time delay as a function of frequency can be fit to Eqs. (3.7) and (3.8) to extract the corresponding pole and zero location for the S-matrix. The fitting parameters are Re z_n and Im $z_n - \eta$ for the zero, and E_n and $\Gamma_n + \eta$ for the pole. Note that the Re$[\tau_W(f)]$ and Im$[\tau_W(f)]$ data are fit simultaneously, and constant offsets C_{R} and C_{I} are added to each fit.

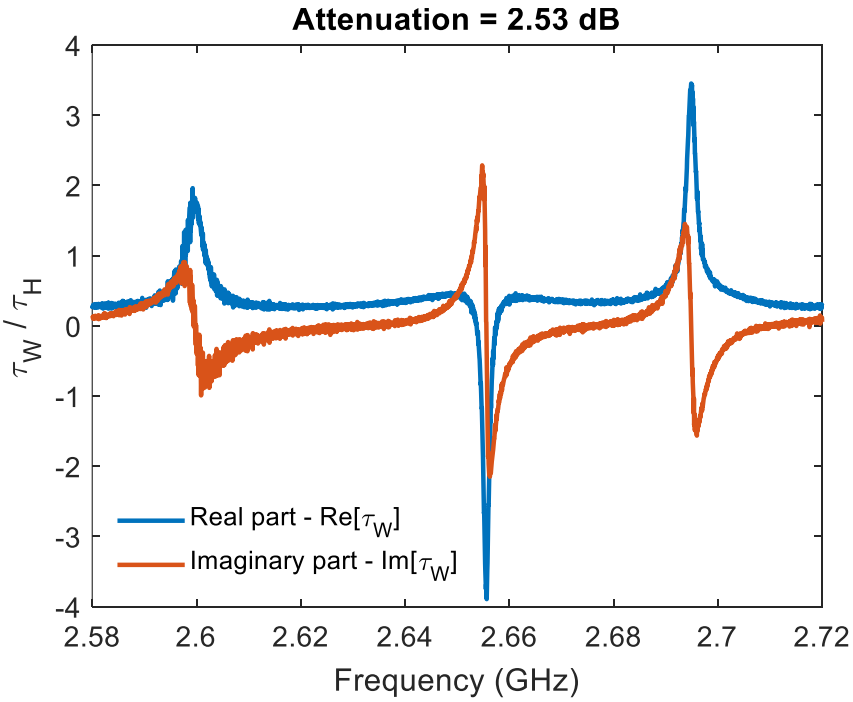

Figure 3.4: Complex time delay experimental data for the neighboring resonances at an attenuation setting of 2.53 dB. The resonance mode in the middle is the one being analyzed in this study. This figure is taken from Ref. [2].

In this study we used an isolated mode for data fitting and analysis. A good definition of

'isolated resonance' is that the separation is much larger than the width of the resonance. Fig. 3.4 shows the separation between the mode fit in the text and its neighboring resonances, where the nearest-neighbor distance for the middle resonance is $\Delta f = 0.0393$ GHz (with the resonance on the right). Under this attenuation setting, the resonance widths of the two Lorentzians from the zero and pole for the middle resonance are $|\text{Im } z_n - \eta| = 7.1065 \times 10^{-4}$ GHz and $\Gamma_n + \eta = 0.0110$ GHz, which give rise to dimensionless separation estimates of $\frac{\Delta f}{|\text{Im } z_n - \eta|} = 55.3$ and $\frac{\Delta f}{\Gamma_n + \eta} = 3.6$, respectively.

In situations where the isolation between neighboring resonances is not large, the nearby resonances may have some contributions to the complex time delay at the resonance of interest. Here we evaluate this effect by using Eqs. (3.7) and (3.8) for three hypothetical modes. We utilize three similar pairs of zero and pole with adjustable mode spacing between them (see Fig. 3.5). The middle resonance has the same zero and pole from the experimental data, and the neighboring two resonances have the same information except for the variable frequency separation between them. Fig. 3.5 clearly demonstrates that the neighboring resonances can have strong background contributions to $\text{Re}[\tau_W]$, which may lead to a non-negligible constant C_{R} in the fitting process (see Figs. 3.3 and 3.10). The contribution to $\text{Im}[\tau_W]$, on the other hand, is quite small because $\text{Im}[\tau_W](f)$ changes sign through the resonance, hence for a low density of modes the 'tails' of the $\text{Im}[\tau_W]$ contributions cancel out to good approximation. Fig. 3.5(d) shows the background contribution τ_{Bkd} to $\text{Re}[\tau_W]$ and $\text{Im}[\tau_W]$ at the resonance of interest as a function of the mode separation. Clearly $\text{Re}[\tau_W]$ is more sensitive to the presence of nearby modes and requires larger fit values for C_{R}, as compared to C_{I}, consistent with the results in Fig. 3.3.

Figure 3.6 summarizes the parameters required to fit the experimental complex time delay vs. frequency (shown in Fig. 3.2) as the localized loss due to the variable attenuator in the graph

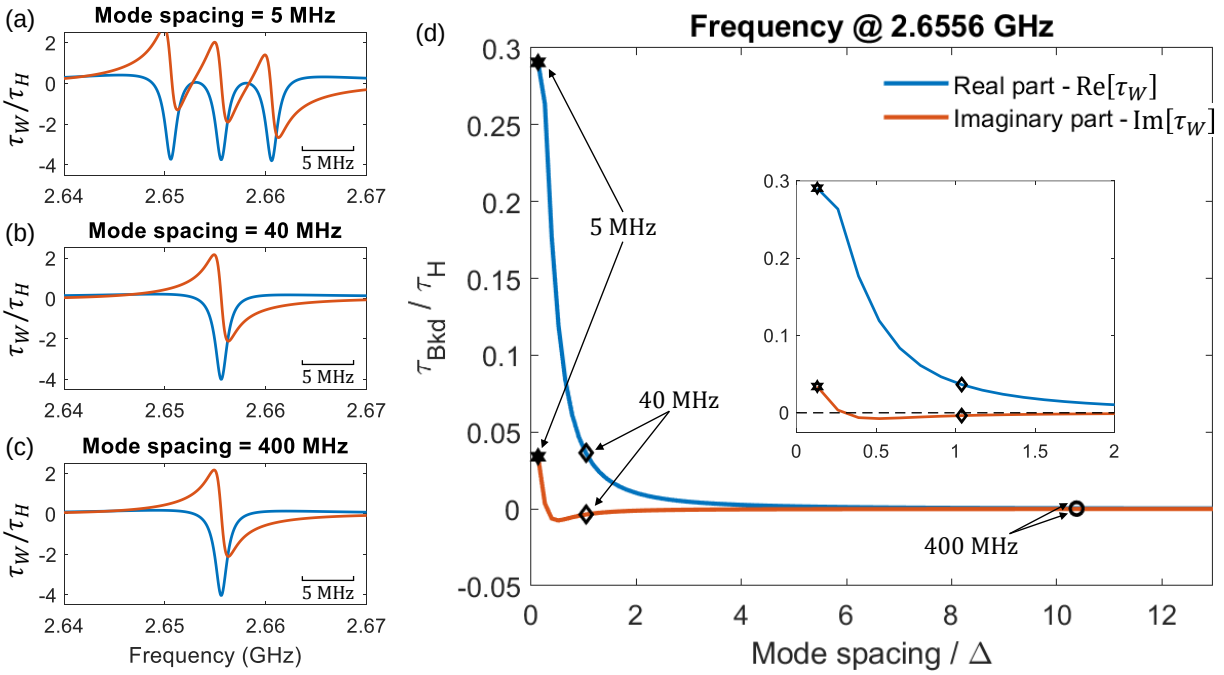

Figure 3.5: Simulations based on Eqs. (3.7) and (3.8) of the effect of neighboring resonances on the background values τ_{Bkd} of $\text{Re}[\tau_W]$ and $\text{Im}[\tau_W]$ at the location of the center resonance. (a) – (c) show the complex time delay for three constructed neighboring resonances with variable mode spacing. A scale bar of 5 MHz is added for reference. Here τ_{H} =163 ns is the Heisenberg time from the experiment. The parameters used for the center resonance are: Re $z_n = 2.6556$ GHz, $E_n = 2.6544$ GHz, Im $z_n - \eta = -7.1065 \times 10^{-4}$ GHz, and $\Gamma_n + \eta = 0.0110$ GHz. (d) shows the background contributions τ_{Bkd} of both the real and imaginary parts of complex time delay from the neighboring two resonances at the center frequency of 2.6556 GHz. Here $\Delta = 38.5$ MHz is the mean mode spacing of the experimental graph, and is simply used as a characteristic frequency scale for normalization. The corresponding data points from (a) – (c) are labelled in the plot. The background contributions decrease dramatically as the mode spacing increases, and the background contribution to $\text{Im}[\tau_W]$ is much smaller compared with the contribution to $\text{Re}[\tau_W]$. Inset in (d) shows a zoom-in view of the two contributions for small mode spacing. This figure is taken from Ref. [2].

is increased. The significant feature here is the zero-crossing of Im $z_n - \eta$ at frequency $f = f_{\text{CPA}}$, which corresponds to the point at which $\text{Re}[\tau_W(f)]$ changes sign. As shown in Fig. 3.6 this coincides with the point at which $|\det(S(f))|$ achieves its minimum value at the CPA frequency f_{CPA}. This demonstrates that one or more eigenvalues of the S-matrix go through a complex zero value precisely as the condition Im $z_n - \eta = 0$ and $f -$ Re $z_n = 0$ is satisfied. Associated with

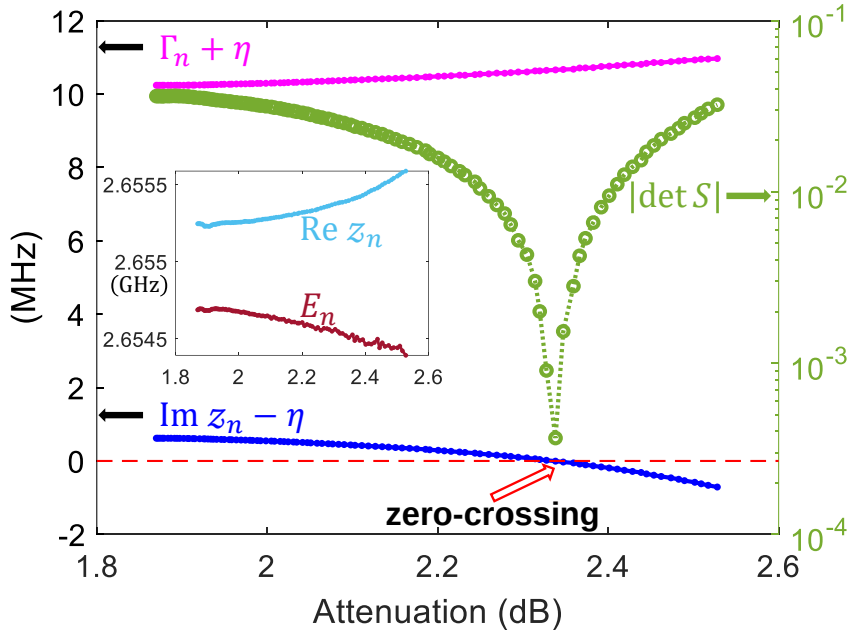

Figure 3.6: Fitted parameters Im $z_n - \eta$ and $\Gamma_n + \eta$ for the complex Wigner time delay from graph experimental data. Also shown is the evolution of $|\det(S)|$ at the specific frequency of interest, f_{CPA}, which reaches its minimum at the zero-crossing point. Inset shows the evolution of Re z_n and $E_n = \text{Re}\ \mathcal{E}_n$ with attenuation. This figure is taken from Ref. [2].

this condition $|\text{Re}[\tau_W(f_{\text{CPA}})]|$ diverges, with corresponding large positive and negative values of $\text{Im}[\tau_W(f)]$ occurring just below and just above $f = f_{\text{CPA}}$. Similar behavior of $\text{Re}[\tau_W(f)]$ was recently observed in a complex scattering system containing re-configurable metasurfaces, as the pixels were toggled [160].

Next we wish to estimate the value of uniform attenuation η for the microwave graph. Using the unitary deficit of the S-matrix (see Appendix B.1) in a setup in which the attenuator is removed [120], we evaluate the uniform loss strength η to be 3.73×10^{-3} GHz.

Figure 3.7 summarizes the locations of the S-matrix pole $\mathcal{E}_n$ and zero z_n of the single isolated mode of the microwave graph in the complex frequency plane as the localized loss is varied. When the S-matrix zero crosses the Im $z_n = \eta$ value, one has the traditional signature of CPA. Note from Fig. 3.7 that the real parts of the zero and pole do not coincide and in fact move

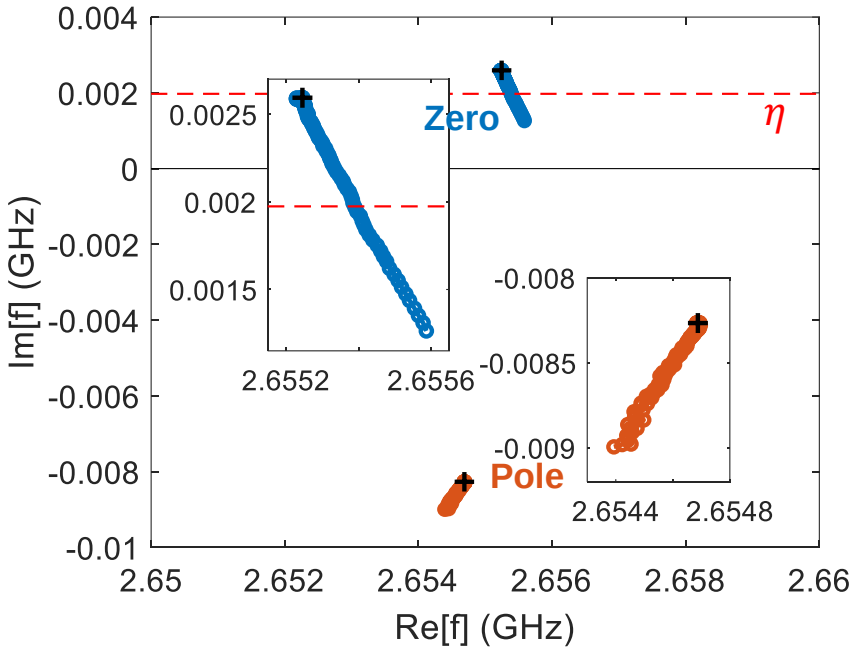

Figure 3.7: Evolution of complex zero and pole of a single mode of the graph in the complex frequency plane as a function of Γ_A. The black crosses are the initial state of the zero and pole at the minimum attenuation setting. Insets show the details of the complex zero and pole migrations. This figure is taken from Ref. [2].

away from each other as localized loss is increased.

3.2.5 Simulations of Graph with Varying Uniform Loss η

We have simulated the microwave graphs using CST Microwave Studio utilizing an idealized simulation model. In this model, an irregular tetrahedral graph similar to that used in the experiment is considered. The graph nodes are represented by Tee-junctions which are set to be ideal (point-like with an ideal scattering matrix), and the only source of loss in the setup comes from uniform dielectric loss of the coaxial cables which can be

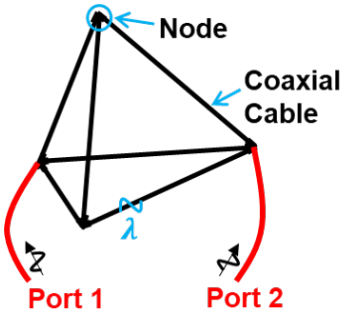

Figure 3.8: Schematic of the graph simulation setup.

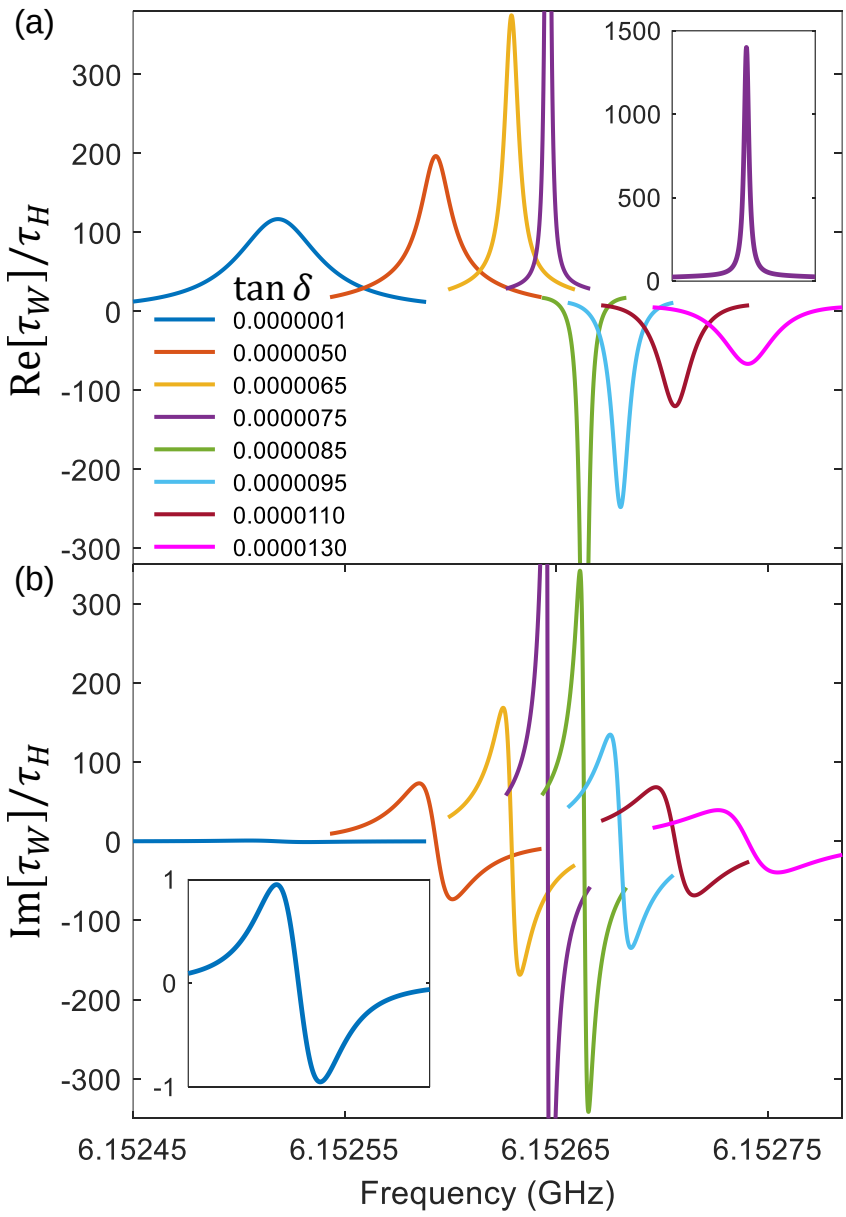

Figure 3.9: Complex Wigner time delay from graph simulation with varying uniform loss η. Figure shows simulation data of both real and imaginary parts of Wigner time delay Re$[\tau_W]$ and Im$[\tau_W]$ (normalized by the Heisenberg time τ_{H}), as a function of frequency under different uniform loss settings for a single isolated mode near 6.1526 GHz. Inset in (a) shows the entire range of Re$[\tau_W]$ for tan$\delta = 7.5 \times 10^{-6}$, and inset in (b) shows the zoom-in view of Im$[\tau_W]$ for tan$\delta = 10^{-7}$. This figure is taken from Ref. [2].

conveniently varied by changing the dielectric loss parameter tanδ. The 2-port graph simulation model has a total electrical length of 8.69 m, Heisenberg time $\tau_{\mathrm{H}} = 364$ ns, equal coupling on

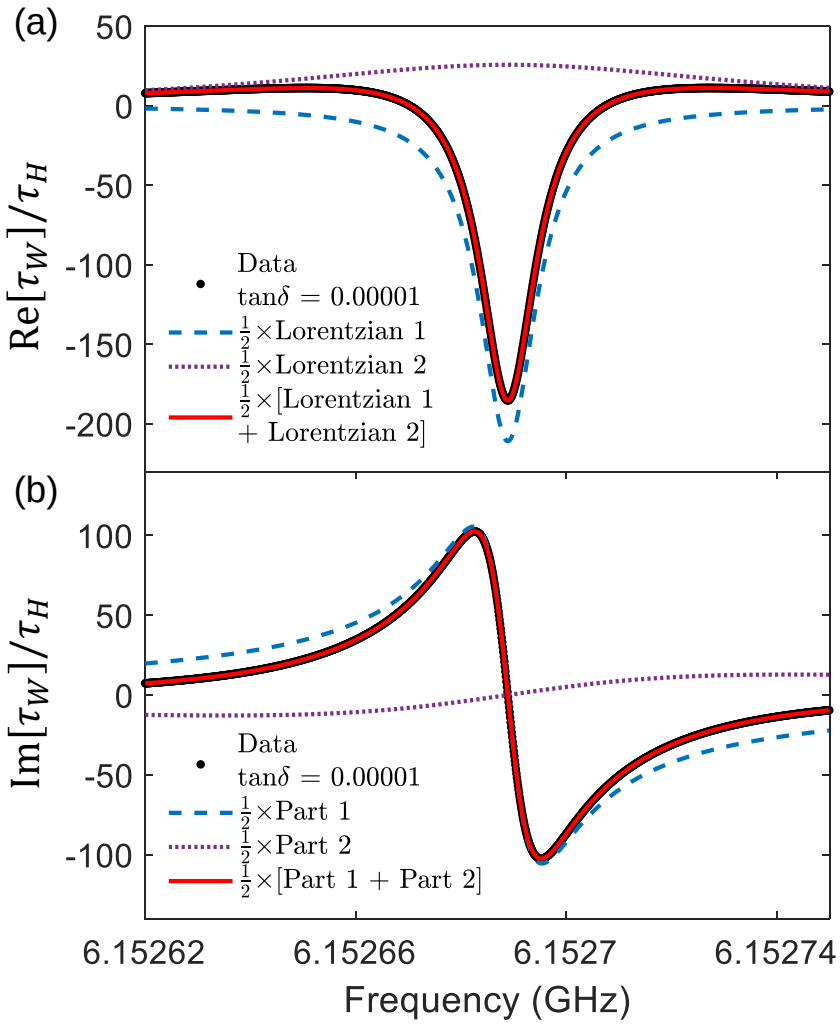

Figure 3.10: Demonstration of the two-Lorentzian nature of the real and imaginary parts of the Wigner time delay (normalized by the Heisenberg time τ_{H}) as a function of frequency. The fitting parameters in these two plots are: Re $z_n = 6.1527$ GHz, $E_n = 6.1527$ GHz, Im $z_n - \eta = -6.5057 \times 10^{-6}$ GHz, and $\Gamma_n + \eta = 5.3547 \times 10^{-5}$ GHz. The constants used in the $\mathrm{Re}[\tau_W]$ and $\mathrm{Im}[\tau_W]$ fits are $C_{\mathrm{R}} = 0.097$ and $C_{\mathrm{I}} = 0.00016$ in units of τ_{H}. This figure is taken from Ref. [2].

both ports, characterized by a nominal value of $T_a = 0.75$, and no lumped loss (i.e. $\Gamma_A = 0$). Note that in contrast to the experiment discussed above, here we consider a time-reversal invariant microwave graph. This is done, in part, to demonstrate that the complex time delay theory applies to all classes of complex scattering systems.

The new insight created by the simulation comes from the ability to systematically vary the

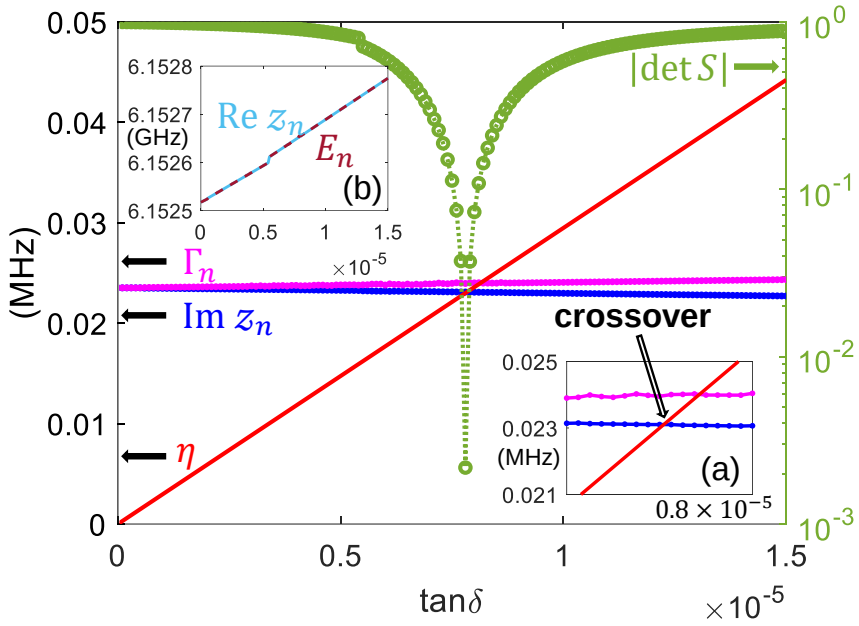

Figure 3.11: Evolution of scattering matrix zero and pole for a single mode in the graph simulation with varying uniform loss η. Plot shows the fitted parameters Im z_n and Γ_n for the complex Wigner time delay from graph simulation data. Also shown is the evolution of $|\det(S)|$ at the specific frequency of interest, f_{CPA}, which reaches its minimum at the crossover point where Im $z_n - \eta = 0$. Inset (a) shows the zoom-in details of the crossover when Im z_n matches with η, and inset (b) shows the evolution of Re z_n and E_n = Re $\mathcal{E}_n$ with varying tanδ. In this case, the real part of zero and pole are equal. This figure is taken from Ref. [2].

uniform loss η while keeping all other parameters fixed. In this way we can show how CPA can be accomplished by simply changing the uniform loss. Results are shown in Figs. 3.9 – 3.11, which are similar to the experimental results shown in Figs. 3.2, 3.3, and 3.6. The CPA condition is achieved for a single isolated mode at $f_{\text{CPA}} = 6.15265$ GHz when the uniform loss tangent value is tuned through a value of tan$\delta = 7.8 \times 10^{-6}$.

3.3 Discussion and Conclusions

In the past, the concept of a complex transmission delay was developed in the context of principal modes in multi-mode waveguides [130], and a similar quantity was later used in the

experimental realization of particle-like scattering states [82]. Complex dwell time was defined for a multiple scattering medium with lossy resonant absorbers [163].

It should be noted that the occurrence of a negative real part of the time delay is an inevitable consequence of sub-unitary scattering, and is also expected for particles interacting with attractive potentials [164].

An early study of Gaussian pulse propagation through an anomalously dispersive medium predicted negative delay [165], and later measurements confirmed the theory [166]. The observed negative delay of the pulse was attributed to the fact that the leading edge of the pulse is attenuated less than the later parts, and the Gaussian shape is approximately preserved, under appropriate circumstances. Negative real parts of reflection delay time have been measured experimentally in a one-dimensional Levy-flight system but were dismissed as an artefact due to prompt reflections [167].

The imaginary part of time delay was in the past discussed in relation to changes in scattering unitary deficit with frequency [82]. Another approach to defining complex time delay has been recently suggested to be based on essentially calculating the time delay of the signal which comes out of the system without being absorbed [160]. It should be noted that this *ad hoc* definition of time delay is not simply related to the poles and zeros of the S-matrix. Moreover, a closer inspection shows that such a definition of complex time delay tacitly assumes that the real parts of the pole and zero are identical. According to our theory such an assumption is incompatible with a proper treatment of localized loss.

Our findings show that in general the real part of the delay as a function of frequency is not symmetric about the resonance as a consequence of the differences in the real parts of z_n and $\mathcal{E}_n$, and that it has a distinctive two-Lorentzian character that had not been appreciated until now.

We emphasize that the correct knowledge of the locations of the poles and zeros is essential for reconstructing the scattering matrix over the entire complex energy plane through Weierstrass factorization [168]. Through graph simulations presented above, we demonstrate that the complex time delay theory presented here also works for time-reversal invariant systems, and for systems with variable uniform absorption strength η. Our results therefore establish a systematic procedure to find the S-matrix zeros and poles of isolated modes of a complex scattering system with an arbitrary number of coupling channels, symmetry class, and arbitrary degrees of both global and localized loss.

Recent work has demonstrated CPA in disordered and complex scattering systems [1, 101]. It has been discovered that one can systematically perturb such systems to induce CPA at an arbitrary frequency [9, 160], and this enables a remarkably sensitive detector paradigm [160]. These ideas can also be applied to optical scattering systems where measurement of the transmission matrix is possible [169]. Here we have uncovered a general formalism in which to understand how CPA can be created in an arbitrary scattering system. In particular this work shows that both the global loss (η), localized loss centers, or changes to the spectrum can be independently tuned to achieve the CPA condition.

We note that at CPA both the peak in $|\mathrm{Re}\ \tau_W|$ and the point at which $\mathrm{Im}\ \tau_W$ changes its sign coincide in energy, but away from CPA these features may occur at different energies. Note that the real and imaginary parts share the same forms in the denominator of the Lorentzians. This leads to a synchronous evolution of their shapes with energy and scattering characteristics.

We also note that CPA can be achieved by tuning either localized loss Γ_A, or uniform loss η, as demonstrated in Fig. 3.6 from experiment and Fig. 3.11 from simulation, respectively.

Next step includes treating the case of overlapping modes, and the development of theoret-

ical predictions for the statistical properties of both the real and imaginary parts of the complex time delay in chaotic and multiple scattering sub-unitary systems.

In conclusion, we have introduced a complex generalization of Wigner time delay which holds for arbitrary uniform/global and localized loss, and directly relates to poles and zeros of the scattering matrix in the complex energy/frequency plane. Based on that we developed theoretical expressions for complex time delay as a function of energy, and found very good agreement with experimental data on a sub-unitary complex scattering system. Time delay and $\det(S)$ share a common feature that CPA and the divergence of $\mathrm{Re}[\tau_W]$ and $\mathrm{Im}[\tau_W]$ coincide. This work opens a new window on time delay in lossy systems, enabling extraction of complex zeros and poles of the S-matrix from data.

Chapter 4: Statistics of Complex Wigner Time Delay in Sub-Unitary Scattering Systems

4.1 Overview

In prior chapter we examined the relationship between the generalized complex time delay and the locations of the S-matrix poles $\mathcal{E}_n$ and zeros z_n in the complex energy plane for isolated modes. In this chapter we are concerned with the statistical properties of complex time delay for large ensembles of scattering systems. It is clear that the statistics of locations of the S-matrix poles and zeros will influence the statistics of the complex time delay.

The subject of interest is the general scattering properties of complex systems, namely finite-size wave systems with one or more channels connected to asymptotic states outside of the scattering domain. The scattering system is complex in the sense that classical ray trajectories will undergo chaotic scattering when propagating inside the closed system. We focus on the properties of the energy-dependent scattering matrix of the system, defined via the linear relationship between the outgoing $|\psi_{\text{out}}\rangle$ and incoming wave amplitudes $|\psi_{\text{in}}\rangle$ on the M coupled channels as $|\psi_{\text{out}}\rangle = S\,|\psi_{\text{in}}\rangle$. In the short wavelength limit the complex $M \times M$ scattering matrix $S(E)$ is a strongly fluctuating function of energy E (or, equivalently, the frequency ω) of the incoming waves, as well as specific system details. Those parts of the fluctuations which reflect

long-time behavior are controlled by the high density of S-matrix poles, or resonances, having their origin at eigenfrequencies (modes) of closed counterparts of the scattering systems. At energy scales comparable to the mean separation Δ between the neighboring eigenfrequencies, the properties of the scattering matrix are largely universal, and depend on very few system-specific parameters. The ensuing statistical characteristics of the S-matrix have been very successfully studied theoretically over the last 3 decades using methods of Random Matrix Theory (RMT) [77, 140, 144, 155–157, 170–172].

One quantity which is closely related to resonances is known to be the Wigner time delay τ_{W}. In its traditional definition [49, 50] for unitary, flux conserving scattering systems the Wigner time delay τ_{W} is a real positive quantity measuring how long an excitation lingers in the scattering region before leaving through one of the M channels. Fluctuations of τ_{W} and related quantities was the subject of a large number of theoretical works in the RMT context [78, 79, 111, 131–135, 173, 174], and more recently [51, 136, 139, 143, 175], as well in a semiclassical context in [55, 138, 164, 176] and references therein. In particular, for the one and two channel cases most relevant to this dissertation the distribution of τ_{W} is known explicitly for all symmetry classes, $\beta = 1$, 2 and 4 [135].

Experimental work on time delays in wave chaotic billiard systems was pioneered by Doron, Smilansky and Frenkel in microwave billiards with uniform absorption [120], where the relation between the Wigner time delays and the unitary deficit of the S-matrix has been explored. Later experiments on time delay statistics were made by Genack and co-workers, who studied microwave pulse delay times through randomized dielectric scatterers [121, 122]. The quantity studied in that case is a type of partial time delay associated with the complex transmission amplitude between channels [177], somewhat different from the Wigner time delay. In particular,

contributions to the transmission time delay due to poles and zeros of the off-diagonal S-matrix entries have been identified [59].

Despite strong interest in the standard Wigner time delay over the years, its use for characterising statistics of S-matrix poles and zeros beyond the regime of well-resolved (isolated) resonances have been always problematic. In our recent paper [2] we noticed that in the presence of losses one may propose a complex-valued generalization of the Wigner time delay $\tau_{\rm W}$ (CWTD) which reflects the phase and amplitude variation of the scattering matrix with energy. Subsequently, we developed a method, both experimentally and theoretically, for exploiting CWTD for identifying the locations of individual S-matrix poles $\mathcal{E}_n$ and zeros z_n in the complex energy plane. The method has been implemented in the regime of well-resolved, isolated resonances, for systems with both localized and uniform sources of absorption. However, no statistical characterization of CWTD for large numbers of modes has been attempted.

To this end it is worth mentioning that one of the oldest yet useful facts about the standard Wigner time delay is that the mean of the $\tau_{\rm W}$ distribution is simply related to the Heisenberg time $\tau_{\rm H}$ of the system, $\langle \tau_{\rm W} \rangle = 2\pi\hbar/M\Delta := \tau_{\rm H}/M$ [159]. As such it is absolutely insensitive to the type of dynamics, chaotic versus integrable. More recently this property was put in a much wider context and tested experimentally [178].

In this chapter we reveal that the mean value of ${\rm Re}[\tau_{\rm W}]$ of CWTD is, in striking contrast to the flux-conserving case, a much richer object and can be used to obtain nontrivial information about the distribution of the imaginary part of the poles of the S-matrix. For this we develop the corresponding theory for the mean values and compare to the experimentally observed evolution of distributions of real and imaginary parts of CWTD with uniform loss variation.

4.2 Complex Wigner Time Delay

The appropriate theoretical framework for our analysis is the so called effective Hamiltonian formalism for wave-chaotic scattering [77, 118, 144, 156, 157]. It starts with defining an $N \times N$ self-adjoint matrix Hamiltonian H whose real eigenvalues are associated with eigenfrequencies of the closed system. Further defining W to be an $N \times M$ matrix of coupling elements between the N modes of H and the M scattering channels, one can in the standard way build the unitary $M \times M$ scattering matrix $S(E)$. In this approach the S-matrix poles $\mathcal{E}_n = E_n - i\Gamma_n$ (with $\Gamma_n > 0$) are complex eigenvalues of the non-Hermitian effective Hamiltonian matrix $\mathcal{H}_{\text{eff}} = H - i\Gamma_W \neq \mathcal{H}_{\text{eff}}^\dagger$, where we defined $\Gamma_W = \pi W W^\dagger$. A standard way of incorporating the uniform absorption with strength η is to replace $E \to E + i\eta$ making S-matrix subunitary, such that its determinant $\det S(E + i\eta)$ is given by the ratio

$$\frac{\det[E - H + i(\eta - \Gamma_W)]}{\det[E - H + i(\eta + \Gamma_W)]} = \prod_{n=1}^{N} \frac{E + i\eta - \mathcal{E}_n^*}{E + i\eta - \mathcal{E}_n}, \tag{4.1}$$

Using the above the expression, the Wigner time delay can be very naturally extended to scattering systems with uniform absorption as suggested in [2] by defining:

$$\tau_{\text{W}}(E;\eta) \coloneqq \frac{-i}{M}\frac{\partial}{\partial E}\log\det S(E + i\eta) = \text{Re}\ \tau_{\text{W}}(E;\eta) + i\text{Im}\ \tau_{\text{W}}(E;\eta), \tag{4.2}$$

$$\text{Re}\ \tau_{\text{W}}(E;\eta) = \frac{1}{M}\sum_{n=1}^{N}\left[\frac{\Gamma_n + \eta}{(E - E_n)^2 + (\Gamma_n + \eta)^2} - \frac{\eta - \Gamma_n}{(E - E_n)^2 + (\Gamma_n - \eta)^2}\right], \tag{4.3}$$

$$\text{Im}\ \tau_{\text{W}}(E;\eta) = -\frac{1}{M}\sum_{n=1}^{N}\left[\frac{4\eta\Gamma_n(E - E_n)}{[(E - E_n)^2 + (\Gamma_n - \eta)^2][(E - E_n)^2 + (\Gamma_n + \eta)^2]}\right] \tag{4.4}$$

For a wave-chaotic system the set of parameters Γ_n, E_n (known as the *resonance widths*

and *positions*, respectively) is generically random. Namely, even minute changes in microscopic shape characteristics of the system will drastically change the particular arrangement of S-matrix poles in the complex plane in systems which are otherwise macroscopically indistinguishable. To study the associated statistics of CWTD most efficiently one may invoke the notion of an *ensemble* of such systems. As a result, both $\mathrm{Re}[\tau_{\mathrm{W}}]$ and $\mathrm{Im}[\tau_{\mathrm{W}}]$ at a given energy will be distributed over a wide range of values. Alternatively, even in a single wave-chaotic system the CWTD will display considerable statistical fluctuations when sampled over an ensemble of different *mesoscopic* energy intervals. Invoking the notion of spectral ergodicity one expects that in wave-chaotic systems the two types of ensembles (i.e. those produced by perturbations to the system at fixed energy vs. those created by considering various energy windows) should be equivalent.

Consider the mean value of the CWTD in systems with uniform absorption $\eta > 0$. In contrast to the case of flux-conserving systems the mean of $\mathrm{Re}[\tau_{\mathrm{W}}]$ becomes highly nontrivial as it counts the number of S-matrix poles whose widths exceed the uniform absorption strength value. In other words,

$$\frac{\langle \mathrm{Re}[\tau_{\mathrm{W}}(E;\eta)]\rangle_E}{\tau_{\mathrm{H}}/M} = \frac{\#[\Gamma_n > \eta \text{ such that } E_n \text{ is inside } I_E]}{\text{total \# resonances inside } I_E} \tag{4.5}$$

where I_E is a mesoscopic energy interval that is much larger than the mean mode spacing Δ, absorption η and the widths Γ_n, but small enough so that the interval has a roughly constant

mode density. To prove this, perform an energy average of Eq. (4.3):

$$\begin{aligned}
&\langle \mathrm{Re}[\tau_{\mathrm{W}}(E;\eta)]\rangle_E \approx \\
&\frac{\pi/2}{M|I|}\sum_{n=1}^{N}\left\{\left[\mathrm{sign}\left(\frac{E_R-E_n}{\eta+\Gamma_n}\right)-\mathrm{sign}\left(\frac{E_L-E_n}{\eta+\Gamma_n}\right)\right]\right. \\
&\left.-\left[\mathrm{sign}\left(\frac{E_R-E_n}{\eta-\Gamma_n}\right)-\mathrm{sign}\left(\frac{E_L-E_n}{\eta-\Gamma_n}\right)\right]\right\} \\
&=\frac{2\pi}{M|I|}\sum_{n=1}^{N}\theta(\Gamma_n-\eta)
\end{aligned} \tag{4.6}$$

where $|I| := |E_R - E_L|$ is the mesoscopic energy interval, and the step function $\theta(x) = 1$ for $x > 0$ and $\theta(x) = 0$ otherwise. Under the assumption that $\#(E_n \in I) \approx |I|/\Delta$ we arrive at the statement Eq. (4.5) above. Alternatively, invoking ergodicity, one may use the RMT for analysing the mean CWTD, which independently confirms Eq. (4.5). Such analysis also predicts that $\langle \mathrm{Im}[\tau_{\mathrm{W}}(E,\eta)\rangle_E = 0$, independent of η. Details of these calculations are presented in Appendix A.2. The distribution of imaginary parts Γ_n of the S-matrix poles relevant for Eq. (4.5) have been examined theoretically in the RMT framework [145–148] and experimentally [124–129] by a number of groups.

4.3 Experiment

We test our theory by using an ensemble of tetrahedral microwave graphs with either $M = 1$ or $M = 2$ channels coupled to the outside world. We focus on experiments involving microwave graphs [1,39,41,161] for a number of reasons: one can precisely vary the uniform loss and the lumped loss over a wide range; one can work in either the time-reversal invariant (TRI) or broken-TRI regimes; one can gather very good statistics with a large ensemble of

graphs; one can vary both the (energy-independent) mode density and loss to go from the limit of isolated modes to strongly overlapping modes. The disadvantages of graphs for statistical studies include significant reflections at nodes, which can create trapped modes on the bonds [179], and the appearance of short periodic orbits in cyclic graphs [45].

4.3.1 Experimental Setup

The microwave graphs are constructed with coaxial cables with center conductors of diameter 0.036 in. (0.92 mm) made with silver plated copper clad steel, and outer shield of diameter 0.117 in. (2.98 mm) made with a copper-tin composite. An ensemble of microwave graphs is created by choosing 6 out of 9 cables with different incommensurate lengths (for a total of $\binom{9}{6} = 84$ realizations) and creating uniquely different tetrahedral graphs. The scattering matrix of the 1 and 2-port graphs are measured with a calibrated Agilent PNA-X N5242A Network Analyzer (see insets of Fig. 4.3) over the frequency range from 1 to 12.4 GHz, which includes about 250 modes in a typical realization of the ensemble. The graphs are measured with a finite coupling strength g_a, which varies from 1.06 to 1.80 as a function of frequency, where $g_a = \frac{2}{T_a} - 1$ and $T_a = 1 - |S_{\text{rad}}|^2$ is the transparency of the graph to the scattering channel a determined by the value of the radiation S-matrix.[1] The effects of the coupling are then removed through application of the Random Coupling Model (RCM) normalization process [17, 20–22] (see more details in Appendix D.3). This is equivalent to creating an ensemble of data with perfect coupling, $g_a = 1$ and $T_a = 1$ for all frequencies, ports, and realizations.

Time-reversal invariance was broken in the graph by means of one of 4 different microwave

[1] The radiation S_{rad} is measured when the graph is replaced by $50\ \Omega$ loads connected to the three output connectors of each node attached to the network analyzer test cables.

circulators [40] operating in partially overlapping frequency ranges going from 1 to 12.4 GHz (see Appendix D.2). The CWTD τ_{W} is calculated using the RCM-normalized scattering matrix S as in Eq. (4.2), and the statistics of the real and imaginary parts are compiled based on realization averaging and frequency averaging in a given frequency band. The overall level of attenuation was varied by adding identical fixed microwave attenuators to each of the 6 bonds of the tetrahedral graphs [180]. The attenuator values chosen were 0.5, 1 and 2 dB.

4.3.2 Comparison of Theory and Experiments

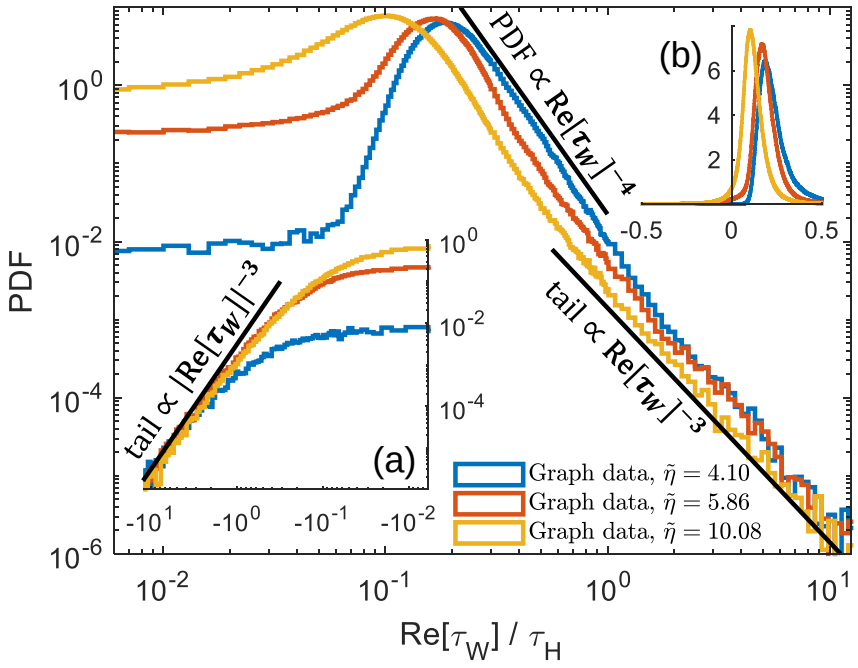

Figure 4.1: Evolution of the PDF of measured Re$[\tau_{\mathrm{W}}]$ with increasing uniform attenuation ($\tilde{\eta}$) from an ensemble of two-port ($M = 2$) tetrahedral microwave graphs with broken-TRI. Main figure and inset (a) show the distributions of the positive and negative Re$[\tau_{\mathrm{W}}]$ on a log-log scale for three values of uniform attenuation, respectively. Reference lines characterizing power-law behavior are added to the tails. Inset (b) shows the distributions of Re$[\tau_{\mathrm{W}}]$ on a linear scale for the same measured data. This figure is taken from Ref. [3].

Our prior work showed that CWTD varied systematically as a function of energy/frequency

for an isolated mode of a microwave graph [2]. The real and imaginary parts of τ_{W} take on both positive and negative values. We now consider an ensemble of graphs and examine the distribution of these values taken over many realizations and modes. We first examine the evolution of the PDF of $\mathrm{Re}[\tau_{\mathrm{W}}]$ (Fig. 4.1(b)) and $\mathrm{Im}[\tau_{\mathrm{W}}]$ (inset of Fig. 4.2) with increasing uniform (normalized) attenuation $\tilde{\eta}$. The uniform attenuation is quantified from the experiment as $\tilde{\eta} = \frac{2\pi}{\Delta}\eta = 4\pi\alpha$, where $\alpha = \delta f_{3\mathrm{dB}}/\Delta_f$, $\delta f_{3\mathrm{dB}}$ is the typical 3-dB bandwidth of the modes and Δ_f is the mean frequency spacing of the modes [18].

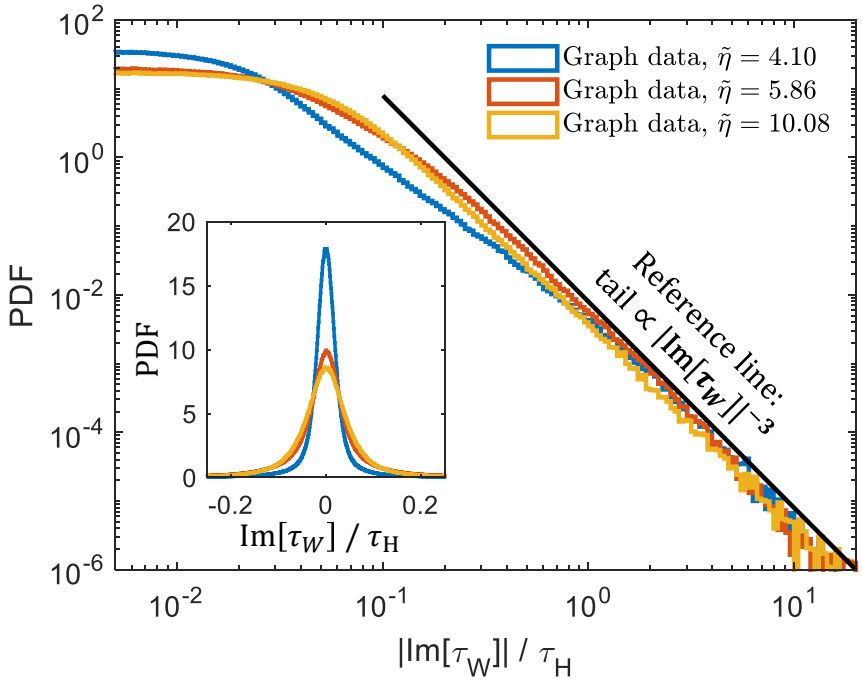

Figure 4.2: Evolution of the PDF of measured $\mathrm{Im}[\tau_{\mathrm{W}}]$ with increasing uniform attenuation ($\tilde{\eta}$) from an ensemble of two-port ($M = 2$) tetrahedral microwave graph data with broken-TRI. The main figure shows a log-log plot of the PDF versus $|\mathrm{Im}[\tau_{\mathrm{W}}]|$ for three values of uniform attenuation. A reference line is added to characterize the power-law tail. Inset shows the distributions of $\mathrm{Im}[\tau_{\mathrm{W}}]$ on a linear scale for the same measured data. This figure is taken from Ref. [3].

Fig. 4.1 shows that as the uniform attenuation ($\tilde{\eta}$) of the graphs increases, the peak of the $\mathrm{Re}[\tau_{\mathrm{W}}]$ distribution shifts to lower values. Furthermore, Fig. 4.1(a) shows that $\mathrm{Re}[\tau_{\mathrm{W}}]$ acquires more negative values as the attenuation increases. Fig. 4.1 demonstrates that the PDF of $\mathrm{Re}[\tau_{\mathrm{W}}]$

exhibits power-law tails on both the negative and positive sides, respectively. The positive-side PDFs shown in Fig. 4.1 have different power-law behaviors for different ranges of $\mathrm{Re}[\tau_W]$, which is further explained theoretically in Appendix A.3. Fig. 4.2 shows the PDF of $|\mathrm{Im}[\tau_W]|$ on both linear and log-log scales for the same values of uniform attenuation. We find that the $\mathrm{Im}[\tau_W]$ distribution is symmetric about zero to very good approximation. Once again a power-law behavior of the tails of the distribution is evident.

Figure 4.3 shows a plot of the $\mathrm{Mean}(\mathrm{Re}[\tau_W])$ vs. uniform attenuation ($\tilde{\eta}$) in ensembles of microwave graphs for both (a) $M = 1$ and (b) $M = 2$ ports. The black circles represent the data taken on an ensemble of microwave graphs with constant $\tilde{\eta}$. The red line is an evaluation of the relation Eq. (4.5) above, based on the analytical prediction for the $P(\Gamma_n)$ distribution for the a) $M = 1$ and b) $M = 2$ cases, both with perfect coupling ($g = 1$) [77, 146]. Note that the distribution of Γ_n for $M = 1$ is very different from the multi-ports cases (see Fig. 4.6). Nevertheless there is excellent agreement between data and theory over the entire experimentally accessible range of uniform attenuation values for both 1-port and 2-port graphs. We can conclude that the theoretical prediction put forward in Eq. (4.5) is in agreement with experimental data. A more detailed comparison with random matrix based computations over a broad range of uniform attenuation is presented in section 4.4.

We have also examined the experimentally obtained statistics of $\mathrm{Im}[\tau_W]$. As seen in the insets of Fig. 4.3 (a) and (b), we find that the mean of $\mathrm{Im}[\tau_W]$ is consistent with theoretically predicted zero value for all levels of uniform attenuation in the graphs.

We now turn out attention back to the power-law tails for the distributions of $\mathrm{Re}[\tau_W]$ and $\mathrm{Im}[\tau_W]$ presented in Figs. 4.1 and 4.2. By examining the statistics of large values of $\mathrm{Re}[\tau_W]$ that appear in Eq. (4.3), one finds that the tails of the PDFs will behave as $\mathcal{P}(\mathrm{Re}[\tau_W]) \propto 1/\mathrm{Re}[\tau_W]^3$,

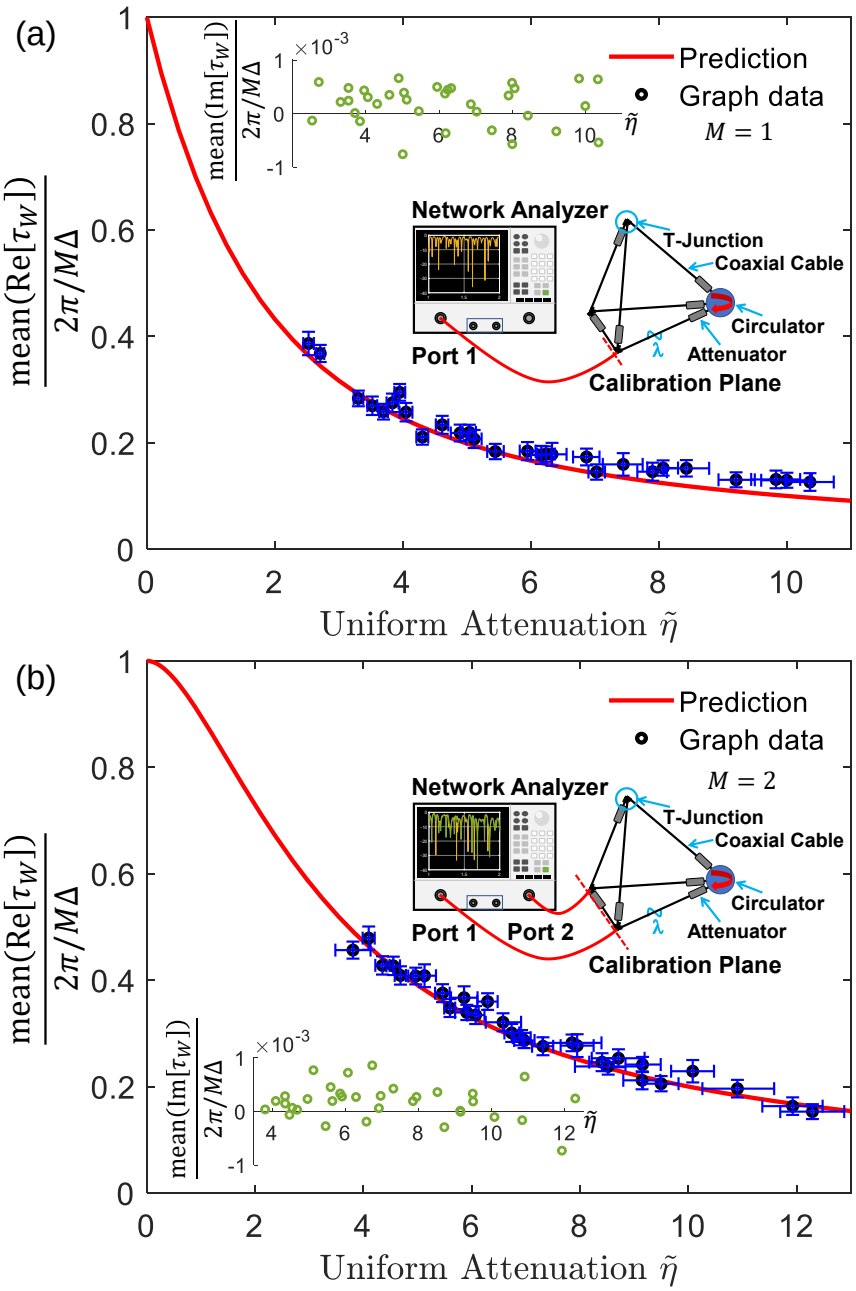

Figure 4.3: Mean of $\text{Re}[\tau_\text{W}]$ as a function of uniform attenuation $\tilde{\eta}$ evaluated using tetrahedral microwave graph data with broken-TRI for both one- and two-port configurations. (a) shows the one-port experimental data (black circles) compared with theory (red line). (b) shows the two-port experimental data (black circles) compared with theory (red line). A detailed discussion about the estimated error bars (blue) can be found in Appendix B.2. Insets show the mean of the $\text{Im}[\tau_\text{W}]$ (green circles) as a function of uniform attenuation $\tilde{\eta}$ evaluated using the same datasets for the one- and two-port configurations, respectively. Other insets show the experimental configurations. This figure is taken from Ref. [3].

on both the positive and negative sides, as long as $M\text{Re}[\tau_\text{W}]/\tau_\text{H} \gg 1/\tilde{\eta}$ (details discussed in Appendix A.3). This behavior is clearly observed on the negative side of the PDF, as shown in Fig. 4.1(a). The tail on the positive side is more complicated due to a second power-law expected in the intermediate range: $\mathcal{P}(\text{Re}[\tau_\text{W}]) \propto 1/\text{Re}[\tau_\text{W}]^4$ when $1 \ll M\text{Re}[\tau_\text{W}]/\tau_\text{H} \ll 1/\tilde{\eta}$. Unfortunately we were not able to obtain such data within this range (requiring very low attenuation $\tilde{\eta}$) experimentally, but a narrow range of $\text{Re}[\tau_\text{W}]/\tau_\text{H}$ between approximately 0.3 and 1 in Fig. 4.1 shows a steeper power-law behavior, consistent with $\mathcal{P}(\text{Re}[\tau_\text{W}]) \propto 1/\text{Re}[\tau_\text{W}]^4$, giving way to a more shallow slope at larger values of $\text{Re}[\tau_\text{W}]/\tau_\text{H}$, consistent with the theory. As seen in Fig. 4.2, the distribution of the imaginary part of the time delay has a wide range with a power law $\mathcal{P}(|\text{Im}[\tau_\text{W}]|) \propto 1/|\text{Im}[\tau_\text{W}]|^3$, consistent with our theoretical prediction.

4.4 Random Matrix Theory Simulation

We utilize numerical data from the Random Matrix Theory (RMT) simulation to further examine the theory presented in this chapter, and provide more insights for discussion. The RMT data is generated using Random Matrix Monte Carlo simulation [7]. Here we adopt the Gaussian Unitary Ensemble (GUE) setting in the Random Matrix calculation.

4.4.1 PDFs of Complex Time Delay in Sub-Unitary Scattering Systems

Figs. 4.4 and 4.5 show the evolution of the PDF of simulated complex time delay $\text{Re}[\tau_W]$ and $\text{Im}[\tau_W]$ with increasing uniform attenuation $\tilde{\eta}$ from an ensemble of GUE RMT data, respectively. The upper figure in Fig. 4.4 is the lin-lin plot of the PDF, while the lower figure shows the log-log plot of the PDF. The zoom-in view in Fig. 4.4(a) shows the detailed evolution of PDF

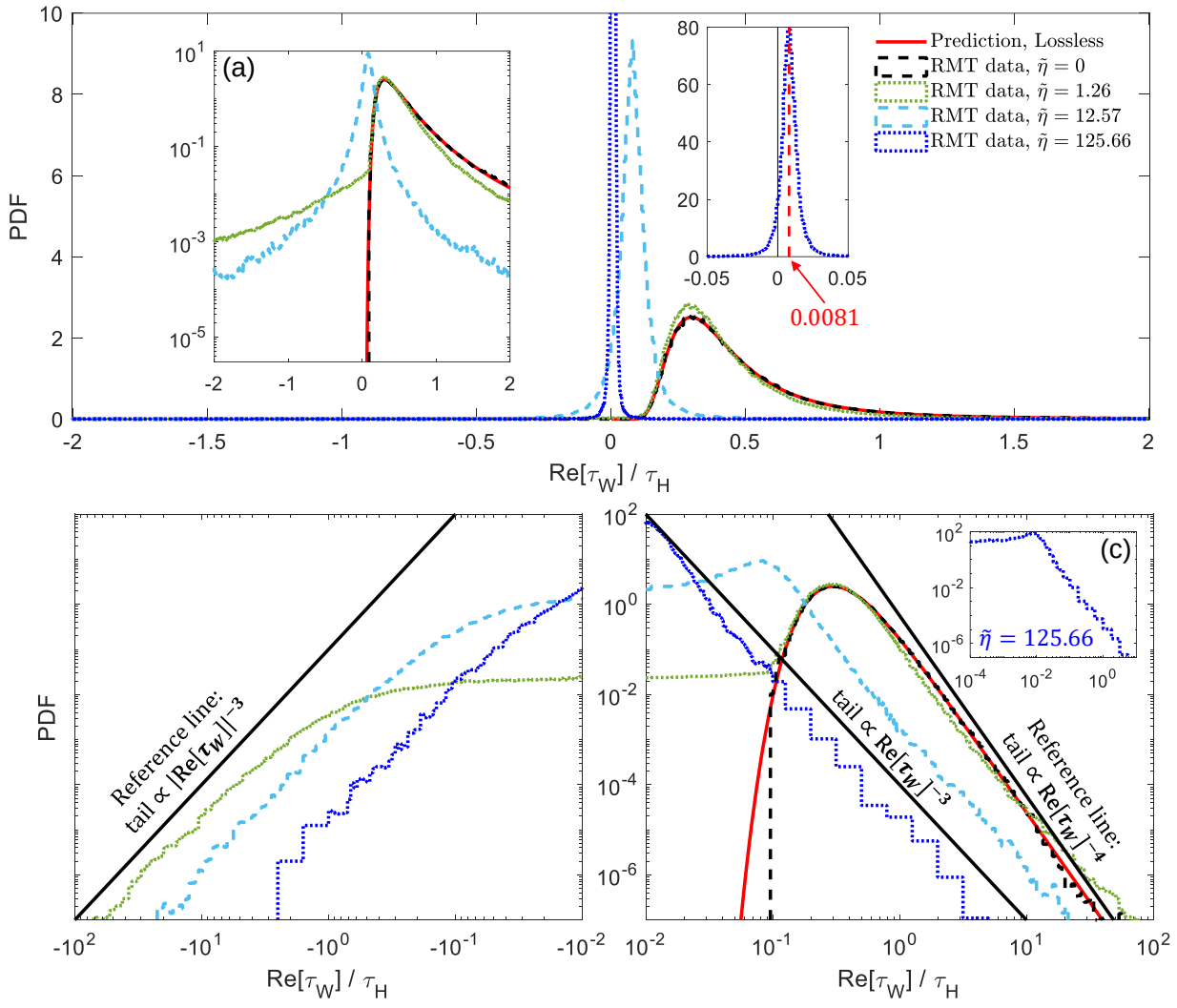

Figure 4.4: Evolution of the PDF of simulated Re$[\tau_W]$ with increasing uniform attenuation $\tilde{\eta}$ from an ensemble of two-port ($M = 2$) GUE RMT data. The upper figure is the lin-lin plot, while the lower one is the log-log plot. Inset (a) and (b) show the zoom-in view of the PDFs for different loss setting, and 0.0081 is the mean value of Re$[\tau_W]$ at $\tilde{\eta} = 125.66$. Inset (c) shows the whole PDF of positive Re$[\tau_W]$ in log-log scale for $\tilde{\eta} = 125.66$. The reference lines are added in the log-log plot to characterize the power-law tail feature of the PDF. This figure is taken from Ref. [3].

of Re$[\tau_W]$ as the uniform loss increases, while Fig. 4.4(b) shows the distribution of Re$[\tau_W]$ will concentrate around its mean value (0.0081) at a very large $\tilde{\eta}$ setting (strong uniform attenuation in the system). Figure 4.4 shows that the peak of the PDF shifts to lower Re$[\tau_W]$ values as the uniform loss increases, and Re$[\tau_W]$ starts to acquire negative values – the same behavior we have

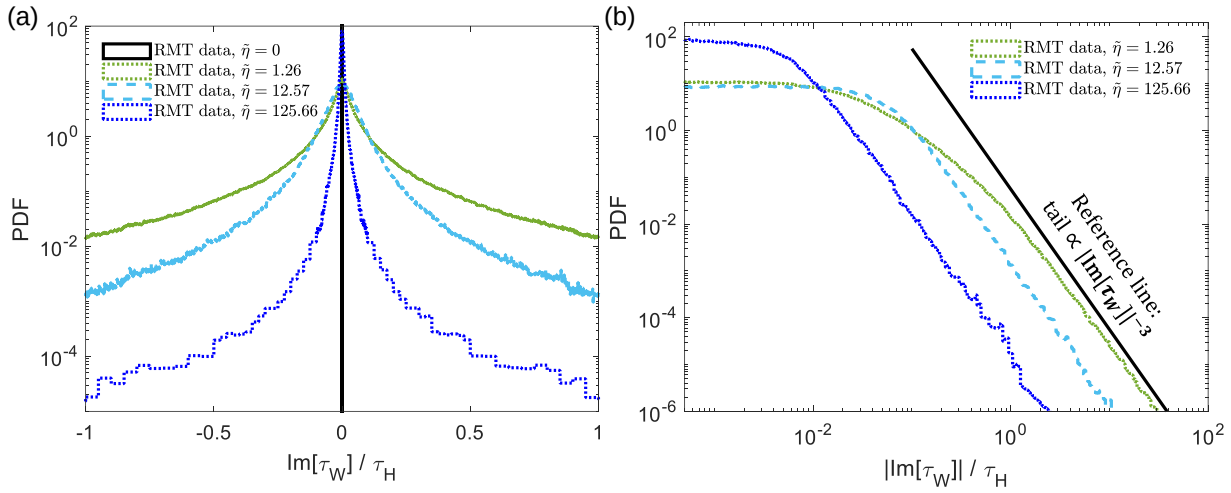

Figure 4.5: Evolution of the PDF of simulated $\mathrm{Im}[\tau_W]$ with increasing uniform attenuation $\tilde{\eta}$ from an ensemble of two-port ($M = 2$) GUE RMT data. (a) shows the PDFs of $\mathrm{Im}[\tau_W]$ in log-lin scale, while (b) shows the PDFs of $|\mathrm{Im}[\tau_W]|$ in log-log scale. The reference lines are added in the log-log plot to characterize the power-law tail feature of the PDF. This figure is taken from Ref. [3].

seen earlier from the experiment. Both positive and negative sides of the PDF have a power-law tail in the log-log view of Fig. 4.4. Fig. 4.5(a) shows the log-lin plot of the PDFs of $\mathrm{Im}[\tau_W]$, while Fig. 4.5(b) shows the log-log plot of the PDFs of $|\mathrm{Im}[\tau_W]|$ (the distributions of $\mathrm{Im}[\tau_W]$ are symmetrical in positive and negative sides). In Fig. 4.5(a), the PDF starts from a δ-function in the lossless case, and it gradually expands and then shrinks as $\tilde{\eta}$ increases. Fig. 4.5(b) shows the power-law tail feature of the PDF, and reference lines are added.

4.4.2 Counting Resonance Widths via Complex Time Delay

We also demonstrate the correctness of the theory for variable coupling settings using the RMT simulation. Fig. 4.6 shows the probability distributions of the resonance width Γ_n for different numbers of scattering channels (M) and variable coupling strength (g) in the GUE lossless setting, where $y = \pi\Gamma_n/\Delta$ is the scaled resonance width [77]. (a) – (c) demonstrates that

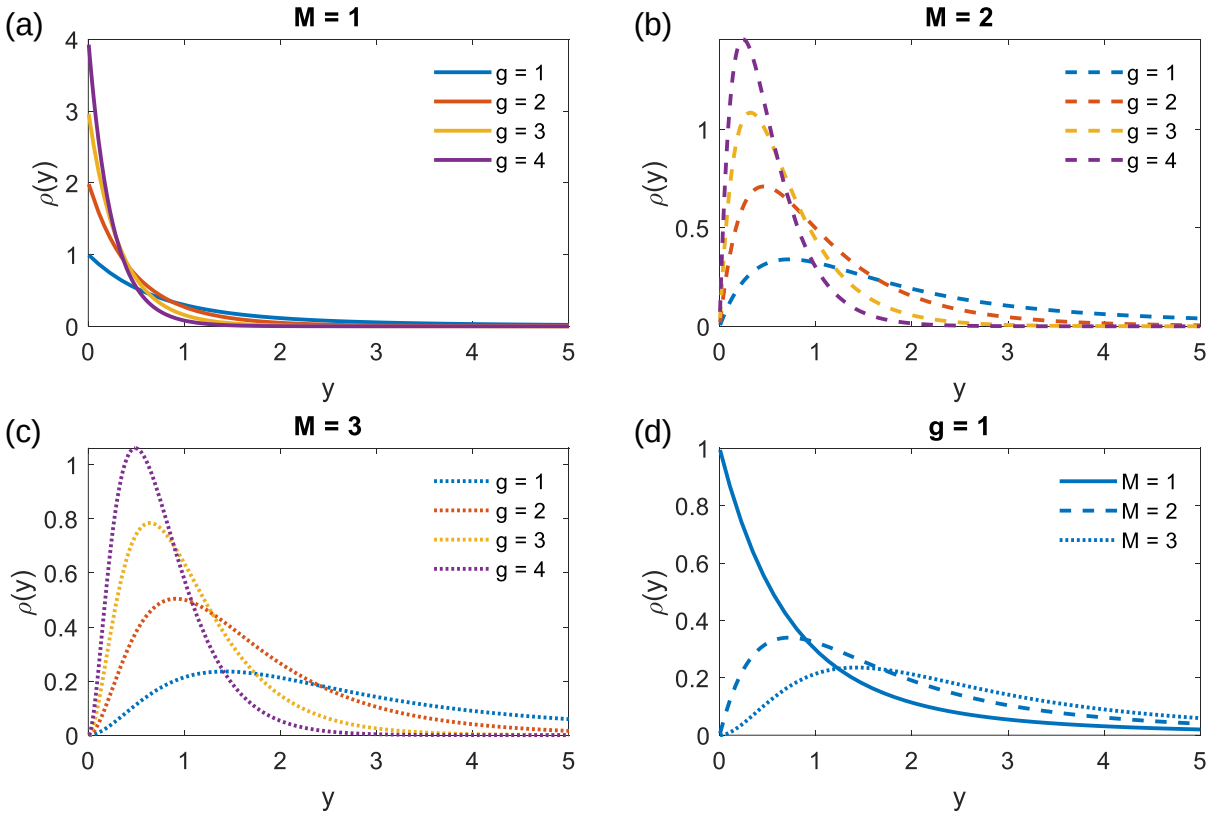

Figure 4.6: Probability distributions of scaled resonance width y ($y = \pi\Gamma_n/\Delta$) for different numbers of scattering channels (M) and variable coupling strength (g) in the GUE lossless setting. (a)–(c) show the probability distributions of the scaled resonance width with different coupling settings ($g = 1,\ 2,\ 3$ and 4) for $M = 1,\ 2,$ and 3, respectively. (d) shows the comparison between the probability distributions for different numbers of scattering channels ($M = 1,\ 2,$ and 3) at perfect coupling setting ($g = 1$). This figure is taken from Ref. [3].

the peak of $\rho(y)$ shifts to lower values as g goes up, which indicates that the majority of poles of S-matrix are closer to the real axis in the lossless case when the coupling gets weaker. Fig. 4.6(d) clearly shows that the one-port ($M = 1$) case is very different from the other multi-port cases. Figs. 4.7 and 4.8 examine the theory further using ensembles of one-port ($M = 1$) and two-port ($M = 2$) GUE RMT data of variable uniform attenuation ($\tilde{\eta}$) with different coupling settings (g), respectively. The RMT data results are directly compared to the theory predictions calculated using the probability distribution functions shown in Fig. 4.6, and they agree quite well.

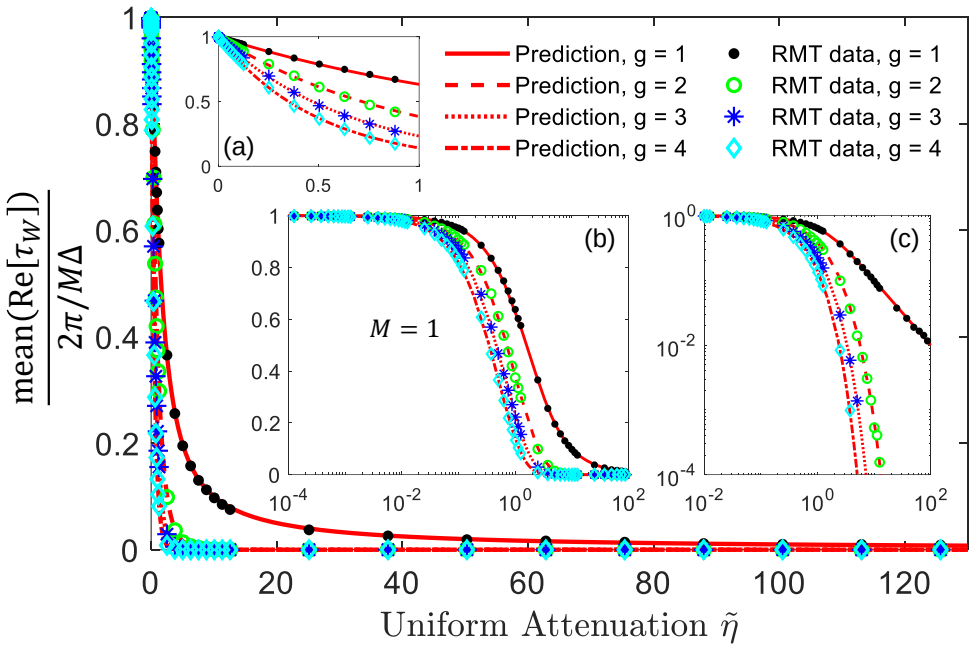

Figure 4.7: Mean of simulated $\mathrm{Re}[\tau_W]$ as a function of uniform attenuation $\tilde{\eta}$ with variable coupling strength (g) evaluated using ensembles of one-port ($M = 1$) GUE RMT data. The markers are RMT data, while the red lines are theoretical predictions. Inset (a) shows the zoom-in details of the plot at small attenuation values. Inset (b) and (c) are the lin-log scale and log-log scale of the plot, respectively. This figure is taken from Ref. [3].

4.4.3 Mean of $|\mathrm{Im}[\tau_W]|$ vs Uniform Attenuation

Similar analysis are being done for $\mathrm{Im}[\tau_W]$ using the same ensembles of one-port ($M = 1$) and two-port ($M = 2$) GUE RMT data of variable uniform attenuation ($\tilde{\eta}$) with different coupling settings (g) in Fig. 4.9. Both one-port ($M = 1$) and two-port ($M = 2$) plots in Fig. 4.9 exhibit interesting and similar power-law tails, with reference lines added.

4.5 Discussion and Conclusions

We demonstrated that the CWTD is an experimentally accessible object sensitive to the statistics of S-matrix poles in the complex energy/frequency plane. In addition to the experimen-

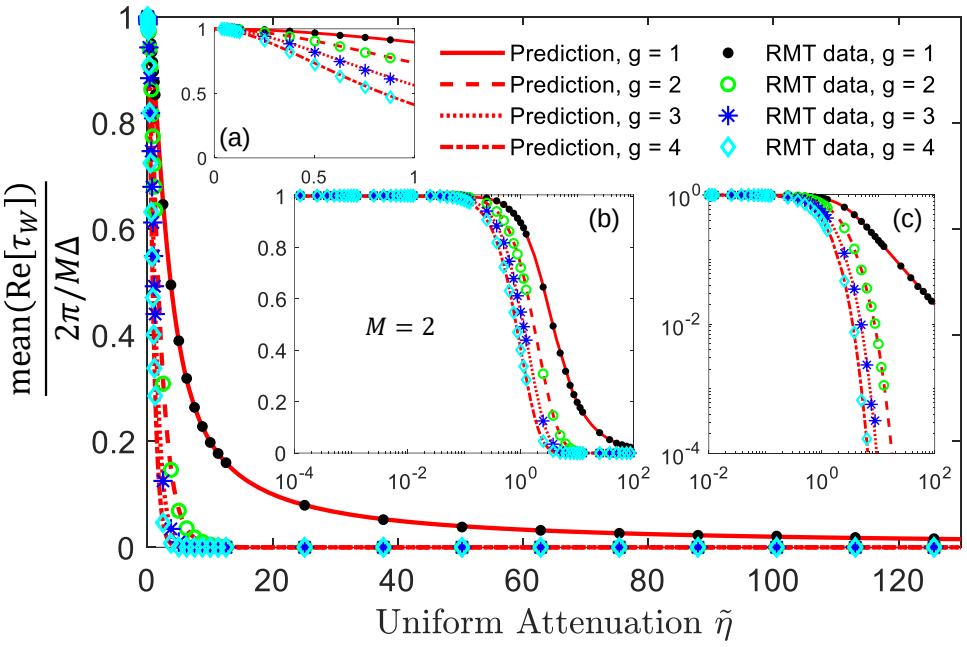

Figure 4.8: Mean of simulated $\mathrm{Re}[\tau_W]$ as a function of uniform attenuation $\tilde{\eta}$ with variable coupling strength (g) evaluated using ensembles of two-port ($M = 2$) GUE RMT data. The markers are RMT data, while the red lines are theoretical predictions. Inset (a) shows the zoom-in details of the plot at small attenuation values. Inset (b) and (c) are the lin-log scale and log-log scale of the plot, respectively. This figure is taken from Ref. [3].

tal results discussed above, we have also employed Random Matrix Theory, as well as associated numerical simulations, for studying the distribution of the CWTD. Through these simulations we can explore much smaller, and much larger, values of uniform attenuation than can be achieved in the experiment. These simulations show agreement with all major predictions of the RMT-based theory, including the existence of an intermediate power-law on the positive side of the $\mathcal{P}(\mathrm{Re}[\tau_\mathrm{W}])$ distribution for low-loss systems. Finally we note that all results in Eqs. (4.1) – (4.5) are insensitive to the presence or absence of TRI. The power-law tail predictions are also insensitive to TRI, as shown in Appendix A.3.

We have experimentally verified the theoretical prediction that the mean value of the $\mathrm{Re}[\tau_\mathrm{W}]$ for a system with uniform absorption strength η counts the fraction of scattering matrix poles with

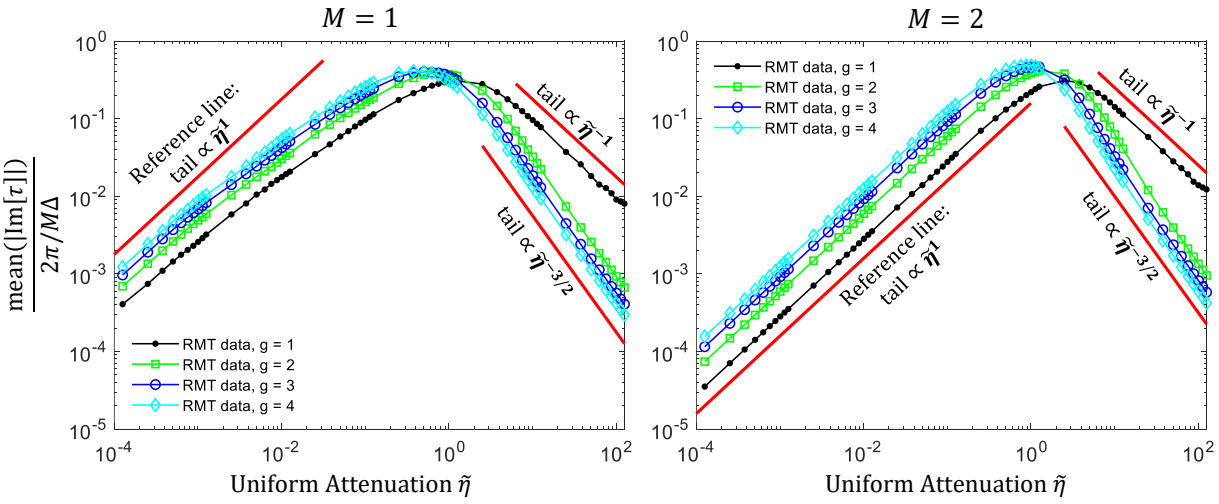

Figure 4.9: Mean of simulated $\mathrm{Im}[\tau_W]$ as a function of uniform attenuation $\tilde{\eta}$ with variable coupling strength (g) evaluated using ensembles of one-port ($M = 1$) and two-port ($M = 2$) GUE RMT data. Left side shows the one-port ($M = 1$) log-log plot, while the right side shows the two-port ($M = 2$) log-log plot. References lines are added to both plots to feature the power-law tails.

imaginary parts exceeding η. This opens a conceptually new opportunity to address resonance distributions experimentally, as we convincingly demonstrated with an ensemble of microwave graphs with either one or two scattering channels, and showing broken time-reversal invariance and variable uniform attenuation. The tails of the distributions of both real and imaginary time delay are found to agree with theory.

Chapter 5: Complex Time Delay Analysis of the Ring Graph

5.1 Overview

In this chapter, we are concerned with the general scattering properties of complex systems connected to the outside world through a finite number of ports or channels. The systems of interest have a closed counterpart, described by a Hamiltonian H, that has a spectrum of modes. Excitations can be introduced to, or removed from, the interaction zone of the scattering system by means of the M ports or channels. The scattering matrix S relates a vector of incoming (complex) waves $|\psi_{in}\rangle$ on the channels to the outgoing waves $|\psi_{out}\rangle$ on the same channels as $|\psi_{out}\rangle = S\,|\psi_{in}\rangle$. The scattering matrix is a complex function of energy (or equivalently frequency) of the waves, and contains all the information about the scattering properties of the system [155, 156, 181, 182].

In unitary (flux conserving) scattering systems, time delay is a real quantity measuring the time an injected excitation resides in the interaction zone before escaping through the ports [49,50]. This is a well-studied quantity in the chaotic wave scattering literature, and it's statistical properties have been extensively investigated [51, 77, 111, 120, 121, 131, 133–135, 143, 164, 176]. Recently, a complex generalization of time delay that applies to sub-unitary scattering systems was introduced, and this quantity turns out to be much richer than its lossless counterpart [2, 3, 160]. It has been demonstrated that complex Wigner-Smith time delay is sensitive to the locations

and statistics of the poles and zeros of the full scattering matrix. One of the goals of this work is to extend the use of complex Wigner-Smith time delay (τ_W, the sum of all partial time delays) to the transmission (τ_T), reflection ($\tau_R^{(1)}, \tau_R^{(2)}$, ...), and reflection time differences ($\tau_R^{(1)} - \tau_R^{(2)}$, etc.) [57, 58] of arbitrary multiport scattering systems. (Note that τ_T and τ_R are complex, even for unitary scattering systems.) This in turn yields new information about the poles and zeros of the reflection and transmission sub-matrices of S. One additional novelty of our approach is the explicit inclusion of uniform attenuation in the description of the scattering system, a feature that is neglected in many other treatments of time delay, as well as treatments of scattering matrix poles and zeros.

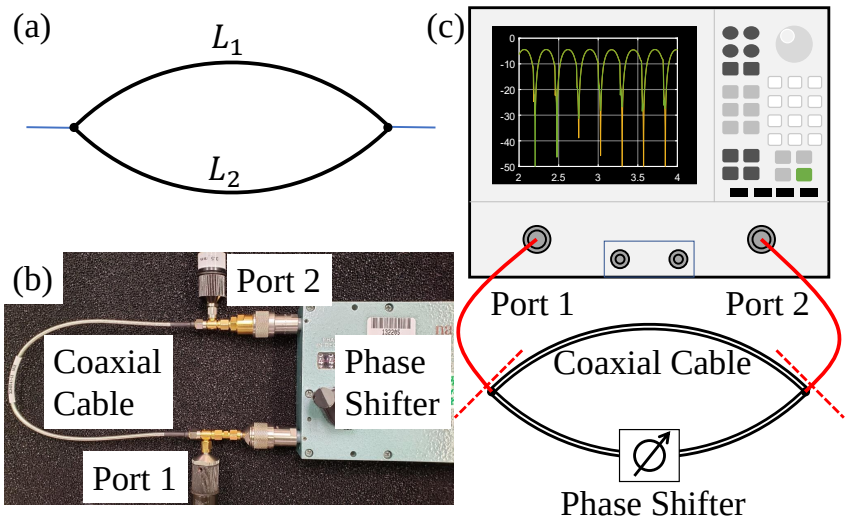

Figure 5.1: (a) Schematic diagram of a generic ring graph connected to two infinite leads. The two bonds have length L_1 and L_2. (b) shows the picture of the experimental microwave ring graph, where a coaxial cable and a coaxial microwave phase shifter are used as the two bonds. (c) shows a schematic of the experimental setup with the microwave network analyzer included. The two dashed red lines indicate the calibration plane for the 2×2 S-matrix measurement. This figure is taken from Ref. [4].

Here our attention is fixed on a simple, but remarkably important, scattering system, namely the quantum ring graph. In this context, a graph is a network of one-dimensional bonds (trans-

mission lines) that meet at nodes. One can solve the Schrodinger equation for waves propagating on the bonds of metric graphs, and enforce boundary conditions at the nodes [183–185]. The result is a closed system in which complicated interference of waves propagating on the bonds and meeting at the nodes gives rise to a discrete set of eigenmodes. Connecting this graph to M ports (infinitely long leads) creates the scattering system of interest to us here [39, 40, 161, 186–188]. The ring graph, consisting of just two bonds connecting the same two nodes, which in turn are connected to $M = 2$ ports (see Fig. 5.1(a)), is a ubiquitous and important scattering system. It appears in many guises in different fields, but there is no unified treatment of its scattering properties, particularly with regard to time delay, to our knowledge. Among other things, it forms the basis of non-reciprocal Aharonov-Bohm mesoscopic devices, as well as various types of superconducting quantum interference devices. The scattering properties of ring graphs have been studied theoretically by a number of groups for their embedded eigenstates [189, 190], and for conditions of perfect transmission [191, 192].

Ring graphs with circumference Σ that are on the order of the wavelength or longer, are utilized as resonators in several areas of research and applications. Such resonators can display very narrow spectral features, which are accompanied by large time delays. Ring resonators very elegantly and simply illustrate several different types of resonances which are known by a variety of names, including: shape modes, Feshbach modes [190, 193, 194], Fano modes [195], electromagnetically-induced transparency (EIT) modes [196], topological resonances [197–199], bound states in the continuum [70, 200–203], quasinormal modes [204, 205], etc. Here we use the shape/Feshbach terminology to discuss the modes, but our results apply to ring graphs in all contexts. To illustrate the ubiquity and importance of the ring graph, we next discuss some of the diverse manifestations and properties of this simple graph.

Fano resonances have been studied by many authors in the context of quantum transport through graph-like structures [69, 206, 207]. The Fano resonance arises from the constructive and destructive interference of a narrow discrete resonance (typically a bound state of the closed system) with a broad spectral line or continuum excitation, thus creating two scattering channels [208, 209]. The interference of these two channels gives rise to the celebrated Fano resonance profile [195, 206].

EIT is a quantum phenomenon that arises from interference between transitions taking place between multiple states [196]. It has a classical analog that can be realized in a wide variety of coupled oscillator scenarios [210]. For example, an EIT/Fano resonance feature was proposed for a generic resonator coupled to an optical transmission line [211]. EIT phenomena have also been created through metamaterial realizations in which a strongly coupled (bright resonator) and weakly coupled (dark resonator) oscillator are brought into interference to completely cancel transmission, and at the same time create 'slow light' (enhanced transmission time delay), all at one wavelength [212–214].

In terms of applications, ring resonators have been employed in microwave circuit devices for many years [215, 216]. It was recognized that pairs of nearly degenerate modes exist in this structure and their interference could be used to advantage [216, 217]. Microstrip ring resonators are routinely created with intentional defects or stubs in one arm, or are coupled asymmetrically, to create interference of the nearly degenerate modes [216].

EIT-like resonant features have been created in optical microring resonators coupled to transmission lines by a number of groups. A classical analog of EIT was demonstrated with two photonic ring resonators coupled to optical fibers [218]. A set of two coupled microspheres, acting as ring resonators, showed the classical analog of EIT for light, and demonstrated large

transmission time delay [219]. An integrated optical waveguide realization of the ring graph, with one arm hosting a variable delay element, has been used to create "EIT dips" with associated large transmission delay [220]. Other work has used a pair of Silicon microring photonic resonators to create a non-reciprocal diode effect for light (1630 nm) by exploiting a Fano resonance and nonlinearity [221].

Mesoscopic ring graph structures made of metals and semiconductors have been studied extensively for evidence of electron interference in their transport properties [222–224]. Much of this work is focused on rings immersed in a magnetic field and showing quantum interference properties arising from the Aharonov-Bohm (AB) effect [225, 226]. Aharonov-Bohm rings with a localized trapping site in one arm have been proposed to generate non-reciprocal transmission time delay [227], and asymmetric transport [6].

Finally, superconducting quantum interference devices (SQUIDs) are based on a loop graph structure that supports a complex superconducting order parameter. The closed loop structure creates a quantization condition for the magnetic fluxoid, and the addition of one or more Josephson junctions to the ring bonds, along with the addition of two leads, creates a sensitive magnetic flux to voltage transducer known as a dc SQUID [228–230].

The purpose of this work is to apply the complex time delay approach to experimental data on a microwave realization of the ring graph with the goal of identifying the complete set of scattering poles, as well as scattering, transmission and reflection zeros, of the graph. With this information we are able to thoroughly characterize the scattering properties of this system, and at the same time establish a basis that unifies the many disparate approaches to describing the scattering properties of this remarkable graph.

The outline of this chapter is as follows. In Section 5.2, we present expressions for the

complex times delays in terms of singularities of the scattering matrix. In Section 5.3, we discuss the properties of the ring graph, including the predicted locations of its poles and zeros in the complex plane. Section 5.4 presents our experiment on the microwave realization of the ring graph and measurements of the scattering matrix, and Section 5.5 presents the complex time delays extracted from the measured S-matrix as a function of frequency, as well as fits to reveal the locations of the scattering singularities. Section 5.6 uses the results from Section 5.5 to reconstruct $\det[S]$ over the entire complex frequency plane. This is followed by discussion of all the results in Section 5.7, and then conclusions in Section 5.8.

5.2 Complex Time Delays and Scattering Poles and Zeros

A useful theoretical framework for the complex time delay analysis is the so called effective Hamiltonian formalism for wave-chaotic scattering [77, 118, 144, 156, 157]. It starts with defining an $N \times N$ self-adjoint matrix Hamiltonian H whose real eigenvalues are associated with eigenfrequencies of the closed system. Further defining W to be an $N \times M$ matrix of coupling elements between the N modes of H and the M scattering channels, one can build the unitary $M \times M$ scattering matrix $S(E)$ in the form:

$$S(E) = 1_M - 2\pi i W^\dagger \frac{1}{E - H + i\Gamma_W} W, \tag{5.1}$$

where we defined $\Gamma_W = \pi W W^\dagger$. Note that in this approach the S-matrix poles $\mathcal{E}_n = E_n - i\Gamma_n$ (with $\Gamma_n > 0$) are complex eigenvalues of the non-Hermitian effective Hamiltonian matrix $\mathcal{H}_{\text{eff}} = H - i\Gamma_W \neq \mathcal{H}_{\text{eff}}^\dagger$.

A standard way of incorporating the uniform absorption with strength η is to replace $E \rightarrow$

$E + i\eta$ in the S matrix definition. Such an S-matrix becomes subunitary and we denote $S(E + i\eta) \coloneqq S_\eta(E)$. The determinant of $S_\eta(E)$ is then given by

$$\det S_\eta(E) \coloneqq \det S(E + i\eta) \tag{5.2}$$

$$= \frac{\det[E - H + i(\eta - \Gamma_W)]}{\det[E - H + i(\eta + \Gamma_W)]} \tag{5.3}$$

$$= \prod_{n=1}^{N} \frac{E + i\eta - z_n}{E + i\eta - \mathcal{E}_n}, \tag{5.4}$$

where Eq. (5.3) follows from Eq. (5.1), and Eq. (5.4) expresses the determinants in terms of the eigenvalues of the non-Hermitian matrices involved. Here the S-matrix zeros z_n are complex eigenvalues of the non-Hermitian matrix $\mathcal{H}_{\text{eff}}^\dagger = H + i\Gamma_W$, i.e. $z_n = \mathcal{E}_n^*$.

5.2.1 Complex Wigner Time Delay

Using the above expression, the Wigner-Smith (which we shall abbreviate as Wigner) time delay can be very naturally extended to scattering systems with uniform absorption as suggested in [2] by defining:

$$\tau_W(E;\eta) \coloneqq \frac{-i}{M} \frac{\partial}{\partial E} \log\det S(E + i\eta) \tag{5.5}$$

$$= \text{Re}\ \tau_W(E;\eta) + i\text{Im}\ \tau_W(E;\eta), \tag{5.6}$$

$$\text{Re}\ \tau_W(E;\eta) = \frac{1}{M} \sum_{n=1}^{N} \left[\frac{\Gamma_n - \eta}{(E - E_n)^2 + (\Gamma_n - \eta)^2} + \frac{\Gamma_n + \eta}{(E - E_n)^2 + (\Gamma_n + \eta)^2} \right], \tag{5.7}$$

$$\text{Im}\ \tau_W(E;\eta) = -\frac{1}{M} \sum_{n=1}^{N} \left[\frac{E - E_n}{(E - E_n)^2 + (\Gamma_n - \eta)^2} - \frac{E - E_n}{(E - E_n)^2 + (\Gamma_n + \eta)^2} \right]. \tag{5.8}$$

We note that the complex Wigner time delay is a sum of Lorentzians whose properties de-

pend on the poles and zeros of the full scattering matrix, as well as the uniform absorption. Prior work has shown that Eqs. (5.7) and (5.8) provide an excellent description of the experimental complex time delay for isolated modes of a lossy tetrahedral microwave graph [2]. The statistical properties of complex time delay in an ensemble of tetrahedral graphs are also in agreement with those based on Eqs. (5.7) and (5.8) and the random matrix theory predictions for the distribution of Γ_n [3].

5.2.2 Complex Transmission Time Delay

We can define the scattering matrix as $S = \begin{pmatrix} R & T' \\ T & R' \end{pmatrix}$ in terms of the reflection sub-matrix R and transmission sub-matrix T [59, 60, 80, 231]. For a system with uniform absorption, the determinant of the transmission sub-matrix can be written as:

$$\det T_\eta(E) = (-2\pi i)^M \frac{\det(E - H + i\eta)\det\left(W_2^\dagger \frac{1}{E-H+i\eta} W_1\right)}{\det[E - H + i(\eta + \Gamma_W)]}, \tag{5.9}$$

where the coupling matrix $W = [W_1\ W_2]$, is decomposed into its port-specific $N \times M$ coupling matrices $W_{1/2}$. We can extend the transmission time delay [59] into a complex quantity:

$$\tau_T(E;\eta) \coloneqq -i\frac{\partial}{\partial E}\log\det T(E+i\eta) \tag{5.10}$$

$$= \text{Re}\ \tau_T(E;\eta) + i\text{Im}\ \tau_T(E;\eta), \tag{5.11}$$

$$\text{Re}\ \tau_T(E;\eta) = \sum_{n=1}^{N-M}\frac{\text{Im}\ t_n - \eta}{(E-\text{Re}\ t_n)^2 + (\text{Im}\ t_n - \eta)^2} + \sum_{n=1}^{N}\frac{\Gamma_n + \eta}{(E-E_n)^2 + (\Gamma_n+\eta)^2}, \tag{5.12}$$

$$\text{Im}\ \tau_T(E;\eta) = -\left\{\sum_{n=1}^{N-M}\frac{E-\text{Re}\ t_n}{(E-\text{Re}\ t_n)^2 + (\text{Im}\ t_n - \eta)^2} - \sum_{n=1}^{N}\frac{E-E_n}{(E-E_n)^2+(\Gamma_n+\eta)^2}\right\}. \tag{5.13}$$

Here $t_n = \text{Re}\ t_n + i\text{Im}\ t_n$ denote the complex zeros of $\det(T)$, while $\mathcal{E}_n = E_n - i\Gamma_n$ are the same poles defined in Eq. (5.4). Note in Eqs. (5.12) and (5.13) that the number of zero-related terms is smaller than the number of pole-related terms [59].

5.2.3 Complex Reflection Time Delay and Difference

Recent interest in the zeros of the S-matrix in the complex energy plane has motivated the use of the Heidelberg model to introduce the concept of reflection time delays [57, 58]. To begin with, consider the special case of a two-channel ($M = 2$) flux-conserving scattering system which can be described by the 2×2 unitary scattering matrix:

$$S(E) = \begin{pmatrix} R_1(E) & t_{12}(E) \\ t_{21}(E) & R_2(E) \end{pmatrix}. \tag{5.14}$$

The two reflection elements $R_{1,2}(E)$ at both channels may have zeros r_n in the complex energy plane.

In the presence of uniform absorption strength η, the full scattering matrix S becomes sub-unitary, and $|R_1(E+i\eta)| \neq |R_2(E+i\eta)|$ in general. In that case, the reflection element $R_1(E+i\eta)$ at channel 1 can be written in a similar form to the $\det S_\eta$ and $\det T_\eta$ formalism:

$$R_1(E+i\eta) = \frac{\det\Big[E - H + i(\eta - \Gamma_W^{(1)} + \Gamma_W^{(2)})\Big]}{\det[E - H + i(\eta + \Gamma_W)]} \tag{5.15}$$

$$= \prod_{n=1}^{N} \frac{E + i\eta - r_n}{E + i\eta - \mathcal{E}_n}, \tag{5.16}$$

where $\Gamma_W = \Gamma_W^{(1)} + \Gamma_W^{(2)}$, and $r_n = u_n + iv_n$ are the positions of reflection zeros, which are the complex eigenvalues of $H + i(\Gamma_W^{(1)} - \Gamma_W^{(2)})$. Similarly, the reflection element $R_2(E+i\eta)$ at channel 2 can be written as

$$R_2(E+i\eta) = \frac{\det\Big[E - H + i(\eta - \Gamma_W^{(2)} + \Gamma_W^{(1)})\Big]}{\det[E - H + i(\eta + \Gamma_W)]} \tag{5.17}$$

$$= \prod_{n=1}^{N} \frac{E + i\eta - r_n^*}{E + i\eta - \mathcal{E}_n}. \tag{5.18}$$

Thus, the reflection time delays in uniformly absorbing systems are introduced as

$$\tau_R^{(1)}(E;\eta) \coloneqq -i\frac{\partial}{\partial E}\log R_1(E+i\eta) \tag{5.19}$$

and

$$\tau_R^{(2)}(E;\eta) \coloneqq -i\frac{\partial}{\partial E}\log R_2(E+i\eta). \tag{5.20}$$

In full analogy with the complex Wigner time delay model, the complex reflection time delay for channel 1, $\tau_R^{(1)}(E;\eta)$, is given by

$$\text{Re}\ \tau_R^{(1)}(E;\eta) = \sum_{n=1}^{N}\left[\frac{v_n-\eta}{(E-u_n)^2+(v_n-\eta)^2}+\frac{\Gamma_n+\eta}{(E-E_n)^2+(\Gamma_n+\eta)^2}\right], \tag{5.21}$$

$$\text{Im}\ \tau_R^{(1)}(E;\eta) = -\sum_{n=1}^{N}\left[\frac{E-u_n}{(E-u_n)^2+(v_n-\eta)^2}-\frac{E-E_n}{(E-E_n)^2+(\Gamma_n+\eta)^2}\right]. \tag{5.22}$$

Similarly, we also have the complex reflection time delay for channel 2, $\tau_R^{(2)}(E;\eta)$:

$$\text{Re}\ \tau_R^{(2)}(E;\eta) = \sum_{n=1}^{N}\left[\frac{-v_n-\eta}{(E-u_n)^2+(v_n+\eta)^2}+\frac{\Gamma_n+\eta}{(E-E_n)^2+(\Gamma_n+\eta)^2}\right], \tag{5.23}$$

$$\text{Im}\ \tau_R^{(2)}(E;\eta) = -\sum_{n=1}^{N}\left[\frac{E-u_n}{(E-u_n)^2+(v_n+\eta)^2}-\frac{E-E_n}{(E-E_n)^2+(\Gamma_n+\eta)^2}\right]. \tag{5.24}$$

Notice that the two reflection time delays share the same terms arising from the S-matrix poles, thus another useful quantity, the complex reflection time difference, can be defined as $\delta\mathcal{T}_R(E;\eta) := \tau_R^{(1)}(E;\eta) - \tau_R^{(2)}(E;\eta)$ [57,58]:

$$\text{Re}\ \delta\mathcal{T}_R(E;\eta) = \text{Re}\ \tau_R^{(1)}(E;\eta) - \text{Re}\ \tau_R^{(2)}(E;\eta) \tag{5.25}$$

$$= \sum_{n=1}^{N}\left[\frac{v_n-\eta}{(E-u_n)^2+(v_n-\eta)^2}+\frac{v_n+\eta}{(E-u_n)^2+(v_n+\eta)^2}\right], \tag{5.26}$$

$$\text{Im}\ \delta\mathcal{T}_R(E;\eta) = \text{Im}\ \tau_R^{(1)}(E;\eta) - \text{Im}\ \tau_R^{(2)}(E;\eta) \tag{5.27}$$

$$= -\sum_{n=1}^{N}\left[\frac{E-u_n}{(E-u_n)^2+(v_n-\eta)^2}-\frac{E-u_n}{(E-u_n)^2+(v_n+\eta)^2}\right]. \tag{5.28}$$

The reflection time difference is determined solely by the position of the reflection zeros, and has no contribution from the poles.

Our approach to defining and utilizing multiple types of complex time delay overcomes a number of issues with prior treatments. First, we treat poles and zeros on an equal footing, as both contribute significantly to the complex time delay. Secondly, the imaginary part of the time delay provides redundant, but nevertheless useful, information about the pole/zero locations. The imaginary part has one advantage over the real part in terms of fitting to find pole and zero locations: the imaginary part changes sign at each singularity, leading to smaller tails at the locations of nearby singularities. This is particularly useful for systems with a dense set of modes. In all examples below, we fit both quantities simultaneously using a single set of fitting parameters. Finally, our approach directly includes the effect of *uniform* loss, frequently ignored in most prior treatments of time delay. Note that we have previously examined the effects of varying *lumped* loss on the complex Wigner time delay [2], and observed the resulting independent motion of the poles and zeros in the complex plane (i.e. violating the condition that $z_n = \mathcal{E}_n^*$, for example) [57, 58, 64, 65].

We note in passing that the use of complex time delay will enhance the study of scattering phenomena governed by pole/zero distributions. We have demonstrated this in the context of CPA [2,9], and the generation of "cold spots", in complex scattering systems [9]. Further opportunities await for the generalized Wigner-Smith operator [54], and for the generation of "slow light".

Finally, we note that although the Wigner-Smith time delay is purely real for unitary scattering systems, the reflection and transmission time delays are always complex, due to the fact that they are derived from sub-unitary parts of the full S-matrix. Thus a proper treatment of these delays must take into account their complex nature, even in the flux-conserving limit.

5.3 The Ring Graph

Ring graph structures have appeared in quantum graph studies, mesoscopic devices, microwave ring resonators, optical micro-ring resonators, and superconducting quantum interference devices. It is a generic and important structure for wave systems because it is a simple way to introduce wave interference phenomena in a controlled manner.

As shown in the schematic diagram in Fig. 5.1(a), the ring graph has two bonds, of lengths L_1 and L_2, connecting two nodes. We assume that the bonds of the graph support travelling waves in both directions, with identical propagation and loss characteristics. The nodes are also connected to infinite leads (ports). Coupling between the leads and ring graph is provided by means of a 3-way tee junction with ideal scattering matrix

$$S_{\text{tee}} = \begin{pmatrix} -1/3 & 2/3 & 2/3 \\ 2/3 & -1/3 & 2/3 \\ 2/3 & 2/3 & -1/3 \end{pmatrix}.$$

We shall investigate the $M = 2$ scattering matrix S between the left lead and the right lead in Fig. 5.1(a). Two cases are of interest to us here: i) rationally-related bond lengths L_1 and L_2, including the case $L_1 = L_2$, and ii) irrationally-related lengths L_1 and L_2.

A metric ring graph with $L_1 = L_2$ can support two distinct eigenmodes. Each involves spanning the circumference of the graph $\Sigma = L_1 + L_2$ with an integer number of wavelengths of the wave excitation. One mode, which we call the shape resonance, has a maximum of the standing wave pattern at the nodes of the graph [189]. The second mode has a standing wave

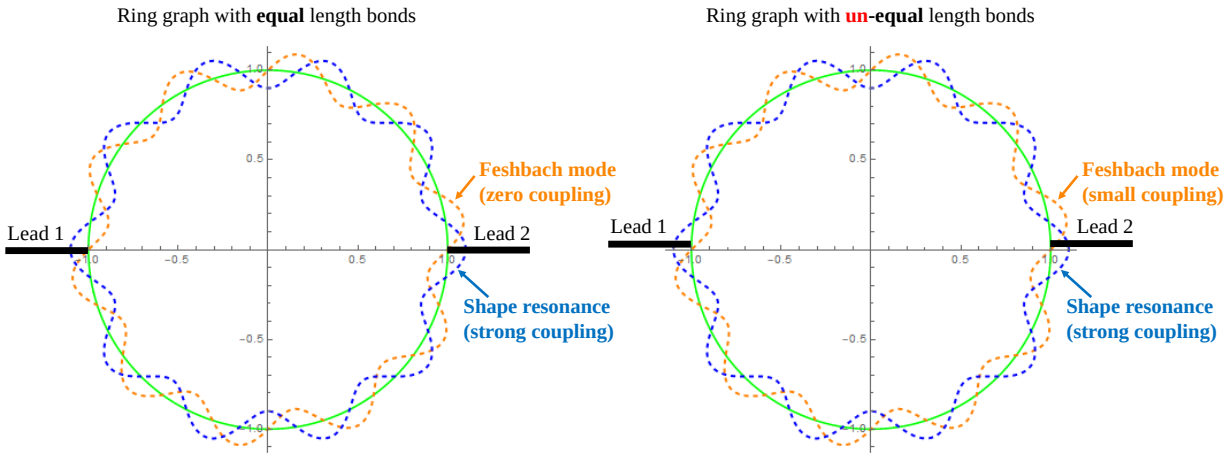

Figure 5.2: Standing wave patterns of Shape and Feshbach modes. Left plot shows a ring graph with equal length bonds, while right plot shows a ring graph with slightly unequal length bonds. The leads in the right plot have been offset vertically to simulate the effect of unequal lengths of the two bonds.

pattern that is rotated one quarter of a wavelength relative to the first and has zero amplitude at the nodes. An intuitive demonstration is shown in Fig. 5.2, where the slight imbalance between the bond lengths gives the Feshbach mode a small (non-zero) coupling effect to the leads. Such an embedded eigenstate on a ring graph with rationally-related bond lengths can have a compact eigenfunction even though the graph extends to infinity. In other words, the eigenmode is nonzero over most of the ring graph, but has zero amplitude at the locations of the leads, preventing the mode from extending into the leads. This means that the the eigenvalue can be in a continuum of states, but the eigenstate can have no amplitude on the leads of the graph. Small perturbations to the length(s) of the bond will move the pole off of the real axis and produce a narrow high-Q resonance, along with a nearby complex zero. This is known as a Feshbach mode.

Waltner and Smilansky [190] have made predictions for the S-matrix zeros and poles for both shape and Feshbach resonances of the ring graph. In the case of a symmetrical graph (i.e. $L_1 = L_2$), or for graphs with rationally related lengths, the scattering properties of the graph

show shape resonances only. The S-matrix poles of the shape resonances are given by

$$\mathcal{E}_n^{S,symm} = nc/\Sigma - i\, c \ln 3/(\pi\Sigma), \tag{5.29}$$

where $\Sigma = L_1 + L_2$ is the total *electrical* length of the ring graph, c is the speed of light in vacuum (here we specialize to the case of microwave ring graphs), and n is the mode index ($n = 1, 2, 3, ...$). The S-matrix zeros are simply the complex conjugates of the poles:

$$z_n^{S,symm} = nc/\Sigma + i\, c \ln 3/(\pi\Sigma). \tag{5.30}$$

The Feshbach modes are not visible in this case.

In the case of a non-symmetrical graph (i.e. $\delta = L_1 - L_2 \neq 0$ and L_1/L_2 is not rational, the graph has both shape and Feshbach resonances. In the limit of $n\delta \ll \Sigma$, the S-matrix poles of the Feshbach resonances are given by

$$\mathcal{E}_n^{F,asymm} \approx nc/\Sigma - i\, (c/2\pi)[(2\pi n\delta)^2/(8\Sigma^3)], \tag{5.31}$$

while the poles of the shape resonances become $\mathcal{E}_n^{S,asymm} \approx (nc/\Sigma + \alpha) - i\, [c \ln 3/(\pi\Sigma) + \beta]$, where $\alpha = nc\delta^2 \ln 3/(2\Sigma^3)$ and $\beta = (c/2\pi)[(2\ln 3)^2 - (2\pi n)^2]\delta^2/(8\Sigma^3)$ are small changes compared to the original pole locations, Eq. (5.29). Again the S-matrix zeros are complex conjugates of the pole locations: $z_n^{F,asymm} = [\mathcal{E}_n^{F,asymm}]^*$ and $z_n^{S,asymm} = [\mathcal{E}_n^{S,asymm}]^*$. These predictions will be tested in our analysis of complex time delay data below.

We note that the imaginary part of the Feshbach pole (and zero) in Eq. (5.31) increases in magnitude as $(n\delta)^2$. The Warsaw group has studied the length asymmetry (δ) dependence of the

lowest frequency ($n = 1$) pole of the ring graph [199]. A cold atom collision experiment has observed the flow of the shape and Feshbach resonance poles as the system is perturbed [194]. In contrast with earlier work, we study the dependence of the poles and zeros at two fixed bond lengths upon the mode index n, among other things.

5.4 Experiment

A picture of the ring graph experimental setup is shown in Fig. 5.1(b). A 15-inch (38.1 cm) long coaxial cable is used as the fixed length bond L_1, while a mechanically-variable coaxial phase shifter is used as the variable length bond L_2. The coaxial cable has a center conductor that is 0.036 in (0.92 mm) in diameter, a Teflon dielectric layer (with $\epsilon_r = 2.1$ and $\mu_r = 1$), and an outer conductor that is 0.117 in (2.98 mm) in diameter. The center conductor is silver-plated copper-clad steel, while the outer conductor is copper-tin composite. The electrical length of the cable is given by the product of the geometrical length and the index of refraction, $\sqrt{\epsilon_r \mu_r}$. The phase shifter is a Model 3753B coaxial phase shifter from L3Harris Narda-MITEQ that provides up to 60 degrees of phase shift per GHz. The measurement cables (leads) are connected to the ring graph through two Tee junctions, acting as the nodes. When the graph is symmetrical (i.e. $L_1 = L_2$), the total electrical length of the graph is $\Sigma_{symm} = 1.0993$ m. The graph shows a mean spacing between shape modes of $\Delta f = 0.2729$ GHz, giving rise to a Heisenberg time $\tau_H = 2\pi/\Delta f$ of 23.02 ns. We measure the scattering response from all the modes spanning the frequency range from 0 to 10 GHz, encompassing modes $n = 1$ to $n = 37$.

To make the graph asymmetric ($L_1 \neq L_2$) we set the phase shifter to produce $\delta = 0.577$ cm. Thus we maintain the condition $n\delta \ll \Sigma$ up to $n = 37$.

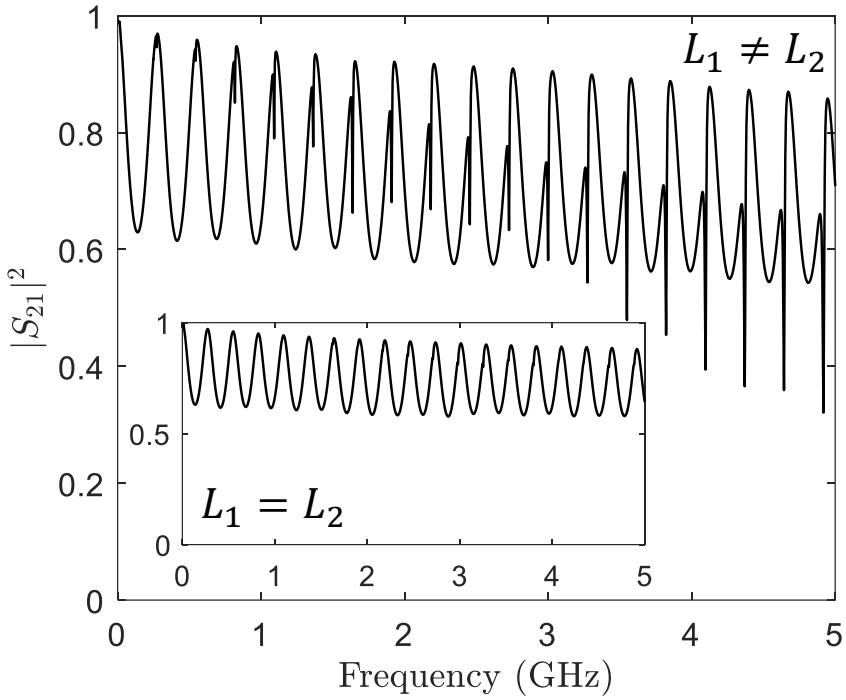

Figure 5.3: Transmission spectrum $|S_{21}|^2$ vs. frequency measured for the first 18 modes of a microwave ring graph. Main figure shows the transmission of non-equal lengths ($L_1 \neq L_2$) between the phase shifter and the coaxial cable, while the inset shows the case of equal lengths ($L_1 = L_2$). The sinusoidal wiggles come from the shape resonances, while the narrow dips come from the Feshbach resonances. Note that the data in the inset shows no narrow resonances. This figure is taken from Ref. [4].

The time delay analysis involves taking frequency derivatives of the measured S-matrix phase and amplitude data, and this demands fine frequency resolution and careful measurement. In order to obtain high-quality data, we first conducted a careful calibration of the Agilent model N5242A microwave vector network analyzer (VNA), utilizing an intermediate frequency (IF) bandwidth of 100 Hz and a frequency step size of 84.375 kHz (about 3×10^{-4} of the mean spacing between shape resonances). The calibration process creates boundary conditions for the microwaves that are equivalent to the presence of the two infinite leads connected to the nodes of the ring graph. In other words, waves exiting the system will never return. In addition, the scattering matrix is evaluated at the plane of calibration as the ratio of ingoing and outgoing complex

waves measured at that point. The plane of calibration is at the two nodes labelled by red dashed lines in Fig. 5.1(c). We then measured the 2×2 S-matrix of the graphs with the same settings of the VNA. By doing so, we minimize the measurement noise and acquire high resolution data. The phase of the S-matrix data was unwound into a continuous variation to eliminate artificial discontinuities in time delay due to 2π phase jumps. We also developed an algorithm for taking numerical derivatives of the experimental data utilizing variable frequency window smoothing settings. Given the number of data points in a smoothing window, we obtained the overall slope through a line fitting of all the data samples. The size of the smoothing window can be dynamically adjusted based on the variability of the phase and amplitude with frequency. All of these steps are required to generate high-quality time delay data for further analysis (see more details in Appendix C). Note that the numerical derivatives are taken on the raw S-matrix data without any normalization step or background subtraction, etc. There is no need to augment or modify the raw S-matrix data, as it contains all the information about the graph, including coupling, loss, and scattering singularities.

The two types of modes present in the ring graph, namely shape resonances and Feshbach resonances, are illustrated in the measured transmission $|S_{21}|^2$ vs. frequency plot shown in Fig. 5.3. The inset in Fig. 5.3 shows the transmission spectrum when the two bond lengths are equal ($L_1 = L_2$). In this case only the shape resonances appear in the scattering data. For the main plot in Fig. 5.3, we tuned the electrical length of the phase shifter so that the two bonds lengths are not equal ($L_1 \neq L_2$) and not rationally related. The narrow Feshbach resonances occur at lower frequencies than the shape resonances and their separation from the shape resonances grows with mode number n, as predicted by Eq. (5.31), and demonstrated in the following analysis.

5.5 Complex Time Delay Analysis on Ring Graph Data

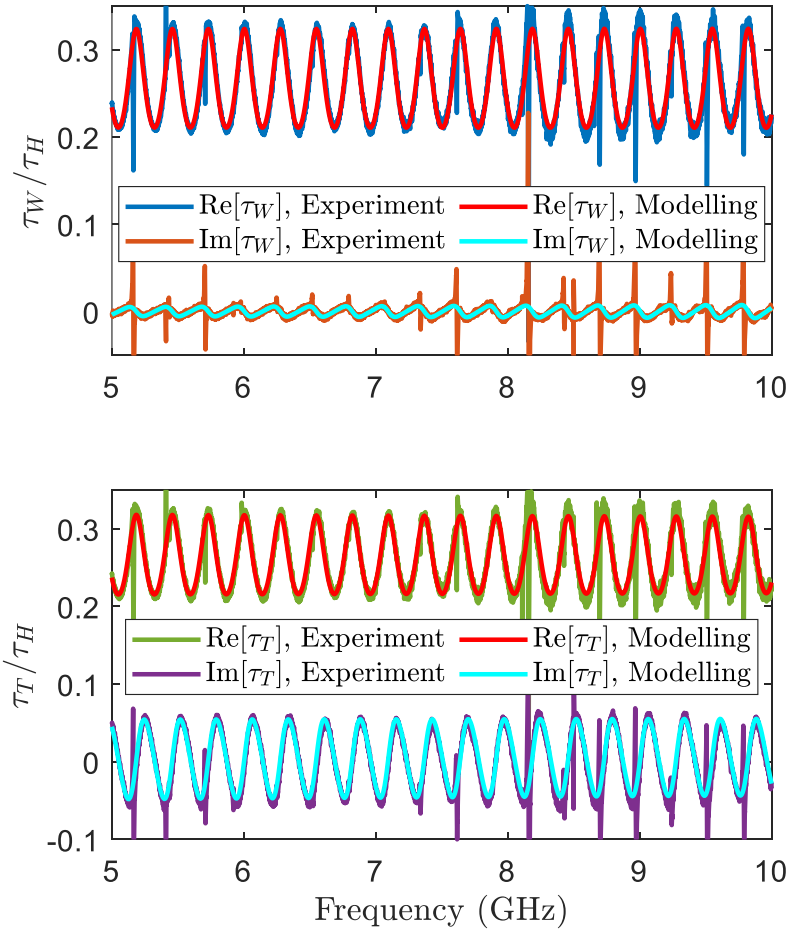

Figure 5.4: Comparisons between the experimental data and the modelling for the complex Wigner time delay (upper plot) and for the complex transmission time delay (lower plot), both normalized by the Heisenberg time τ_H, as a function of frequency for a symmetric ($L_1 = L_2$) microwave ring graph. The modelling data are plotted on top of the experimental data, and are in good agreement. This figure is taken from Ref. [4].

In the case of a symmetrical graph, we analyze the complex Wigner time delay and transmission time delay properties of the shape resonances alone. Figure 5.4 shows the complex Wigner (τ_W) and transmission (τ_T) time delay as a function of frequency over 18 modes of the ring graph. The two time delays are calculated from the measured S-matrix based on Eqs. (5.5)

(Wigner) and (5.10) (Transmission), respectively. Note that in all comparisons of data and theory we treat frequency f and energy E as equivalent. We also reconstruct the two time delays based on the models from Eqs. (5.7) & (5.8) (Wigner) and Eqs. (5.12) & (5.13) (Transmission), using the scattering matrix poles prediction from Eq. (5.29) and the zeros from Eq. (5.30). The poles are calculated based on the measured dimension (electrical length) of the ring graph, and the zeros are assumed to be the complex conjugates of the poles. The modelled complex time delays are plotted with the experimental data in Fig. 5.4, and are in good agreement. (Due to uncertainties in the lengths of the components, we adjusted Σ slightly to precisely match the τ_W frequency dependence in Fig. 5.4.) Note that in the complex transmission time delay modelling we use only the pole information (there are no transmission zeros in this case due the absence of an interfering mode [208]), while in the complex Wigner time delay modelling we use both the pole and zero information.

We note that although the model is in very good agreement with the data in Fig. 5.4 there are a number of sharp vertical features in the data that are not reproduced by the model. Theoretical treatments of a delta function scatterer in the ring graph shows that imperfections in a symmetric graph ($L_1 = L_2$) can give rise to Feshbach resonances [190, 232]. We interpret the spikes seen in τ_W and τ_T as arising from impedance discontinuities in the phase shifter and its coaxial connectors, acting effectively as delta-function scatterers. To verify this, we measured a symmetric graph made up of two identical fixed-length (15 inch) coaxial cables and found that there are no sharp vertical features in the time delays in that case.

Then we present the complex Wigner-Smith (τ_W) (Fig. 5.5), transmission (τ_T) (Fig. 5.6), and reflection (τ_R) (Fig. 5.7) time delays over the full measurement frequency range (0 – 10 GHz), including all 37 modes of the asymmetrical ($L_1 \neq L_2$) microwave ring graph. Examining

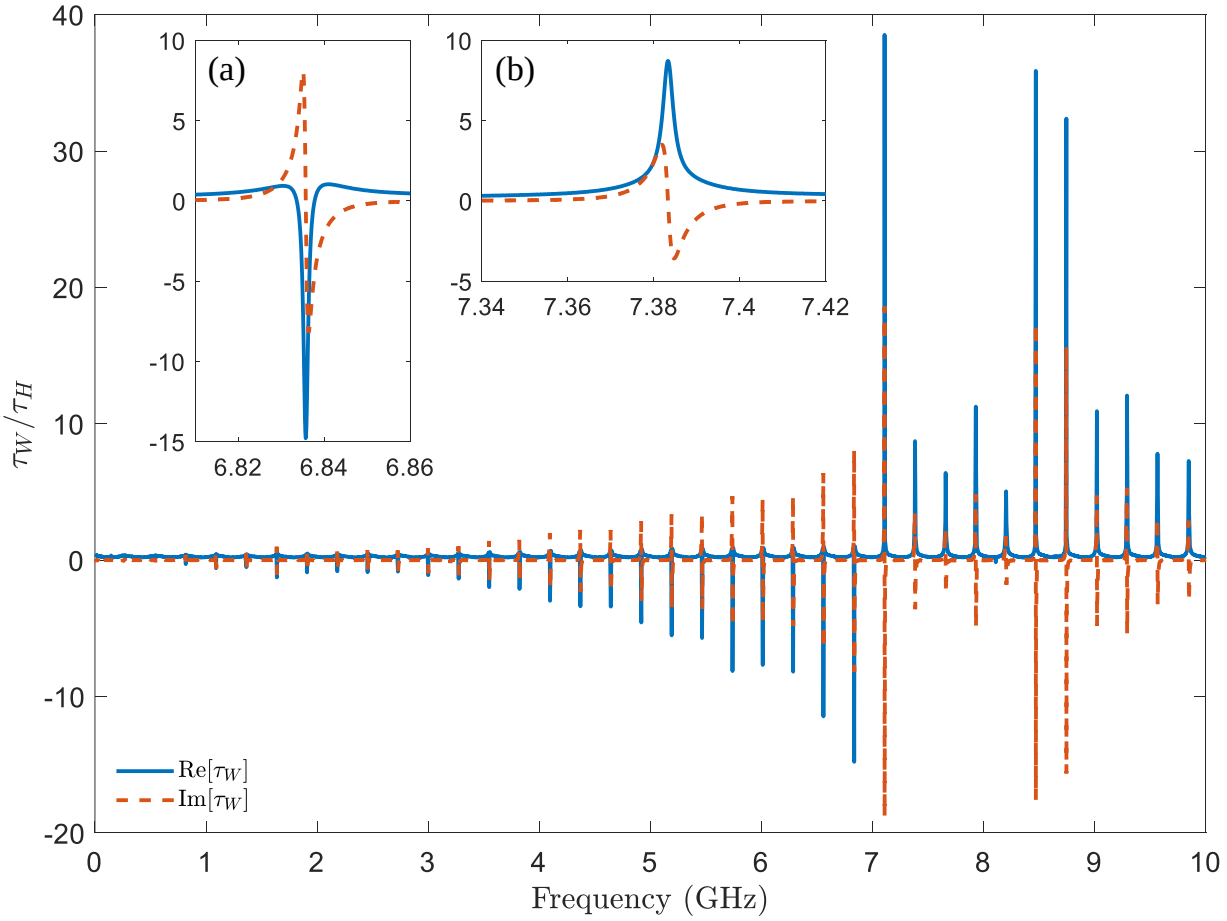

Figure 5.5: Complex Wigner time delay τ_W (normalized by the Heisenberg time τ_H) determined from measured S-matrix data for 37 modes ($0 - 10$ GHz) in an asymmetrical ($L_1 \neq L_2$) microwave ring graph. The extreme values of τ_W are dominated by Feshbach resonances. Note the sign change of the Re$[\tau_W]$ extreme values near 7 GHz, which corresponds to the crossover between Γ_n and η in Fig. 5.8. Insets (a) and (b) show zoom-in details of the complex Wigner time delay for individual modes on either side of the crossover. This figure is taken from Ref. [4].

the complex time delays over a broad range of frequency brings out new aspects of the data.

Figure 5.5 shows the complex Wigner time delay extracted from the experiment over the entire measurement frequency range. We have already noted in Section 5.5 the change in sign of Re$[\tau_W]$ as a function of frequency due to the crossover of the imaginary part of the Feshbach pole Γ_n and the uniform attenuation η. Another feature to note is that the shape resonances produce a relatively small variation in τ_W compared to the sharp features arising from the Feshbach modes.

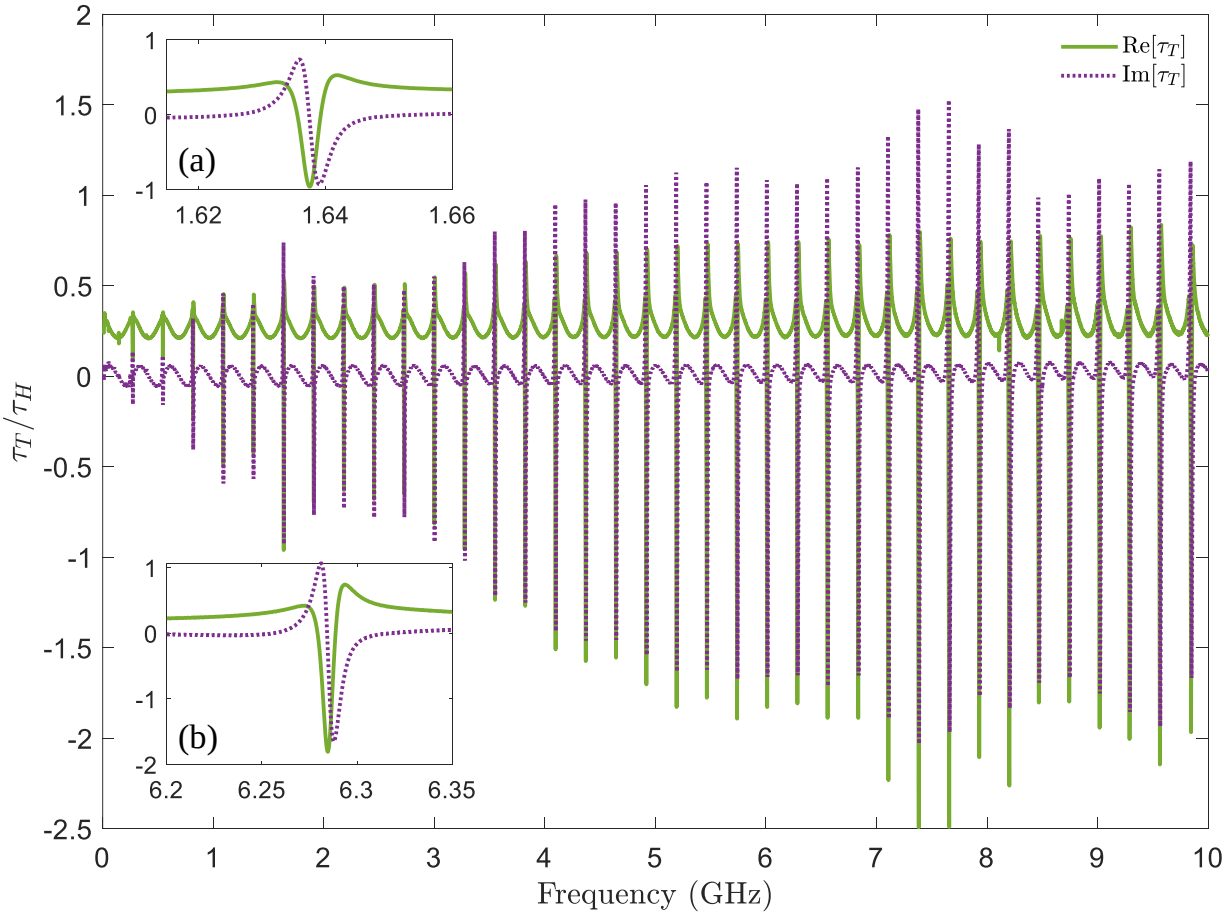

Figure 5.6: Complex transmission time delay τ_T determined from measured S-matrix data for 37 modes ($0 - 10$ GHz) in an asymmetrical ($L_1 \neq L_2$) microwave ring graph normalized by the Heisenberg time τ_H. The extreme values of τ_T are dominated by Feshbach resonances. The nearly sinusoidal variations of Re$[\tau_T]$ and Im$[\tau_T]$ with frequency are due to the shape resonances. Insets (a) and (b) show the zoom-in details of the complex transmission time delay for two individual modes. This figure is taken from Ref. [4].

Both features together create time delays on the scale of at most 10's of Heisenberg times in this particular experimental realization and frequency range.

Figure 5.6 shows the complex transmission time delay extracted from the experiment over the entire measurement frequency range. We note that the magnitude of the transmission time delays are limited in magnitude to approximately 2 times the Heisenberg time in this case. The reason for such small variations is that the transmission time delays have contributions from both

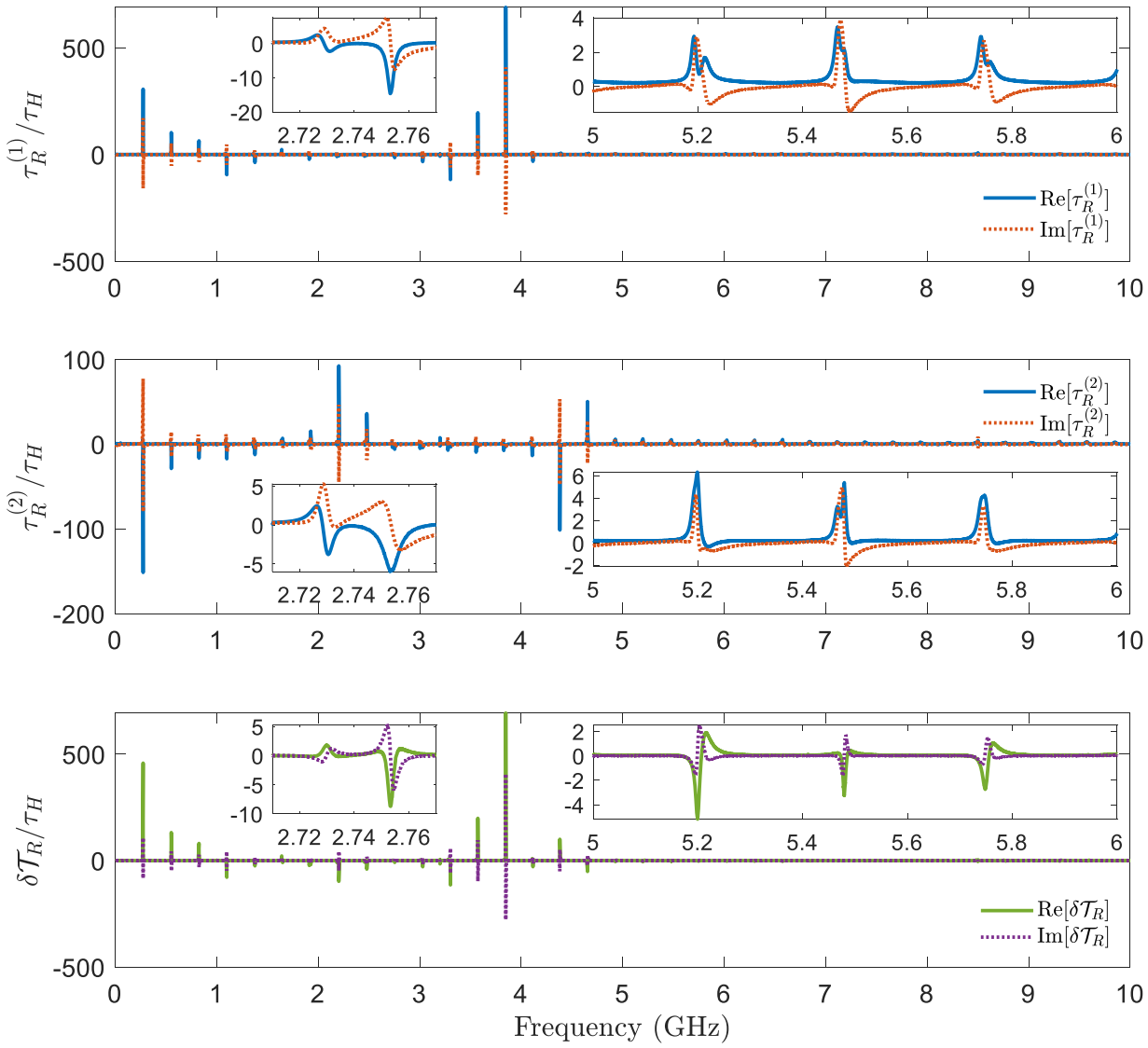

Figure 5.7: Complex reflection time delays $\tau_R^{(1)}$, $\tau_R^{(2)}$ and their difference $\delta\mathcal{T}_R = \tau_R^{(1)} - \tau_R^{(2)}$ determined from measured S-matrix data for 37 modes ($0 - 10$ GHz) in an asymmetrical ($L_1 \neq L_2$) microwave ring graph, normalized by the Heisenberg time τ_H. Insets show the zoom-in details of the complex reflection time delay/difference for individual sets of shape and Feshbach modes. This figure is taken from Ref. [4].

the zeros and the poles, and the two contributions have similar magnitudes but opposite signs. Thus the resulting transmission time delays are rather small compared to τ_W and τ_R.

The reflection time delays shown in Fig. 5.7 show significantly larger range of variation as compared to the Wigner and transmission time delays. To see why this is the case, we can

examine Eqs. (5.21) – (5.24), which model the behavior of the reflection time delays. One can see that the width and the extreme value of the first Lorentzian term is determined by $|v_n \pm \eta|$. The reflection zeros $r_n = u_n + iv_n$ are the complex eigenvalues of $H + i(\Gamma_W^{(1)} - \Gamma_W^{(2)})$. In our experimental setup, we have very similar coupling properties for ports 1 and 2, i.e. $\Gamma_W^{(1)} \approx \Gamma_W^{(2)}$. Thus, the imaginary part of the reflection zeros v_n should be fairly small. At low frequencies, the uniform attenuation η is also very small, and is comparable to v_n. This leads to a very small width of the Lorentzian resonance, which in turn produces very large extreme values of the reflection time delay, on the order of 100's of Heisenberg times, at low frequencies. At larger frequencies, however, the uniform attenuation η becomes fairly large, and dominates the width of the Lorentzian resonance. Therefore, the reflection time delays change back to the order of a few Heisenberg times.

Next we analyze the complex Wigner time delay and transmission time delay properties for the Feshbach resonances of the ring graph. We tuned the electrical length of the phase shifter so that the two bonds lengths are not equal or rationally related (with $\delta \approx 0.577$ cm), and a set of Feshbach resonances appear, as in Fig. 5.3. We followed the same procedure to calculate the complex Wigner and transmission time delay from the newly measured S-matrix. Note that the shape resonances are always present in the system. We first removed the effects of the shape resonances from the overall time delay data by subtracting their contributions to the time delay data. The contributions from the shape resonances are modelled in the same way as demonstrated in Fig. 5.4. (Σ has been slightly adjusted to accommodate the length change of the ring graph system.) We then fit the remaining complex time delay data with the model Eqs. (5.7) & (5.8) (Wigner) and Eqs. (5.12) & (5.13) (Transmission), for each individual Feshbach mode. Both the zero and pole locations, as well as the uniform absorption strength η, are used as fitting parameters

in this process. Note that the real and imaginary parts of each time delay are fit simultaneously with a single set of parameters. We also constrain the zeros to be complex conjugates of the poles during the Wigner time delay fitting. One fitting example is shown in Figs. 5.8(b) (Wigner) and 5.9(b) (Transmission), respectively. The fitting process was repeated for all 37 modes measured, and all fits were very successful. The fit parameters for the complex zeros and poles, as well as the uniform attenuation, are plotted in Figs. 5.8 (Wigner) and 5.9 (Transmission), respectively.

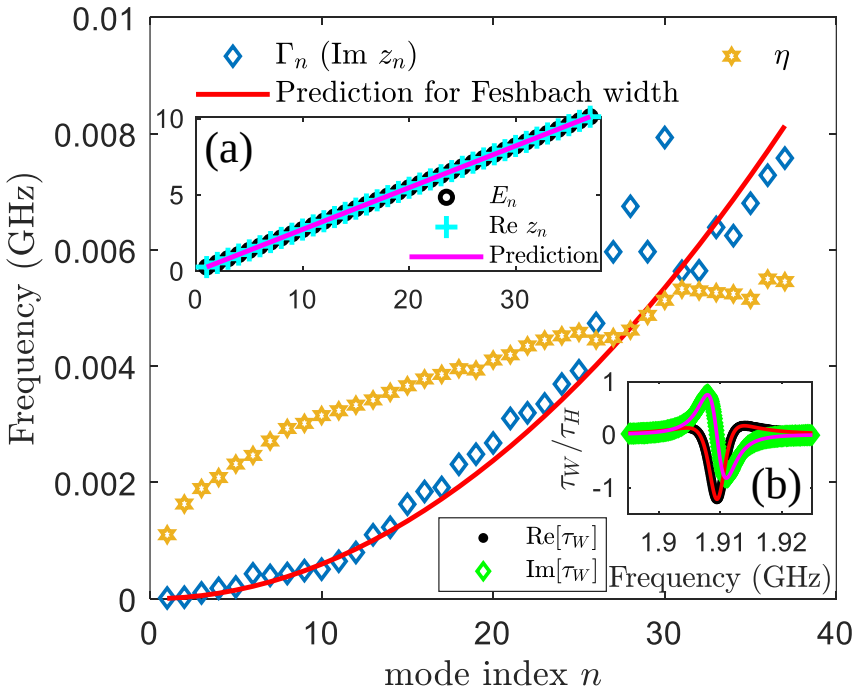

Figure 5.8: Comparison between fitted pole location parameters ($\mathcal{E}_n = E_n - i\Gamma_n$) and predictions for multiple Feshbach modes of the asymmetric microwave ring graph ($L_1 \neq L_2$). Inset (a) shows the comparison between fitted real parts of the zeros and the poles, along with the prediction by Eq. (5.31) shown as a straight purple line. Inset (b) shows such a representative fit to $\tau_W(f)$ for a single Feshbach mode ($n = 7$). This figure is taken from Ref. [4].

We note that Eq. (5.31) predicts that the resonance width Γ_n (imaginary part of the pole) increases as $(c/2\pi)[(2\pi n\delta)^2/(8\Sigma^3)]$. Putting the measured values of Σ and δ into this expression gives the red solid curve in Fig. 5.8, which demonstrates very good agreement between the

data and the prediction in Eq. (5.31). Figure 5.8 also shows the uniform absorption strength η increases with frequency. A more detailed discussion of uniform loss, with comparisons to independent measurements and modeling, can be found in Appendix B.3.

There is an interesting competition between Γ_n and η with regards to the complex Wigner time delay in this graph. Figure 5.8 shows that Γ_n crosses over the value of η at approximately mode 27. Equation (5.7) shows that this will give rise to a change in sign of the nearly-resonant contribution to Re$[\tau_W]$. This crossover-related sign change is clearly evident in the full plot of Re$[\tau_W]$ vs. frequency in Fig. 5.5. Further, Fig. 5.8(a) shows the fitted real parts of the zeros and poles from the complex Wigner time delay, and they both increase in proportion to n, as predicted in Eqs. (5.29) and (5.30) [190]. The solid red line in Fig. 5.8(a) shows the prediction based on the measured value of Σ.

In Fig. 5.9, we plot the fitted imaginary location of the poles (in the form of $\Gamma_n+\eta$) from the complex transmission time delay data together with the previously extracted Wigner poles data from Fig. 5.8, and they agree very well. This validates the hypothesis that the two time delays (τ_W and τ_T) share the same pole information. Fig. 5.9 also shows the fitted imaginary parts of the zeros (in the form of Im $t_n - \eta$) from the complex transmission time delay for the Feshbach modes, together with the previously extracted uniform attenuation value ($-\eta$) from Fig. 5.8, and they match very well. This implies the transmission zeros are purely real (i.e. Im $t_n = 0$), and the data is consistent with this interpretation. Further detailed discussion on the transmission zeros can be found below.

In the transmission zeros analysis for the Feshbach resonances, we fit the experimental data to Eqs. (5.12) and (5.13), after removing the contributions from the shape resonances. We may rewrite the complex transmission time delay as $\tau_T = \tau_T^Z + \tau_T^P$ [59], where τ_T^Z and τ_T^P are the

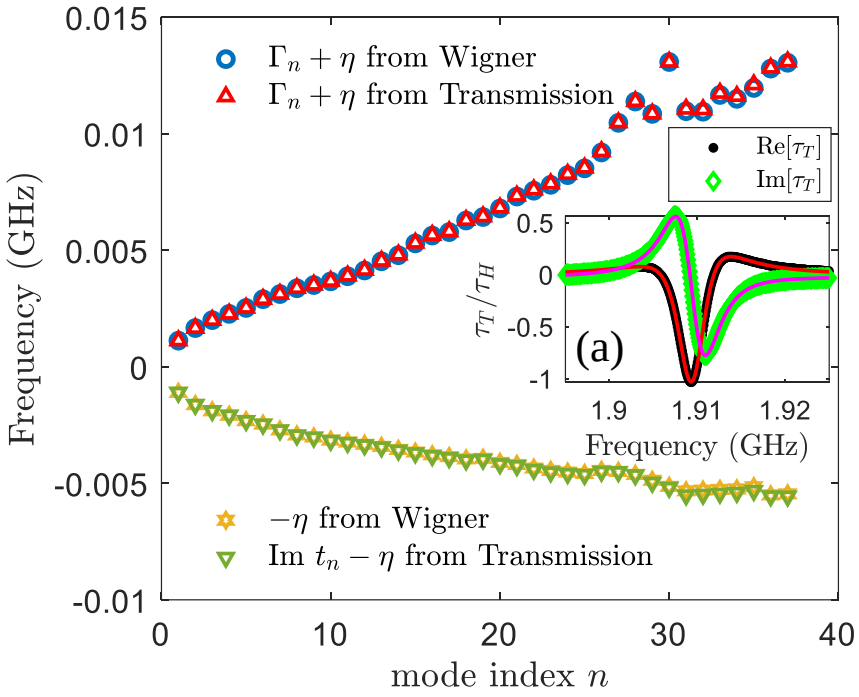

Figure 5.9: Comparison between fitted pole location parameters ($\mathcal{E}_n = E_n - i\Gamma_n$) obtained from the complex Wigner time delay (blue circles) and the complex transmission time delay (red triangles) for Feshbach modes of the asymmetric ring graph. The lower part of the figure shows the comparison between fitted uniform attenuation ($-\eta$) obtained from the complex Wigner time delay (yellow stars) in Fig. 5.8 and fitted imaginary parts of the transmission zeros (Im $t_n - \eta$) obtained from the complex transmission time delay (green triangles) on all measured Feshbach modes. Inset (a) shows a representative fit to $\tau_T(f)$ for a single Feshbach mode ($n = 7$). This figure is taken from Ref. [4].

contributions from zeros and poles, respectively. Then Eqs. (5.12) and (5.13) can be rewritten as

$$\text{Re}\,\tau_T^Z(E;\eta) = \sum_{n=1}^{N-M} \frac{\text{Im}\,t_n - \eta}{(E - \text{Re}\,t_n)^2 + (\text{Im}\,t_n - \eta)^2}, \tag{5.32}$$

$$\text{Im}\,\tau_T^Z(E;\eta) = -\sum_{n=1}^{N-M} \frac{E - \text{Re}\,t_n}{(E - \text{Re}\,t_n)^2 + (\text{Im}\,t_n - \eta)^2}, \tag{5.33}$$

$$\text{Re}\,\tau_T^P(E;\eta) = \sum_{n=1}^{N} \frac{\Gamma_n + \eta}{(E - E_n)^2 + (\Gamma_n + \eta)^2}, \tag{5.34}$$

$$\text{Im}\,\tau_T^P(E;\eta) = \sum_{n=1}^{N} \frac{E - E_n}{(E - E_n)^2 + (\Gamma_n + \eta)^2}. \tag{5.35}$$

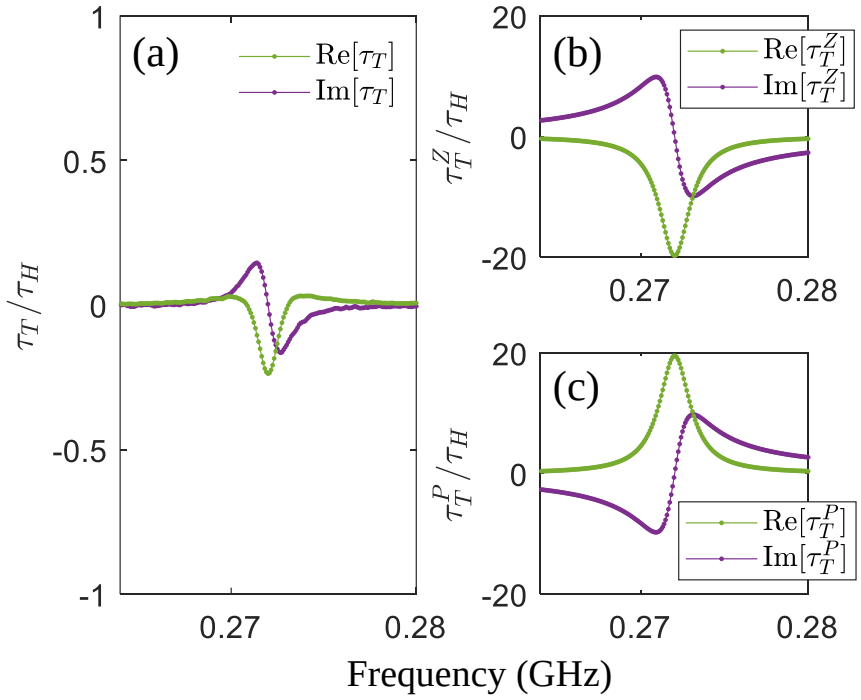

Figure 5.10: Complex transmission time delay data for a single Feshbach mode ($n = 1$) and its contributions from zeros and poles. (a) shows the total complex transmission time delay data (τ_T), while (b) and (c) show the contribution from the zero (τ_T^Z) and the pole (τ_T^P), respectively. Here τ_T is from experimental data, while τ_T^P is calculated based on Eqs. (5.34) & (5.35) with the pole information extracted from the complex Wigner time delay analysis (see Fig. 5.8). τ_T^Z is obtained by $\tau_T^Z = \tau_T - \tau_T^P$. This figure is taken from Ref. [4].

We plot τ_T^Z and τ_T^P for a single Feshbach mode ($n = 1$) in Fig. 5.10. Here τ_T^P is calculated using the pole information extracted from the complex Wigner time delay analysis (see Fig. 5.8), since all three time delays share the same poles. τ_T^Z can then be obtained through $\tau_T^Z = \tau_T - \tau_T^P$, where τ_T is the experimental data. Fig. 5.10 shows that τ_T^Z and τ_T^P are approximately equal in magnitude, both much larger than τ_T, but have opposite signs. From [59, 60] we learned that the transmission zeros t_n will be on the real axis, i.e. $\mathrm{Im}[t_n] = 0$, such that $\mathrm{Im}[t_n] - \eta = -\eta$. For this ($n = 1$) Feshbach mode, the imaginary part of the pole Γ_n is very small compared to the uniform attenuation η (see Fig. 5.8), thus we have $\Gamma_n + \eta \approx \eta$. Under such conditions, Eqs. (5.32) – (5.35) can be written as $\mathrm{Re}[\tau_T^Z]_{n=1} = -\eta/[(E - \mathrm{Re}\, t_n)^2 + \eta^2]$, $\mathrm{Re}[\tau_T^P]_{n=1} \approx +\eta/[(E - E_n)^2 + \eta^2]$,

$\mathrm{Im}[\tau_T^Z]_{n=1} = -(E - \mathrm{Re}\, t_n)/[(E - \mathrm{Re}\, t_n)^2 + \eta^2]$, and $\mathrm{Im}[\tau_T^P]_{n=1} \approx (E - E_n)/[(E - E_n)^2 + \eta^2]$. Since $\mathrm{Re}\, t_n \approx E_n$, we then arrive at $[\tau_T^Z]_{n=1} \approx -[\tau_T^P]_{n=1}$, which is consistent with what is shown in Fig. 5.10. This also explains why $\tau_T = \tau_T^Z + \tau_T^P$ is so small for this Feshbach mode ($n = 1$) (see Fig. 5.10(a)).

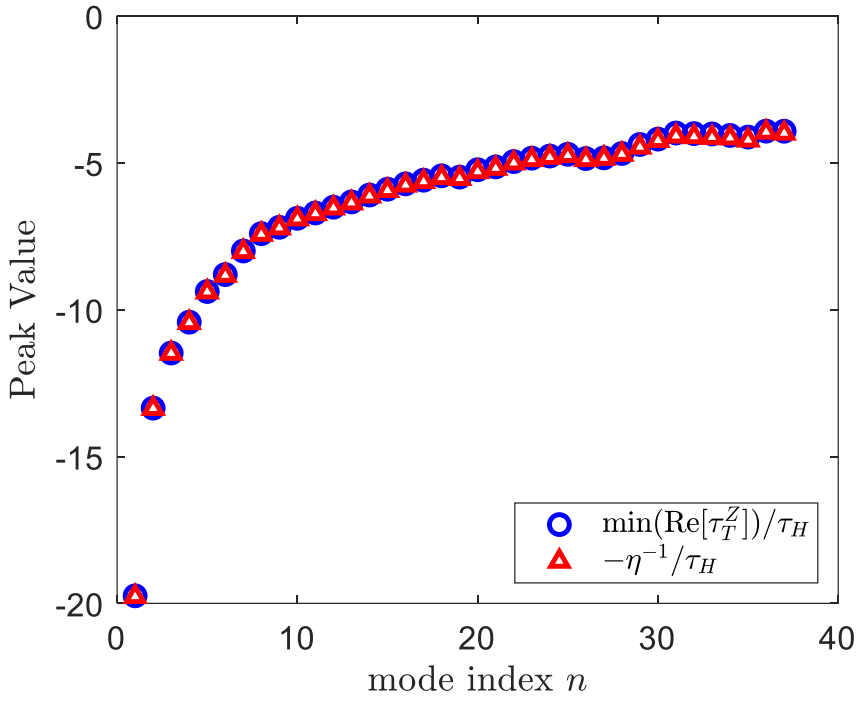

Figure 5.11: Comparison between the peak value of $\mathrm{Re}[\tau_T^Z]$ and $-\eta^{-1}$ for all 37 modes of the microwave ring graph. Blue circles show the peak value of $\mathrm{Re}[\tau_T^Z]$ from experimental data, while red triangles show $-\eta^{-1}$ calculated from the data in Fig. 5.8. Both quantities are presented normalized by the Heisenberg time τ_H of the loop graph. This figure is taken from Ref. [4].

When analyzing the transmission time delay data, one may assume either a single zero or a conjugate pair of zeros in the modelling [59,60]. We tried using a conjugate pair of zeros to fit the data, but were unable to achieve reasonable fitting results. A pair of zeros would contribute to the real part of transmission time delay with a local extremum at $E = \mathrm{Re}\, t_n$ of $\mathrm{Re}[\tau_T^Z] = \frac{2\eta}{(\mathrm{Im}\, t_n)^2 - \eta^2}$. Unfortunately this expression demands negative values for $(\mathrm{Im}\, t_n)^2$ for our data, therefore the pair of zeros assumption is inconsistent with the data. On the other hand, the contribution of a

single zero to $\mathrm{Re}[\tau_T]$ is $\mathrm{Re}[\tau_T^Z] = \frac{-\eta}{(E-\mathrm{Im}\ t_n)^2-\eta^2}$, with peak value $-\eta^{-1}$. We plot the comparison between the peak value of $\mathrm{Re}[\tau_T^Z]$ (from data) vs $-\eta^{-1}$ (from Fig. 5.8) for all 37 modes in Fig. 5.11, and they agree extremely well, justifying our single-zero hypothesis. In summary, placing all of the transmission zeros on the real axis is consistent with the data.

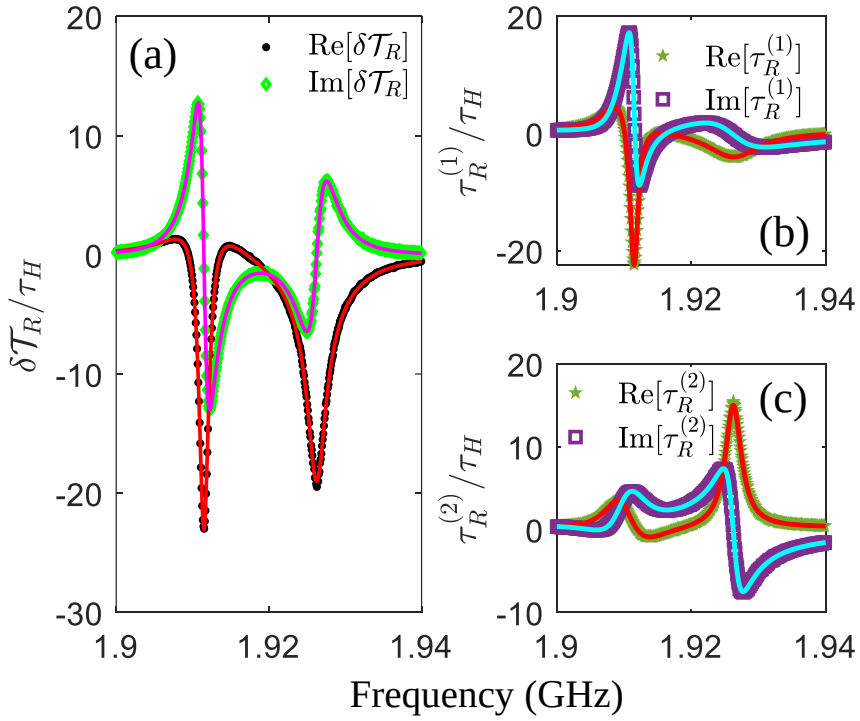

Figure 5.12: Fitting example of reflection time difference/delay for a single pair of shape and Feshbach resonances for a ring graph with $L_1 \neq L_2$. (a) shows an example of fitting complex reflection time difference ($\delta\mathcal{T}_R = \tau_R^{(1)} - \tau_R^{(2)}$) experiment data for mode $n = 7$. The left feature is due to the Feshbach resonance, while the right one is due to the shape resonance. Parts (b) and (c) demonstrate the reconstruction of the individual reflection time delays on both ports, compared to the data, using the fitted reflection zeros and Wigner poles (see Fig. 5.8) information. All time delays are presented normalized by the Heisenberg time τ_H of the loop graph. This figure is taken from Ref. [4].

For the reflection time delay analysis, there are two sets of zeros and poles, one each from the shape and Feshbach resonances. One can use the reflection time difference quantity to simplify the analysis, as it contains only the contribution from the zeros. Figure 5.12 illustrates the reflection time delay/difference analysis process. Figure 5.12(a) is an example of fitting the com-

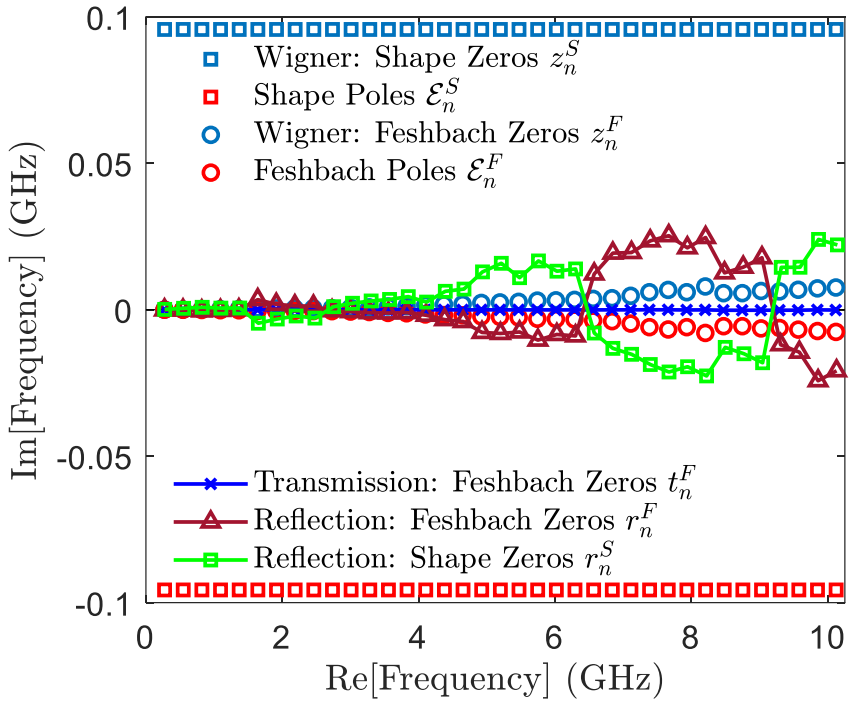

Figure 5.13: Summary of all zeros and poles in the complex frequency plane for shape and Feshbach resonances extracted from Wigner/Transmission/Reflection time delay analysis for the first 37 modes of the microwave ring graph. The Wigner zeros z_n^S (blue squares) and poles $\mathcal{E}_n^S$ (red squares) of the shape resonances are located far from the real axis. The Wigner zeros z_n^F (blue circles) and poles $\mathcal{E}_n^F$ (red circles) of the Feshbach resonances are close to, and symmetrically arrayed about, the real axis. The transmission zeros t_n^F (blue crosses) of the Feshbach resonances lie on the real axis. The reflection zeros $r_n^F \& r_n^S$ of the Feshbach resonances (dark red triangles) and the shape resonances (green squares) are symmetrically arrayed about the real axis. This figure is taken from Ref. [4].

plex reflection time difference to Eqs. (5.26) and (5.28) for a single pair of shape and Feshbach resonances. The fitting process was repeated for all 37×2 modes utilizing two sets of the reflection zeros ($r_n^F = u_n^F + iv_n^F$ & $r_n^S = u_n^S + iv_n^S$) as fitting parameters (along with a single value for η for each pair), and all fits were very successful. We then examined the complex reflection time delay data for the individual channels, by putting the extracted two sets of reflection zeros (r_n^F & r_n^S) and the previously extracted Wigner poles ($\mathcal{E}_n^F$ & $\mathcal{E}_n^S$) into the modelling formula Eqs. (5.21) – (5.24). The modelling prediction (with no further fitting adjustments) are plotted with the

experimental data in Figs. 5.12(b) and 5.12(c), and they agree remarkably well. This indicates that the individual reflection time delays also share the same pole information with the other time delays.

Finally, we present a summary of all zeros and poles extracted from the time delays analysis for the first 37 modes of the microwave ring graph in Fig. 5.13.

5.6 S-matrix Reconstruction over the Complex Plane

Now that we have all the zeros and poles information for the scattering system, we would like to examine the modelling for $\det S$ on the real frequency axis utilizing Eq. (5.4). We reconstructed $\det S$ based on Eq. (5.4) and the extracted Wigner zeros and poles information summarized in Fig. 5.13. Figure 5.14 shows the comparison between the modelling of $\det S$ and the experimental data for a symmetric graph that has the shape resonances only, while Fig. 5.15 shows a similar plot with both the Shape and Feshbach resonances present in the scattering system. The modelling agrees very well with the experiment for both the magnitude and phase of $\det S$. Note that a small delay (0.08 ns) had to be added to the model to show detailed agreement with the data. We attribute this to about 2.4 cm of un-calibrated transmission line outside of the loop graph, occurring in the third port of each of the tee junctions.

Reconstructing the S-matrix over the entire complex frequency plane is generally difficult to accomplish experimentally. Here we construct complex $\det S$ on the complex frequency plane (E or f being complex) by continuation of Eq. (5.4), along with the extracted Wigner zeros and poles information. Fig. 5.16 (and Fig. 5.17) shows a 3D reconstruction of the complex $\det S$ for an asymmetric ring graph evaluated over the complex frequency plane with both the shape and

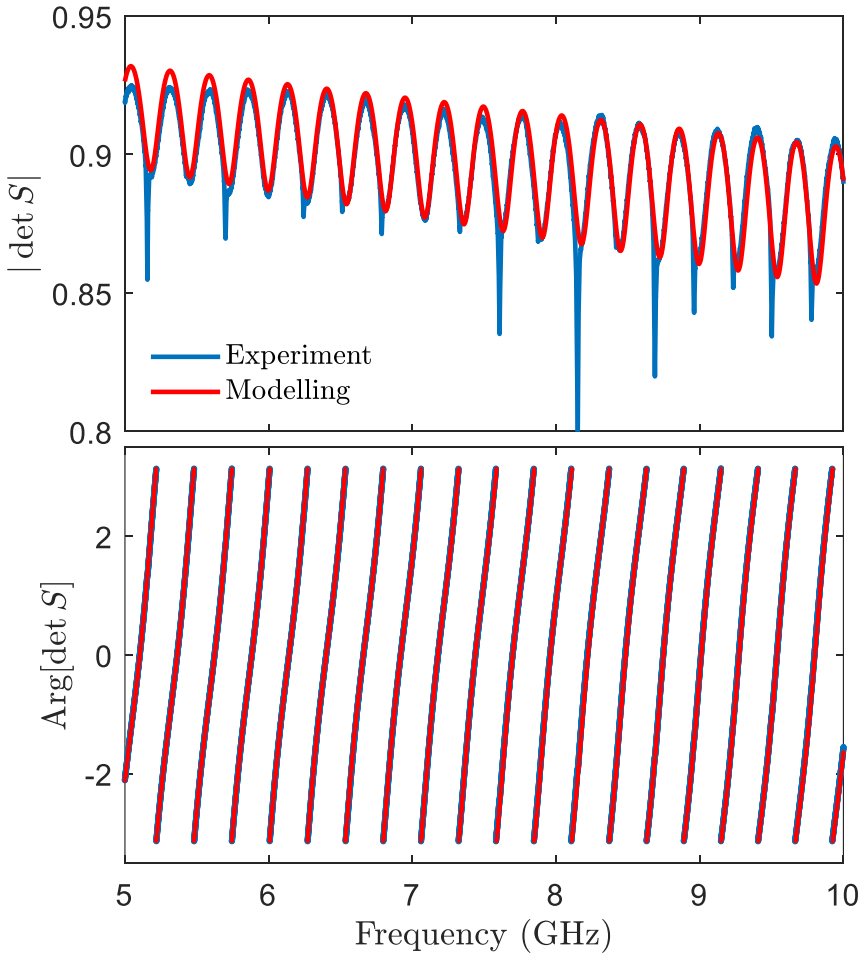

Figure 5.14: Comparison of modelling (red line) and experimental data (blue line) for $\det S$ with shape resonances only in a symmetrical ($L_1 = L_2$) ring graph. The modelling data is calculated from Eq. (5.4) using the Wigner zeros and poles for the shape resonances (see the blue and red squares in Fig. 5.13). Upper plot shows the magnitude of $\det S$, while the lower plot shows the phase of $\det S$. This figure is taken from Ref. [4].

Feshbach resonances present. We can see a series of dips and peaks, which reveal the zero and pole locations in the complex frequency domain. We also show in Fig. 5.17 the reconstruction of complex $\det[S]$ over the complex frequency plane from a different perspective compared to Fig. 5.16, highlighting the phase variation in the region between the shape and Feshbach resonances.

Other methods exist for S-matrix reconstruction. One approach is to use harmonic inversion, in which frequency domain data is transformed into the time domain and fit to a time-decay

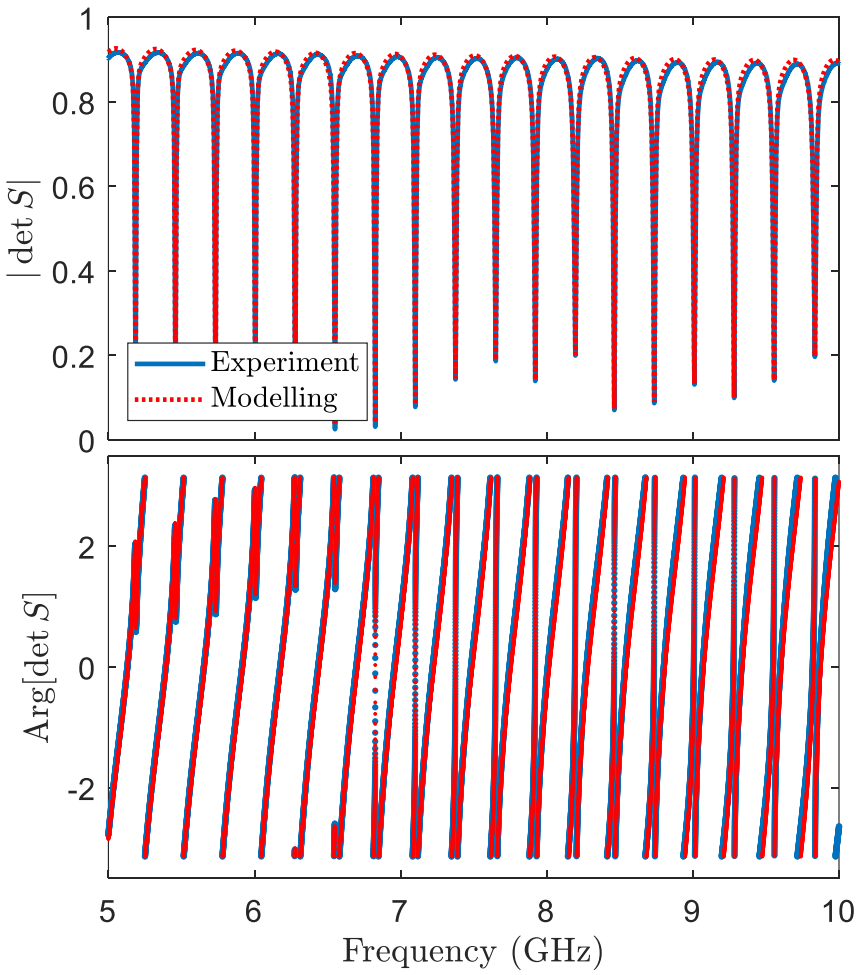

Figure 5.15: Comparison of modelling (red dashed line) and experimental data (blue line) for $\det S$ with both shape and Feshbach resonances in an asymmetrical ($L_1 \neq L_2$) ring graph. The modelling data is calculated from Eq. (5.4) using the Wigner zeros and poles for the shape resonances (see the blue and red squares in Fig. 5.13) and the Wigner zeros and poles for the Feshbach resonances (see the blue and red circles in Fig. 5.13). Upper plot shows the magnitude of $\det S$, while the lower plot shows the phase of $\det S$. This figure is taken from Ref. [4].

made up of a sum of many poles [124, 233, 234]. This technique is quite successful for finding poles, but does not directly determine the zeros of the S-matrix. Note that complex time delay can be used to augment a harmonic inversion search for S-matrix poles. Another approach to finding scattering poles is to use numerical methods to find outgoing-only solutions to wave equations in terms of quasinormal modes, and therefore identify the complex pole positions [204, 205].

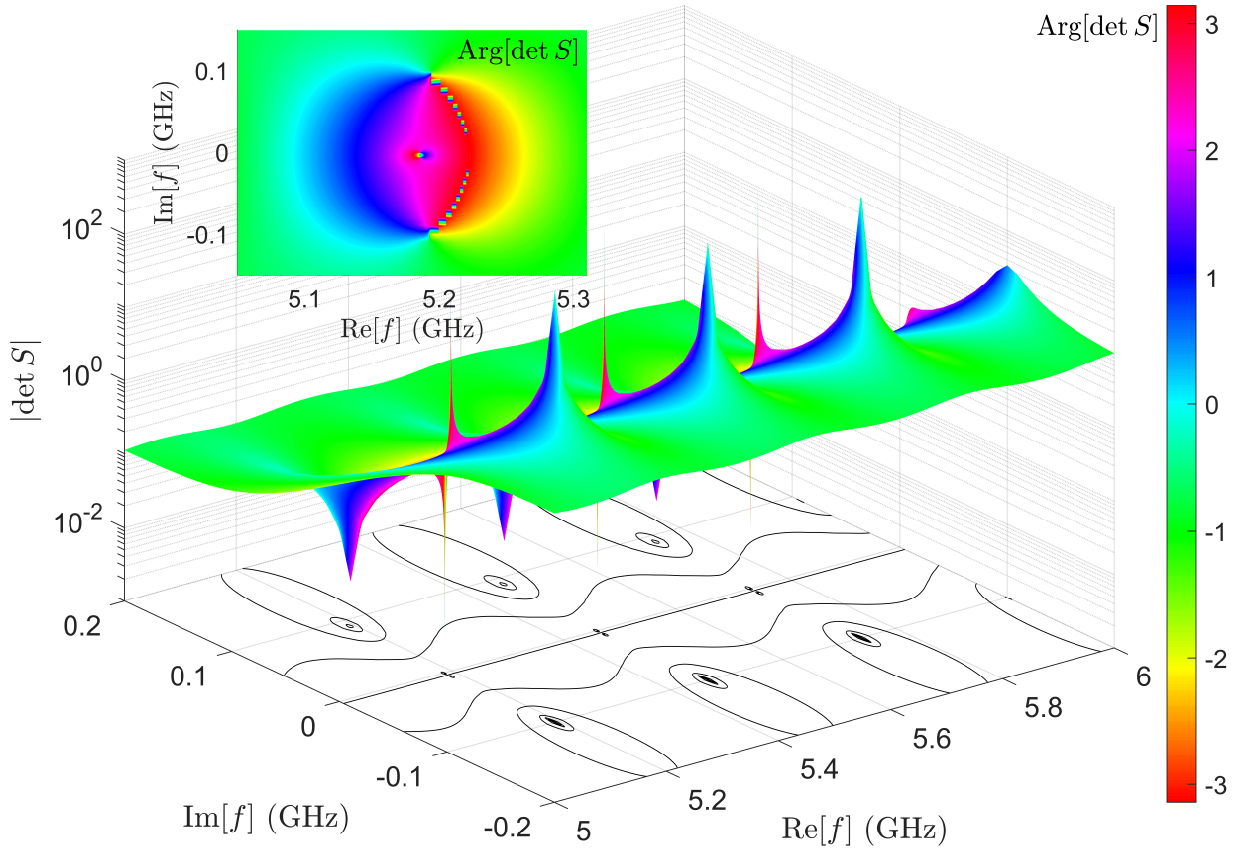

Figure 5.16: Complex representation of $\det S$ evaluated over the complex frequency plane for several modes of an asymmetric ($L_1 \neq L_2$) ring graph. $\det S$ is calculated from Eq. (5.4) using complex frequency and the Wigner zeros and poles for the shape resonances (see the blue and red squares in Fig. 5.13) and the Wigner zeros and poles for the Feshbach resonances (see the blue and red circles in Fig. 5.13). The 3D plot represents $|\det S|$ on a log scale and reveals the zeros (dips) and poles (peaks) at different locations in complex frequency. The base plane shows contour lines of the magnitude of $|\det S|$ in the complex frequency plane. The colorbar on the right shows the phase of the constructed $\det S$. The inset shows a 2D top view of Arg$[\det S]$ for a single pair of shape and Feshbach zeros and poles. This figure is taken from Ref. [4].

A more complete approach is to use Weierstrass factorization of the S-matrix, and to also include solutions to the wave equations that involve ingoing-only solutions to identify the zeros of S [168, 235]. This approach allows one to re-expresses the scattering matrix in terms of a sum of Lorentzians due to the poles, with residues that depend on both the zeros and the poles. Note that here we retrieve only $\det[S]$, but the full S matrix can also be reconstructed [168, 235].

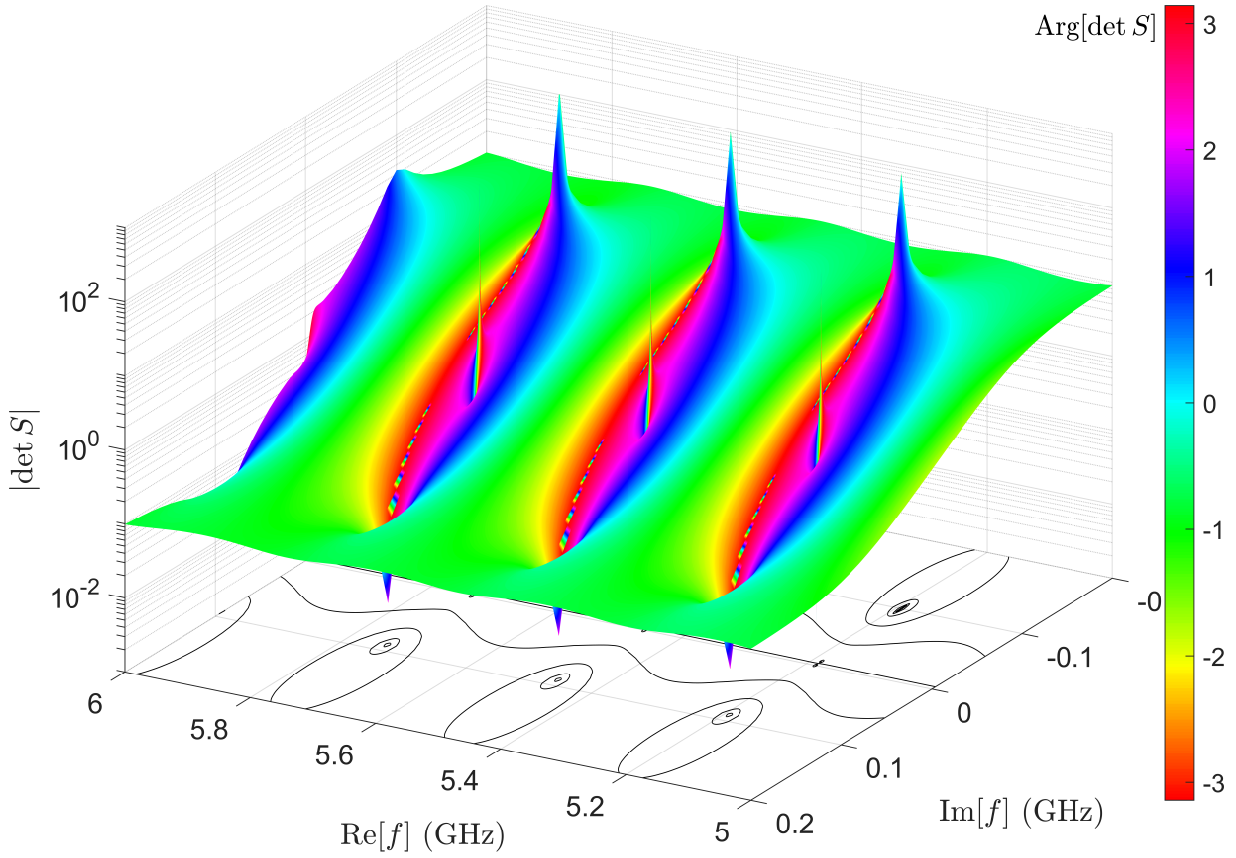

Figure 5.17: Complex representation of $\det S$ evaluated over the complex frequency plane for several modes of an asymmetric ($L_1 \neq L_2$) microwave ring graph. This 3D plot shows another perspective of Fig. 5.16. This figure is taken from Ref. [4].

If a passive zero loss system hosts an embedded eigenstate, i.e., a mode with zero-decay rate, the corresponding S-matrix pole will lie on the real frequency axis. In a passive system with finite loss, this is only possible if there is also a degenerate S-matrix zero occurring at the same real frequency, where they merge and cancel each other [66, 71, 76]. This seems to describe the Feshbach poles and zeros of the ring graph in the limit as $n \to 0$. To measure the degree of coincidence of the pole and zero, we can evaluate the residue of the Feshbach poles as a function of mode number. The residue of $\det[S]$ due to a single (assumed simple) Feshbach pole is given by $\rho_n^F = \det[S(\mathcal{E})](\mathcal{E} - \mathcal{E}_n^{F,asymm})|_{\mathcal{E}\to\mathcal{E}_n^{F,asymm}}$. This in turn can be written as

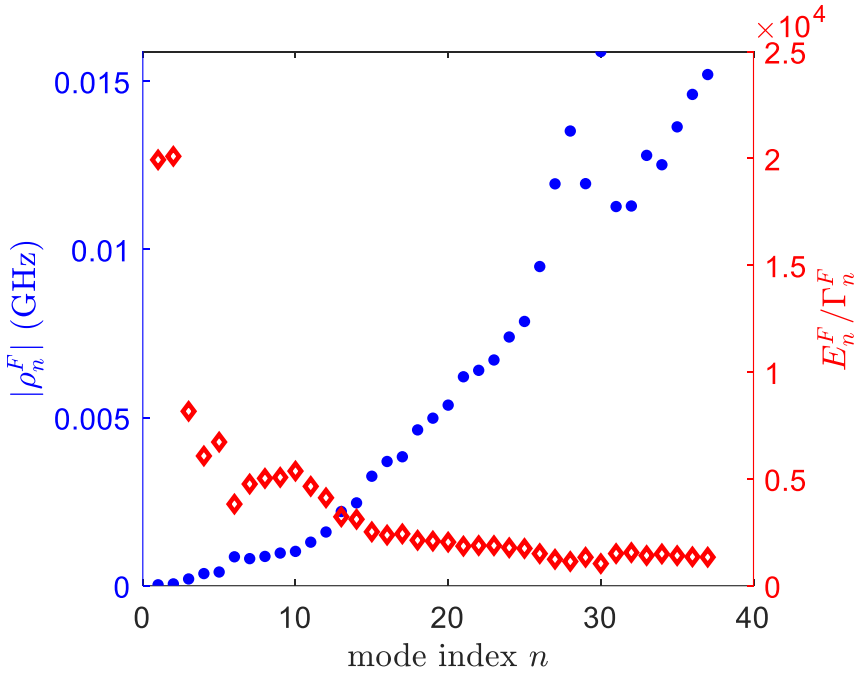

Figure 5.18: Plot of residue ρ_n^F and the 'quality factor' of the Feshbach poles, versus mode index n, for an asymmetric microwave loop graph. The blue filled circles show the absolute magnitude of the residue $|\rho_n^F|$ as a function of mode index based on the extracted Feshbach poles and zeros, while the red open diamonds show the associated ratio of E_n^F/Γ_n^F of the Feshbach poles. This figure is taken from Ref. [4].

$\rho_n^F \propto \frac{\mathcal{E}-z_n^{F,asymm}}{\mathcal{E}-\mathcal{E}_n^{F,asymm}}(\mathcal{E}-\mathcal{E}_n^{F,asymm})|_{\mathcal{E}\to\mathcal{E}_n^{F,asymm}} = \mathcal{E}_n^{F,asymm} - z_n^{F,asymm}$, which is just the distance between the Feshbach pole and zero. Figure 5.18 shows the absolute magnitude of ρ_n^F as a function of mode number based on the extracted Feshbach poles and zeros. It is clear that in the limit of index going to zero that the pole and zero approach each other, consistent with the development of an embedded eigenstate. Also shown in Fig. 5.18 is the associated 'Q' value of the pole in terms of the ratio E_n^F/Γ_n^F of the modes.

5.7 Discussion

Our comprehensive discussion of Wigner, transmission, and the reflection complex time delays in section 5.2 gives us the opportunity to address the question: what is the general strategy

to maximize the real part of all the complex time delays? From Eq. (5.7) we see that the real part of τ_W is maximized when the imaginary part of a scattering pole Γ_n is equal to the uniform attenuation rate η. This divergence of the Wigner time delay has been previously demonstrated in the context of coherent perfect absorption by several groups [2, 160]. Also, for the microwave ring graph studied here, we see from the plot of τ_W vs. frequency in Fig. 5.5 that this condition is nearly met somewhere around 7 GHz. With tuning of either δ and/or η we could achieve the divergence of Re$[\tau_W]$ for one or more modes.

From Eq. (5.12) we see that the real part of τ_T is maximized when the imaginary part of a transmission zero Im$[t_n]$ is equal to the uniform attenuation rate η. In our data on the microwave ring graph, the imaginary part of the transmission zero is always negative and much smaller in magnitude than the uniform attenuation, so the associated divergence is not visible here. The data for complex τ_T vs. frequency for all 37 modes is shown in Fig. 5.6. The transmission time delay shows nearly sinusoidal oscillations arising from the shape modes, and a series of spikes arising from the Feshbach modes. As expected, the transmission time delays are generally small in magnitude and show no irregular variations associated with a near degeneracy of Im$[t_n]$ and η.

Finally, from Eqs. (5.21), (5.23), and (5.26) we see that the real part of either $\tau_R^{(1)}$ or $\tau_R^{(2)}$, and the magnitude of $\delta\mathcal{T}_R = \tau_R^{(1)} - \tau_R^{(2)}$, is maximized when the imaginary part of a reflection zero v_n is equal to either plus or minus the uniform attenuation rate, $\pm\eta$. For our microwave ring graph, we see from the plots of complex τ_R vs. frequency in Fig. 5.7 that this condition is nearly met for a number of modes, including modes 1 and 14. The extreme values of reflection time delay, on the order of hundreds of Heisenberg times, dwarfs those of the Wigner and transmission times. In this case we have $v_1^F = -8.65\times10^{-5}$ GHz, $v_1^S = 1.05\times10^{-4}$ GHz and $\eta = 3.79\times10^{-5}$ GHz for mode 1, and $v_{14}^F = 0.0010$ GHz, $v_{14}^S = 0.0045$ GHz and $\eta = 0.0044$ GHz for mode 14,

resulting in large values for the real and imaginary parts of τ_R.

To summarize, we note that divergences in all time delays can be tuned into existence through variation of uniform attenuation η, or perturbations that systematically vary E_n, Γ_n, t_n, or r_n.

What is the practical limit for the maximum value of time delay? Constructing time delay from experimental S-parameter data requires two nearby data points with which we calculate a finite difference approximation to the derivative of $\ln(\det[S])$. However, the singularity is at a single point in frequency, hence we can never achieve the true divergence this way, although we can get arbitrarily close by taking finer steps in parameter space. On the other hand, one can tune to the CPA condition of a physical system containing a non-zero loss and create an unbounded time delay at one frequency, as demonstrated with CPA experiments in microwave graphs [2].

The introduction of complex time delay analysis now offers the opportunity to study the detailed evolution of poles and zeros in the complex plane when scattering systems are subjected to a variety of perturbations. A number of methods to controllably drive poles and zeros around the complex plane have been developed in different contexts. As an example in the case of the ring graph, several authors have examined the question of what trajectory an embedded eigenvalue pole leaves the real axis as the ring graph is perturbed [189, 199, 236]. Another opportunity is the manipulation of reflection zeros in the complex frequency plane for multi-port scattering systems to create what are known as reflectionless scattering modes (RSM) [62, 63]. Reflection (τ_R) and reflection difference ($\delta\mathcal{T}_R$) complex time delays will enable monitoring of reflection zeros so that they can be tuned to the real axis to establish RSMs.

Wave chaotic systems have scattering properties that are very sensitive to changes in boundary conditions. This makes such systems well suited to act as sensors of perturbation, such as

motion or displacement of objects located in the scattering domain, through the concept of scattering fidelity [237–241]. In addition, there exists a class of sensors that are based on the coalescence of two or more eigenmodes [242, 243]. In all cases, the longer the dwell time of a wave in a monitored space, the greater its sensitivity to small perturbations [160, 244].

Finally, we discuss a number of important issues associated with our approach to modeling the complex time delays. In this chapter we have taken two distinctly different approaches to modeling the measured time delay. In the case of the shape resonances, the poles and zeros are relatively far removed from the real axis; the ratio of imaginary part of the pole (and zero) to the mean spacing is approximately $\Gamma_n^S/\Delta E_n^S \sim 0.35$. In this case, many poles and zeros contribute to the Wigner time delay (as an example) at any given point on the real frequency axis. For this reason, we fit all of the pole and zero locations at once for the data in Fig. 5.4. In addition, the product over modes in Eq. (5.4) extends over ± 200 modes in order to properly reproduce $\det S$ in Figs. 5.14 and 5.15. On the other hand, when poles and zeros are close to the real axis, it is possible to treat each pole/zero pair individually. This is the case for the Feshbach resonances where we find the ratio of imaginary part of the pole to the mean spacing is roughly $\Gamma_n^F/\Delta E_n^F \sim 0.01$. In this case the contribution to the time delay in a given narrow frequency window is dominated by the nearest pole and zero. This is the case for the fits shown in the insets of Figs. 5.8 and 5.9, and the fits shown in Fig. 5.12. We have checked this assumption by a number of methods. First, our correct recovery of the measured $\det S$ on the real axis, as shown in Fig. 5.15, is a clear test of the assumption that the fitting of individual Feshbach poles and zeros is adequate to model the global scattering matrix at arbitrary real frequencies. Secondly, we have checked that adding terms to the complex time delay arising from neighboring poles and zeros has no effect on our fitting of individual mode data, such as those shown in the insets of

Figs. 5.8 and 5.9.

There is one additional potential limitation of the above description of complex time delay. Assuming a single uniform value of the loss parameter η at a given frequency is an approximation, especially for our ring graph. The graph has a variable phase shifter in it that is not a homogeneous transmission line. There may be point-like loss centers that exist in this microwave graph, which we are not modelling properly with just a uniform attenuation. Also, in the fitting of complex time delay vs. frequency, we assume that the value of η is constant in the narrow frequency range around each pair of shape/Feshbach modes (as in Fig. 5.12), although we believe that this is a good approximation for the data and analysis presented here.

5.8 Conclusions

We provide a comprehensive analysis of the ring graph scattering response in terms of poles and zeros of the S-matrix, and the reflection and transmission submatrices. We have treated the complex Wigner-Smith, reflection and transmission time delays on equal footing, all in one experimental setting. We also create a faithful reconstruction of the complex determinant of the S-matrix over the complex frequency plane from the experimentally extracted poles and zeros. More generally, we provide the first comprehensive treatment of complex Wigner, transmission, reflection, and reflection difference time delays. We also provide a prescription for maximizing the real part of all complex time delays in terms of the poles and zeros of the scattering matrix, and the uniform attenuation in the system.

Chapter 6: Aharonov–Bohm Ring Graph

6.1 Overview

The Aharonov–Bohm (AB) effect is a quantum mechanical phenomenon, where an electron or an electrically charged particle is affected by an electromagnetic potential ($\mathbf{A}$) even in the absence of a magnetic or electric field at the location of the particle [245]. This gives rise to a kind of "action at a distance" in which a particle can be affected by electromagnetic fields even if it does not experience them directly. In [5], the authors propose a two-port Aharonov–Bohm ring in a mesoscopic sample and demonstrate a number of interesting results. Specifically, they consider a 2-channel AB ring in a perpendicular magnetic field. They treat electron wavepackets travelling through the ring in opposite directions. The ring is engineered to treat the left-going and right-going wavepackets differently. Fig. 6.1 shows the schematic of the proposed mesoscopic Aharonov–Bohm ring, along with a schematic of the equivalent microwave graph. The key feature is to create a constant phase difference of π in the quantum wavepacket between the forward and backward travelling paths by means of a magnetic flux through the ring. As a result, the electrons emitted from one source into the ring would experience a three times greater transmission time as the electrons injected from the other source. Furthermore, it has been proposed that a finite degree of quantum dephasing can enable non-reciprocal transport through the Aharonov–Bohm ring structure. This is possible due to the non-reciprocal dwell times in the ring

and the selective action of a de-phasing center on the long-lingering wave packets.

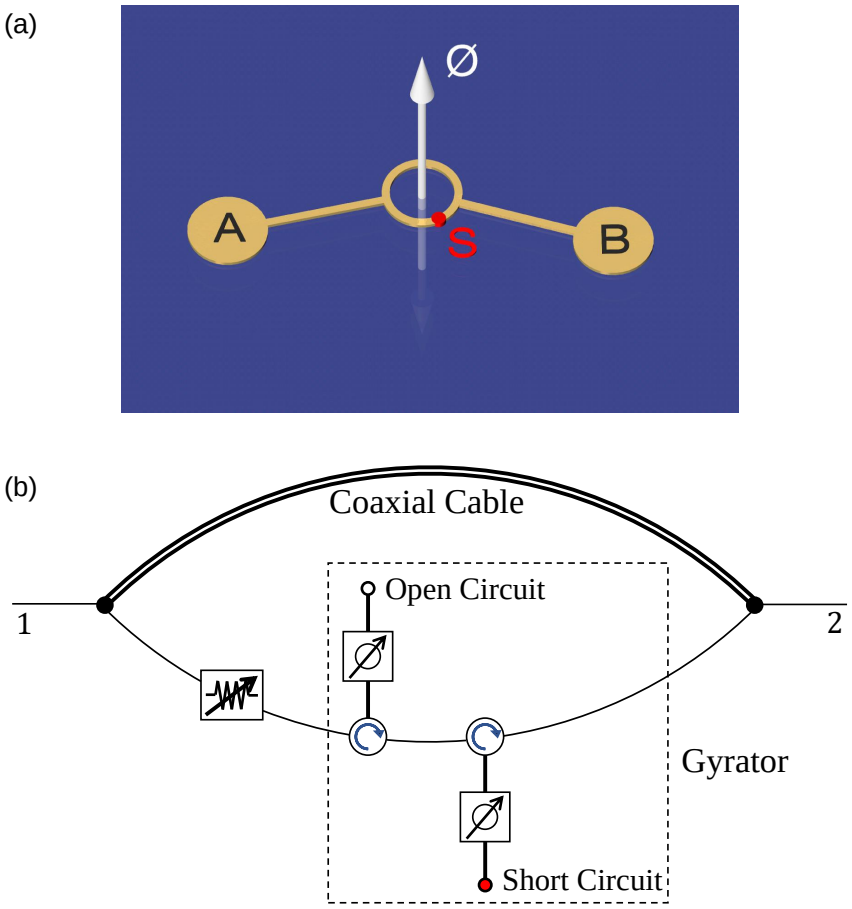

Figure 6.1: The schematic layout of an Aharonov–Bohm ring and its corresponding microwave graph design. (a) shows the device layout of a two-port Aharonov–Bohm ring made of semiconductor. The penetrating magnetic flux Φ causes a shift of π phase difference between the electron wave packets travelling along two arms of the ring. The red dot S marks an inelastic scattering center. (b) shows the equivalent microwave graph realization of the Aharonov–Bohm ring. The two circulators together with the open/short circuits and a pair of phase trimmers in the dashed box make up a gyrator (see Fig. 6.2), which creates the π phase difference for waves travelling in different directions. The variable attenuator acts as a lossy/de-phasing center. Panel (a) is taken from Ref. [5].

In this chapter, my objective is to explore the physics of mesoscopic transport and demonstrate anisotropic transport in the presence of finite de-phasing, in the regime between purely quantum and fully classical physics, through a microwave analog of the Aharonov–Bohm ring. We introduce a two-channel microwave graph realization of the Aharonov–Bohm ring, and study

its scattering properties in both the frequency domain and the time domain. In the frequency domain, we measure the scattering (S)-matrix and calculate the complex transmission time delay for both directions. We demonstrate that the forward transmission time delay and backward transmission time delay has a 3:1 ratio in a broad range of frequency, which agrees with the Aharonov–Bohm ring expectations. We also introduce a localized loss (dephasing center) in the ring graph (simulation), and adjust the transmission coefficients by varying the attenuation. We demonstrate the dependence of non-reciprocal transport on the de-phasing (loss) rate through the attenuation variation. In the time domain, we measure the transmission time delays of short pulse excitations, approximating the behavior of electron wave packets, and verify the 3:1 ratio of the transmission time delays in both directions. This establishes the analogy between mesoscopic and microwave Aharonov–Bohm rings, and leads to the surprising result that a net transport of wave excitations can be created by means of partial de-phasing.

6.2 Experiment

The Aharonov–Bohm ring uses magnetic flux to produce a π phase shift between waves travelling on the two arms of a simple electron interferometer. In order to mimic that effect, we use a gyrator to create the π phase difference in microwave networks. Fig. 6.2 shows the schematic design and the actual picture of the microwave gyrator setup. The open/short circuits are designed to provide a π phase difference for waves travelling in different directions, but due to the finite electrical length inside the circuits, the phase difference is not exactly π. Thus, we use a pair of phase trimmers in the design to compensate for the difference in electrical lengths through fine-tuning. (This basic idea of creating 0 and π phase shifts for left and right-going waves was

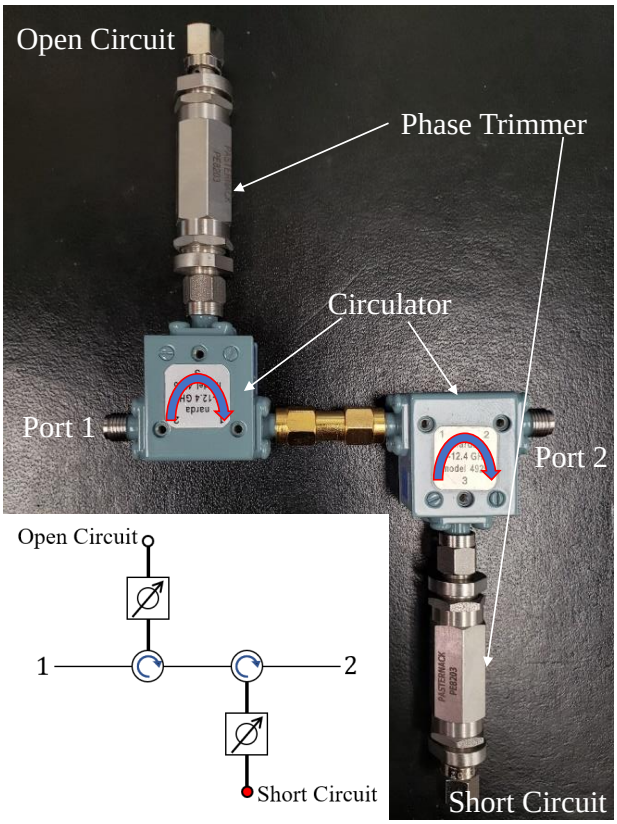

Figure 6.2: The schematic design and the actual picture of a microwave gyrator offering non-reciprocal π phase difference between the left-going waves and right-going waves traveling between ports 1 and 2. Two identical circulators are used to guide the wave propagation directions, and a pair of the open/short circuits are used to create the π phase difference for waves travelling in different directions. Between the open/short circuits and the circulators, there are a pair of phase trimmers for fine-tuning of the phase difference.

inspired by the Gaussian Symplectic Ensemble graph developed by [43]) The measured phase difference between S_{12} and S_{21} is shown in Fig. 6.3. The circulators used in the experiment have a working frequency range of $7 - 12.4$ GHz, and we measure the S-matrix of the gyrator in that frequency range. After doing some fine-tuning of the two phase trimmers, we are able to get the phase difference from the gyrator to be close to π. There are some wiggles in the plot, which is due to the imperfection of the circulators and standing waves inside the circuit.

Next, we construct the Aharonov–Bohm ring graph (see Fig. 6.4) using the gyrator design.

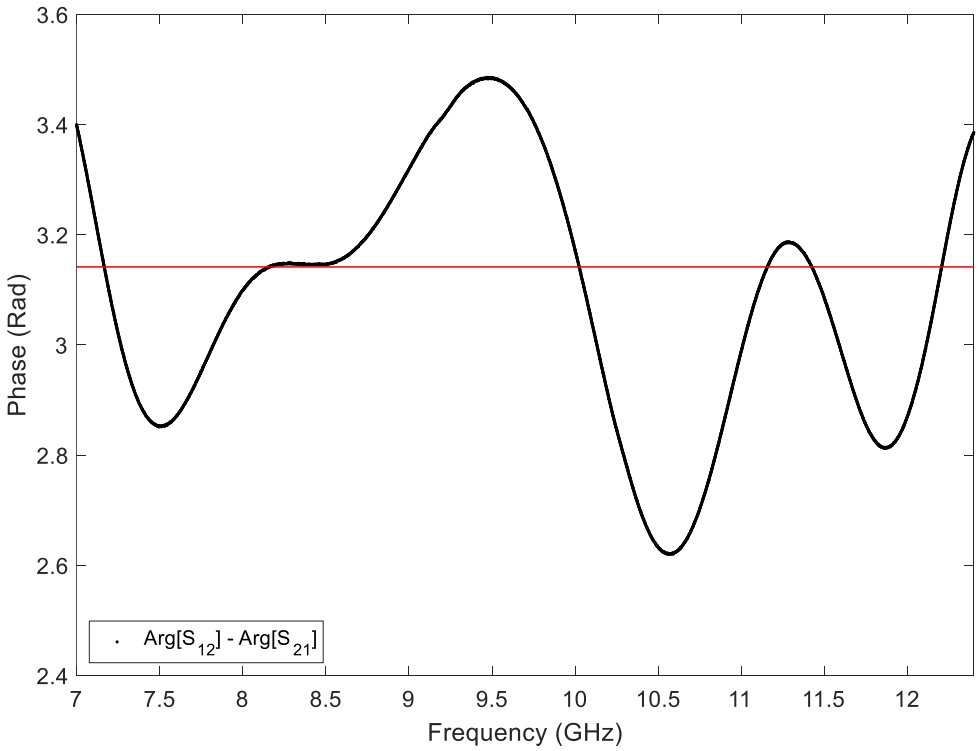

Figure 6.3: Measured phase difference between S_{12} and S_{21} for the gyrator shown in Fig. 6.2. The red line shows a reference phase difference of π.

The key is to add an upper branch that has the same electrical length of the gyrator, so that waves travelling in both branches would go through the same distance. This also has the effect of eliminating the Feshbach modes, leaving on the shape resonances of the ring graph (see Chapter 5). We measure the electrical length of the gyrator and a series of single coaxial cables, and selected a 12-inch-long coaxial cable as the upper branch. We then perform some fine-tuning on both phase trimmers to achieve the electrical length as close as possible to the 12-inch cable. The 12-inch coaxial cable has a electrical length of 0.4386 m, and we manage to adjust the electrical length of the gyrator to be 0.4385 m while maintaining a near π phase difference for left/right transmission. The resulting microwave analog of the AB graph is shown in Fig. 6.4.

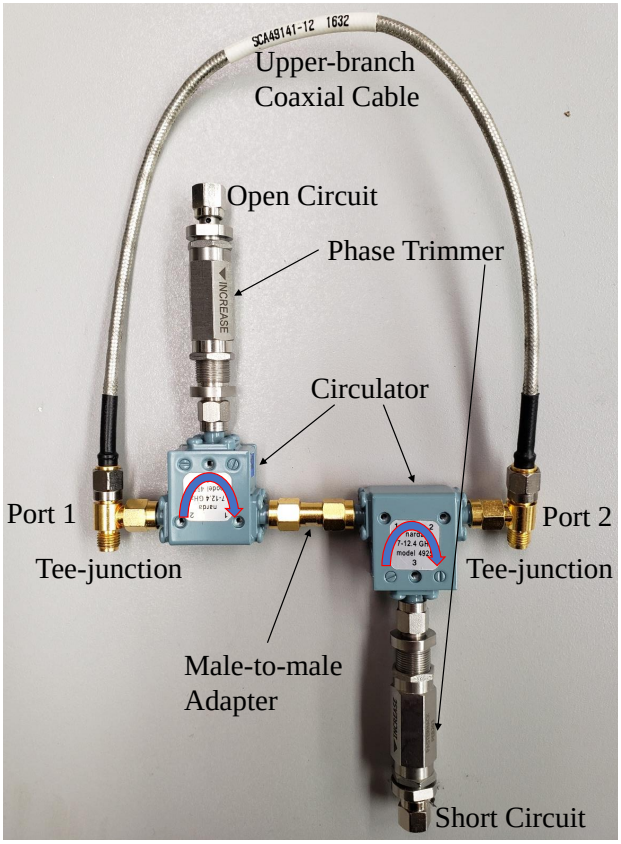

Figure 6.4: Picture of the Aharonov–Bohm ring graph constructed from the gyrator from Fig. 6.2. The upper branch is a single coaxial cable matching the electrical length of the lower branch. This is the experimental realization of the schematic shown in Fig. 6.1(b).

6.3 Frequency-domain Results

6.3.1 S-matrix Measurements

We measure the 2×2 S-matrix of the Aharonov–Bohm ring graph from 7 to 12.4 GHz, and plot the results in Fig. 6.5. The wiggles in the plot come from the Shape resonances of the graph, which has been thoroughly studied in Chapter 5. The periodicity of the shape resonances depends on the total length of the graph $\Sigma = 0.8771$ m, which corresponds to a repetition frequency of 0.342 GHz. This accounts for much of the periodic structure in the S-parameters. One can

also notice a rough doubling of the repetition frequency scale, which arises from differences in the locations of the S-matrix poles and zeros for even and odd shape modes, which shall be discussed below. The inset shows a clear comparison between $|S_{21}|$ and $|S_{12}|$, where it can be seen that $|S_{21}| > |S_{12}|$ for all frequencies. This qualitatively agrees with the prediction, where waves travelling from port 2 to port 1 are experiencing three times of the time delay as the waves travelling from port 1 to port 2, thus resulting in a larger attenuation on the magnitude.

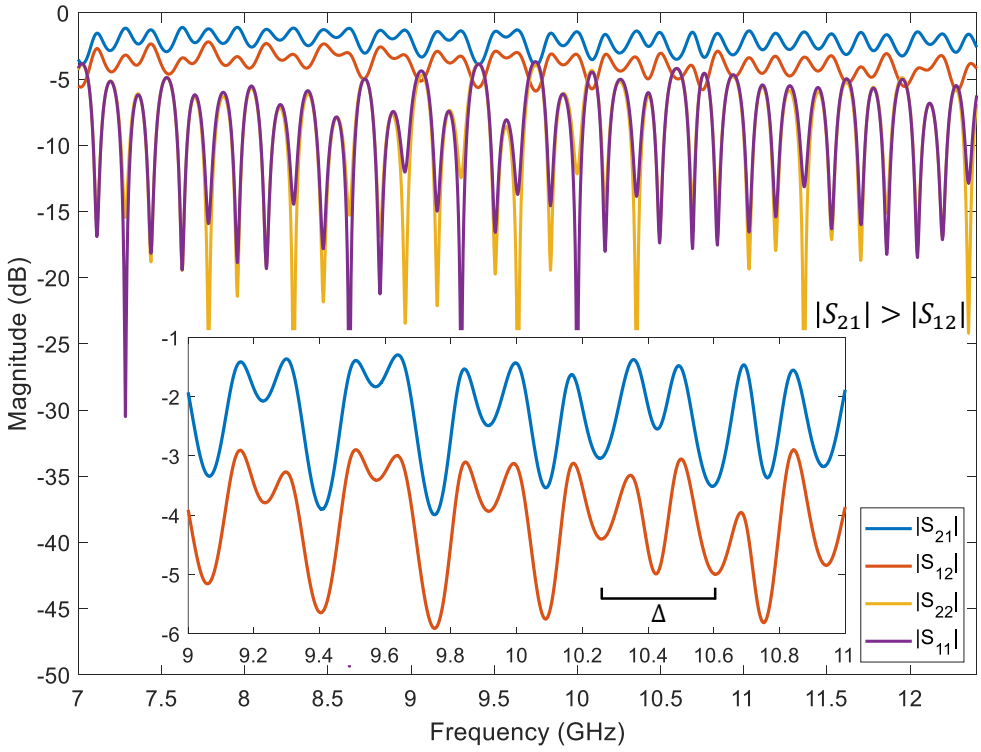

Figure 6.5: Measured S-matrix data for the Aharonov–Bohm ring graph in Fig. 6.4. Inset shows a zoom-in comparison of the two transmission coefficients $|S_{21}|$ and $|S_{12}|$. The scale bar in the inset gives the expected periodicity frequency scale (0.342 GHz) for the shape resonances.

6.3.2 Transmission Time Delays

The transmission time delays for both directions (S_{21} and S_{12}) can be calculated from data using Eq. (5.10). The results of both (from S_{21} and S_{12}) transmission time delays τ_T^{21}, τ_T^{12}

are shown in Fig. 6.6. The wiggles from the transmission time delay plot come from the shape resonances of the ring graph, but we are more interested in the ratio between the two transmission time delays. In the inset we plot $\mathrm{Re}[\tau_T^{12}]/3$ against $\mathrm{Re}[\tau_T^{21}]$, so that they are relatively on the same vertical position. This proves the 3:1 ratio for the two transmission time delays in the Aharonov–Bohm ring graph, at least for single-frequency excitations.

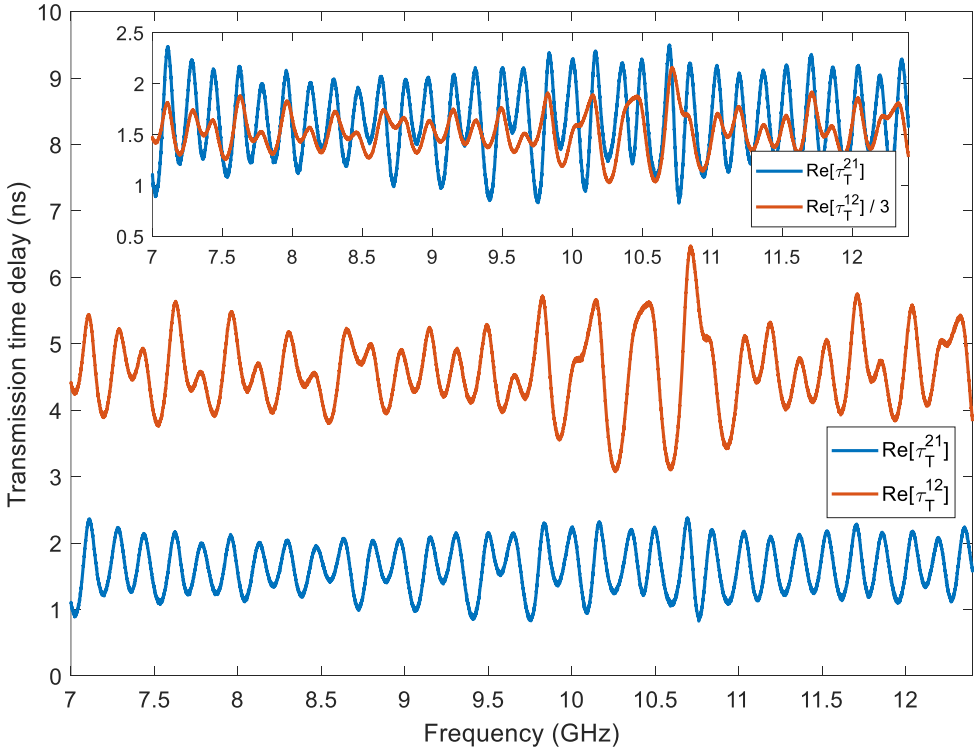

Figure 6.6: Comparison between the transmission time delays for both directions in the Aharonov–Bohm ring graph. Blue line shows the real part of the transmission time delay calculated from measured S_{12}, while the red line shows the real part of the transmission time delay calculated from measured S_{21}. Inset shows a direct comparison for the 3:1 ratio between the two transmission time delays.

6.3.3 Non-reciprocal Transport

One important result from [5] is the non-reciprocal transport through the Aharonov–Bohm ring structure due to de-phasing. In the microwave regime, we utilize loss/attenuation as an anal-

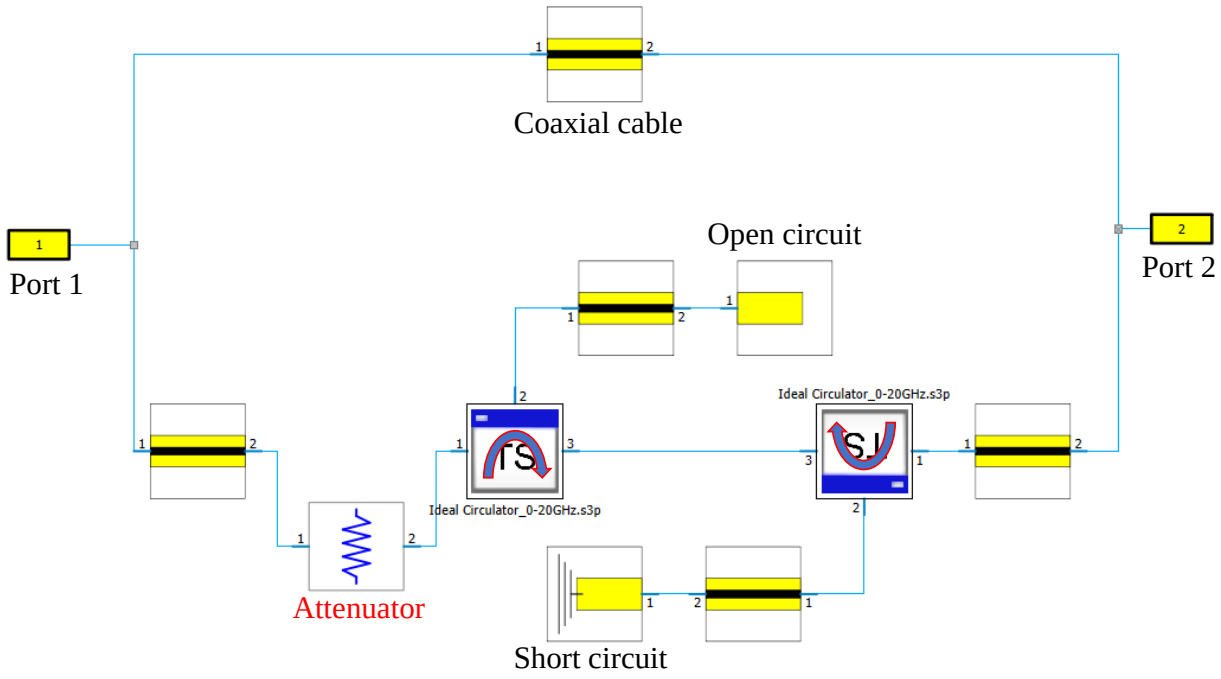

Figure 6.7: Simulation schematic of the Aharonov–Bohm ring graph in CST. A variable attenuator is added to the lower branch of the graph. The transmission line blocks represent the coaxial cables used in the experiment, which has an inner diameter of 0.036 inch, an outer diameter of 0.1175 inch, and a relative dielectric constant of 2.1. The coaxial cables are set to be lossless, i.e. the dielectric loss tangent of the medium $\tan\delta = 0$, and the resistivity of the metals in the cable $\rho = 0$. The open and short circuit blocks have a finite length of 0.005 inch with the same relative dielectric constant of 2.1. The two circulator blocks are imported from TOUCHSTONE files with ideal circulation. The only loss mechanism in this model comes from the attenuator with variable attenuation setting.

ogy to de-phasing [18]. In Ref. [18] it was shown that microwave loss in a two-dimensional billiard was exactly analogous to the rate of de-phasing for electrons in a corresponding mesoscopic quantum dot. We now extend this analogy to transport through a mesoscopic AB device. Here we simulate the non-reciprocal transport effect in CST Microwave Studio. In particular we use the circuit modeling package to create a faithful model of the microwave quantum graph. Fig. 6.7 shows the simulation schematic of the Aharonov–Bohm ring graph as a CST circuit model. We introduce a lumped loss (variable attenuator) to the graph, and eliminate all other loss mechanisms for simplicity. Fig. 6.8 shows the simulation comparison between $|S_{12}|$ and $|S_{21}|$ under

different attenuation settings. When attenuation is 0 dB, i.e. no loss, the two transmission paths have the same transmission magnitude. As the attenuation increases, some differences begin to show up between the two transmission amplitudes. When the attenuation reaches 7.5 dB, there are periodic resonance frequencies which have zero transmission in one direction (in this case, S_{12}). The periodic wiggles in the transmission spectrum come from the shape resonances, and the plot implies there are two distinct sets of shape resonances (even and odd) in this ring graph.

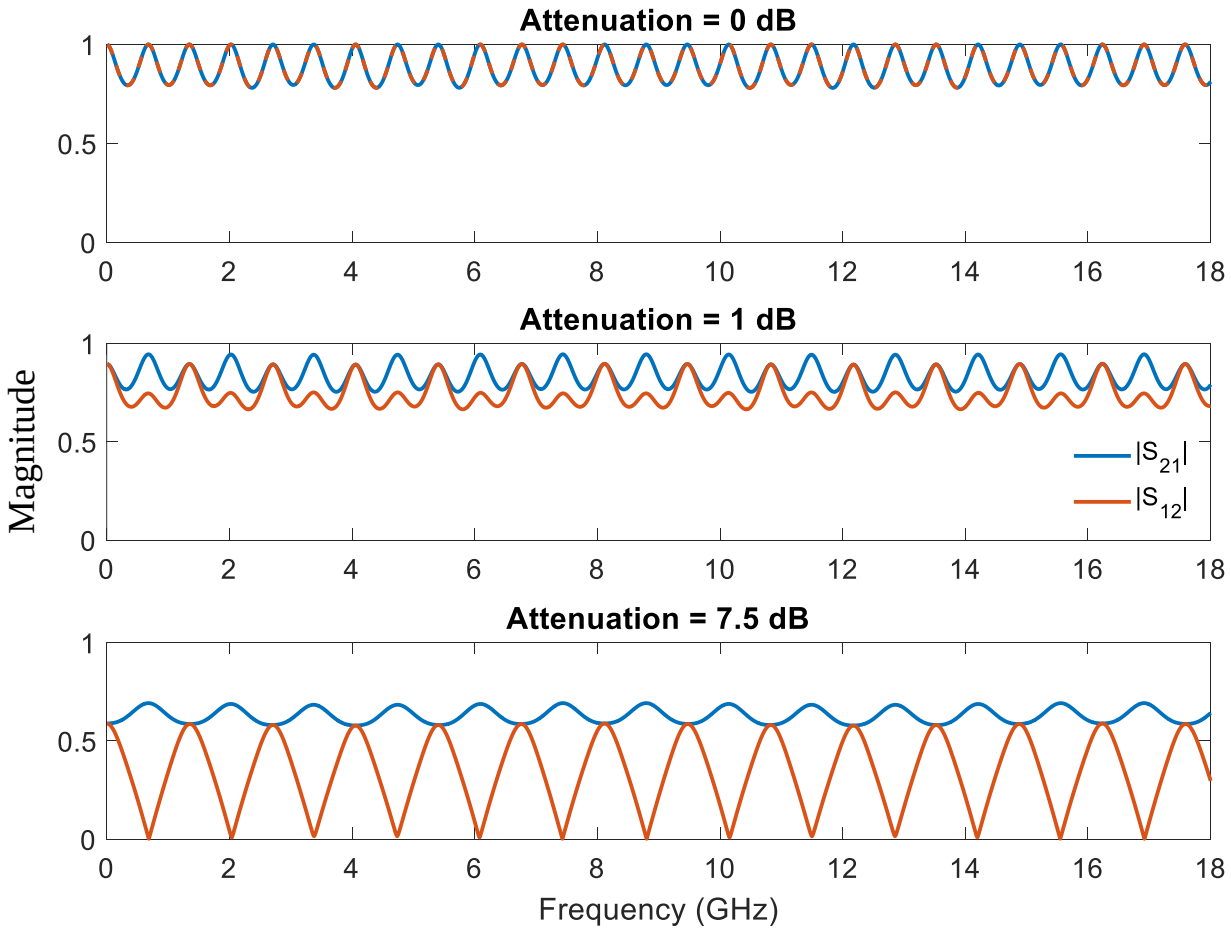

Figure 6.8: Comparison between transmission magnitudes of both directions in the Aharonov–Bohm microwave ring graph under different attenuation settings on the lower bond. Blue curve shows the magnitude of S_{21}, while red curve shows the magnitude of S_{12}.

The non-reciprocal transport behavior can be quantified as: $\sigma_A = \frac{||S_{21}|^2-|S_{12}|^2|}{|S_{21}|^2+|S_{12}|^2}$. Note that

σ_A is bounded between 0 and 1. If there is no non-reciprocal transport then σ_A is equal to 0, while a non-zero value implies some degree of non-reciprocal transport. Fig. 6.9(a) shows σ_A as a function of attenuation. Due to the wiggles of the shape resonances, we need to do an average calculation of σ_A over a range of frequencies corresponding to one period of the shape resonances. It is clear that in Fig. 6.8 σ_A will reach a value of 1 at certain resonance frequencies as $|S_{12}|$ goes to 0 at those points. On an average basis, σ_A shows a non-monotonic bell shape behavior as the attenuation increases, which agrees with expectations from mesoscopic theory (see Fig. 6.9(b)), where they calculate a non-monotonic dependence of non-reciprocal transport as a function of de-phasing rate in the mesoscopic version of the AB graph [6, 227]. They find it advantageous to create a finite amount of decoherence to create asymmetric transport, suggesting that working in the regime between purely quantum and purely classical physics may be optimal.

6.4 Time-domain Results

After getting the 3:1 ratio between the two transmission time delays from the frequency-domain data, we now demonstrate the non-reciprocity directly in the time domain. The reason for this is the fact that electrons travel as wave-packets, and do not have a single energy, as implied by our time-delay results obtain from S-matrix data, presented above. Therefore it is imperative that we examine the transport properties of our microwave graph with microwave wavepackets that are analogous to electron wavepackets in mesoscopic transport. These measurements were done by my colleague Isabella L. Giovannelli. Figure 6.10 shows the time-domain results of transmitted pulses at each port when sending in the pulse from the other port. Here, AWG stands for the Model AWG70001B arbitrary waveform generator from Tektronix, Inc., which generates

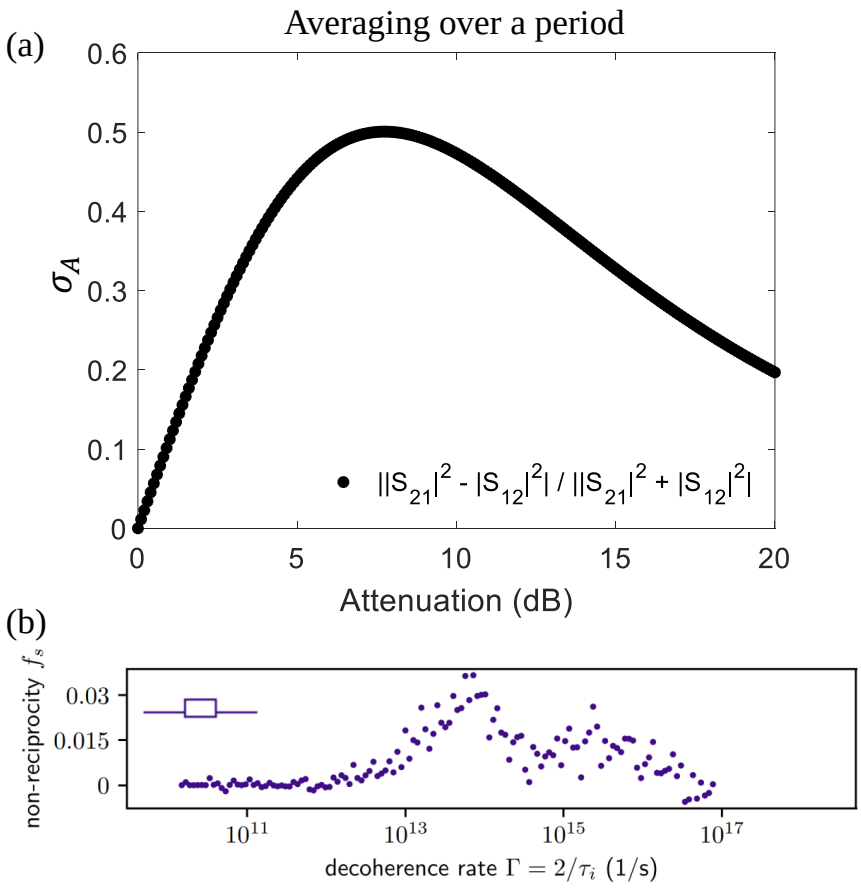

Figure 6.9: (a) shows the non-reciprocal transport factor σ_A of an Aharonov–Bohm microwave ring graph simulation in Fig. 6.7 averaged over a period of the shape resonances as a function of attenuation. The frequency period selected in this plot is $12.19 - 13.54$ GHz. (b) shows the calculated non-reciprocal transmission of an asymmetric Aharonov–Bohm mesoscopic ring device as obtained with the Monte Carlo wave function method from mesoscopic theory. Panel (b) is taken from Ref. [6].

the gaussian pulse used in the time-domain measurements. The pulse is a 1-ns wide Gaussian amplitude modulation of a 8.4-GHz carrier signal. Such a pulse includes approximately 1 GHz bandwidth, which is well within the bandwidth of our gyrator-based AB microwave graph. This will have the effect of averaging the non-reciprocal properties of the graph over a finite bandwidth. Here DUT is the device under test (which is the AB microwave ring graph), and DSO is the Model UXR0104A oscilloscope from Keysight Technologies, Inc. to record the transmitted signal. We measured the pulse transmission from both directions, and plot them on the same time

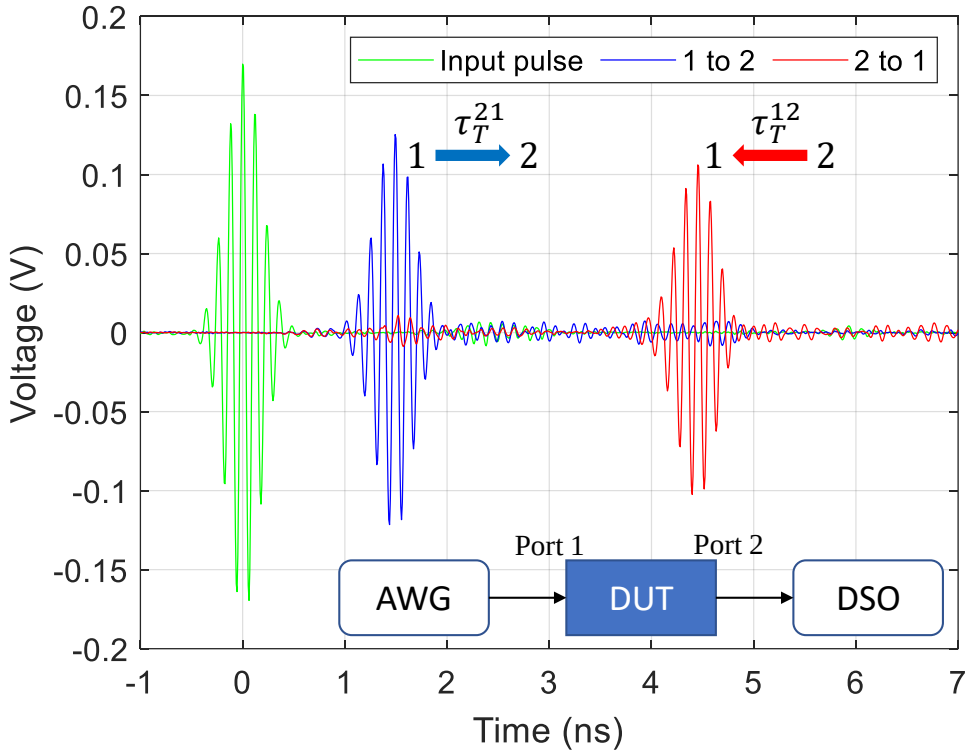

Figure 6.10: Time-domain measurements for the Aharonov–Bohm ring graph (the DUT here) shown in Fig. 6.4. Inset shows the schematic of the time-domain setup. The green pulse is a measurement of the pulse (a 1-ns wide Gaussian amplitude modulation of a 8.4-GHz carrier signal) from the AWG to the DSO in the absence of the DUT, which sets the zero-delay point on the time axis. The blue pulse shows the transmitted pulse from port 2 to port 1, while red pulse shows the transmitted pulse from port 1 to port 2. Note that the DUT device orientation is reversed from that shown in the inset for the port 2 to port 1 measurement.

axis. Shown for reference (green pulse in Figure 6.10) is the case where the DUT is absent, and this sets the zero of time for the pulse measurements, as well as illustrating the relatively modest effects of pulse dispersion in the experiment. Figure 6.10 demonstrates directly a 3:1 ratio of the transmission time delays for pulses propagating through the AB graph in opposite directions. From the plot, the transmitted pulse from port 2 to port 1 has smaller amplitude compared to the transmitted pulse from port 1 to port 2. That is because the transmitted pulse from port 2 to port 1 gets a larger attenuation by lingering in the AB graph for a much longer time.

Fig. 6.11 shows a plot of the two transmission times and amplitudes, as a function of

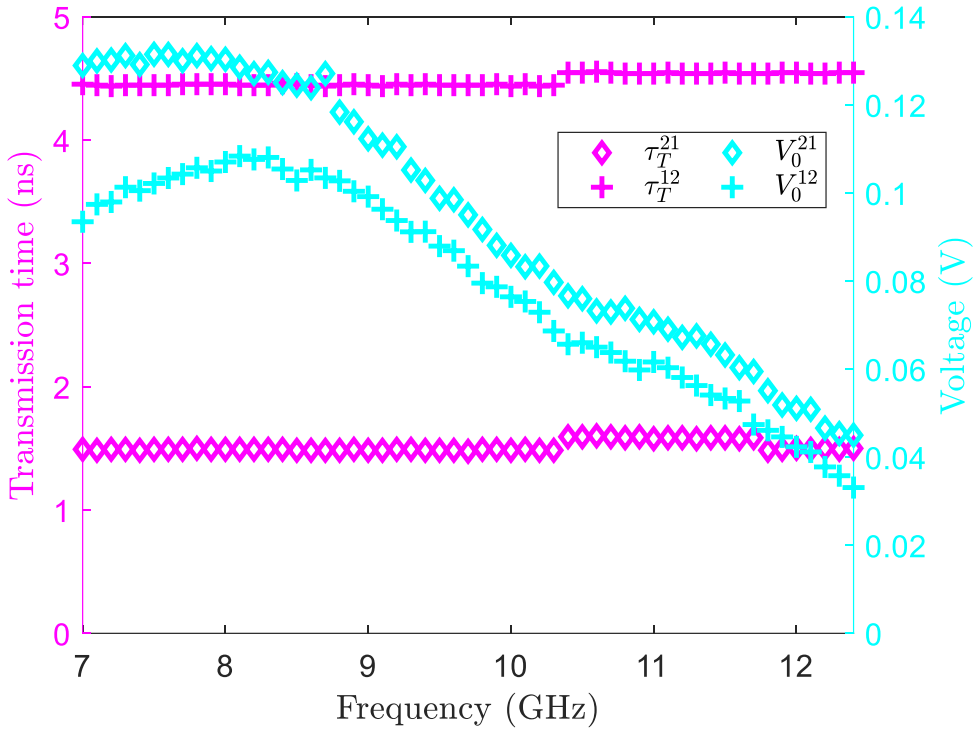

Figure 6.11: The two transmission times and amplitudes as a function of center frequency of the 1-ns wide pulse over the bandwidth of the device. The left axis (magenta) shows the two transmission time delays, while the right axis (cyan) shows the two amplitudes of the transmitted pulses. The diamond points represent the measured data from port 1 to port 2, while the plus-sign points represents the measured data from port 2 to port 1.

center frequency of the 1-ns wide pulse, over the bandwidth of the device. The left axis (magenta) demonstrates a consistent 3:1 ratio of the transmission time delays for pulses propagating through the AB graph in opposite directions. The right axis (cyan) shows that the transmitted pulse from port 2 to port 1 always has smaller amplitude compared to the transmitted pulse from port 1 to port 2. As the pulse center frequency increases, both amplitudes go down since the microwave graph is more lossy at higher frequency. These data were taken by by my colleague Isabella L. Giovannelli.

6.5 Discussion and Conclusions

In this chapter, I present a microwave network structure to mimic the mesoscopic electron transport in an Aharonov–Bohm ring, and demonstrate a 3:1 ratio of the transmission time delays from different directions. The 3:1 ratio of the time delay has been illustrated in both frequency-domain and time-domain experiments. I also demonstrate the non-reciprocal transport through the microwave Aharonov–Bohm ring and show that it agrees with expectations from mesoscopic theory.

Chapter 7: Conclusions and Future Work

7.1 Conclusions

In this dissertation, I demonstrate the success of applying CPA protocols in generic complex scattering systems without any geometric or hidden symmetries. Importantly, this general scheme allows for much broader opportunities in multiple applications, including designing efficient absorbers, sensitive reconfigurable switches, enabling practical long-range wireless power transfer, wavefront shaping, highly-efficient energy deposition systems, and next-generation telecommunications.

Furthermore, I develop the theoretical representation of the S-matrix by its zeros and poles, and generalized the traditional Wigner time delay to a complex quantity in sub-unitary scattering systems. Through the inherent connection between the complex Wigner time delay and coherent perfect absorption, I have established an effective approach for control of the zeros and poles of S-matrix in the complex scattering systems, by tuning either localized loss or uniform loss inside the system. Such a capability will be extremely useful for understanding the wave properties in the complex scattering systems, and for controlling the wave behavior in optics, electromagnetics, acoustics, quantum transport in condensed matter systems, etc.

I also show some interesting statistics of the new complex Wigner time delay in sub-unitary scattering systems, and demonstrate that it can be used as a practical counter of the resonance

widths of the scattering systems.

I take one step further, and look over the broad time delay community, and treat Wigner, transmission, and reflection time delays on equal footing. I am able to develop a comprehensive time delay analysis framework to include all these three time delays, and analyze their zeros and poles from the S-matrix. This tool provides us with great benefits in analyzing the complete scattering properties of any kinds of scattering system, which deepens our understanding of the physics behind complex scattering systems.

Based on our understandings of the ring graph and its time delays, I built a microwave realization of the Aharonov–Bohm ring, and demonstrated promising results for non-reciprocal transport that agree with the mesoscopic predictions. This allows us to explore the transmission time delay further to the non-reciprocal regime, and shows the possibility of simulating a mesoscopic device with a microwave graph.

The significance of this dissertation is the following: it reveals new capabilities to engineer the locations of zeros and poles of the scattering matrix through various manipulations of the scattering system, which will inevitably lead to many interesting applications. Various examples include: finding the coherent perfect absorption (CPA) state by looking for a peak/divergence of complex Wigner time delay [1, 2]; creating exceptional points where two poles come together, or where two zeros come together [246]; identifying degenerate modes through the sweeping of uniform attenuation in complex time delay [247]; resonance trapping by varying the coupling strengths of the ports to change the zero and pole locations [162, 248–251]; excitation of off-axis poles and zeros [72, 73]; changing the length imbalance of the ring graph to achieve extremely high-Q Feshbach mode [4]; and manipulating zeros and poles of transmission and reflection time delay to get perfect or no transmission/reflection [57–63].

7.2 Future Work

One interesting direction would be the study of complex transmission time delay and difference in a broken time-reversal invariance system. In Chapter 6 of this dissertation, I demonstrate the non-reciprocal transport behavior of an Aharonov–Bohm ring graph, and it would be a great candidate for carrying out the study on complex transmission time delay in a non-reciprocal scattering system. Once we deepen our understandings on the Wigner, transmission, reflection time delays and their zeros & poles, we will have more control over the S-matrix.

In addition to the time delay analysis, the generalized Wigner-Smith operator looks very useful and can be a promising tool in various applications, including wavefront shaping and scattering property engineering. It would be interesting to introduce that operator to the 2D billiard or 3D cavity case, and vary all degrees of freedom in order to manipulate the S-matrix.

In terms of the S-matrix engineering, one interesting idea would be to create a S-matrix that eliminates all transmission from the interior port in a complex system to the outside world. This means that one would create shielding of an internal signal and create a "cone of silence". Another idea would be to have two ports inside the system that communicate with each other, but none of their signals escape through the other $M-2$ ports of the system.

For the applications presented in this dissertation, one important type of future work is to broaden the bandwidth of features like CPA, impedance matching, zero-reflection, long-lived transmission or reflection time delay, etc. The nonlinearity might be able to help with this.

There are still some puzzles about CPA: are there any limits on how many CPA events can be created in a given system with a given set of coupling coefficients? If many of the ports are poorly coupled, does this restrict the number of CPAs that one can create by means of varying

other parameters, such as lumped loss, or the settings on a metasurface array inside the enclosure? Those are the valuable questions that hopefully can be resolved in the future research.

In this dissertation, I have utilized mainly two methods in terms of zeros and poles engineering/movements, including a point-like attenuator/perturber in Chapter 2 and 3, and the spatially uniform loss/attenuation in Chapter 4. There are also other interesting ways to move zeros and poles effectively: reconfigurable metasurfaces [9, 160, 252], nonlinear elements [253], and port/channel coupling variations [162, 248]. Exploration of these methods as well as finding new perturbation approaches will be a great addition to this dissertation.

Appendix A: Theoretical Supplements for Complex Wigner Time Delay

This appendix provides additional details for some of the calculations described in the text of the dissertation. Appendix A.1 presents the mathematical foundation for extracting the positions of both poles and zeros in the complex plane from experimental measurements in the regime of well-resolved resonances. Appendix A.2 shows the detailed calculation for Eq. (4.5) on counting resonance widths via complex time delays. Appendix A.3 gives the theoretical derivations of the tails distribution of the complex Wigner time delay in the presence of uniform loss. I acknowledge Prof. Yan V. Fyodorov for providing the detailed proof and derivations in this appendix.

A.1 Extracting Poles and Zeros from Experimental Data

Here we shall assume that there is a single isolated mode in the spectrum of a scattering system. Consider a pair of single terms in the sum over n in Eqs. (3.7–3.8)

$$\mathrm{Re}\,\tau_n(f) = \left[\frac{\mathrm{Im}z_n - \eta}{(f-\mathrm{Re}z_n)^2 + (\mathrm{Im}z_n-\eta)^2} + \frac{\Gamma_n+\eta}{(f-E_n)^2+(\Gamma_n+\eta)^2}\right], \tag{A.1}$$

$$-\mathrm{Im}\,\tau_n(f) = \left[\frac{f-\mathrm{Re}z_n}{(f-\mathrm{Re}z_n)^2 + (\mathrm{Im}z_n-\eta)^2} - \frac{f-E_n}{(f-E_n)^2+(\Gamma_n+\eta)^2}\right] \tag{A.2}$$

where we 'relabeled' the energy parameter E as 'frequency' f.

Extracting the parameters $\mathrm{Re}z_n, \mathrm{Im}z_n, E_n, \Gamma_n$ and the uniform absorption strength η from the experimentally measured curves $\mathrm{Im}\,\tau_n(f)$ and $\mathrm{Re}\,\tau_n(f)$ is possible by the following procedure.

1. Let us **define** the "resonance frequency" value $f = f^*$ by the condition

$$\mathrm{Im}\,\tau_n(f^*) = 0 \tag{A.3}$$

2. Measure from the two above curves the following 3 parameters:

$$s = -\frac{d}{df}\mathrm{Im}\,\tau_n(f)|_{f=f^*}, \quad m = \mathrm{Re}\,\tau_n(f^*), \quad \delta = -\frac{1}{2}\frac{d}{df}\ln\left[\mathrm{Re}\,\tau_n(f)\right]|_{f=f^*} \tag{A.4}$$

and use them to build combinations:

$$\alpha_- = \frac{1}{2}\left(-\frac{s}{m} + m\right), \quad \alpha_+ = \frac{1}{2}\left(\frac{s}{m} + m\right) \tag{A.5}$$

The following relations then can be derived for the positions of resonance poles and zeros.

For the real parts:

$$E_n = f^* - \frac{\delta}{\delta^2 + \alpha_-^2}, \quad \mathrm{Re}\,z_n = f^* - \frac{\delta}{\delta^2 + \alpha_+^2} \tag{A.6}$$

For the imaginary parts:

$$\Gamma_n = -\eta + \frac{\alpha_-}{\delta^2 + \alpha_-^2}, \quad \mathrm{Im}\,z_n = \eta + \frac{\alpha_+}{\delta^2 + \alpha_+^2} \tag{A.7}$$

Derivation of relations (A.6) – (A.7)

Define for brevity $x_n := f^* - \mathrm{Re} z_n$, $r_n := \mathrm{Im} z_n - \eta$, $\epsilon_n := f^* - E_n$ and $p_n := \Gamma_n + \eta$.

Then condition (A.3) implies

$$\frac{x_n}{x_n^2 + r_n^2} = \frac{\epsilon_n}{\epsilon_n^2 + p_n^2} \tag{A.8}$$

Also we have by the definition

$$m = \mathrm{Re}\, \tau_n(f)|_{f=f^*} = \frac{r_n}{x_n^2 + r_n^2} + \frac{p_n}{\epsilon_n^2 + p_n^2} \tag{A.9}$$

On the other hand differentiating (A.2) gives with this notation:

$$s = -\frac{d}{df} \mathrm{Im}\, \tau_n(f)|_{f=f^*} = \frac{r_n^2 - x_n^2}{(x_n^2 + r_n^2)^2} - \frac{p_n^2 - \epsilon_n^2}{(p_n^2 + \epsilon_n^2)^2} \tag{A.10}$$

Now using the condition (A.8) the above equation simplifies to

$$s = \frac{r_n^2}{(x_n^2 + r_n^2)^2} - \frac{p_n^2}{(p_n^2 + \epsilon_n^2)^2} = \left[\frac{r_n}{(x_n^2 + r_n^2)} - \frac{p_n}{(p_n^2 + \epsilon_n^2)}\right] \left[\frac{r_n}{(x_n^2 + r_n^2)} + \frac{p_n}{(p_n^2 + \epsilon_n^2)}\right] \tag{A.11}$$

which after using (A.9) gives

$$s/m = \left[\frac{r_n}{(x_n^2 + r_n^2)} - \frac{p_n}{(p_n^2 + \epsilon_n^2)}\right] \tag{A.12}$$

Now the pair (A.9)–(A.12) implies

$$\alpha_+ := \frac{1}{2}\left(\frac{s}{m} + m\right) = \frac{r_n}{x_n^2 + r_n^2}, \quad \alpha_- := \frac{1}{2}\left(-\frac{s}{m} + m\right) = \frac{p_n}{p_n^2 + \epsilon_n^2} \tag{A.13}$$

Finally, let us consider

$$-\frac{1}{2}\frac{d}{df}\mathrm{Re}\,\tau_n(f)|_{f=f^*} = \frac{r_n x_n}{(x_n^2+r_n^2)^2} + \frac{p_n\epsilon_n}{(p_n^2+\epsilon_n^2)^2} \tag{A.14}$$

which after first using (A.8) and then (A.9) can be further rewritten as

$$= \frac{\epsilon_n}{p_n^2+\epsilon_n^2}\left[\frac{r_n}{x_n^2+r_n^2} + \frac{p_n}{p_n^2+\epsilon_n^2}\right] = \frac{\epsilon_n}{p_n^2+\epsilon_n^2}\mathrm{Re}\,\tau_n(f)|_{f=f^*}$$

implying finally

$$\delta := -\frac{1}{2}\frac{d}{df}\ln\left[\mathrm{Re}\,\tau_n(f)\right]|_{f=f^*} = \frac{\epsilon_n}{p_n^2+\epsilon_n^2} = \frac{r_n}{x_n^2+r_n^2} \tag{A.15}$$

The pair of equations (A.13) and (A.15) can be easily solved and gives (A.6) – (A.7).

So the only parameter which remains to be found from independent measurement is the uniform absorption η.

Note: Note that generically both $s = -\frac{d}{df}\mathrm{Im}\,\tau_n(f)|_{f=f^*} \neq 0$ and $m = \mathrm{Re}\,\tau_n(f)|_{f=f^*} \neq 0$ so $|\alpha_+| \neq |\alpha_-|$. We then see from Eq. (A.6) that to have $E_n = \mathrm{Re}\,z_n$ is only possible if $\delta = 0$, which in turn is only possible if $\frac{d}{df}\left[\mathrm{Re}\,\tau_n(f)\right]|_{f=f^*} = 0$. The latter condition would mean that the maximum or minimum on the curve $\mathrm{Re}\,\tau_n(f)$ happens exactly at the same frequency f^* where the imaginary part vanishes. Generically this never happens due to the two-Lorentzian nature of $\mathrm{Re}\,\tau_n(f)$.

A.2 Counting Resonance Widths via Complex Time Delays

Using complex Wigner time delay, one can obtain non-trivial information about the distribution of the imaginary part of the poles (resonance width) of the S-matrix. Denote by H the $N \times N$ Hamiltonian of the closed system, by W the $N \times M$ matrix of coupling elements between the N modes of H and the M scattering channels. The total S matrix has the form:

$$\mathcal{S}(E) = 1_M - 2\pi i W^\dagger \frac{1}{E - H + i\Gamma_W} W \text{ where } \Gamma_W = \pi W W^\dagger \tag{A.16}$$

Note that the S-matrix poles $\mathcal{E}_n = E_n - i\Gamma_n$ (with $\Gamma_n > 0$) are eigenvalues of $H - i\Gamma_W$.

In the presence of uniform absorption with strength η, the S matrix is evaluated at complex energy $S(E + i\eta) := S_\eta(E)$. The determinant of $S_\eta(E)$ is then:

$$\det S_\eta(E) \coloneqq \det S(E + i\eta) \tag{A.17}$$

$$= \frac{\det[E - H + i(\eta - \Gamma_W)]}{\det[E - H + i(\eta + \Gamma_W)]} \tag{A.18}$$

$$= \prod_{n=1}^{N} \frac{E + i\eta - \mathcal{E}_n^*}{E + i\eta - \mathcal{E}_n}, \tag{A.19}$$

Extending the definition of the Wigner time delay to uniformly absorbing systems as

$$\tau_{\mathrm{W}}(E;\eta) \coloneqq \frac{-i}{M} \frac{\partial}{\partial E} \log \det S_\eta(E) \tag{A.20}$$

we now have a complex quantity

$$\tau_{\rm W}(E;\eta) = -\frac{i}{M}\sum_{n=1}^{N}\left(\frac{1}{E+i\eta-E_n-i\Gamma_n}-\frac{1}{E+i\eta-E_n+i\Gamma_n}\right) \tag{A.21}$$

whose real and imaginary part is given by:

$$\text{Re }\tau_{\rm W}(E;\eta) = \frac{1}{M}\sum_{n=1}^{N}\left[\frac{\Gamma_n+\eta}{(E-E_n)^2+(\Gamma_n+\eta)^2}-\frac{\eta-\Gamma_n}{(E-E_n)^2+(\Gamma_n-\eta)^2}\right], \tag{A.22}$$

$$\text{Im }\tau_{\rm W}(E;\eta) = -\frac{1}{M}\sum_{n=1}^{N}\left[\frac{4\eta\Gamma_n(E-E_n)}{[(E-E_n)^2+(\Gamma_n-\eta)^2][(E-E_n)^2+(\Gamma_n+\eta)^2]}\right] \tag{A.23}$$

When the S-matrix is unitary, i.e. $\eta = 0$, the time delay is purely real and reduces to conventional Wigner time delay:

$$\tau_{\rm W}(E;0) = \frac{1}{M}\sum_{n=1}^{N}\frac{2\Gamma_n}{(E-E_n)^2+\Gamma_n^2} \coloneqq \tau_{\rm W}(E) \tag{A.24}$$

All the equations above are valid for arbitrary η. There are two characteristic energy scales in the system for energies around a value E. First is the *microscopic* one, the mean spacing between E_n in the 'closed' counterpart of our scattering system $\Delta = 1/(N\nu(E))$ where $\nu(E) = \frac{1}{N}\langle\sum_{n=1}^{N}\delta(E-E_n)\rangle$ is the mean density of resonance positions (in the case of Random Matrix Theory (RMT) the latter is the Wigner semicircle $\nu(E) = \frac{1}{2\pi}\sqrt{4-E^2}$). A second scale J is *macroscopic* and reflects a characteristic scale on which the mean density substantially changes (in RMT it is simply the width of the semicircle, $J \sim 1$). We will also introduce a useful notion of *mesoscopic* energy intervals I_E defined by $E_L < E < E_R$. Those are intervals with the length $|I| \coloneqq |E_R - E_L|$ satisfying $\Delta \ll |I| \ll J$. In other words, they contain a lot of resonances

inside, but the density of those resonances along the real axis can be assumed to be constant. Correspondingly, we will introduce the notion of the *mesoscopic energy average*, defined for any energy-dependent function $f(E)$ as

$$\langle f(E)\rangle_E = \frac{1}{|I|}\int_{E_L}^{E_R} f(E)\,dE \tag{A.25}$$

We will be interested in situations when both the typical resonance widths Γ_n and the absorption parameter η are of the order of the microscopic scale Δ (which does not necessarily mean that the resonances are isolated: some Γ_n can be several times larger than Δ, but they are considered to be always smaller than any *mesoscopic* scale). The above situation is always typical as long as the number of open channels M is of the order of unity ($M = 1$ and $M = 2$ for example). In such a situation no more than M (out of N) resonances can violate the above condition.

Our main statement is the following: under the above assumptions the mesoscopic energy average of $\mathrm{Re}[\tau_{\mathrm{W}}(E;\eta)]$ is given by

$$\langle \mathrm{Re}[\tau_{\mathrm{W}}(E;\eta)]\rangle_E = \frac{2\pi}{M\Delta} \times \text{Prob(resonance widths} > \eta) \tag{A.26}$$

where we defined

$$\text{Prob(resonance widths} > \eta) := \frac{\#[\Gamma_n > \eta \text{ such that } E_n \text{ is inside } I_E]}{\text{total \# resonances inside } I_E}$$

To verify the above statement we consider the integral:

$$\int_{E_L}^{E_R} \frac{\delta_n}{(E-E_n)^2+\delta_n^2}\,dE = \mathrm{sign}(\delta_n)\int_{(E_L-E_n)/|\delta_n|}^{(E_R-E_n)/|\delta_n|} \frac{dx}{x^2+1} \tag{A.27}$$
$$= \mathrm{sign}(\delta_n)\left\{\arctan\left(\frac{E_R-E_n}{|\delta_n|}\right) - \arctan\left(\frac{E_L-E_n}{|\delta_n|}\right)\right\}$$

We need to apply it to the right-hand side of Eq. (A.22) where $\delta_n = \eta \pm \Gamma_n$. We see that for the overwhelming majority of the summation index $n = 1, 2, \ldots, N$ there simultaneously holds two strong inequalities

$$\frac{|E_R - E_n|}{|\delta_n|} \gg 1 \quad \text{and} \quad \frac{|E_L - E_n|}{|\delta_n|} \gg 1.$$

Indeed, those inequalities can be violated only in the vicinity of the ends of the mesosocopic interval, i.e. when $|E_R, L - E_n| \sim \Delta$. The number of such terms is clearly of the order $\Delta/|I|$ which is a small parameter in the mesoscopic case. Neglecting those cases, we always can consider the arguments of $\arctan$ to be large in absolute value, hence to use $\arctan(a) \approx \frac{\pi}{2}\mathrm{sign}(a) - \frac{1}{a} + \ldots$. The contribution of subleading terms can be estimated separately (and indeed shown to be small, this time as Δ/J), and the leading terms give:

$$\langle \mathrm{Re}[\tau_{\mathrm{W}}(E;\eta)]\rangle_E \approx \frac{\pi/2}{M|I|}\sum_{n=1}^{N}\left\{\left[\mathrm{sign}\left(\frac{E_R-E_n}{\eta+\Gamma_n}\right) - \mathrm{sign}\left(\frac{E_L-E_n}{\eta+\Gamma_n}\right)\right]\right.$$
$$\left. - \left[\mathrm{sign}\left(\frac{E_R-E_n}{\eta-\Gamma_n}\right) - \mathrm{sign}\left(\frac{E_L-E_n}{\eta-\Gamma_n}\right)\right]\right\} \tag{A.28}$$

It is now evident that if E_n is outside of the mesoscopic interval (that is $E_n < E_L < E_R$ or $E_n > E_R > E_L$) the corresponding terms in the sum (A.28) vanish, whereas inside the interval

(for $E_L < E_n < E_R$) remembering $\eta + \Gamma_n > 0$ we see the corresponding terms in the summand are equal to $2(1 - \mathrm{sign}(\eta - \Gamma_n)) = 4\theta(\Gamma_n - \eta)$ where we introduced the step function $\theta(x) = 1$ for $x > 0$ and $\theta(x) = 0$ otherwise.

$$\langle \mathrm{Re}[\tau_{\mathrm{W}}(E;\eta)] \rangle_E \approx \frac{2\pi}{M|I|} \sum_{n=1}^{N} \theta(\Gamma_n - \eta) \tag{A.29}$$

Finally, remembering that under our assumptions $\#(E_n \in I) \approx |I|/\Delta$ we arrive at the statement Eq. (5) in the main text.

Remarks: The mesoscopic energy average is defined in a given system and does not involve any ensemble average. Actually, we separately proved that if one employs the RMT ensemble average (which we denote with the bar below) instead of the *mesoscopic energy average* the relation Eq. (5) holds even if we use $\tau_{\mathrm{W}}(E;\eta)$ rather than $\mathrm{Re}[\tau_{\mathrm{W}}(E;\eta)]$, namely:

$$\overline{\tau_{\mathrm{W}}(E;\eta)} = \frac{2\pi}{M\Delta} \int_{\tilde{\eta}}^{\infty} \rho_{\beta}^{(M)}(y)\, dy \tag{A.30}$$

where $\tilde{\eta} = 2\pi\eta/\Delta$ and $\rho_{\beta}^{(M)}(y)$ is the probability density of scaled resonance widths $y_n = 2\pi|\Gamma_n|/\Delta$. We see that is exactly equivalent to mesoscopic energy averaging. This means that the mesoscopic average of $\mathrm{Im}[\tau_{\mathrm{W}}(E;\eta)]$ should be parametrically smaller than for $\mathrm{Re}[\tau_{\mathrm{W}}(E;\eta)]$, and tend to zero when the length of the mesoscopic interval formally tends to infinity.

Thus, one can compare the result to known RMT expressions. In particular, for $\beta = 2$ and general two-port system one has [77, 146, 147]:

$$\rho_{\beta=2}^{(M=2)}(y) = \frac{e^{-yg_1} - e^{-yg_2}}{g_1 - g_2} \left(g_1 g_2 \phi(y) - (g_1 + g_2)\frac{d\phi}{dy} + \frac{d^2\phi}{dy^2} \right) \tag{A.31}$$

where we denoted $\phi(y) = \frac{\sinh y}{y}$ and introduced coupling constants $g_1 \geqslant 1,\ g_2 \geqslant 1$ are determined from the mean (ensemble-averaged) scattering matrix which is in that model diagonal $\overline{S_{ab}} = \delta_{ab}\overline{S_{aa}}$. Namely:

$$|\overline{S_{ab}}|^2 = \frac{g_a - 1}{g_a + 1} \tag{A.32}$$

Closed channel a corresponds to $g_a \to \infty$, perfect coupling to $g_a = 1$. If two channels are equivalent: $g_1 = g_2 = g$ we have a more compact formula:

$$\rho^{(M=2)}_{\beta=2}(y) = y\frac{d^2}{dy^2}\left(e^{-yg}\phi(y)\right) \tag{A.33}$$

Similar, but more complicated (still explicit, but in terms of 3-fold integrals) expressions are available for $\beta = 1$, see [148]. For a single-channel GOE system a much simpler explicit formula for the resonance density has been recently derived [254], with only one-fold integrals involved.

A.3 Statistical Distribution of complex Wigner time delays: Tails

Using the standard resonance representation for the unitary time delay (A.24) one can describes mechanisms [77] responsible for the formation of various regimes in the far tail of the probability density for normalized Wigner time delays $t_w = \frac{\Delta}{2\pi}\tau_{\rm W}$. Here we provide a similar consideration for the normalized real part: $\tilde{t}_w = M\frac{\Delta}{2\pi}{\rm Re}[\tau_{\rm W}]$ in the presence of a uniform absorption $\eta > 0$. Inspection of the representation Eq. (A.22) makes it clear that anomalously high values of the time delays happen when (**i**) the observation energy value E is anomalously close to

E_n and simultaneously (**ii**) the resonance widths Γ_n comes anomalously close to the absorption value η, that is $\Gamma_n - \eta \ll \eta$. In such an event the second term in Eq. (A.22) is dominant, and therefore a faithful model for the tail formation can be obtained by considering the following approximation:

$$\tilde{t}_w \approx \frac{\Delta}{2\pi} \frac{\Gamma_n - \eta}{(E - E_n)^2 + (\Gamma_n - \eta)^2} \equiv \frac{y - \tilde{\eta}}{x^2 + (y - \tilde{\eta})^2} \tag{A.34}$$

where the scaled resonance widths $y = \frac{2\pi}{\Delta}\Gamma_n$ is distributed with the probability density $\rho_\beta^{(M)}(y)$ and the variable $x = \frac{2\pi}{\Delta}(E - E_n)$ can be considered for our purposes as uniformly distributed in the interval $[-a, a]$ where a is any constant of the order of unity. We will take $a = 1$ for simplicity. Using the symmetry $x \to -x$ and introducing $w = x^2$ one can write the probability density $\mathcal{P}(\tilde{t}_w)$ in this approximation as

$$\mathcal{P}(\tilde{t}_w) = \int_0^\infty \rho_\beta^{(M)}(y)\, dy \int_0^1 \delta\left(\tilde{t}_w - \frac{y - \tilde{\eta}}{w + (y - \tilde{\eta})^2}\right) \frac{dw}{\sqrt{w}} \tag{A.35}$$

Solving the δ-constraint we find that $w = (y - \tilde{\eta})\left(\frac{1}{\tilde{t}_w} - (y - \tilde{\eta})\right)$. Due to the constraint $w > 0$ we see that this implies that the integral over x is nonzero only for y in the range $\tilde{\eta} < y < \tilde{\eta} + \frac{1}{\tilde{t}_w}$ for the right tail values $\tilde{t}_w > 0$, whereas for the left tail $\tilde{t}_w < -\tilde{\eta}^{-1}$ we have $\tilde{\eta} + \frac{1}{\tilde{t}_w} < y < \tilde{\eta}$. On the other hand it is easy to see that the upper limit constraint $w < 1$ is immaterial if we are interested in the tail $\tilde{t}_w \gg 1$, and can be replaced with $w < \infty$. Performing the integration over w gives

$$\mathcal{P}(\tilde{t}_w) = \frac{1}{\tilde{t}_w^2} \int_{\tilde{\eta}}^{\tilde{\eta} + \frac{1}{\tilde{t}_w}} \rho_\beta^{(M)}(y) \frac{y - \tilde{\eta}}{\sqrt{(y - \tilde{\eta})(\frac{1}{\tilde{t}_w} - (y - \tilde{\eta}))}}\, dy \tag{A.36}$$

and introducing $v = (y - \tilde{\eta})\tilde{t}_w$ we finally get the right tail

$$\equiv \frac{1}{\tilde{t}_w^3} \int_0^1 \rho_\beta^{(M)} \left(\frac{v}{\tilde{t}_w} + \tilde{\eta} \right) \sqrt{\frac{v}{1-v}}\, dv \tag{A.37}$$

We see that the following two situations are possible. First (using $\int_0^1 \sqrt{\frac{v}{1-v}}\, dv = \frac{\pi}{2}$) we see that for any $\tilde{\eta} > 0$ the most distant right tail has a universal exponent (for any β) given by

$$\mathcal{P}(\tilde{t}_w) \approx \frac{\pi}{2} \frac{\rho_\beta^{(M)}(\tilde{\eta})}{\tilde{t}_w^3}, \quad \tilde{t}_w \gg \frac{1}{\tilde{\eta}} \tag{A.38}$$

However, if absorption is small: $\tilde{\eta} \ll 1$ then there exists another tail regime: $1 \ll \tilde{t}_w \ll \frac{1}{\tilde{\eta}}$ where

$$\mathcal{P}(\tilde{t}_w) \approx \frac{1}{\tilde{t}_w^3} \int_0^1 \rho_\beta^{(M)} \left(\frac{v}{\tilde{t}_w} \right) \sqrt{\frac{v}{1-v}}\, dv, \tag{A.39}$$

and finally using that for small argument $\rho_\beta^{(M)}(y \ll 1) \sim \text{const}\ y^{\frac{M\beta}{2}-1}$ we arrive at the intermediate tail:

$$\mathcal{P}(\tilde{t}_w) \approx \text{const}\ \tilde{t}_w^{-\frac{M\beta}{2}-2}, \quad 1 \ll \tilde{t}_w \ll \frac{1}{\tilde{\eta}} \tag{A.40}$$

In fact this tail is exactly the same as that derived in [77, 133] for $\tilde{\eta} = 0$. Note that for the $M = 2$ port, $\beta = 2$ data shown in Fig. 1 of the main text, the power-law of the intermediate tail is expected to be $\mathcal{P}(\tilde{t}_w) \propto \tilde{t}_w^{-4}$.

Finally, for negative time delay it is easy to show that the far tail for $\tilde{t}_w < -\tilde{\eta}^{-1}$ is given by the same result (A.38), with $\tilde{t}_w \to |\tilde{t}_w|$, and this is the only asymptotic regime on the left ($\tilde{t}_w < 0$).

Now we study the far tails of the $J_w = -M\mathrm{Im}[\tau_\mathrm{W}]/\tau_\mathrm{H}$ which in the same approximation can be extracted from (A.23) as

$$J_w \approx \frac{4\tilde{\eta}yx}{[x^2+(y-\tilde{\eta})^2][x^2+4\tilde{\eta}^2]} \approx \frac{yx}{\tilde{\eta}[x^2+(y-\tilde{\eta})^2]} \tag{A.41}$$

where we used that the far tail values $|J_w| \gg 1/\tilde{\eta}$ come when $x \ll \tilde{\eta}$. Hence we also can safely consider $-\infty < x < \infty$ and write the probability density $\mathcal{P}(\tilde{t}_w)$ in this approximation as

$$\mathcal{P}\left(|J_w| \gg \tilde{\eta}^{-1}\right) = \int_0^\infty \rho_\beta^{(M)}(y)\,dy \int_{-\infty}^\infty \delta\left(J_w - \frac{1}{\tilde{\eta}}\frac{yx}{x^2+(y-\tilde{\eta})^2}\right)\,dx \tag{A.42}$$

Note that such a density is symmetric: $\mathcal{P}\left(J_w\right) = \mathcal{P}\left(-J_w\right)$, so we consider $J_w > 0$. Solving the delta-functional constraint for x, we find two values of x contributing:

$$x_{1,2} = \frac{1}{2}\left(\frac{y}{J_w\tilde{\eta}} \mp \sqrt{\left(4 - \frac{1}{J_w^2\tilde{\eta}^2}\right)(y-y_+)(y_- - y)}\right) \tag{A.43}$$

as long as $y_+ < y < y_-$ where we defined

$$y_\pm = \frac{\tilde{\eta}}{1 \pm \frac{1}{2J_w\tilde{\eta}}} \tag{A.44}$$

This gives

$$\mathcal{P}\left(|J_w| \gg \tilde{\eta}^{-1}\right) = \frac{1}{2}\int_{y_+}^{y_-} \rho_\beta^{(M)}(y)\left(\frac{1}{|\phi'(x_1)|} + \frac{1}{|\phi'(x_2)|}\right)\,dy, \quad \phi(x) := \frac{1}{\tilde{\eta}}\frac{yx}{x^2+(y-\tilde{\eta})^2} \tag{A.45}$$

Note that for $J_w\tilde{\eta} \gg 1$ the width of the integration domain over y is much smaller than the typical values $y \sim \tilde{\eta}$ as $y_- - y_+ \approx \frac{1}{J_w} \ll \tilde{\eta}$. Using this and exploiting the relation $J = \phi(x_{1,2})$ we can approximate

$$\frac{1}{|\phi'(x_{1,2})|} \approx \frac{1}{J_w^2} \frac{x_{1,2}^2}{\left|(y-\tilde{\eta})^2 - x_{1,2}^2\right|}$$

and in this way arrive to:

$$\mathcal{P}\left(J_w \gg \tilde{\eta}^{-1}\right) \approx \frac{\rho_\beta^{(M)}(\tilde{\eta})}{2J_w^2}\left(I_1 + I_2\right), \quad I_{1,2} = \int_{y_+}^{y_-} \frac{x_{1,2}^2}{\left|(y-\tilde{\eta})^2 - x_{1,2}^2\right|}\, dy \tag{A.46}$$

where $x_{1,2} \approx \frac{y}{2J_w\tilde{\eta}} \pm \sqrt{(y-y_+)(y_- - y)}$. Evaluation of the two integrals goes in a similar way, so we consider only

$$I_1 = \int_{y_+}^{y_-} \frac{\left(\frac{y}{2J_w\tilde{\eta}} + \sqrt{(y-y_+)(y_- - y)}\right)^2}{\left|\left(y - \tilde{\eta} - \frac{y}{2J_w\tilde{\eta}} - \sqrt{(y-y_+)(y_- - y)}\right)\left(y - \tilde{\eta} + \frac{y}{2J_w\tilde{\eta}} + \sqrt{(y-y_+)(y_- - y)}\right)\right|}\, dy$$

We first change variables as $y = y_+ + (y_- - y_+)t$, $0 < t < 1$ and use that for $J_w\tilde{\eta} \gg 1$ we can write

$$\frac{y_+}{2J_w\tilde{\eta}} \approx \frac{1}{2J_w}, \quad y_+ - \tilde{\eta} - \frac{y}{2J_w\tilde{\eta}} \approx 0, \quad y_+ - \tilde{\eta} + \frac{y}{2J_w\tilde{\eta}} \approx \frac{1}{J_w}, \quad y_- - y_+ \approx \frac{1}{J_w}$$

Applying the above systematically and keeping only the leading order one finds after further algebraic manipulations that

$$I_1 \approx \frac{1}{J_w}\int_0^1 \frac{\left(\frac{1}{2} + \sqrt{t(1-t)}\right)^2}{\sqrt{t(1-t}\left(\sqrt{t} + \sqrt{1-t}\right)^2}\, dt$$

The integral is well-defined and convergent and yields some positive constant whose value is however immaterial for us (in fact, substituting $t = \sin^2 \alpha,\ \alpha \in (0, \pi/2)$ brings it to a nice form). We therefore conclude that asymptotiucally both I_1 and I_2 are proportional to the factor J_w^{-1} which finally implies the tail formula:

$$\mathcal{P}\left(|J_w| \gg \tilde{\eta}^{-1}\right) \approx \text{const} \times \frac{\rho_\beta^{(M)}(\tilde{\eta})}{2J_w^3} \tag{A.47}$$

Appendix B: Evaluation of System Uniform Loss

This appendix provides additional details for the methods being used in this dissertation to evaluate the system uniform loss strength, which is denoted as η throughout the dissertation.

B.1 Evaluation of Uniform Attenuation η using Unitary Deficit of the S-matrix

The value of η is estimated in a situation in which the uniform attenuation of the coaxial cables dominates the overall loss of the system. These losses arise from metallic and dielectric loss in the cables and are quite homogeneously distributed in the system. Here we estimate the value of uniform attenuation η for the microwave graph using the unitary deficit of the S-matrix [120]. We measured the graph with the variable attenuator removed (see Fig. 3.1), and measured the 2×2 S-matrix under this no-attenuator condition. The unitary deficit of the S-matrix is expected to be $\ln|\det S| \approx -M\eta \mathrm{Re}[\tau_W]$ in the limit of low loss [120], where M is the number of channels ($M = 2$ in this setup). Fig. B.1 shows the $\det S$ and $\mathrm{Re}[\tau_W]$ versus frequency experimental data for the resonance of interest when no attenuator is present. The linear fitting function in Fig. B.1(b) determines the uniform loss strength to be $\eta = 3.73 \times 10^{-3}$ GHz. It should be noted that this method only works in the limit of very low uniform loss.

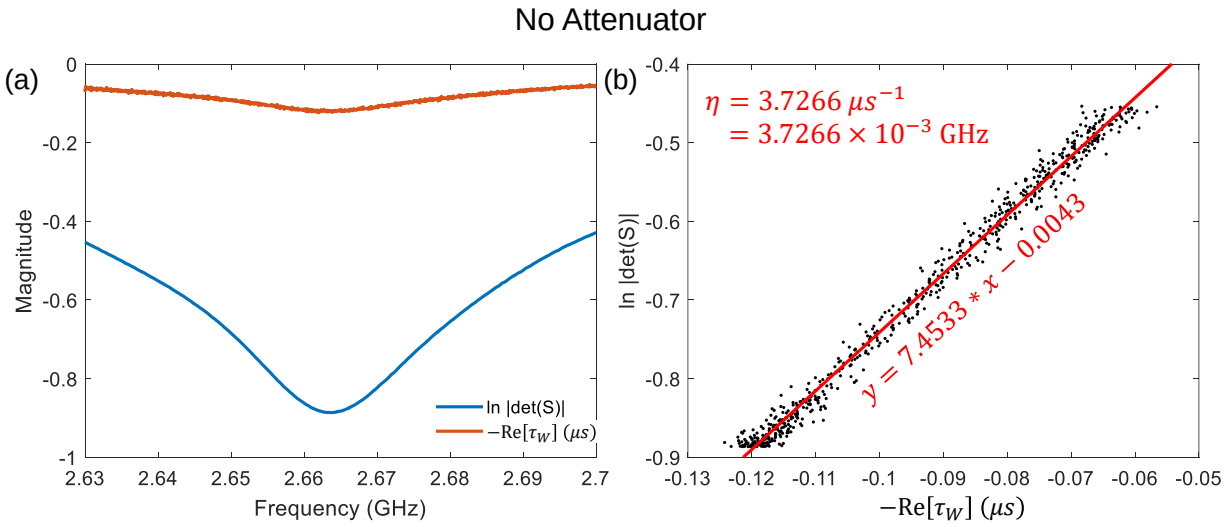

Figure B.1: (a) Measurement of $\ln|\det S|$ and $-\mathrm{Re}[\tau_W]$ as a function of frequency for the resonance of interest in a no-attenuator tetrahedral graph. (b) Plot of $\ln|\det S|$ vs. $-\mathrm{Re}[\tau_W]$ (with frequency as a parameter) and a linear fit between these two quantities to evaluate the uniform loss strength η.

B.2 Estimation of Loss Parameter α and Error Bars

In the experiment presented in Chapter 4, each frequency band is chosen to have a large number of modes (approximately 40) but small enough so that the uniform attenuation value is approximately constant. A total of 84 realizations of the graphs were created, and the data was broken into 7 frequency bands of approximately equal attenuation.

In Fig. 4.3, we plot the data points for the mean of the $\mathrm{Re}[\tau_\mathrm{W}]$ vs loss with error bars. The vertical error bars are determined by the statistical binning error $\sigma \sim \frac{1}{\sqrt{N_\mathrm{ensemble} \times N_\mathrm{mode}}}$, where N_ensemble is the number of realizations in one ensemble, and N_mode is the number of resonant modes in one realization, such that $N_\mathrm{ensemble} \times N_\mathrm{mode}$ is the total number of modes studied in one ensemble data set. The horizontal error bar is estimated from the fitting process in calculation of the system loss parameter α. The loss parameter α is defined as the ratio of the typical 3-dB

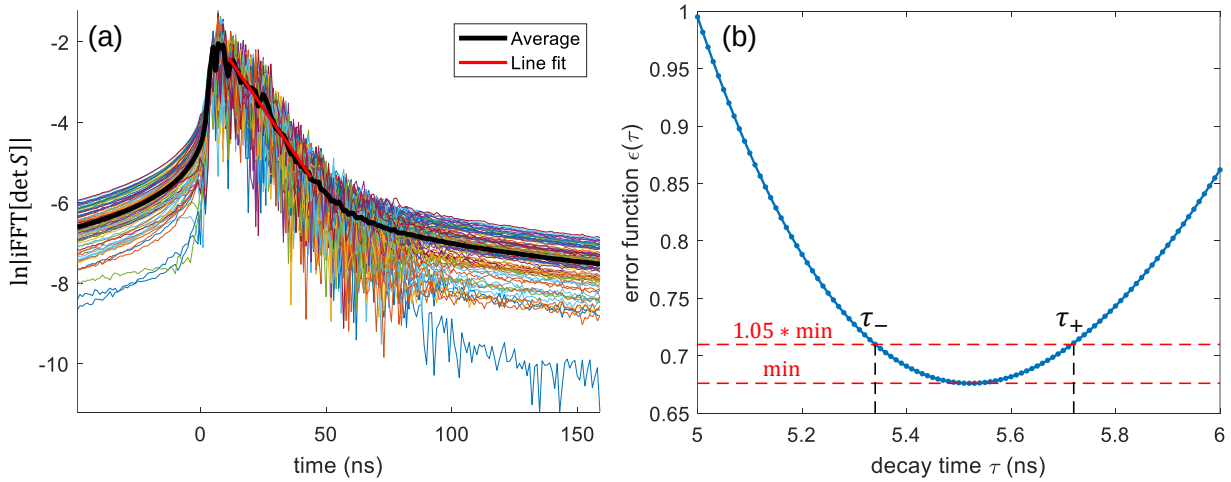

Figure B.2: (a) shows the fitting process of the inverse Fourier transformed $\det[S]$ data to the time domain. Multi-color lines show the data from each realization, and the black line is the average of all realizations. The red line shows the linear fit. (b) shows the error bar estimation for the decay time τ. Blue dotted line shows the error function $\epsilon(\tau)$ vs the decay time τ. The lower red dashed line shows the minimum level of the error function, and the upper red dashed line shows the $1.05 \times$ minimum level. The cross points of the upper red dashed line with the blue line give the error bar $[\tau_-, \tau_+]$ for the decay time τ.

bandwidth of the resonant modes to the mean mode-spacing, and it can be written as $\alpha = \frac{L_e}{2\pi c\tau}$ in the case of graph systems, where L_e is the total electrical length of the graph, c is the speed of light in vacuum, and τ is the energy decay time for the system. The energy decay time τ is obtained from the power decay profile (see Fig. B.2(a)) by inverse Fourier transforming the RCM-normalized measured data for $\det[S]$ to the time domain. By fitting to the linear portion of the ensemble average power decay profile (black line), one can get the slope and the decay time τ can be computed by $\tau = -1/(2 * \text{slope})$. Fig. B.2(b) shows the estimation of error bars for the decay time τ. The fitting process in Fig. B.2(a) gives the sample dataset $(x_i,\ y_i)$, $i = 1, 2, ..., N$ and linear function $y = kx + b$ for extracting the decay time τ. Here we define an error function $\epsilon(k) = \min\left\{\sum_i (y_i - (kx_i + b))^2\right\}$. It is easy to prove that $\epsilon(k) = \sum_i (y_i - kx_i)^2 - \frac{1}{N}\left(\sum_i (y_i - kx_i)\right)^2$. By varying the decay time τ, we can get different values of the

slope k and plot the error function $\epsilon(\tau)$ as a function of the decay time τ (see Fig. B.2(b)). The minimum error function determines the best decay time τ and we use an error level of 1.05 to estimate the error bar $[\tau_-, \tau_+]$ of decay time τ. The error bars of the decay time τ will then be transferred to the attenuation parameter $\tilde{\eta} = 4\pi\alpha = \frac{2L_e}{c\tau}$, and plotted as the horizontal error bars in Fig. 4.3.

B.3 Uniform Attenuation Estimation for Coaxial Cable

We estimate the uniform attenuation η in the ring graph system both theoretically and experimentally. From [255], we derived the corresponding expression for the uniform attenuation (Γ) of a homogeneous coaxial cable, expressed in terms of an angular frequency:

$$\Gamma = \frac{1}{2}\left[2\pi f \tan\delta + \sqrt{\frac{2\pi f\rho}{2\mu_0}}\frac{1}{\sqrt{\epsilon_r}}\frac{1}{\ln(b/a)}(\frac{1}{a}+\frac{1}{b})\right], \tag{B.1}$$

where f is the linear frequency, $\tan\delta = 0.00028$ and $\epsilon_r = 2.1$ are the dielectric loss tangent the relative dielectric constant of the Teflon dielectric, $\rho = 4.4 \times 10^{-8}\ \Omega \cdot m$ is the resistivity of the metals in the cable, $\mu_0 = 4\pi \times 10^{-7}$ H/m is the permeability of vacuum, and $a = 0.46 \times 10^{-3}$ m and $b = 1.49 \times 10^{-3}$ m are the radii of the inner and outer conductors, respectively. These values are typical for the coaxial cables used in our experiments.

We also performed a direct measurement of the uniform attenuation for the components making up the ring graph. We connected the coaxial cable and the phase shifter from Fig. 5.1(b) in series and measured the transmission S_{21} insertion loss as a function of frequency. The comparison of uniform attenuation between direct measurement (from S_{21}), fitting results (η) and the modelling (Γ) is plotted in Fig. B.3. The agreement between these three independent estimates

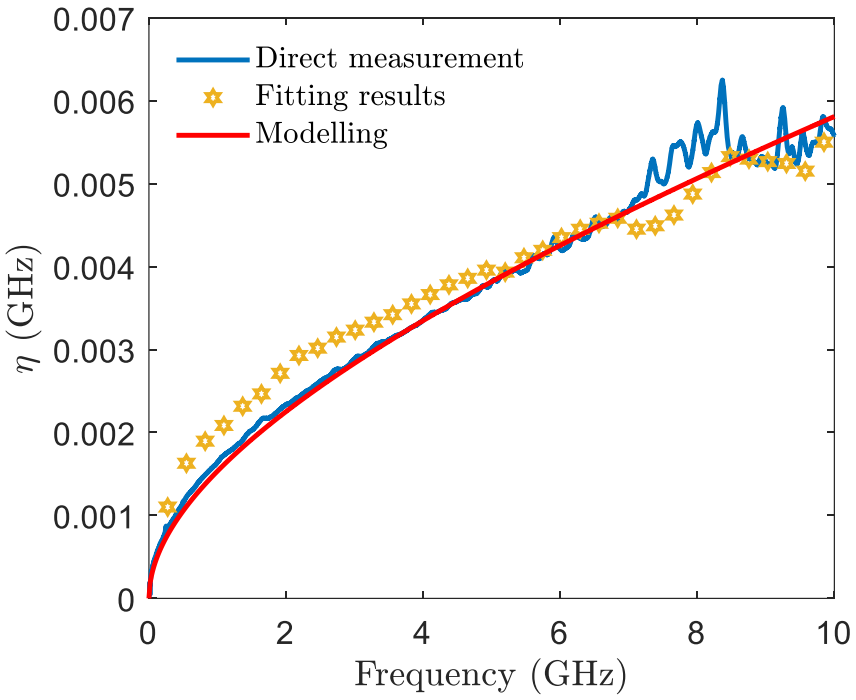

Figure B.3: Comparison of three different ways to determine the uniform attenuation of the loop graph: by means of direct measurement of insertion loss through S_{21}, fitting results to complex time delays (η), and direct modelling (Γ). The blue line shows the data obtained by measuring the S_{21} insertion loss of a serial connection of the coaxial cable and the phase shifter shown in Fig. 5.1(b). The yellow stars show the fitting results for η from the complex Wigner time delay analysis in Fig. 5.8. The red line shows the theoretical modelling (Eq. (B.1)) of $\Gamma/2\pi$ in a coaxial cable.

is reasonably good. Note that the coaxial phase shifter is not a uniform coaxial structure, and evidence of internal resonances are visible in Fig. B.3 above 7 GHz. Note that the fit η values are slightly higher than the direct loss measurement below 7 GHz, but then are slightly lower above that frequency. This comparison gives us confidence that the values of η extracted from complex time delay analysis are quite reasonable.

Appendix C: High-Precision Measurements and Numerical Calculation for Complex Time Delays

Time delay calculations (Eqs. (5.5), (5.10), (5.19), and (5.20)) require extremely high precision on the data. Both phase and amplitude information of the S-matrix are involved in the numerical derivative calculations. In order to acquire high-quality time delay data for zeros and poles extraction or statistical analysis, one must ensure that the raw data obtained from experiment are "clean".

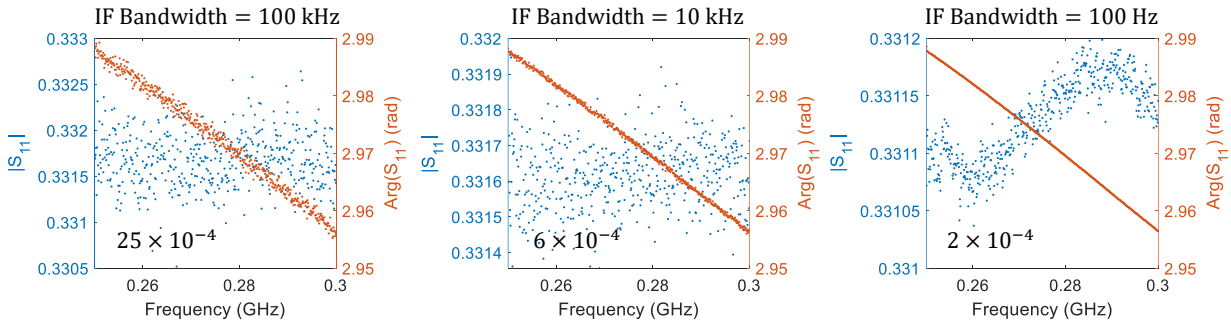

Figure C.1: Measured data for S_{11} under different settings of IF Bandwidth. Blue dots show the measured amplitude of S_{11}, while red dots show the measured phase of S_{11}. From left to right, IF Bandwidth decreases from 100 kHz to 10 kHz to 100 Hz, and the data quality has been greatly improved. An estimated fluctuation of the amplitude data is shown in each plot.

A typical workflow of the S-matrix measurement is to perform a calibration first, then do the actual measurement. The calibration process in the time delay experiments are very important, as it sets the upper limit for the quality of the measured data. In this scenario, the most significant

parameter in the setting is the "IF Bandwidth", where IF stands for intermediate frequency. When measuring S-matrix data for time delay calculations, one must reduce the IF Bandwidth setting for to improve data quality, and keep that IF Bandwidth setting through the whole process including calibration and measurement. Fig. C.1 shows the effects of different IF Bandwidth settings on the data quality of measured S_{11}, both phase and amplitude. The data is much "cleaner" as the IF Bandwidth decreases. However, there is a trade-off between IF Bandwidth and measurement time consumption. The calibration time and measurement time would increases significantly as we decrease the IF Bandwidth, especially when measuring a large number of data points. In the graph measurements, I found the sweet spot for the IF Bandwidth setting to be 100 Hz. One may use other IF Bandwidth setting as long as it offers enough precision for the time delay derivative calculations.

After getting high-quality S-matrix data from measurements, the next step is to do the numerical calculation. The straightforward way would be $\tau = \frac{\text{diff(data)}}{\text{diff(freq)}}$, with possible data smoothing techniques combined (e.g. the *movmean* function in MATLAB). A more sophisticated method is to select a window which contains a few frequency points, and solve for the linear slope fitting of these data points. The former method is usually faster, while the latter one should in principal be more accurate. For most cases with very high-quality data, the two methods usually produce similar results. Another important parameter to consider is the smoothing window size. Increasing the window size would make the data smoother, but may lose some extreme time delay information, especially if the resonance is approaching a time delay divergence (CPA) state. This also emphasizes the importance of having high-quality raw data in the first place.

Appendix D: Quantum Graphs Measurements

D.1 Microwave Networks

Through this dissertation, I have studied quantum graphs extensively. The experimental realization of quantum graph in my dissertation is to use microwave coaxial cables constructed as microwave networks.

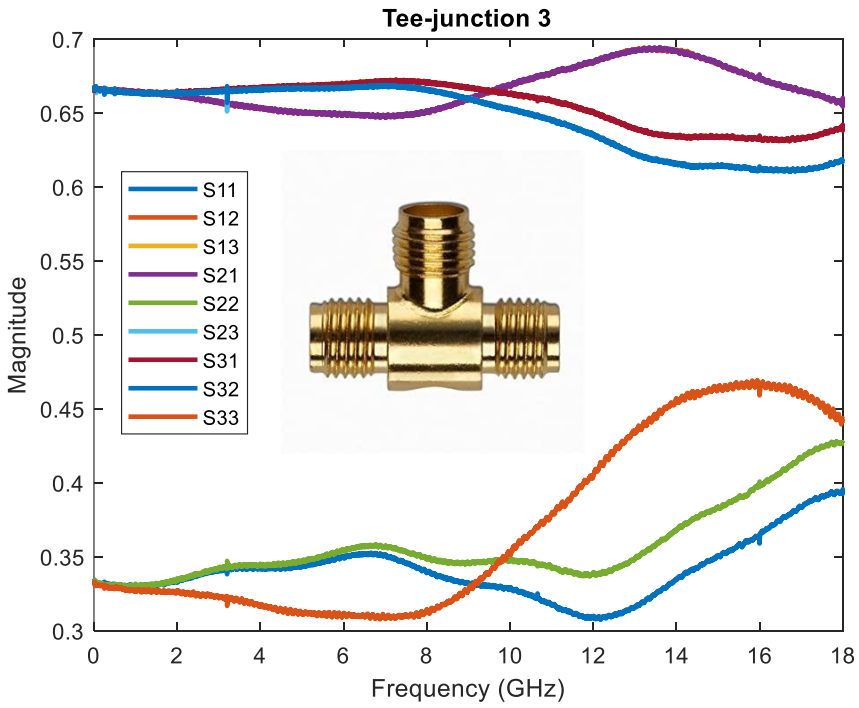

Figure D.1: S-matrix meausurement for a Tee junction. Inset shows the picture of a Tee junction with all three female ports.

In Chapter 2 and 3, I use a tetrahedral graph with a point-like attenuator (see Fig. 2.1) as the

experimental object. The tetrahedral graph is constructed from six coaxial cables and several Tee junctions. The lengths of the six coaxial cables should be incommensurate, to avoid degenerate modes in the graph. The coaxial cables used in the experiment can be flexible to form any shape of graph, but they should be kept stationary during the measurement to avoid any perturbation to the resonances. The cables have certain loss which is uniform among the whole graph, but is frequency-dependent which has been well characterized in Appendix B.3. The Tee junction (see Fig. D.1) is a three-port adapter that has finite size. It may trap waves of certain wavelength which will increase the effective loss for those frequencies. The point-like attenuator is a voltage-variable attenuator which can be easily controlled using a programmable power supply, and its attenuation can be changed continuously by sweeping the applied voltage. The attenuation from the voltage-variable attenuator is also dependent on frequency, and it has variable phase shift among different frequencies. Therefore, it does a very good job acting as a point-like perturber which offers enough perturbation to the zeros and poles. All these components have the SMA connector, and have a working frequency range of near DC to 18 GHz. Depending on whether we would like to preserve the time-reversal invariance or break it, we could put in a ordinary Tee junction or a circulator into one node of the graph. The circulator is a three-port device which has certain frequency limits. Due to the nature of the circulator design, it can be very lossy and has a large electrical length inside. As the frequency range of the circulator decreases, the size can be quite bulky. The typical workflow of measuring such a graph is to sweep the applied voltage and measure the S-matrix automatically. All procedures can be integrated to the MATLAB code and done very nicely.

In Chapter 4, I use a tetrahedral graph with fixed attenuators on each bond (see the insets of Fig. 4.3) as the experimental object. Unlike the point-like attenuator, the fixed attenuators have

a fixed value of attenuation (0.5 dB, 1 dB, 2 dB, and etc.), and offer almost constant attenuation for the whole frequency range. These fixed attenuators also have a constant phase shift (i.e. electrical length) for all frequencies. The inconvenience of these fixed attenuators is that we have to manually swap all six attenuators at once to vary the attenuation. This can be improved with motorized variable attenuators. In order to create high-quality ensemble data, we need to change the cable length every time. For now, I choose six cables out of nine ones every time, and swap the cables every time manually. In total, I get $\binom{9}{6} = 84$ combinations. The process is very time-consuming and can take up to a whole day easily. This can be much improved with motorized variable phase shifters. The typical workflow of measuring an ensemble of graph is to manually swap the coaxial cables and attenuators then measure the S-matrix. The whole process can be significantly optimized using motorized phase shifters and attenuators.

In Chapter 5 and 6, I use a ring graph structure as the experimental object. The lengths of the coaxial cables are carefully chosen for the phase-matching condition, and the S-matrix measurement is very straightforward.

D.2 Time-Reversal Invariance Breaking in Graphs by a Microwave Circulator

The issue of time-reversal invariance breaking (TRIB) is a bit subtle. It is widely believed that attenuation and dissipation in a wave propagation medium serves to break TRI. However, if one could manage to reverse all the microscopic degrees of freedom involved in dissipation, one could restore the full time-reversed propagation of the waves. In a scattering experiment time-reversal can be effectively accomplished simply by interchanging ports of the system [256]. In other words, showing that $S_{ab} \neq S_{ba}$ is direct proof that TRI is broken in the scattering system.

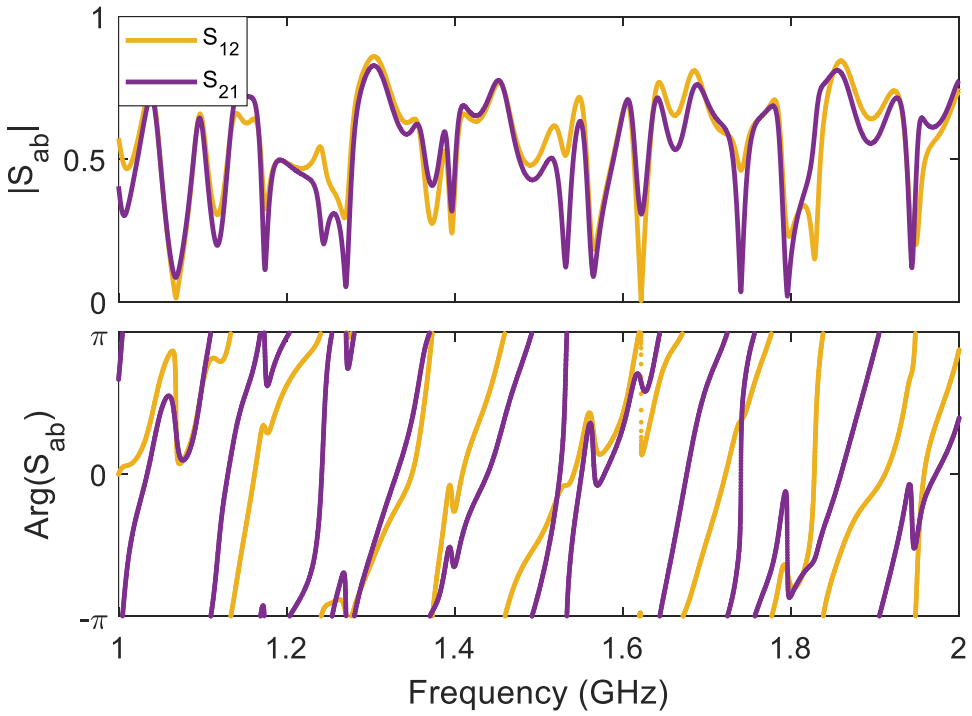

Figure D.2: Figure shows differences between S_{12} (yellow line) and S_{21} (purple line) vs frequency in a tetrahedral microwave graph containing a circulator on one internal node of the graph. In the working frequency range ($1-2$ GHz) of the microwave circulator, the two transmission parameters do not agree, neither in amplitude (upper plot) nor in phase (lower plot).

A scattering system that suffers from dissipation/loss alone will still have a symmetric scattering matrix ($S_{ab} = S_{ba}$), in general. The property of non-reciprocal wave propagation is precisely what the microwave circulator in our graph delivers, and the degree of non-reciprocity is quantified below. The microwave circulator (which contains a ferrite material biased by a dc magnetic field) creates a situation for the microwave signals that is directly analogous to the application of a magnetic field to the motion of a charged particle [257]. If we consider reversing the direction of time for wave propagation, but the magnetic field direction is not reversed, the waves will follow different trajectories when propagating through the system upon reversal of time. This effect puts the system into the unitary universality class.

We introduce microwave circulators to the graph experiments to break the time-reversal

invariance of the system [40]. From the schematic insets of Fig. 4.3, we have one internal node of the graph being replaced by a microwave circulator. This non-reciprocal device brings differences to the two transmission (S_{12} & S_{21}) parameters of the system, which is demonstrated in Fig. D.2. In order to quantitatively evaluate the degree of time-reversal invariance breaking, we use the definition of time-forward and time-reversed transmission asymmetry [256] to perform the analysis:

$$\tilde{a} = \frac{S_{12} - S_{21}}{|S_{12}| + |S_{21}|} \tag{D.1}$$

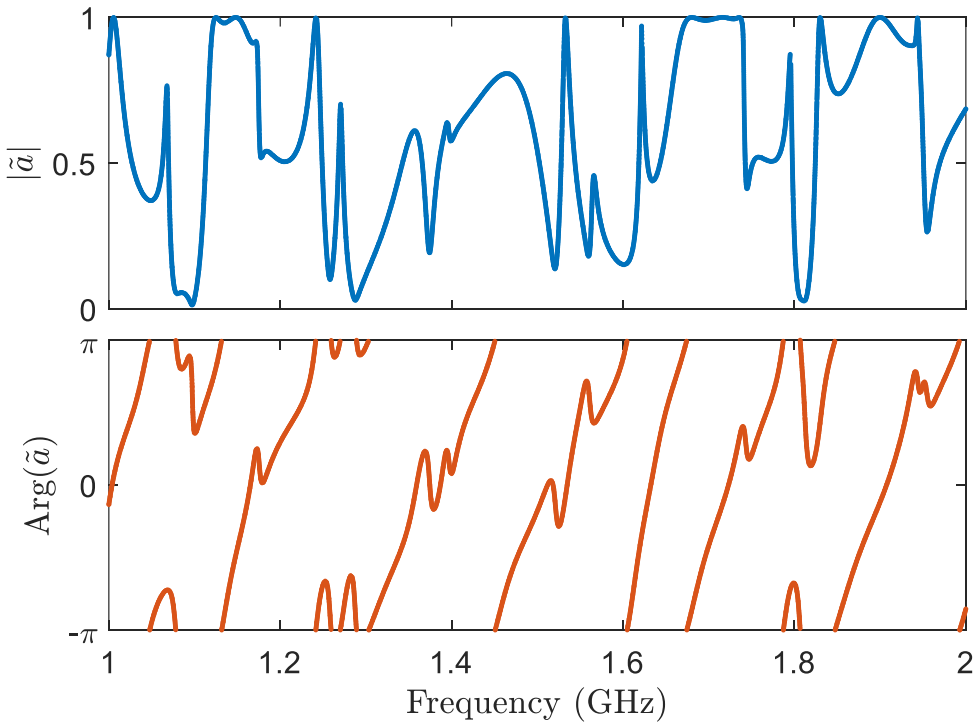

Figure D.3: Figure shows the time-reversal transmission asymmetry function $\tilde{a}$ vs frequency in a microwave graph with circulator ($1-2$ GHz). Upper plot shows the magnitude of $\tilde{a}$ vs frequency, and lower plot shows the phase of $\tilde{a}$ vs frequency.

This function has an absolute value from 0 (no symmetry breaking) to 1 (maximum sym-

metry breaking). Fig. D.3 shows an example of the asymmetry function analysis on experimental data from a realization of the tetrahedral microwave graph ($M = 2$) with circulator. The asymmetry $\tilde{a}$ shows strong fluctuations as a function of frequency, but the magnitude of $\tilde{a}$ is close to 1 for many of the frequencies. The asymmetry plot in other frequency ranges shows similar behaviors. It is then well demonstrated that one circulator in such a graph setup has a satisfactory time-reversal invariance breaking effect.

D.3 Quantifying Coupling Effects

The measured S-matrix contains not only the system-specific information, but also the coupling effects from the scattering channels (ports). The coupling channels connect the closed system to the outside world, enabling the excitation waves/energies travelling into and out of the closed system. In Chapter 4, the theoretical predictions are calculated in the limit of perfect coupling. In this dissertation, I use Random Coupling Model (RCM) [22] to remove the finite coupling effects from the experiment data, and prepare the data to be "perfectly coupled" for comparison with theory.

Figs. D.4 and D.5 show the coupling effects on the experiment data. In both plots, the radiation impedance data in yellow line is a slow-varying curve which represents the specific port property. The single realization data in blue shows strong fluctuations around the yellow line which are the resonances. The averaged impedance data in red is very close to the radiation curve with additional contributions from the short orbits. I use Eq. (1.1) to remove the finite coupling effects from measured $\hat{Z}_{\text{cav}}$ impedance matrix, and obtain the "perfectly coupled" impedance matrix $\hat{z}$ (see examples in section 4.3). Note that sometimes one can use the averaged impedance

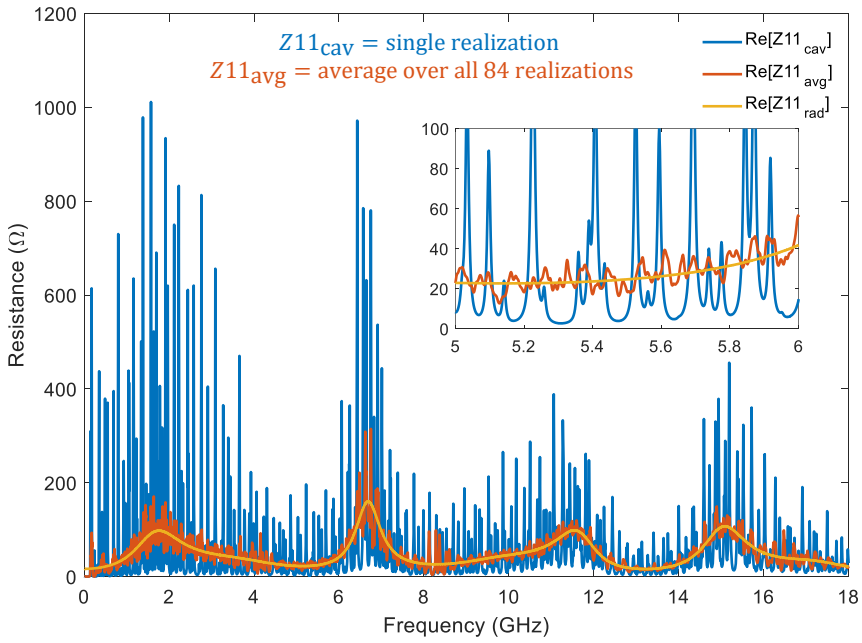

Figure D.4: Impedance experimental data Re$[Z_{11}]$ for tetrahedral graphs. Blue line is the data for a single realization. Red line shows the averaged data over all 84 realizations in this ensemble. Yellow line shows the measured radiation impedance data of port 1.

matrix $\hat{Z}_{\text{avg}}$ as the radiation impedance $\hat{Z}_{\text{rad}}$ in the formula, if the radiation data is hard to get.

In Figs. 4.7 and 4.8, I also utilize the formula to add the effects of coupling back into the RMT numerical data. One can calculate the corresponding radiation impedance matrix from the coupling strength g, and use that to generate impedance data with arbitrary coupling effects. The coupling strength g is defined as $g_a = \frac{2}{T_a} - 1$, where $T_a = 1 - |S_{\text{rad}}|^2$ is the transparency of the system to the scattering channel a determined by the value of the radiation S-matrix. Given any coupling strength g, one can get its corresponding radiation S-matrix (S_{rad}), and put that information back into Eq. (1.1) to add the finite coupling effects to the data. This approach should be very useful for the poles study, as the imaginary parts of the poles are directly related to the coupling effects.

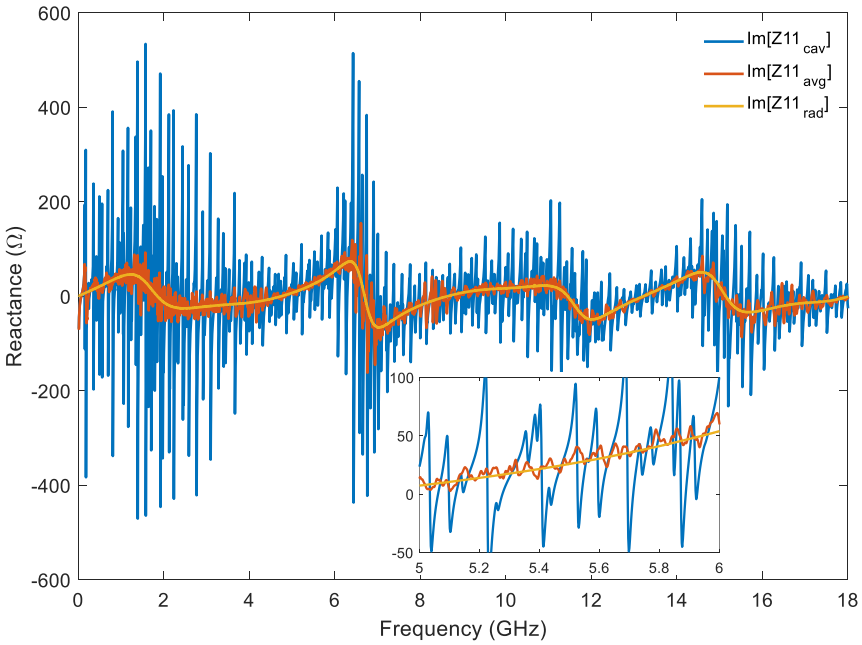

Figure D.5: Impedance experimental data Im$[Z_{11}]$ for tetrahedral graphs. The blue line is the data for a single realization. The red line shows the averaged data over all 84 realizations in this ensemble. The yellow line shows the measured radiation impedance data of port 1.

Bibliography

[1] Lei Chen, Tsampikos Kottos, and Steven M. Anlage. Perfect absorption in complex scattering systems with or without hidden symmetries. *Nature Communications*, 11(1):5826, Dec 2020.

[2] Lei Chen, Steven M. Anlage, and Yan V. Fyodorov. Generalization of Wigner time delay to subunitary scattering systems. *Physical Review E*, 103(5):L050203, May 2021.

[3] Lei Chen, Steven M. Anlage, and Yan V. Fyodorov. Statistics of complex wigner time delays as a counter of s-matrix poles: Theory and experiment. *Physical Review Letters*, 127(20):204101, 2021.

[4] Lei Chen and Steven M. Anlage. Use of transmission and reflection complex time delays to reveal scattering matrix poles and zeros: Example of the ring graph. *Phys. Rev. E*, 105:054210, May 2022.

[5] Jochen Mannhart. Beyond Superconductivity. *Journal of Superconductivity and Novel Magnetism*, 33(1):249–251, Jan 2020.

[6] P. Bredol, H. Boschker, D. Braak, and J. Mannhart. Decoherence effects break reciprocity in matter transport. *Physical Review B*, 104(11):115413, 2021.

[7] Sameer Dileep Hemmady. *A wave-chaotic approach to predicting and measuring electromagnetic field quantities in complicated enclosures*. Ph.D. Thesis, University of Maryland, 2006. available at http://hdl.handle.net/1903/3979.

[8] Matthew Frazier, Biniyam Taddese, Thomas Antonsen, and Steven M. Anlage. Nonlinear time reversal in a wave chaotic system. *Phys. Rev. Lett.*, 110:063902, Feb 2013.

[9] Benjamin W. Frazier, Thomas M. Antonsen, Steven M. Anlage, and Edward Ott. Wavefront shaping with a tunable metasurface: Creating cold spots and coherent perfect absorption at arbitrary frequencies. *Physical Review Research*, 2(4):043422, 2020.

[10] Paul So, Steven M. Anlage, Edward Ott, and Robert N. Oerter. Wave chaos experiments with and without time reversal symmetry: GUE and GOE statistics. *Physical Review Letters*, 74(14):2662–2665, Apr 1995.

[11] Min Zhou, Edward Ott, Thomas M Antonsen Jr, and Steven M Anlage. Scattering statistics in nonlinear wave chaotic systems. *Chaos: An Interdisciplinary Journal of Nonlinear Science*, 29(3):033113, 2019.

[12] G. Casati, F. Valz-Gris, and I. Guarnieri. On the connection between quantization of non-integrable systems and statistical theory of spectra. *Lettere al Nuovo Cimento*, 28(8):279–282, Jun 1980.

[13] O. Bohigas, M. J. Giannoni, and C. Schmit. Characterization of chaotic quantum spectra and universality of level fluctuation laws. *Physical Review Letters*, 52(1):1–4, Jan 1984.

[14] Hans-Jürgen Stöckmann. *Quantum Chaos: An Introduction*. Cambridge University Press, 1999.

[15] J. A. Hart, T. M. Antonsen, and E. Ott. Effect of short ray trajectories on the scattering statistics of wave chaotic systems. *Physical Review E*, 80(4):041109, Oct 2009.

[16] B. Dietz, T. Friedrich, M. Miski-Oglu, A. Richter, and F. Schäfer. Spectral properties of Bunimovich mushroom billiards. *Physical Review E*, 75(3):035203, Mar 2007.

[17] S. Hemmady, X. Zheng, E. Ott, T. M. Antonsen, and S. M. Anlage. Universal impedance fluctuations in wave chaotic systems. *Physical Review Letters*, 94(1):014102, 2005.

[18] Sameer Hemmady, James Hart, Xing Zheng, Thomas M. Antonsen, Edward Ott, and Steven M. Anlage. Experimental test of universal conductance fluctuations by means of wave-chaotic microwave cavities. *Physical Review B*, 74(19):195326, Nov 2006.

[19] Sameer Hemmady, Xing Zheng, James Hart, Thomas M. Antonsen, Edward Ott, and Steven M. Anlage. Universal properties of two-port scattering, impedance, and admittance matrices of wave-chaotic systems. *Phys. Rev. E*, 74:036213, Sep 2006.

[20] Xing Zheng, Thomas Antonsen, and Edward Ott. Statistics of impedance and scattering matrices in chaotic microwave cavities: Single channel case. *Electromagnetics*, 26(1):3–35, 2006.

[21] X. Zheng, T. M. Antonsen, and E. Ott. Statistics of impedance and scattering matrices of chaotic microwave cavities with multiple ports. *Electromagnetics*, 26(1):37–55, 2006.

[22] Gabriele Gradoni, Jen-Hao Yeh, Bo Xiao, Thomas M. Antonsen, Steven M. Anlage, and Edward Ott. Predicting the statistics of wave transport through chaotic cavities by the random coupling model: A review and recent progress. *Wave Motion*, 51(4):606–621, Jun 2014.

[23] Min Zhou, Edward Ott, Thomas M Antonsen Jr, and Steven M Anlage. Nonlinear wave chaos: statistics of second harmonic fields. *Chaos: An Interdisciplinary Journal of Nonlinear Science*, 27(10):103114, 2017.

[24] Bo Xiao, Thomas M Antonsen, Edward Ott, Zachary B Drikas, Jesus Gil Gil, and Steven M Anlage. Revealing underlying universal wave fluctuations in a scaled ray-chaotic cavity with remote injection. *Physical Review E*, 97(6):062220, 2018.

[25] Min Zhou, Edward Ott, Thomas M Antonsen Jr, and Steven M Anlage. Scattering statistics in nonlinear wave chaotic systems. *Chaos: An Interdisciplinary Journal of Nonlinear Science*, 29(3):033113, 2019.

[26] Shukai Ma, Bo Xiao, Zachary Drikas, Bisrat Addissie, Ronald Hong, Thomas M. Antonsen, Edward Ott, and Steven M. Anlage. Wave scattering properties of multiple weakly coupled complex systems. *Physical Review E*, 101(2):022201, Feb 2020.

[27] D. Kowal, U. Sivan, O. Entin-Wohlman, and Y. Imry. Transmission through multiply-connected wire systems. *Physical Review B*, 42(14):9009–9018, Nov 1990.

[28] Tsampikos Kottos and Uzy Smilansky. Quantum chaos on graphs. *Physical Review Letters*, 79(24):4794–4797, 1997.

[29] Tsampikos Kottos and Uzy Smilansky. Chaotic scattering on graphs. *Physical Review Letters*, 85(5):968–971, Jul 2000.

[30] Sven Gnutzmann and Uzy Smilansky. Quantum graphs: applications to quantum chaos and universal spectral statistics. *Advances in Physics*, 55(5-6):527–625, Jul 2006.

[31] Fritz Haake, Sven Gnutzmann, and Marek Kuś. *Quantum Signatures of Chaos*. Springer Series in Synergetics. Springer, 4 edition, 2018.

[32] Sven Gnutzmann and Alexander Altland. Universal spectral statistics in quantum graphs. *Physical Review Letters*, 93(19):194101, Nov 2004.

[33] Z. Pluhař and H. A. Weidenmüller. Universal chaotic scattering on quantum graphs. *Physical Review Letters*, 110(3):034101, Jan 2013.

[34] Z. Pluhař and H. A. Weidenmüller. Universal quantum graphs. *Physical Review Letters*, 112(14):144102, Apr 2014.

[35] Holger Schanz and Tsampikos Kottos. Scars on quantum networks ignore the lyapunov exponent. *Physical Review Letters*, 90(23):234101, Jun 2003.

[36] S. Gnutzmann, J. P. Keating, and F. Piotet. Quantum ergodicity on graphs. *Physical Review Letters*, 101(26):264102, Dec 2008.

[37] Z. Fu, T. Koch, Thomas M. Antonsen, E. Ott, and Steven M. Anlage. Experimental study of quantum graphs with simple microwave networks: non-universal features. *Acta Physica Polonica A*, 132(6):1655–1660, Dec 2017.

[38] Tsampikos Kottos and Holger Schanz. Statistical properties of resonance widths for open quantum graphs. *Waves in Random Media*, 14(1):S91–S105, 2004.

[39] Oleh Hul, Szymon Bauch, Prot Pakoński, Nazar Savytskyy, Karol Życzkowski, and Leszek Sirko. Experimental simulation of quantum graphs by microwave networks. *Physical Review E*, 69(5):056205, May 2004.

[40] Michał Ławniczak, Szymon Bauch, Oleh Hul, and Leszek Sirko. Experimental investigation of the enhancement factor for microwave irregular networks with preserved and broken time reversal symmetry in the presence of absorption. *Physical Review E*, 81(4):046204, Apr 2010.

[41] Oleh Hul, Michał Ławniczak, Szymon Bauch, Adam Sawicki, Marek Kuś, and Leszek Sirko. Are Scattering Properties of Graphs Uniquely Connected to Their Shapes? *Physical Review Letters*, 109(4):040402, Jul 2012.

[42] Małgorzata Białous, Vitalii Yunko, Szymon Bauch, Michał Ławniczak, Barbara Dietz, and Leszek Sirko. Power spectrum analysis and missing level statistics of microwave graphs with violated time reversal invariance. *Physical Review Letters*, 117(14):144101, Sep 2016.

[43] A. Rehemanjiang, M. Allgaier, C. H. Joyner, S. Müller, M. Sieber, U. Kuhl, and H.-J. Stöckmann. Microwave realization of the gaussian symplectic ensemble. *Physical Review Letters*, 117(6):064101, Aug 2016.

[44] Oleh Hul, Petr Šeba, and Leszek Sirko. Investigation of parameter-dependent properties of quantum graphs with and without time-reversal symmetry. *Physica Scripta*, T135:014048, Jul 2009.

[45] Barbara Dietz, Vitalii Yunko, Małgorzata Białous, Szymon Bauch, Michał Ławniczak, and Leszek Sirko. Nonuniversality in the spectral properties of time-reversal-invariant microwave networks and quantum graphs. *Physical Review E*, 95(5):052202, May 2017.

[46] Y. D. Chong, Li Ge, Hui Cao, and A. D. Stone. Coherent Perfect Absorbers: Time-Reversed Lasers. *Physical Review Letters*, 105(5):053901, Jul 2010.

[47] Wenjie Wan, Yidong Chong, Li Ge, Heeso Noh, A. Douglas Stone, and Hui Cao. Time-reversed lasing and interferometric control of absorption. *Science*, 331(6019):889–892, 2011.

[48] Denis G. Baranov, Alex Krasnok, Timur Shegai, Andrea Alù, and Yidong Chong. Coherent perfect absorbers: linear control of light with light. *Nature Reviews Materials*, 2(12):17064, Dec 2017.

[49] Eugene P. Wigner. Lower Limit for the Energy Derivative of the Scattering Phase Shift. *Physical Review*, 98(1):145–147, Apr 1955.

[50] Felix T. Smith. Lifetime Matrix in Collision Theory. *Physical Review*, 118(1):349–356, Apr 1960.

[51] Christophe Texier. Wigner time delay and related concepts: Application to transport in coherent conductors. *Physica E: Low-dimensional Systems and Nanostructures*, 82:16–33, Aug 2016.

[52] Stefan Rotter, Philipp Ambichl, and Florian Libisch. Generating Particlelike Scattering States in Wave Transport. *Physical Review Letters*, 106(12):120602, Mar 2011.

[53] Joel Carpenter, Benjamin J. Eggleton, and Jochen Schröder. Observation of Eisenbud–Wigner—Smith states as principal modes in multimode fibre. *Nature Photonics*, 9(11):751–757, Nov 2015.

[54] Michael Horodynski, Matthias Kühmayer, Andre Brandstötter, Kevin Pichler, Yan V. Fyodorov, Ulrich Kuhl, and Stefan Rotter. Optimal wave fields for micromanipulation in complex scattering environments. *Nature Photonics*, 14(3):149–153, Mar 2020.

[55] Jack Kuipers, Dmitry V. Savin, and Martin Sieber. Efficient semiclassical approach for time delays. *New Journal of Physics*, 16(12):123018, Dec 2014.

[56] Matthieu Davy, Zhou Shi, Jing Wang, Xiaojun Cheng, and Azriel Z. Genack. Transmission Eigenchannels and the Densities of States of Random Media. *Physical Review Letters*, 114(3):033901, Jan 2015.

[57] Y. V. Fyodorov. Reflection Time Difference as a Probe of S-Matrix Zeroes in Chaotic Resonance Scattering. *Acta Physica Polonica A*, 136(5):785–789, Nov 2019.

[58] Mohammed Osman and Yan V. Fyodorov. Chaotic scattering with localized losses: S-matrix zeros and reflection time difference for systems with broken time-reversal invariance. *Physical Review E*, 102(1):012202, Jul 2020.

[59] Yuhao Kang and Azriel Z. Genack. Transmission zeros with topological symmetry in complex systems. *Physical Review B*, 103(10):L100201, 2021.

[60] Yiming Huang, Yuhao Kang, and Azriel Z. Genack. Wave excitation and dynamics in non-hermitian disordered systems. *Physical Review Research*, 4(1):013102, 2022.

[61] S. M. I. Tsuzuki, Ye Shen, and S. Berkowitz. Ultra-selective 22-pole 10-transmission zero superconducting bandpass filter surpasses 50-pole chebyshev filter. *IEEE Transactions on Microwave Theory and Techniques*, 50(12):2924–2929, 2002.

[62] Anne-Sophie Bonnet-Ben Dhia, Lucas Chesnel, and Vincent Pagneux. Trapped modes and reflectionless modes as eigenfunctions of the same spectral problem. *Proceedings of the Royal Society A: Mathematical, Physical and Engineering Sciences*, 474(2213):20180050, 2018.

[63] William R. Sweeney, Chia Wei Hsu, and A. Douglas Stone. Theory of reflectionless scattering modes. *Physical Review A*, 102(6):063511, 2020.

[64] Huanan Li, Suwun Suwunnarat, Ragnar Fleischmann, Holger Schanz, and Tsampikos Kottos. Random matrix theory approach to chaotic coherent perfect absorbers. *Physical Review Letters*, 118(4):044101, Jan 2017.

[65] Yan V. Fyodorov, Suwun Suwunnarat, and Tsampikos Kottos. Distribution of zeros of the S -matrix of chaotic cavities with localized losses and coherent perfect absorption: non-perturbative results. *Journal of Physics A: Mathematical and Theoretical*, 50(30):30LT01, Jul 2017.

[66] Alex Krasnok, Denis Baranov, Huanan Li, Mohammad-Ali Miri, Francesco Monticone, and Andrea Alú. Anomalies in light scattering. *Advances in Optics and Photonics*, 11(4):892–951, 2019.

[67] Gabor C. Temes and Jack W. LaPatra. *Introduction to circuit synthesis and design*. McGraw-Hill, New York, 1977.

[68] L. Gao, L. Sun, F. Li, Q. Zhang, Y. Wang, T. Yu, J. Guo, Y. Bian, C. Li, X. Zhang, H. Li, J. Meng, and Y. He. 8-ghz narrowband high-temperature superconducting filter with high selectivity and flat group delay. *IEEE Transactions on Microwave Theory and Techniques*, 57(7):1767–1773, 2009.

[69] Wolfgang Porod, Zhi-an Shao, and Craig S. Lent. Resonance-antiresonance line shape for transmission in quantum waveguides with resonantly coupled cavities. *Physical Review B*, 48(11):8495–8498, 1993.

[70] Chia Wei Hsu, Bo Zhen, Jeongwon Lee, Song-Liang Chua, Steven G. Johnson, John D. Joannopoulos, and Marin Soljačić. Observation of trapped light within the radiation continuum. *Nature*, 499(7457):188–191, 2013.

[71] Zarko Sakotic, Alex Krasnok, Norbert Cselyuszka, Nikolina Jankovic, and Andrea Alú. Berreman embedded eigenstates for narrow-band absorption and thermal emission. *Physical Review Applied*, 13(6):064073, 2020.

[72] Denis G. Baranov, Alex Krasnok, and Andrea Alù. Coherent virtual absorption based on complex zero excitation for ideal light capturing. *Optica*, 4(12):1457–1461, 2017.

[73] Huanan Li, Ahmed Mekawy, Alex Krasnok, and Andrea Alù. Virtual parity-time symmetry. *Physical Review Letters*, 124(19):193901, 2020.

[74] T. R. Zhan and S. T. Chui. Theory of the spontaneous-decay enhancement in plasmonic nanoparticles based on a singularity representation of the scattering matrix. *Physical Review A*, 90(2):023802, 2014.

[75] Grant N. Remmen. Amplitudes and the riemann zeta function. *Physical Review Letters*, 127(24):241602, 2021.

[76] Francesco Monticone and Andrea Alù. Embedded photonic eigenvalues in 3d nanostructures. *Physical Review Letters*, 112(21):213903, 2014.

[77] Yan V. Fyodorov and Hans-Jürgen Sommers. Statistics of resonance poles, phase shifts and time delays in quantum chaotic scattering: Random matrix approach for systems with broken time-reversal invariance. *Journal of Mathematical Physics*, 38(4):1918–1981, Apr 1997.

[78] P. W. Brouwer, K. M. Frahm, and C. W. J. Beenakker. Quantum mechanical time-delay matrix in chaotic scattering. *Physical Review Letters*, 78(25):4737–4740, 1997.

[79] Dmitry V. Savin and Hans-Jürgen Sommers. Delay times and reflection in chaotic cavities with absorption. *Physical Review E*, 68(3):036211, Sep 2003.

[80] Stefan Rotter and Sylvain Gigan. Light fields in complex media: Mesoscopic scattering meets wave control. *Reviews of Modern Physics*, 89(1):015005, 2017.

[81] Benoît Gérardin, Jérôme Laurent, Philipp Ambichl, Claire Prada, Stefan Rotter, and Alexandre Aubry. Particlelike wave packets in complex scattering systems. *Physical Review B*, 94(1):014209, Jul 2016.

[82] Julian Böhm, Andre Brandstötter, Philipp Ambichl, Stefan Rotter, and Ulrich Kuhl. In situ realization of particlelike scattering states in a microwave cavity. *Physical Review A*, 97(2):021801(R), 2018.

[83] Wen Xiong, Philipp Ambichl, Yaron Bromberg, Brandon Redding, Stefan Rotter, and Hui Cao. Spatiotemporal Control of Light Transmission through a Multimode Fiber with Strong Mode Coupling. *Physical Review Letters*, 117(5):053901, Jul 2016.

[84] Andre Brandstötter, Adrian Girschik, Philipp Ambichl, and Stefan Rotter. Shaping the branched flow of light through disordered media. *Proceedings of the National Academy of Sciences*, 116(27):13260–13265, 2019.

[85] Hui Cao, Allard Pieter Mosk, and Stefan Rotter. Shaping the propagation of light in complex media. *Nature Physics*, 18(9):994–1007, 2022.

[86] Philipp Ambichl, Andre Brandstötter, Julian Böhm, Matthias Kühmayer, Ulrich Kuhl, and Stefan Rotter. Focusing inside disordered media with the generalized Wigner–Smith operator. *Physical Review Letters*, 119(3):033903, 2017.

[87] Michael Horodynski, Matthias Kühmayer, Clément Ferise, Stefan Rotter, and Matthieu Davy. Anti-reflection structure for perfect transmission through complex media. *Nature*, 607(7918):281–286, 2022.

[88] Shourya Dutta-Gupta, O. J. F. Martin, S. Dutta Gupta, and G. S. Agarwal. Controllable coherent perfect absorption in a composite film. *Optics Express*, 20(2):1330–1336, 2012.

[89] Shourya Dutta-Gupta, Rahul Deshmukh, Achanta Venu Gopal, Olivier J. F. Martin, and S. Dutta Gupta. Coherent perfect absorption mediated anomalous reflection and refraction. *Optics Letters*, 37(21):4452–4454, 2012.

[90] Ming Kang, Fu Liu, Teng-Fei Li, Qing-Hua Guo, Jensen Li, and Jing Chen. Polarization-independent coherent perfect absorption by a dipole-like metasurface. *Optics Letters*, 38(16):3086–3088, 2013.

[91] Jianfa Zhang, Chucai Guo, Ken Liu, Zhihong Zhu, Weimin Ye, Xiaodong Yuan, and Shiqiao Qin. Coherent perfect absorption and transparency in a nanostructured graphene film. *Optics Express*, 22(10):12524–12532, May 2014.

[92] Weiren Zhu, Fajun Xiao, Ming Kang, and Malin Premaratne. Coherent perfect absorption in an all-dielectric metasurface. *Applied Physics Letters*, 108(12):121901, 2016.

[93] Jianfa Zhang, Kevin F. MacDonald, and Nikolay I. Zheludev. Controlling light-with-light without nonlinearity. *Light: Science & Applications*, 1(7):e18, Jul 2012.

[94] Shraddha M. Rao, Julius J. F. Heitz, Thomas Roger, Niclas Westerberg, and Daniele Faccio. Coherent control of light interaction with graphene. *Optics Letters*, 39(18):5345–5347, Sep 2014.

[95] Joseph Schindler, Zin Lin, JM Lee, Hamidreza Ramezani, Fred M Ellis, and Tsampikos Kottos. $\mathcal{PT}$-symmetric electronics. *Journal of Physics A: Mathematical and Theoretical*, 45(44):444029, Nov 2012.

[96] Zi Jing Wong, Ye Long Xu, Jeongmin Kim, Kevin O'Brien, Yuan Wang, Liang Feng, and Xiang Zhang. Lasing and anti-lasing in a single cavity. *Nature Photonics*, 10(12):796–801, 2016.

[97] Chong Meng, Xiaonan Zhang, Suet To Tang, Min Yang, and Zhiyu Yang. Acoustic coherent perfect absorbers as sensitive null detectors. *Scientific Reports*, 7(1):43574, Apr 2017.

[98] Maxime Lanoy, Reine-Marie Guillermic, Anatoliy Strybulevych, and John H. Page. Broadband coherent perfect absorption of acoustic waves with bubble metascreens. *Applied Physics Letters*, 113(17):171907, Oct 2018.

[99] Jae Woong Yoon, Gang Min Koh, Seok Ho Song, and Robert Magnusson. Measurement and modeling of a complete optical absorption and scattering by coherent surface plasmon-polariton excitation using a silver thin-film grating. *Physical Review Letters*, 109(25):257402, 2012.

[100] Sucheng Li, Jie Luo, Shahzad Anwar, Shuo Li, Weixin Lu, Zhi Hong Hang, Yun Lai, Bo Hou, Mingrong Shen, and Chinhua Wang. Broadband perfect absorption of ultrathin conductive films with coherent illumination: Superabsorption of microwave radiation. *Physical Review B*, 91(22):220301, 2015.

[101] Kevin Pichler, Matthias Kühmayer, Julian Böhm, Andre Brandstötter, Philipp Ambichl, Ulrich Kuhl, and Stefan Rotter. Random anti-lasing through coherent perfect absorption in a disordered medium. *Nature*, 567(7748):351–355, Mar 2019.

[102] Klaus Richter and Martin Sieber. Semiclassical theory of chaotic quantum transport. *Physical Review Letters*, 89(20):206801, Oct 2002.

[103] Sebastian Muller and Martin Sieber. Quantum chaos and quantum graphs. In *The Oxford Handbook of Random Matrix Theory*. Oxford: Oxford University Press, 2011. edited by G. Akemann, J. Baik, and P. Di Francesco.

[104] Oleh Hul, Oleg Tymoshchuk, Szymon Bauch, Peter M. Koch, and Leszek Sirko. Experimental investigation of Wigner's reaction matrix for irregular graphs with absorption. *Journal of Physics A: Mathematical and General*, 38(49):10489–10496, Dec 2005.

[105] Ziyuan Fu. A wave chaotic study of quantum graphs with microwave networks. Master's thesis, University of Maryland, 2017. available at http://hdl.handle.net/1903/20040.

[106] Michał Ławniczak and Leszek Sirko. Investigation of the diagonal elements of the Wigner's reaction matrix for networks with violated time reversal invariance. *Scientific Reports*, 9(1):5630, 2019.

[107] Dong Ho Wu, Jesse S. A. Bridgewater, Ali Gokirmak, and Steven M. Anlage. Probability amplitude fluctuations in experimental wave chaotic eigenmodes with and without time-reversal symmetry. *Physical Review Letters*, 81(14):2890–2893, Oct 1998.

[108] Frank Cangialosi, Tyler Grover, Patrick Healey, Tim Furman, Andrew Simon, and Steven M. Anlage. Time reversed electromagnetic wave propagation as a novel method of wireless power transfer. In *2016 IEEE Wireless Power Transfer Conference (WPTC)*, pages 1–4. IEEE, May 2016.

[109] Rony Ibrahim, Damien Voyer, Arnaud Breard, Julien Huillery, Christian Vollaire, Bruno Allard, and Youssef Zaatar. Experiments of time-reversed pulse waves for wireless power transmission in an indoor environment. *IEEE Transactions on Microwave Theory and Techniques*, 64(7):2159–2170, Jul 2016.

[110] Hatem Zeine. Wireless power transmission system, February 18 2020. US Patent 10,566,846.

[111] Yan V. Fyodorov and Hans-Jürgen Sommers. Parametric Correlations of Scattering Phase Shifts and Fluctuations of Delay Times in Few-Channel Chaotic Scattering. *Physical Review Letters*, 76(25):4709–4712, Jun 1996.

[112] Petr Šeba, Karol Życzkowski, and Jakub Zakrzewski. Statistical properties of random scattering matrices. *Physical Review E*, 54(3):2438–2446, Sep 1996.

[113] Alex Krasnok, Denis G. Baranov, Andrey Generalov, Sergey Li, and Andrea Alù. Coherently enhanced wireless power transfer. *Physical Review Letters*, 120(14):143901, Apr 2018.

[114] Weijian Chen, Şahin Kaya Özdemir, Guangming Zhao, Jan Wiersig, and Lan Yang. Exceptional points enhance sensing in an optical microcavity. *Nature*, 548(7666):192–196, Aug 2017.

[115] Andreas Müllers, Bodhaditya Santra, Christian Baals, Jian Jiang, Jens Benary, Ralf Labouvie, Dmitry A. Zezyulin, Vladimir V. Konotop, and Herwig Ott. Coherent perfect absorption of nonlinear matter waves. *Science Advances*, 4(8):eaat6539, Aug 2018.

[116] F. Barra and P. Gaspard. Classical dynamics on graphs. *Physical Review E*, 63(6):066215, May 2001.

[117] A. Richter. Wave dynamical chaos: An experimental approach in billiards. *Physica Scripta*, T90(1):212–212, 2001.

[118] Ulrich Kuhl, Olivier Legrand, and Fabrice Mortessagne. Microwave experiments using open chaotic cavities in the realm of the effective Hamiltonian formalism. *Fortschritte der Physik*, 61(2-3):404–419, Feb 2013.

[119] B. Dietz and A. Richter. Quantum and wave dynamical chaos in superconducting microwave billiards. *Chaos: An Interdisciplinary Journal of Nonlinear Science*, 25(9):097601, Sep 2015.

[120] E. Doron, U. Smilansky, and A. Frenkel. Experimental demonstration of chaotic scattering of microwaves. *Physical Review Letters*, 65(25):3072–3075, 1990.

[121] A. Z. Genack, P. Sebbah, M. Stoytchev, and B. A. van Tiggelen. Statistics of wave dynamics in random media. *Physical Review Letters*, 82(4):715–718, 1999.

[122] A. A. Chabanov, Z. Q. Zhang, and A. Z. Genack. Breakdown of Diffusion in Dynamics of Extended Waves in Mesoscopic Media. *Physical Review Letters*, 90(20):203903, May 2003.

[123] H. Schanze, H.-J. Stöckmann, M. Martínez-Mares, and C. H. Lewenkopf. Universal transport properties of open microwave cavities with and without time-reversal symmetry. *Physical Review E*, 71(1):016223, Jan 2005.

[124] U. Kuhl, R. Höhmann, J. Main, and H.-J. Stöckmann. Resonance Widths in Open Microwave Cavities Studied by Harmonic Inversion. *Physical Review Letters*, 100(25):254101, Jun 2008.

[125] A. Di Falco, T. F. Krauss, and A. Fratalocchi. Lifetime statistics of quantum chaos studied by a multiscale analysis. *Applied Physics Letters*, 100(18):184101, Apr 2012.

[126] S. Barkhofen, T. Weich, A. Potzuweit, H.-J. Stöckmann, U. Kuhl, and M. Zworski. Experimental Observation of the Spectral Gap in Microwave n-Disk Systems. *Physical Review Letters*, 110(16):164102, Apr 2013.

[127] J.-B. Gros, U. Kuhl, O. Legrand, F. Mortessagne, E. Richalot, and D. V. Savin. Experimental Width Shift Distribution: A Test of Nonorthogonality for Local and Global Perturbations. *Physical Review Letters*, 113(22):224101, Nov 2014.

[128] C. Liu, A. Di Falco, and A. Fratalocchi. Dicke Phase Transition with Multiple Superradiant States in Quantum Chaotic Resonators. *Physical Review X*, 4(2):021048, Jun 2014.

[129] Matthieu Davy and Azriel Z. Genack. Selectively exciting quasi-normal modes in open disordered systems. *Nature Communications*, 9(1):4714, Dec 2018.

[130] Shanhui Fan and Joseph M. Kahn. Principal modes in multimode waveguides. *Optics Letters*, 30(2):135–137, Jan 2005.

[131] N. Lehmann, D.V. Savin, V.V. Sokolov, and H.-J. Sommers. Time delay correlations in chaotic scattering: random matrix approach. *Physica D: Nonlinear Phenomena*, 86(4):572–585, Oct 1995.

[132] Víctor A. Gopar, Pier A. Mello, and Markus Büttiker. Mesoscopic Capacitors: A Statistical Analysis. *Physical Review Letters*, 77(14):3005–3008, Sep 1996.

[133] Yan V. Fyodorov, Dmitry V. Savin, and Hans-Jürgen Sommers. Parametric correlations of phase shifts and statistics of time delays in quantum chaotic scattering: Crossover between unitary and orthogonal symmetries. *Physical Review E*, 55(5):R4857(R)–R4860(R), May 1997.

[134] P W Brouwer, K.M. Frahm, and C W J Beenakker. Distribution of the quantum mechanical time-delay matrix for a chaotic cavity. *Waves Random Media*, 9:91–104, 1999.

[135] Dmitry V. Savin, Yan V. Fyodorov, and Hans-Jürgen Sommers. Reducing nonideal to ideal coupling in random matrix description of chaotic scattering: Application to the time-delay problem. *Physical Review E*, 63(3):035202(R), Feb 2001.

[136] F. Mezzadri and N. J. Simm. Tau-Function Theory of Chaotic Quantum Transport with β = 1, 2, 4. *Communications in Mathematical Physics*, 324(2):465–513, Dec 2013.

[137] Christophe Texier and Satya N. Majumdar. Wigner time-delay distribution in chaotic cavities and freezing transition. *Physical Review Letters*, 110(25):250602, 2013.

[138] Marcel Novaes. Statistics of time delay and scattering correlation functions in chaotic systems. I. Random matrix theory. *Journal of Mathematical Physics*, 56(6):062110, Jun 2015.

[139] Fabio Deelan Cunden. Statistical distribution of the Wigner–Smith time-delay matrix moments for chaotic cavities. *Physical Review E*, 91(6):060102(R), Jun 2015.

[140] Y. V. Fyodorov, D. V. Savin, and H-J Sommers. Scattering, reflection and impedance of waves in chaotic and disordered systems with absorption. *Journal of Physics A: Mathematical and General*, 38(49):10731–10760, Dec 2005.

[141] C.W.J Beenakker and P.W Brouwer. Distribution of the reflection eigenvalues of a weakly absorbing chaotic cavity. *Physica E: Low-dimensional Systems and Nanostructures*, 9(3):463–466, Mar 2001.

[142] Y. V. Fyodorov. Induced vs. Spontaneous breakdown of S-matrix unitarity: Probability of no return in quantum chaotic and disordered systems. *Journal of Experimental and Theoretical Physics Letters*, 78(4):250–254, Aug 2003.

[143] Aurélien Grabsch. Distribution of the Wigner-–Smith time-delay matrix for chaotic cavities with absorption and coupled Coulomb gases. *Journal of Physics A: Mathematical and Theoretical*, 53(2):025202, Jan 2020.

[144] V.V. Sokolov and V.G. Zelevinsky. Dynamics and statistics of unstable quantum states. *Nuclear Physics A*, 504(3):562–588, Nov 1989.

[145] Fritz Haake, Felix Izrailev, Nils Lehmann, Dirk Saher, and Hans-Jürgen Sommers. Statistics of complex levels of random matrices for decaying systems. *Zeitschrift für Physik B Condensed Matter*, 88(3):359–370, Oct 1992.

[146] Y. V. Fyodorov and H. J. Sommers. Statistics of S-matrix poles in few-channel chaotic scattering: Crossover from isolated to overlapping resonances. *Journal of Experimental and Theoretical Physics Letters*, 63(12):1026–1030, Jun 1996.

[147] Yan V. Fyodorov and Boris A. Khoruzhenko. Systematic Analytical Approach to Correlation Functions of Resonances in Quantum Chaotic Scattering. *Physical Review Letters*, 83(1):65–68, Jul 1999.

[148] Hans-Jürgen Sommers, Yan V. Fyodorov, and Mikhail Titov. S-matrix poles for chaotic quantum systems as eigenvalues of complex symmetric random matrices: from isolated to overlapping resonances. *Journal of Physics A: Mathematical and General*, 32(5):L77–L85, Feb 1999.

[149] Yan V. Fyodorov and B. Mehlig. Statistics of resonances and nonorthogonal eigenfunctions in a model for single-channel chaotic scattering. *Physical Review E*, 66(4):045202(R), Oct 2002.

[150] Charles Poli, Dmitry V. Savin, Olivier Legrand, and Fabrice Mortessagne. Statistics of resonance states in open chaotic systems: A perturbative approach. *Physical Review E*, 80(4):046203, Oct 2009.

[151] G. L. Celardo, N. Auerbach, F. M. Izrailev, and V. G. Zelevinsky. Distribution of Resonance Widths and Dynamics of Continuum Coupling. *Physical Review Letters*, 106(4):042501, Jan 2011.

[152] Yan V. Fyodorov. Random matrix theory of resonances: An overview. In *2016 URSI International Symposium on Electromagnetic Theory (EMTS), Espoo, Finland*, pages 666–669. IEEE, 2016.

[153] Alex Krasnok, Denis Baranov, Huanan Li, Mohammad-Ali Miri, Francesco Monticone, and Andrea Alù. Anomalies in light scattering. *Advances in Optics and Photonics*, 11(4):892–951, 2019.

[154] Mohammadreza F. Imani, David R. Smith, and Philipp del Hougne. Perfect absorption in a disordered medium with programmable meta-atom inclusions. *Advanced Functional Materials*, 30(52):2005310, 2020.

[155] G. E. Mitchell, A. Richter, and H. A. Weidenmüller. Random matrices and chaos in nuclear physics: Nuclear reactions. *Reviews of Modern Physics*, 82(4):2845–2901, Oct 2010.

[156] Y V Fyodorov and D V Savin. Resonance scattering of waves in chaotic systems. In G. Akemann, J. Baik, and P. Di Francesco, editors, *The Oxford Handbook of Random Matrix Theory*, pages 703–722. Oxford University Press, 2011.

[157] Henning Schomerus. Random matrix approaches to open quantum systems. In Grégory Schehr, Alexander Altland, Yan V. Fyodorov, Neil O'Connell, and Leticia F. Cugliandolo, editors, *Stochastic Processes and Random Matrices: Lecture Notes of the Les Houches Summer School 2015*, pages 409–473. Oxford University Press, 2017.

[158] Ingrid Rotter. A non-Hermitian Hamilton operator and the physics of open quantum systems. *Journal of Physics A: Mathematical and Theoretical*, 42(15):153001, Apr 2009.

[159] V.L. Lyuboshitz. On collision duration in the presence of strong overlapping resonance levels. *Physics Letters B*, 72(1):41–44, Dec 1977.

[160] Philipp del Hougne, K. Brahima Yeo, Philippe Besnier, and Matthieu Davy. On-demand coherent perfect absorption in complex scattering systems: Time delay divergence and enhanced sensitivity to perturbations. *Laser & Photonics Reviews*, 15(7):2000471, 2021.

[161] Michał Ławniczak, Oleh Hul, Szymon Bauch, Petr Seba, and Leszek Sirko. Experimental and numerical investigation of the reflection coefficient and the distributions of Wigner's reaction matrix for irregular graphs with absorption. *Physical Review E*, 77(5):056210, May 2008.

[162] E. Persson, K. Pichugin, I. Rotter, and P. Šeba. Interfering resonances in a quantum billiard. *Physical Review E*, 58(6):8001–8004, Dec 1998.

[163] M. Durand, S. M. Popoff, R. Carminati, and A. Goetschy. Optimizing light storage in scattering media with the dwell-time operator. *Physical Review Letters*, 123(24):243901, 2019.

[164] Uzy Smilansky. Delay-time distribution in the scattering of time-narrow wave packets. (I). *Journal of Physics A: Mathematical and Theoretical*, 50(21):215301, May 2017.

[165] C. G. B. Garrett and D. E. McCumber. Propagation of a gaussian light pulse through an anomalous dispersion medium. *Physical Review A*, 1(2):305–313, 1970.

[166] S. Chu and S. Wong. Linear pulse propagation in an absorbing medium. *Physical Review Letters*, 48(11):738–741, 1982.

[167] L. A. Razo-López, A. A. Fernández-Marín, J. A. Méndez-Bermúdez, J. Sánchez-Dehesa, and V. A. Gopar. Delay time of waves performing lévy walks in 1d random media. *Scientific reports*, 10(1):20816, 2020.

[168] V. Grigoriev, A. Tahri, S. Varault, B. Rolly, B. Stout, J. Wenger, and N. Bonod. Optimization of resonant effects in nanostructures via Weierstrass factorization. *Physical Review A*, 88(1):011803(R), Jul 2013.

[169] S. M. Popoff, G. Lerosey, R. Carminati, M. Fink, A. C. Boccara, and S. Gigan. Measuring the Transmission Matrix in Optics: An Approach to the Study and Control of Light Propagation in Disordered Media. *Physical Review Letters*, 104(10):100601, Mar 2010.

[170] J.J.M. Verbaarschot, H.A. Weidenmüller, and M.R. Zirnbauer. Grassmann integration in stochastic quantum physics: The case of compound-nucleus scattering. *Physics Reports*, 129(6):367–438, Dec 1985.

[171] Pier A. Mello, Pedro Pereyra, and Thomas H. Seligman. Information theory and statistical nuclear reactions. I. General theory and applications to few-channel problems. *Annals of Physics*, 161(2):254–275, May 1985.

[172] A. Nock, S. Kumar, H.-J. Sommers, and T. Guhr. Distributions of off-diagonal scattering matrix elements: Exact results. *Annals of Physics*, 342:103–132, Mar 2014.

[173] Alexander Ossipov and Yan V. Fyodorov. Statistics of delay times in mesoscopic systems as a manifestation of eigenfunction fluctuations. *Physical Review B*, 71(12):125133, Mar 2005.

[174] Tsampikos Kottos. Statistics of resonances and delay times in random media: beyond random matrix theory. *Journal of Physics A: Mathematical and General*, 38(49):10761–10786, Dec 2005.

[175] Christophe Texier and Satya N. Majumdar. Wigner Time-Delay Distribution in Chaotic Cavities and Freezing Transition. *Physical Review Letters*, 110(25):250602, Jun 2013.

[176] Uzy Smilansky and Holger Schanz. Delay-time distribution in the scattering of time-narrow wave packets (II)—quantum graphs. *Journal of Physics A: Mathematical and Theoretical*, 51(7):075302, Feb 2018.

[177] B. A. van Tiggelen, P. Sebbah, M. Stoytchev, and A. Z. Genack. Delay-time statistics for diffuse waves. *Physical Review E*, 59(6):7166–7172, Jun 1999.

[178] Romain Pierrat, Philipp Ambichl, Sylvain Gigan, Alexander Haber, Rémi Carminati, and Stefan Rotter. Invariance property of wave scattering through disordered media. *Proceedings of the National Academy of Sciences*, 111(50):17765–17770, Dec 2014.

[179] Z. Fu, T. Koch, T. M. Antonsen, E. Ott, and S. M. Anlage. Experimental study of quantum graphs with simple microwave networks: Non-universal features. *Acta Physica Polonica A*, 132(6):1655–1660, 2017.

[180] Michał Ławniczak and Leszek Sirko. Investigation of the diagonal elements of the wigner's reaction matrix for networks with violated time reversal invariance. *Scientific Reports*, 9(1):5630, 2019.

[181] D. Agassi, H. A. Weidenmüller, and G. Mantzouranis. The statistical theory of nuclear reactions for strongly overlapping resonances as a theory of transport phenomena. *Physics Reports*, 22(3):145–179, 1975.

[182] Hans A Weidenmüller. Stochastic scattering theory random-matrix models for fluctuations in microscopic and mesoscopic systems. In *Chaos and Quantum Chaos*, pages 121–166. Springer Berlin Heidelberg, 1992.

[183] Tsampikos Kottos and Uzy Smilansky. Quantum chaos on graphs. *Phys. Rev. Lett.*, 79:4794–4797, Dec 1997.

[184] Tsampikos Kottos and Uzy Smilansky. Periodic orbit theory and spectral statistics for quantum graphs. *Annals of Physics*, 274(1):76–124, 1999.

[185] S. Gnutzmann and U. Smilansky. Quantum graphs: Applications to quantum chaos and universal spectral statistics. *Advances in Physics*, 55(5-6):527–625, 2006.

[186] Tsampikos Kottos and Uzy Smilansky. Chaotic scattering on graphs. *Phys. Rev. Lett.*, 85:968–971, Jul 2000.

[187] Tsampikos Kottos and Uzy Smilansky. Quantum graphs: a simple model for chaotic scattering. *Journal of Physics A: Mathematical and General*, 36(12):3501–3524, Mar 2003.

[188] O. Hul, O. Tymoshchuk, S. Bauch, P. M. Koch, and L. Sirko. Experimental investigation of wigner's reaction matrix for irregular graphs with absorption. *Journal of Physics a-Mathematical and General*, 38(49):10489–10496, 2005.

[189] Pavel Exner and Jiří Lipovský. Resonances from perturbations of quantum graphs with rationally related edges. *Journal of Physics A: Mathematical and Theoretical*, 43(10):105301, 2010.

[190] D. Waltner and U. Smilansky. Scattering from a ring graph - a simple model for the study of resonances. *Acta Physica Polonica A*, 124:1087–1090, 12 2013.

[191] A. Drinko, F. M. Andrade, and D. Bazeia. Narrow peaks of full transmission in simple quantum graphs. *Physical Review A*, 100(6):062117, 2019.

[192] A. Drinko, F. M. Andrade, and D. Bazeia. Simple quantum graphs proposal for quantum devices. *The European Physical Journal Plus*, 135(6):451, 2020.

[193] Herman Feshbach. Unified theory of nuclear reactions. *Annals of Physics*, 5(4):357–390, 1958.

[194] Matthew Chilcott, Ryan Thomas, and Niels Kjærgaard. Experimental observation of the avoided crossing of two s-matrix resonance poles in an ultracold atom collider. *Phys. Rev. Research*, 3:033209, Sep 2021.

[195] U. Fano. Effects of configuration interaction on intensities and phase shifts. *Physical Review*, 124(6):1866–1878, 1961.

[196] Michael Fleischhauer, Atac Imamoglu, and Jonathan P. Marangos. Electromagnetically induced transparency: Optics in coherent media. *Reviews of Modern Physics*, 77(Copyright (C) 2010 The American Physical Society):633, 2005.

[197] Sven Gnutzmann, Holger Schanz, and Uzy Smilansky. Topological resonances in scattering on networks (graphs). *Physical Review Letters*, 110(9):094101, 2013.

[198] Evgeny N. Bulgakov and Dmitrii N. Maksimov. Topological bound states in the continuum in arrays of dielectric spheres. *Physical Review Letters*, 118(26):267401, 2017.

[199] Michał Ławniczak, Ji ří Lipovský, Małgorzata Białous, and Leszek Sirko. Application of topological resonances in experimental investigation of a fermi golden rule in microwave networks. *Phys. Rev. E*, 103:032208, Mar 2021.

[200] D. C. Marinica, A. G. Borisov, and S. V. Shabanov. Bound states in the continuum in photonics. *Physical Review Letters*, 100(18):183902, 2008.

[201] Bo Zhen, Chia Wei Hsu, Ling Lu, A. Douglas Stone, and Marin Soljačić. Topological nature of optical bound states in the continuum. *Phys. Rev. Lett.*, 113:257401, Dec 2014.

[202] Chia Wei Hsu, Bo Zhen, A. Douglas Stone, John D. Joannopoulos, and Marin Soljačić. Bound states in the continuum. *Nature Reviews Materials*, 1(9):16048, 2016.

[203] Hugo M. Doeleman, Francesco Monticone, Wouter den Hollander, Andrea Alù, and A. Femius Koenderink. Experimental observation of a polarization vortex at an optical bound state in the continuum. *Nature Photonics*, 12(7):397–401, 2018.

[204] E. S. C. Ching, P. T. Leung, A. Maassen van den Brink, W. M. Suen, S. S. Tong, and K. Young. Quasinormal-mode expansion for waves in open systems. *Reviews of Modern Physics*, 70(4):1545–1554, 1998.

[205] Philip Trøst Kristensen, Kathrin Herrmann, Francesco Intravaia, and Kurt Busch. Modeling electromagnetic resonators using quasinormal modes. *Advances in Optics and Photonics*, 12(3):612–708, 2020.

[206] Andrey E. Miroshnichenko, Sergej Flach, and Yuri S. Kivshar. Fano resonances in nanoscale structures. *Reviews of Modern Physics*, 82(3):2257, 2010.

[207] Liang Huang, Ying-Cheng Lai, Hong-Gang Luo, and Celso Grebogi. Universal formalism of fano resonance. *AIP Advances*, 5(1):017137, 2015.

[208] Zhi-an Shao, Wolfgang Porod, and Craig S. Lent. Transmission resonances and zeros in quantum waveguide systems with attached resonators. *Physical Review B*, 49(11):7453–7465, 1994.

[209] Boris Luk'yanchuk, Nikolay I. Zheludev, Stefan A. Maier, Naomi J. Halas, Peter Nordlander, Harald Giessen, and Chong Tow Chong. The fano resonance in plasmonic nanostructures and metamaterials. *Nature Materials*, 9(9):707–715, 2010.

[210] C. L. Garrido Alzar, M. A. G. Martinez, and P. Nussenzveig. Classical analog of electromagnetically induced transparency. *American Journal of Physics*, 70(1):37–41, 2002.

[211] Shanhui Fan. Sharp asymmetric line shapes in side-coupled waveguide-cavity systems. *Applied Physics Letters*, 80(6):908–910, 2002.

[212] V. A. Fedotov, M. Rose, S. L. Prosvirnin, N. Papasimakis, and N. I. Zheludev. Sharp trapped-mode resonances in planar metamaterials with a broken structural symmetry. *Physical Review Letters*, 99:147401, 2007.

[213] N. Papasimakis, V. A. Fedotov, N. I. Zheludev, and S. L. Prosvirnin. Metamaterial analog of electromagnetically induced transparency. *Physical Review Letters*, 101(25):253903, 2008.

[214] Cihan Kurter, Philippe Tassin, Lei Zhang, Thomas Koschny, Alexander P. Zhuravel, Alexey V. Ustinov, Steven M. Anlage, and Costas M. Soukoulis. Classical analogue of electromagnetically induced transparency with a metal-superconductor hybrid metamaterial. *Physical Review Letters*, 107(4):043901, 2011.

[215] P. Troughton. High Q factor resonators in microstrip. *Electronics Letters*, 4:520–522(2), November 1968.

[216] Kai Chang and Lung-Hwa Hsieh. *Microwave Ring Circuits and Related Structures*. Wiley Interscience, Hoboken, New Jersey, 2nd edition, 2004.

[217] Il Wolff. Microstrip bandpass filter using degenerate modes of a microstrip ring resonator. *Electronics letters*, 8(12):302–303, 1972.

[218] Qianfan Xu, Sunil Sandhu, Michelle L. Povinelli, Jagat Shakya, Shanhui Fan, and Michal Lipson. Experimental realization of an on-chip all-optical analogue to electromagnetically induced transparency. *Physical Review Letters*, 96(12):123901, 2006.

[219] Kouki Totsuka, Norihiko Kobayashi, and Makoto Tomita. Slow light in coupled-resonator-induced transparency. *Physical Review Letters*, 98(21):213904, 2007.

[220] Ang Li and Wim Bogaerts. Tunable electromagnetically induced transparency in integrated silicon photonics circuit. *Optics Express*, 25(25):31688–31695, 2017.

[221] Li Fan, Jian Wang, Leo T. Varghese, Hao Shen, Ben Niu, Yi Xuan, Andrew M. Weiner, and Minghao Qi. An all-silicon passive optical diode. *Science*, 335(6067):447–450, 2012.

[222] M. Büttiker, Y. Imry, and M. Ya. Azbel. Quantum oscillations in one-dimensional normal-metal rings. *Phys. Rev. A*, 30:1982–1989, Oct 1984.

[223] D. Kowal, U. Sivan, O. Entin-Wohlman, and Y. Imry. Transmission through multiply-connected wire systems. *Physical Review B*, 42(14):9009–9018, 1990.

[224] Supriyo Datta. *Electronic transport in mesoscopic systems*. Cambridge studies in semiconductor physics and microelectronic engineering ; 3. Cambridge University Press, Cambridge ;, 1995.

[225] Y. Aharonov and D. Bohm. Significance of electromagnetic potentials in the quantum theory. *Physical Review*, 115(3):485–491, 1959.

[226] R. A. Webb, S. Washburn, C. P. Umbach, and R. B. Laibowitz. Observation of $\frac{h}{e}$ aharonov-bohm oscillations in normal-metal rings. *Physical Review Letters*, 54(25):2696–2699, 1985.

[227] J. Mannhart, H. Boschker, and P. Bredol. Non-unitary quantum electronics: Novel functions from the edge of the quantum world. *Nano Express*, 2(1):014008, 2021.

[228] R. C. Jaklevic, John Lambe, A. H. Silver, and J. E. Mercereau. Quantum interference effects in josephson tunneling. *Physical Review Letters*, 12(7):159–160, 1964.

[229] A. H. Silver and J. E. Zimmerman. Quantum states and transitions in weakly connected superconducting rings. *Physical Review*, 157:317–341, 1967.

[230] M. Tinkham. *Introduction to Superconductivity*. McGraw-Hill, New York, 2nd edition, 1996.

[231] Daniel S. Fisher and Patrick A. Lee. Relation between conductivity and transmission matrix. *Physical Review B*, 23(12):6851–6854, 1981.

[232] Daniel Waltner and Uzy Smilansky. Transmission through a noisy network. *Journal of Physics A: Mathematical and Theoretical*, 47(35):355101, 2014.

[233] Vladimir A. Mandelshtam and Howard S. Taylor. Harmonic inversion of time signals and its applications. *The Journal of Chemical Physics*, 107(17):6756–6769, 1997.

[234] Jan Wiersig and Jörg Main. Fractal weyl law for chaotic microcavities: Fresnel's laws imply multifractal scattering. *Physical Review E*, 77(3):036205, 2008.

[235] V. Grigoriev, S. Varault, G. Boudarham, B. Stout, J. Wenger, and N. Bonod. Singular analysis of fano resonances in plasmonic nanostructures. *Physical Review A*, 88(6):063805, 2013.

[236] Minjae Lee and Maciej Zworski. A fermi golden rule for quantum graphs. *Journal of Mathematical Physics*, 57(9):092101, 2016.

[237] R. Schäfer, T. Gorin, T. H. Seligman, and H. J. Stöckmann. Fidelity amplitude of the scattering matrix in microwave cavities. *New Journal of Physics*, 7:152–152, 2005.

[238] R. Schäfer, H.-J. Stöckmann, T. Gorin, and T. H. Seligman. Experimental verification of fidelity decay: From perturbative to fermi golden rule regime. *Phys. Rev. Lett.*, 95:184102, Oct 2005.

[239] B. Taddese, J. Hart, T. Antonsen, E. Ott, and S. Anlage. Sensor based on extending the concept of fidelity to classical waves. *Applied Physics Letters*, 95(11):114103, 2009.

[240] B. Taddese, T. Antonsen, E. Ott, and S. Anlage. Sensing small changes in a wave chaotic scattering system. *Journal of Applied Physics*, 108(11):114911–14, 2010.

[241] B. Taddese, G. Gradoni, F. Moglie, T. Antonsen, E. Ott, and S. Anlage. Quantifying volume changing perturbations in a wave chaotic system. *New Journal of Physics*, 15(2):023025, 2013.

[242] Jan Wiersig. Enhancing the sensitivity of frequency and energy splitting detection by using exceptional points: Application to microcavity sensors for single-particle detection. *Physical Review Letters*, 112(20):203901, 2014.

[243] Hossein Hodaei, Absar U. Hassan, Steffen Wittek, Hipolito Garcia-Gracia, Ramy El-Ganainy, Demetrios N. Christodoulides, and Mercedeh Khajavikhan. Enhanced sensitivity at higher-order exceptional points. *Nature*, 548(7666):187–191, 2017.

[244] Michael del Hougne, Sylvain Gigan, and Philipp del Hougne. Deeply subwavelength localization with reverberation-coded aperture. *Physical Review Letters*, 127(4):043903, 2021.

[245] Y. Aharonov and D. Bohm. Significance of electromagnetic potentials in the quantum theory. *Phys. Rev.*, 115:485–491, Aug 1959.

[246] William R. Sweeney, Chia Wei Hsu, Stefan Rotter, and A. Douglas Stone. Perfectly absorbing exceptional points and chiral absorbers. *Physical Review Letters*, 122(9):093901, 2019.

[247] Shukai Ma. *Wave chaos in microwave coupled enclosures, reservoir computing, and photonic topological insulator graphs: theory and experiment*. Ph.D. Thesis, University of Maryland, 2022. available at https://doi.org/10.13016/3xvu-91k1.

[248] E. Persson, I. Rotter, H.-J. Stöckmann, and M. Barth. Observation of Resonance Trapping in an Open Microwave Cavity. *Physical Review Letters*, 85(12):2478–2481, Sep 2000.

[249] H. J. Stockmann, E. Persson, Y. H. Kim, M. Barth, U. Kuhl, and I. Rotter. Effective hamiltonian for a microwave billiard with attached waveguide. *Physical Review E*, 65(6):066211, 2002.

[250] B Belchev, SG Neale, and MA Walton. Flow of s-matrix poles for elementary quantum potentials. *Canadian Journal of Physics*, 89(11):1127–1140, 2011.

[251] S. Ceci, M. Hadžimehmedović, H. Osmanović, A. Percan, and B. Zauner. Fundamental properties of resonances. *Scientific Reports*, 7(1):45246, 2017.

[252] Benjamin W. Frazier, Thomas M. Antonsen, Steven M. Anlage, and Edward Ott. Deep-learning estimation of complex reverberant wave fields with a programmable metasurface. *Phys. Rev. Applied*, 17:024027, Feb 2022.

[253] Suwun Suwunnarat, Yaqian Tang, Mattis Reisner, Fabrice Mortessagne, Ulrich Kuhl, and Tsampikos Kottos. Non-linear coherent perfect absorption in the proximity of exceptional points. *Communications Physics*, 5(1):1–7, 2022.

[254] Yan V Fyodorov and Mohammed Osman. Eigenfunction non-orthogonality factors and the shape of CPA-like dips in a single-channel reflection from lossy chaotic cavities. *Journal of Physics A: Mathematical and Theoretical*, 55(22):224013, May 2022.

[255] David M Pozar. *Microwave Engineering*. John Wiley & Sons, Inc., 2011.

[256] Florian Schäfer. *Time-reversal symmetry breaking in quantum billiards*. Ph.D. Thesis, Technische Universität Darmstadt, 2009. available at https://tuprints.ulb.tu-darmstadt.de/id/eprint/1329.

[257] Paul So, Steven M. Anlage, Edward Ott, and Robert N. Oerter. Wave Chaos Experiments with and without Time Reversal Symmetry: GUE and GOE Statistics. *Physical Review Letters*, 74(14):2662–2665, Apr 1995.